Air-Filled Substrate Integrated Waveguide (AFSIW) Filters and multiplexers for space application

Tifenn Martin

université de BORDEAUX

THÈSE PRÉSENTÉE

POUR OBTENIR LE GRADE DE

DOCTEUR DE

L'UNIVERSITÉ DE BORDEAUX

ÉCOLE DOCTORALE SCIENCES PHYSIQUES ET DE L'INGÉNIEUR

SPÉCIALITÉ ÉLECTRONIQUE

Par Tifenn MARTIN

Air-Filled Substrate Integrated Waveguide (AFSIW) Filters and Multiplexers for Space Applications

Sous la direction de : Anthony GHIOTTO
(co-directeur : Tan-Phu VUONG)

Soutenue le 17 décembre 2019

Membres du jury :

Mme. MANEUX, Cristell	Professeur	Université de Bordeaux	Présidente
M. BLONDY, Pierre	Professeur	Université de Limoges	Rapporteur
M. BOZZI, Maurizio	Professeur	Université de Pavie	Rapporteur
M. CARPENTIER, Ludovic	Docteur	CNES	Examinateur
M. MARTIN IGLESIAS, Petronilo	Ingénieur	ESA/ESTEC	Examinateur
M. GHIOTTO, Anthony	MCF, HDR	Bordeaux INP	Directeur de thèse
M. VUONG, Tan-Phu	Professeur	Université de Grenoble Alpes	Co-directeur de thèse
M. LOTZ, Frédéric	Ingénieur	Cobham	Co-encadrant
M. DEBORGIES, François	Ingénieur	ESA/ESTEC	Membre invité
M. GOUJON, Christophe	Ingénieur	DGA	Membre invité

Synthèse en français

Le Chapitre 1 présente un bref historique de l'avènement des micro-ondes avec une attention particulière sur leurs implémentations dans les applications spatiales. Le développement des premiers satellites ainsi que les différentes avancées techniques mises en œuvre pour améliorer les performances des filtres et multiplexeurs sont expliquées. Le Chapitre 1 donne quelques comparatifs entre les différentes orbites de lancement d'un satellite ainsi que les tendances économiques actuelles du secteur du spatial qui permettent de mieux comprendre la forte ascension des constellations de satellites. Ensuite, dans ce même Chapitre, les technologies émergentes de filtrage sont introduites. Ces technologies sont toutes de bonnes candidates pour leurs implémentations dans les futures générations de charges utiles de satellites. Un focus particulier est donné à la technologie Air-Filled Substrate Integrated Waveguide (AFSIW), qui est la technologie avec laquelle les travaux de thèse ont été développés. Enfin, pour appuyer le choix de la technologie AFSIW, un comparatif des facteurs de qualités obtenus avec les technologies conventionnelles est donné. Il en ressort que la technologie AFSIW semble être une excellente candidate en termes de compromis entre la taille, la masse, le coût, et les performances obtenues.

Le Chapitre 2 introduit d'une manière technique la technologie AFSIW. Cette technologie, basée sur les techniques de circuit imprimé multicouches standard, a pour but d'atteindre les performances électriques de guides d'ondes métalliques conventionnels tout en gardant un coût de production très faible, car facilement implémentable en production de masse. La structure du AFSIW y est détaillée ainsi que les différents moyens d'implémenter les murs électriques. Un comparatif des facteurs de qualités obtenus suivant le choix d'implémentation des murs électriques est donné. Il s'en suit une démonstration en mesure d'une ligne de transmission basée sur la technologie AFSIW. Les pertes d'insertion obtenues sont en accord avec les simulations, ce qui démontre la validité de la structure. Pour étudier la technologie plus en profondeur, des tests en puissance ont été faits sur le prototype de ligne de transmission. Afin de se rapprocher des conditions d'utilisations du domaine du spatial, le test de puissance a été mené dans une étuve à vide permettant de descendre à des pressions de l'ordre de 10^{-5} mbar. Les tests ont démontré que la structure proposée était capable de tenir au minimum une puissance de 190 W en CW (Continuous Wave) à une pression de 10^{-5} mbar. La ligne de transmission a donc été validée théoriquement, en simulations, en mesures petits signaux, et en mesures de puissance. De par les bons résultats de cette ligne, un filtre basé sur la technologie AFSIW a été développé. Ce filtre est un passe-bande du 4ème ordre avec une fréquence de travail de 21 GHz et une bande passante relative de 1.45%. Le filtre a été conçu en utilisant les méthodes conventionnelles de synthèse de filtre. Puis, il a été fabriqué et assemblé. Les mesures de ce filtre montrent d'excellents résultats. En effet, toutes les caractéristiques principales du filtre mesuré sont très proches du filtre simulé. Dans un souci de rigueur et de comparaison, le filtre a aussi été caractérisé en tests de puissance. Additionnellement au test de puissance sous vide, il a aussi été choisi d'effectuer un test de multipaction et un test d'effet corona sur le filtre. Ces deux phénomènes sont très présents dans les applications spatiales et demandent une attention particulière pour les caractériser. Tous les tests prévus ont été menés à bien et il a été conclu que le filtre développé tenait une puissance de 190 W sous une pression de 10^{-5} mbar avec une température stabilisée de 90 °C. De plus, le filtre n'a montré aucun effet multipactor jusqu'à une puissance de 190 W. Enfin, un effet corona a été déclenché dans le filtre à une pression critique de 26 mbar avec une puissance d'entrée de 10 W.

Dans le Chapitre 3, une nouvelle topologie de ligne de transmission est développée. Elle a pour but de souligner le caractère versatile de la technologie AFSIW. Pour cela, les procédés standards des circuits imprimés sont associés aux procédés de report de composants traversants. Cela ouvre de nouvelles possibilités pour le développement de la plateforme technologique AFSIW. En effet, la topologie de ligne de transmission développée permet d'implémenter des composants dits configurables, tels que des déphaseurs, des résonateurs, et des filtres grâce à un réseau de trous situé dans la couche inférieure et supérieure de la technologie. Dans un premier temps, la ligne de transmission est étudiée théoriquement. L'implémentation du réseau de trous augmente les pertes d'insertion de la ligne de transmission. Néanmoins, d'un point de vue masse et thermique, cette structure est plus performante qu'une ligne de transmission AFSIW conventionnelle. Pour illustrer ce propos, une ligne de transmission dite PAFSIW (basée sur le principe énoncé précédemment) est fabriquée et comparée à la ligne de transmission AFSIW développée dans le Chapitre 2. Ces deux lignes sont pesées dans un premier temps, il est constaté que la ligne perforée permet une réduction de la masse de 22%, ce qui n'est pas négligeable pour une charge utile. Un test de puissance est ensuite effectué sur les deux structures. Il y est démontré que l'échauffement de la ligne AFSIW est de 25 °C comparé à l'échauffement de la ligne PAFSIW de 18 °C. La structure permet donc d'améliorer la diffusion thermique grâce au réseau de trous. Il s'en suit le développement de fonction de base telle que des déphaseurs, des résonateurs, et des filtres. Grâce à l'insertion de barreaux métalliques traversant de haut en bas la structure, des murs électriques discontinus sont créés, assurant ainsi la fonction hyperfréquence du composant. Enfin, le principe de diffusion thermique est appliqué sur un filtre basé sur la structure PAFSIW et est comparé au même filtre basé sur la structure AFSIW. Il est démontré que le filtre PAFSIW a une meilleure diffusion thermique. Ce principe peut donc être utile dans les applications à fortes contraintes thermiques.

Le Chapitre 4 détaille l'introduction de zéro de transmission dans des fonctions de filtrage basées sur la technologie AFSIW. L'aspect multicouche de la technologie est judicieusement utilisé pour implémenter un chemin secondaire, aussi appelé couplage croisé, pour l'onde électromagnétique. Ainsi, en jouant avec les déphasages des deux chemins, il est possible de créer une annulation de signal qui causera l'apparition de zéro de transmission dans les bandes de réjection du filtre. Pour démontrer le principe proposé, un filtre du 3ème ordre est développé. Les différentes phases des chemins sont étudiées pour trouver la topologie adéquate à implémenter. Puis, dans un souci de reproductibilité, une analyse de Monte Carlo est menée pour évaluer l'impact des tolérances de fabrication sur la structure. Une étude sur le possible désalignement des couches et son impact sur la réponse du filtre est aussi faite. Enfin, comme une partie de l'onde se propage dans un matériau diélectrique, une étude prenant en compte l'incertitude de la permittivité du matériau est menée pour étudier son influence sur le comportement du filtre. Il s'en suit une fabrication du prototype et une validation par la mesure. Le principe ayant été validé sur un filtre d'ordre 3, de manière incrémentale, le principe est adapté à un filtre d'ordre 4. Les déphasages sont encore une fois étudiés ainsi que les études d'incertitudes. Le prototype est fabriqué, assemblé, et mesuré. Les résultats sont en excellent accord avec les simulations. Il s'en suit une remarque critique sur l'implémentation de couplage croisé sur des structures dites "en long". En effet, le couplage croisé est implémenté grâce à une ligne de transmission SIW qui possède une longueur électrique définie. Plus cette longueur est grande, plus la réponse large bande du filtre est susceptible d'être polluée. Pour contrer cet effet, le principe du couplage croisé est implémenté sur une structure de filtre dite "repliée". Ce type de structure permet de rapprocher les résonateurs qui doivent être couplés par le couplage croisé et ainsi réduire

la longueur électrique de la ligne de transmission SIW. Le filtre replié est fabriqué et mesuré. Les résultats sont en accord avec les simulations. L'amélioration de la réponse large bande du filtre est bien démontrée. Enfin, dans ce Chapitre, un filtre répondant à des spécifications industrielles est proposé. Ce filtre doit fonctionner en bande Ku en se conformant à des spécifications sur ses réjections, variations de pertes d'insertion et variations de temps de groupe. Le filtre proposé pour répondre à cette demande met en application le principe expliqué ci-dessus. Il est enfin montré par la mesure que le prototype fabriqué respecte bien toutes les spécifications attendues.

Le Chapitre 5 aborde une problématique souvent négligée par les concepteurs de filtres. Il s'agit de l'étude du comportement d'un filtre en température. Les filtres embarqués dans des charges utiles de satellites subissent souvent des changements drastiques de température. Un changement de température du filtre impacte directement les dimensions physiques du filtre par le biais de dilatations dimensionnelles des matériaux de base du filtre. Ces changements de dimensions physiques ont pour conséquence de changer la fréquence de résonance du filtre. Ainsi, si les spécifications de filtrage demandées sont sévères et ne permettent pas de latitude, le filtre ne remplira plus sa fonction à une température autre que la température ambiante. Pour résoudre ce problème, l'idée développée dans le Chapitre 5 est de compenser thermiquement le filtre. Ainsi, la fréquence de résonance du filtre deviendrait indépendante de la température, ce qui assurerait le bon fonctionnement du filtre, peu importe la température à laquelle il est. Pour cela, la technologie AFSIW est encore une fois utilisée judicieusement. Le principe proposé pour compenser thermiquement les filtres est de laisser des barreaux de diélectriques sur le côté des cavités résonantes. En choisissant correctement le diélectrique, il est possible de trouver un matériau qui a une permittivité qui décroit avec une augmentation de la température et qui augmente avec une diminution de la température. Pour une augmentation de température donnée, les dimensions de la cavité se dilateront, causant ainsi la diminution de la fréquence de résonance vers les fréquences basses. Néanmoins, pour cette même augmentation de température, la permittivité du matériau diminuera, causant l'augmentation de la fréquence de résonance vers les fréquences hautes. Ainsi, il est possible de trouver les dimensions adéquates de la cavité et des barreaux de diélectrique pour assurer une stabilisation de la fréquence de résonance de la cavité avec le changement de température. Les briques de base d'un filtre AFSIW sont des cavités résonantes et des fenêtres de couplage. Une étude théorique est menée sur l'impact des variations de température sur les fenêtres de couplage. Il est démontré que cet impact est négligeable. Il est en déduit qu'un filtre AFSIW peut être compensé thermiquement si et seulement si les cavités de ce filtre sont compensées thermiquement. La mise en application du principe proposé est démontrée en mesure. Dans un premier temps et dans un souci de comparaison, un filtre non-compensé et un filtre compensé thermiquement sont fabriqués et comparés à température ambiante. Le filtre compensé thermiquement présente une augmentation de ses pertes d'insertion, ce qui est attendu, car des pertes diélectriques sont ajoutées. Puis, une mesure en température est réalisée. Il est démontré expérimentalement que le filtre compensé thermiquement permet d'avoir une stabilité thermique de la fréquence de résonance de l'ordre du ppm/°C, ce qui est très semblable à la stabilité thermique de matériau thermiquement noble, comme l'Invar, qui a cependant un coût très élevé.

Le Chapitre 6 présente la mise en application de tous les principes développés dans les Chapitres précédents pour la conception d'un multiplexeur d'entrée, plus communément appelé IMUX, d'une charge utile de satellite. Les spécifications demandées pour cet IMUX portent dans un premier temps sur la réduction de

masse et d'empreinte au sol. La technologie AFSIW développée dans le Chapitre 2 est un très bon candidat pour répondre à ces contraintes. De plus, l'IMUX présente de fortes contraintes sur ses isolations entre bandes passantes. Pour répondre à ce critère, le principe développé dans le Chapitre 4 est implémenté sur cet IMUX. L'IMUX doit également pouvoir être opérationnel sur la gamme de température -20 °C/+70 °C. Ainsi, le principe développé dans le Chapitre 5 est implémenté afin de s'affranchir de la gamme de température. Enfin, l'IMUX peut être sensible aux défauts de fabrication. Pour contrer cela, les principes expliqués dans le Chapitre 3 peuvent être mis en place pour contrer ce phénomène. Différentes configurations d'IMUX sont données et les avantages et inconvénients de chaque configuration sont regroupés dans un tableau. En se basant sur les spécifications demandées en termes de taille, poids, et performances, la configuration d'IMUX couplé par un « manifold » est adoptée. Puis, la configuration géométrique dite « herringbone » est choisie en prenant en compte les mêmes arguments énoncés précédemment. L'IMUX est ensuite développé avec la technologie AFSIW en mettant en application les principes développés tout au long de cette thèse. Les simulations du composant sont données. Cependant, la fabrication n'étant pas encore terminée à l'heure où cette thèse est rédigée, les résultats expérimentaux de l'IMUX seront présentés durant la soutenance orale de ces travaux.

La thèse est ensuite conclue en récapitulant les éléments majeurs développés. Ces travaux de thèse représentent une base solide pour les développements futurs de la technologie AFSIW. Une analyse critique est ensuite donnée sur les travaux qu'il serait judicieux de mener pour étayer les techniques développées.

Contents

Acronyms

AFSIW	Air-Filled Substrate Integrated Waveguide
APHC	Average Power Handling Capability
BW	Bandwidth
CM	Coupling Matrix
CNES	Centre National d'Études Spatiales
CTE	Coefficient of Thermal Expansion
CW	Continuous Wave
DUT	Device Under Test
DR	Dielectric Resonator
EM	Electromagnetic
EMC	Electromagnetic Compatibility
EPC	Electronic Power Conditioner
ESA	European Space Agency
FR-4	Flame Resistant 4
GEO	Geostationary Earth Orbit
GNSS	Global Navigation Satellite System
GPS	Global Positioning System
HPA	High-Power Amplifier
HTS	High-Temperature Superconductors
IL	Insertion Loss
IMUX	Input Multiplexer
IoT	Internet of Thing
ITU	International Telecommunication Union
LEO	Low Earth Orbit
LNA	Low Noise Amplifier
LO	Local Oscillator
LTCC	Low Temperature Co-Fired Ceramics
MEO	Medium Earth Orbit
MMIC	Monolithic Microwave Integrated Circuit
OMUX	Output Multiplexer
PAFSIW	Perforated Air-Filled Substrate Integrated Waveguide
PCB	Printed Circuit Board
PEC	Perfect Electric Conductors
PIM	Passive InterModulation
RF	Radio Frequency
RL	Return Loss
RMS	Root Mean Square
RWG	Rectangular Waveguide
SEY	Secondary Electron Yield
SISL	Substrate Integrated Suspended Line
SIW	Substrate Integrated Waveguide
SL	Suspended Line
SLA	Stereolithographic
SNR	Signal Noise Ratio
SoS	System-on-Substrate
SWaP-C	Size Weight Power and Cost
tanδ	Loss tangent
TCP	Thermal Coefficient of Permittivity
TE	Transverse Electric
TEM	Tranverse Electric Magnetic
Tg	Glass Transition Temperature
THM	Through-Hole Mounted
TM	Transverse Magnetic

TMTC	Telemetry and Telecommand
TRL	Thru-Reflect-Line
Tz	Transmission zero
VNA	Vector Network Analyzer
VSAT	Very Small Aperture Terminals
WR	Waveguide, Rectangular
3D	Three-dimensional space
5G	Fifth generation of mobile

Introduction

With the emergence of novel microwave and millimeter-wave applications in the automotive and communication sectors including the internet of things (IoT), the fifth generation of mobile (5G), and the new space, innovative technologies providing size, weight, power, and cost (SWaP-C) reduction are highly desired. In fact, since the last decades, the space market has significantly grown and is expected to provide satellite services (television, the Internet…) to more people on the Earth's surface. Hence, the space industry is undergoing a change of paradigm that pushes it to implement mega-constellation satellite to furnish a global communication service. To meet the projected high-volume market demands, future microwave and millimeter-wave components are expected to provide high integrability, lightweight, high power-handling, and low loss at a reduced cost compared to their counterparts based on conventional technologies. Furthermore, the stringent specifications of the foreseen systems require rapid synthesis, with high robustness to manufacturing tolerances, and a low sensitivity to external environment. All those challenges represent a technological gap for the new generation of satellite payload.

Among the satellite payload components, filters and multiplexers are crucial components in the architecture. The stringent specifications in terms of low loss, selectivity, out-of-band rejections guide the microwave community to use the conventional air-filled metallic waveguide technology to meet the desired electrical performances. Moreover, the conventional air-filled metallic waveguide technology has a low sensitivity to the space environment and is well mastered by the space industry. Nevertheless, the prohibitive cost, large size, and high weight characteristics are detrimental for the foreseen applications, in particular for implementation in the emerging new space applications. Indeed, with the foreseen rise in frequency, the future generation of filters and multiplexers need to have high performance at an effective cost.

In the presented new space context, the Air-Filled Substrate Integrated Waveguide (AFSIW) technology combining the advantages of the planar technologies and the conventional air-filled rectangular waveguide technology is expected to contribute to the development and democratization of the emerging novel microwave and millimeter-wave low-cost space applications. Furthermore, the AFSIW technology inherits the high integration characteristics of the Substrate Integrated Waveguide (SIW) and the so-called System on Substrate (SoS) paradigm can be implemented for the future satellite communication systems. The AFSIW technological platform has demonstrated to be a successful technological trade-off in terms of size, weight, power, and cost (SWaP-C) and seems to be a good candidate for the implementation of next future generations of filters and multiplexers.

Consequently, this Doctoral Thesis investigates the feasibility of Air-Filled Substrate Integrated Waveguide technology applied to space applications, in particular, to microwave filters and multiplexers.
The Thesis is organized as follows:

Chapter 1 is devoted to a general context of the study. A brief sum up of the milestones in microwave engineering with particular focus on space applications is described. The space context is then presented with

the different important aspect to take into account for the implementation of a microwave filter in a satellite payload. Finally, the emerging filter technologies and techniques are presented.

The second Chapter presents an overview of the AFSIW technological platform. A transmission line and a bandpass filter operating in the Ka-band satellite communication frequency range are designed and demonstrated. A mechanical test fixture is also fabricated to be able to characterize those components in small and high-power signal. The first power-handling tests (continuous wave power-handling test, multipactor test, and corona test) on AFSIW technology are also reported.

In Chapter 3, an original AFSIW structure based on the conventional PCB and the through-hole mounting (THM) process, with enhanced robustness to manufacturing tolerances is introduced. It opens up new possibilities for the AFSIW technological platform as a configurable transmission line is demonstrated. This configurable component is able to implement different microwave component functions, such as phase shifters, resonators, and filters. Moreover, an original method to tune resonator frequency is proposed. Finally, the high interest of this structure is highlighted with an enhanced thermal dissipation compared to conventional AFSIW.

Chapter 4 is dedicated to the implementation of transmission zeros in the AFSIW technological platform. Thus, the multilayer aspect of the technology is profitably used to create transmission zeros in AFSIW filters using an SIW transmission line in the bottom substrate to cross-couple non-adjacent cavities. The principle is first demonstrated on classical topologies, such as third-order and fourth-order filter. The concept is extended to a higher order filter face to real filtering specifications, in terms of rejections, insertion loss variation, and group delay variation. The specifications were proposed by ESA (European Space Agency) and CNES (Centre National d'Études Spatiales) with the aim of implementing this filter in an Input Multiplexer.

Chapter 5 details the problems linked to temperature drift for microwave filter. Two temperature compensation techniques for AFSIW filters are introduced. The two techniques are developed such as it can be adapted to any component based on AFSIW cavities. The principles are developed in the Ku-band, for the need of ESA and CNES, and extended in the Ka-band for future implementation. It is demonstrated that the AFSIW technology, based on PCB process, can achieve a comparable thermal stability than costly and high-performance materials, such as Invar.

Finally, Chapter 6 presents the implementation of all the principles introduced in the previous Chapters into an IMUX using the AFSIW technology. The IMUX specifications were proposed by ESA and CNES to address most of the actual IMUX problematic. Unfortunately, the measurements of this IMUX are not done yet. Thus, only simulations will be shown in this manuscript.

In the Conclusions, the results of this Doctoral thesis are summarized. An overview of the developed techniques for AFSIW filters are given as well as the foreseen future work.

Chapter 1

General Context of the Study

1. 1. Milestones in Microwave Engineering with Particular Focus on Space Applications

The foundations of microwave theory were established by scientists like Maxwell (1879), Hertz (1894), Marconi (1937), Lodge (1940), Tesla (1943), and Loomis (1975) over about 100 years ago [1]. The formal and theoretical foundations of electromagnetic theory was presented by Maxwell in *A treatise on Electricity and Magnetism*. Even though many contributors participated in the development of the electromagnetic before 1900, Maxwell's work stated the existence of electromagnetic waves traveling at the speed of light [2]. Maxwell's theory and equations, by associating electricity and magnetism, write down the microwave theory and engineering. The past, present, and future applications based on electromagnetic theory, such as radio, television, generation of mobile networks, satellite systems, and radio detection and ranging (radar) systems, are based on the theoretical foundations of Maxwell.

World War II has substantially contributed to technological innovations. It is sometimes referred to as the Physicist's War because for the first time, technological innovation was at the heart of the battlefield [3]. In the early 1920s, emerging radar technology providing the potential of detecting planes, ships, and submarines and to determine their location attracted the attention of military researchers. This is why, in the 1940s, the first major radar installation was constructed along the southern and eastern English coast by the Royal Air Force to detect the incoming German bombers. This installation was called Chain Home and is one of the first practical application of microwave theory. The effectiveness of the radar technology led to unprecedented stimulus to develop microwave theory and technique for civil and military applications [4].

In the 1890s, the development of radio was growing, and many scientists and physicists believed that radio waves could not travel long distances. This was assumed because the direction of propagation of waves was in straight lines. In 1901, Marconi proved them wrong with the first message transfer from Great Britain to Canada over the Atlantic Ocean using a wireless telegraph [5]. Later on, Kennelly and Heaviside proposed that the long radio waves used by Marconi were bouncing off an atmospheric layer of ions, today called ionosphere. The British scientist Appleton proved its existence in 1924. The proposed concept of bouncing off the ionosphere foreshadowed the modern communications satellite.

Satellite communications were some of the first commercial microwave worldwide application. The world's first satellite was launched in October 1957, by the Soviet Union, under the name of Sputnik I. The satellite was launched into an elliptical orbit and was a 58 cm diameter metal sphere and weighted 84 kg. Following Sputnik I, the Soviet Union launched Sputnik II and thus triggered what is today called the Space Race. The first United States artificial satellite was launched in January 1958, under the name of Explorer I. It was the first satellite to detect the Van Allen radiation belt. On August 12, 1960, the United States deployed Echo I in low orbit earth (LEO), this satellite was designed specifically for microwave communications.

Indeed, the metallic surface of Echo I was used to reflecting the incident waves to link two different ground stations. Hence, Echo I was the first and the last satellite to be described as a passive satellite, as the next communication satellites implement active components such as mixers and amplifiers.

Satellite communications became more and more popular due to their diverse applications and turned out to be the first major civilian applications of microwave engineering, after TV. In the late 1960s, the launch of Intelsat I, II, and III series established the strong basis of satellite applications for voice communications. In 1971, Intelsat IV series was launched and based on a channelized architecture [6], [7]. At that time, the microwave filters used for channelization used conventional rectangular waveguide structure based on filter synthesis techniques developed in [8].

In order to maximize bandwidth and signal efficiency for the satellite, filters, input multiplexers (IMUXs), and output multiplexers (OMUXs) with low insertion loss are essential. Thus, the chosen filter technology to implement the uplink/downlink was conventional metallic waveguide. Filters and multiplexers were fabricated using iris-coupled Invar cavities to ensure low insertion loss and a good thermal behavior. Based on the proposed technology, the developed filters and multiplexers were bulky and heavy, a typical channel filter had a mass approximating 4 kg [7]. At that time, multiplexers represented nearly 40% of the payload weight. The mass of these filters became crucial and many methods were introduced to reduce it. The first technique to reduce the mass of these multiplexers was to reduce the waveguide wall thickness while meeting the necessary manufacturing constraints [7]. The second technique introduced to minimize the mass of the filters and multiplexers was to use lightweight materials, such as Kevlar or graphite [9]. This technique enabled sufficient weight reduction to accommodate 24 channels for the first time in the U.S. domestic satellite launched in 1975 [10]. Nevertheless, these filters were more complex to fabricate than conventional Invar filters, and new ideas were needed to develop the future of satellite communications.

The use of two orthogonal degenerate modes in a single cavity was first suggested by Lin [11] in 1951. Then, a practical implementation of dual-mode filters was established by [12] in 1969. This led to an impetus for the development of dual-mode filters which settled the theoretical foundations and viability of this topology [13]-[15]. A classical dual-mode in-line waveguide filter is presented in Fig. 1.1. Taking advantage of perpendicular modes, dual-mode filters allow a single physical cavity to behave as two electrical ones. In the classical dual-mode in-line filter, each cavity supports two orthogonal transverse electric (TE) modes TE_{101} and TE_{111} [13]. The two modes are coupled with a tuning screw orientated at 45° to the input iris [14]. The proposed structure also had the advantage to allow coupling between non-adjacent cavities, permitting the implementation of transmission zeros. Moreover, the principle of dual-mode filters provides a substantial mass and space savings as the number of physical resonators can be divided by 2, while achieving comparable electrical function, compared to conventional iris-coupled metallic waveguide filters [15]. The major development of dual-mode filters were incorporated in Intelsat IV in 1976 [16]. From then on, dual-mode filters became the satellite industry standard.

Next to the dual-mode filter development, it was intuitive for microwave researchers to focus their work in implementing more than two modes in a single physical cavity. Triple- and quadruple-mode resonators have been investigated. In order to have a single cavity that supports three modes, researchers had to find a mode that could resonate at the same frequency and be orthogonal with the two existing TE_{101} and TE_{111} modes. The challenge was to find an iris structure that can control three inter-cavity simultaneously. In [17], variety of

mode charts for rectangular and circular waveguide had been developed. After identifying the potential three existing modes in a single cavity, a new iris structure capable of providing three independent inter-cavity couplings must be implemented. This type of iris structure is presented in [18], it also reports the first true elliptic six-pole triple-mode filter. Later on, quadruple-mode resonators have been studied. This configuration is based on a cylindrical cavity dual orthogonal transverse magnetic (TM) mode. In [19], an eight-pole bandpass filter based on quadruple-mode is reported. Nevertheless, the triple- and quadruple-mode filter structure were too sensitive to manufacturing tolerances and have demonstrated poor thermal stability. This is why, most of the triple-mode and all the quadruple-mode filter has not been used for satellite applications.

The Intelsat IV established the commercial viability of the C-band (6/4 GHz) satellite systems [7]. This impetus led to the adoption of higher frequencies, in particular, the Ku-band (14/12 GHz) for satellite communications. This rise in frequencies led to a large reduction in size of microwave components. It also led the standard designs to be obsolete as with the rise in frequencies comes the ascent in insertion loss. Thus, it raises the challenge of designing high performance microwave components for Ku-band applications. The logical way to achieve this goal was to increase the unloaded *Q* of resonators to counter effect the increase of insertion loss. The practical realization of this principle was the introduction of filters similar to the dual-mode filter represented in Fig. 1.1. Those filters were based on TE_{10n} and TE_{11n} modes [20]. The physical realization of these filters implemented the cavity length equal to *n* time the half-wavelength [21].

Another major advance in microwave filter technology was the introduction of dielectric resonators. The work on dielectric resonators started in the 1930s. The use of high permittivity dielectric materials offers large reduction in size and weight compared to conventional waveguide technology [22]. However, high performance thermally-stable dielectric material was not available until the 1970s. The most significant development in the implementation of dielectric resonator in a filter function was made by Fiedziuszko [23] in 1982. The proposed filter is shown in Fig. 1.2, it is similar to the dual-mode filter presented previously except the resonator are loaded with dielectric material. The concentration of electric fields inside dielectric resonators allows a significant mass and size reduction of the filter while maintaining the same performance of conventional dual-mode counterparts. To date, the structure has been implemented on several satellite systems.

As for the work on dielectric resonator, the first work on superconductivity started with Onnes who investigated the behavior of materials when cooled to nearly absolute zero. Later on, Onnes liquefied helium for the first time in 1908 [24]. Onnes also discovered the superconductivity phenomena in 1911. Thanks to the work of Bardeen, Cooper, and Schrieffer, the first theory of superconductivity was developed [24]. In 1986, the discovery of high-temperature superconductors (HTS) by Bednorz and Müller has stimulated the interest of the microwave community. The main advantage of HTS is to offer a lightweight, compact, and with near-infinite unloaded *Q* which made it a good candidate to compete with conventional technologies developed at that time [25]. The use of HTS technology allowed the implementation of new input and output multiplexers working in the C-band with a dramatic size and mass saving compared to conventional technologies, typically dielectric resonator technology [26]. To have a comprehensive view of the different technology, Table 1.1 compares the mass and volume of a C-band IMUX for Intelsat VIII. It is demonstrated that with the use of this technology, a potential considerable mass and size saving can be achieved and thus extend the life of the spacecraft and save money [27]. However, reliability is a crucial criterion for space applications and the HTS technology has not fully proved its performance with highly reliable cryo-cooler operating in space

environment. Moreover, the lack of tuning technique for IMUX application has substantially slowed implementation of this technology in space applications.

Today, most of the IMUX are designed and fabricated with dielectric resonator technology. This technology is currently the best trade-off in terms of low insertion loss, thermally stable, high-*Q*, while maintaining a low volume and low weight. Some IMUX examples developed by Thales Alenia Space are shown in Fig. 1.3 and Fig. 1.4.

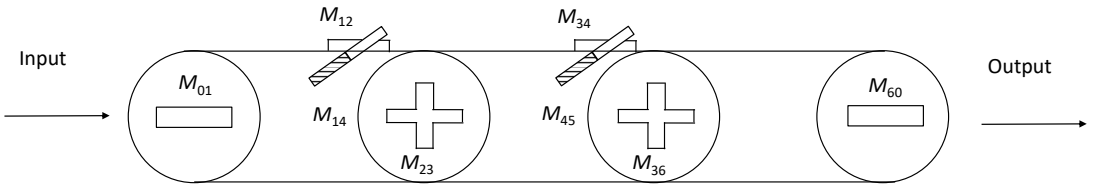

Figure. 1.1. A dual-mode in-line waveguide filter [20].

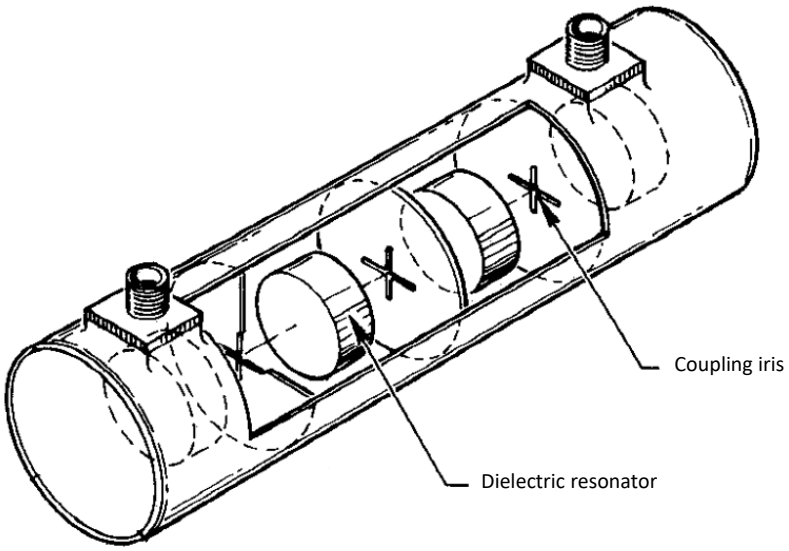

Figure. 1.2. A dual-mode in-line dielectric resonator waveguide filter [23].

TABLE 1.1
COMPARISON BETWEEN DIELECTRIC RESONATOR AND HTS TECHNOLOGY FOR A C-BAND IMUX [27]

Parameter	Dielectric resonator technology	Hybrid DR/HTS technology	HTS thin film technology
Channel filters (kg)	26.2	9	4.2
Cryo-cooler + electronics (kg)	/	3	3
Cryogenic package (kg)	/	3	2
Total mass (kg)	26.2	15	9.2
Total volume (cm^3)	51128	12946	7866

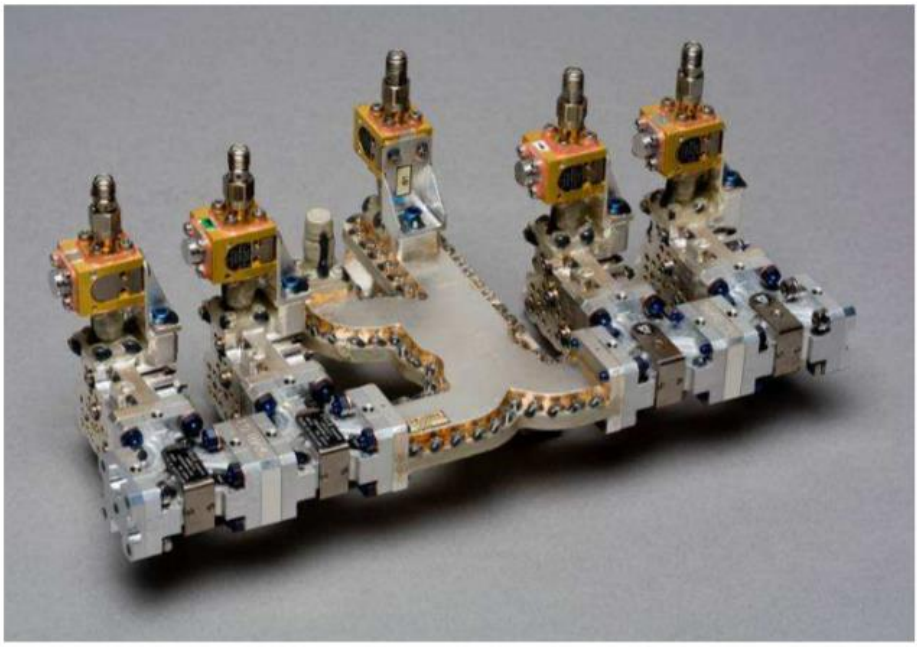

Figure. 1.3. A Ka-band IMUX [28].

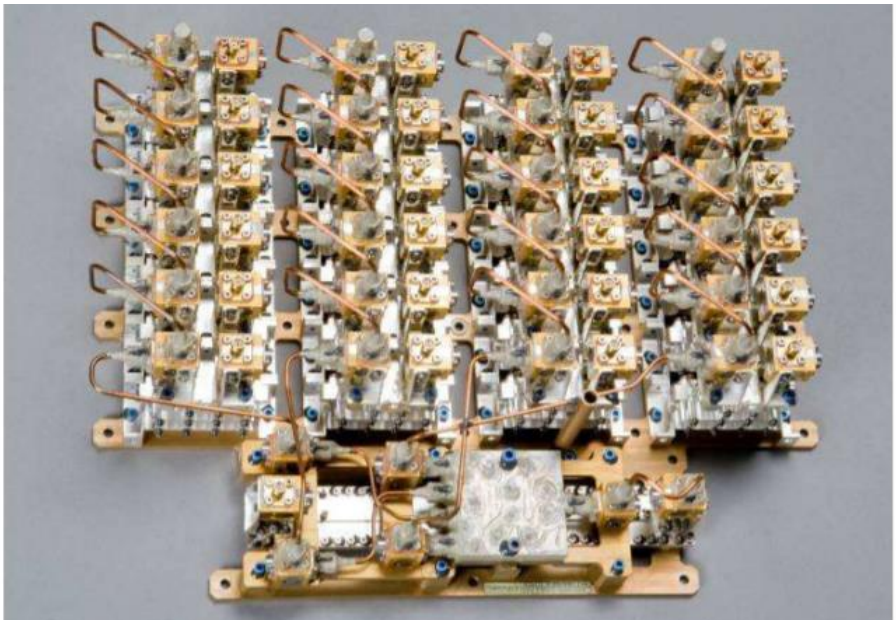

Figure. 1.4. A Ku-band self-equalized IMUX [28].

1. 2. Satellites Orbits and Constellations

The success of Sputnik I had stimulated the development of satellite communication applications. Today, almost 5000 satellites are orbiting around the planet out of 8378 satellites that have been launched in total since 1957 [30]. The orbit of a satellite represents the distance from the earth. The orbit of a satellite is chosen depending on the application, the cost, the lifetime, and the launch. The different orbits are listed below and a brief description is given in the next paragraphs:

- Geostationary Earth Orbit (GEO)
- Medium Earth Orbit (MEO)
- Low Earth Orbit (LEO)

A short list of pros and cons of the different orbits is given in Fig. 1.5.

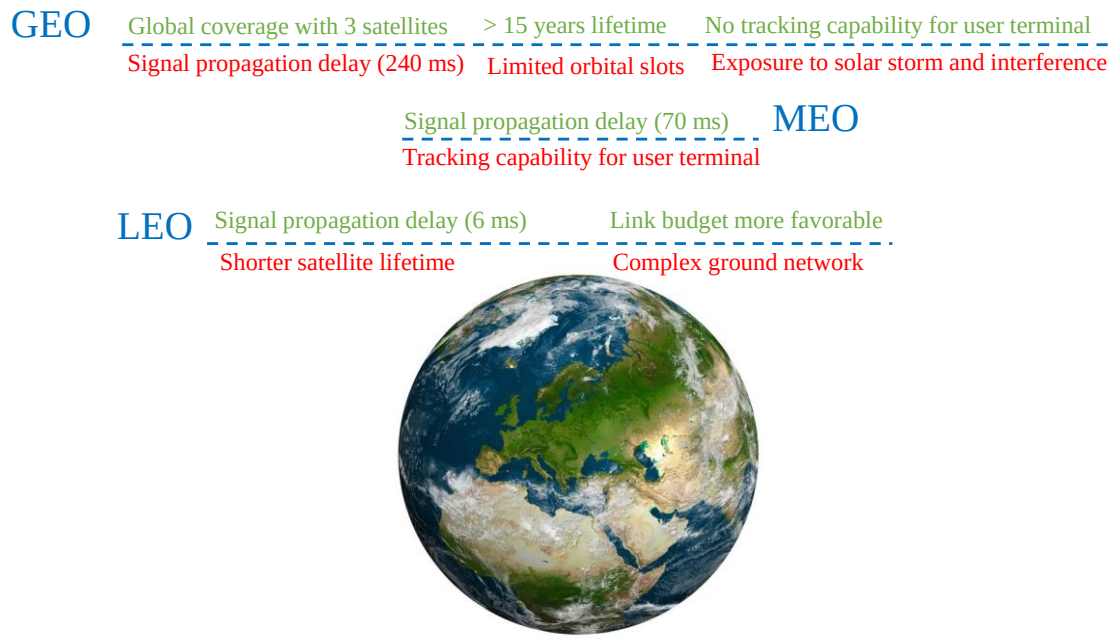

Figure. 1.5. Comparison between the different satellite orbits [29].

1. 2. 1 Geostationary Earth Orbit

A Geostationary Earth Orbit is a geocentric orbit with an altitude around 35786 km above the Earth surface. The particularity of this orbit enables the satellite to have an orbital period equal to the Earth's rotation period. Thus, a satellite placed in GEO maintain the same position over the Earth's surface a sidereal day. As a result, a GEO satellite appears fixed in space and do not need a complex tracking system in the ground, hence reduce the total cost of the communication system.

Due to the high distance in GEO, the signal of those satellites can broadcast to most of the Earth's surface, which makes them ideal candidate for observation, television broadcasting, meteorology (Meteosat) or internet access. Additionally, to those applications, GEO satellites find military applications and weather monitoring applications as they provide a constant view of the same surface area. A constellation of 3 GEO satellites equally placed can cover the entire surface of the Earth except for the Polar Regions.

Nevertheless, the connections with GEO satellites can suffer from high latency because of the long distance from Earth's surface which makes them prohibitive for any communication application.

Today, the GEO is by far the most used orbit for satellites with more than 300 satellite launches in this orbit. Fig. 1.6 represents the occupancy of the GEO.

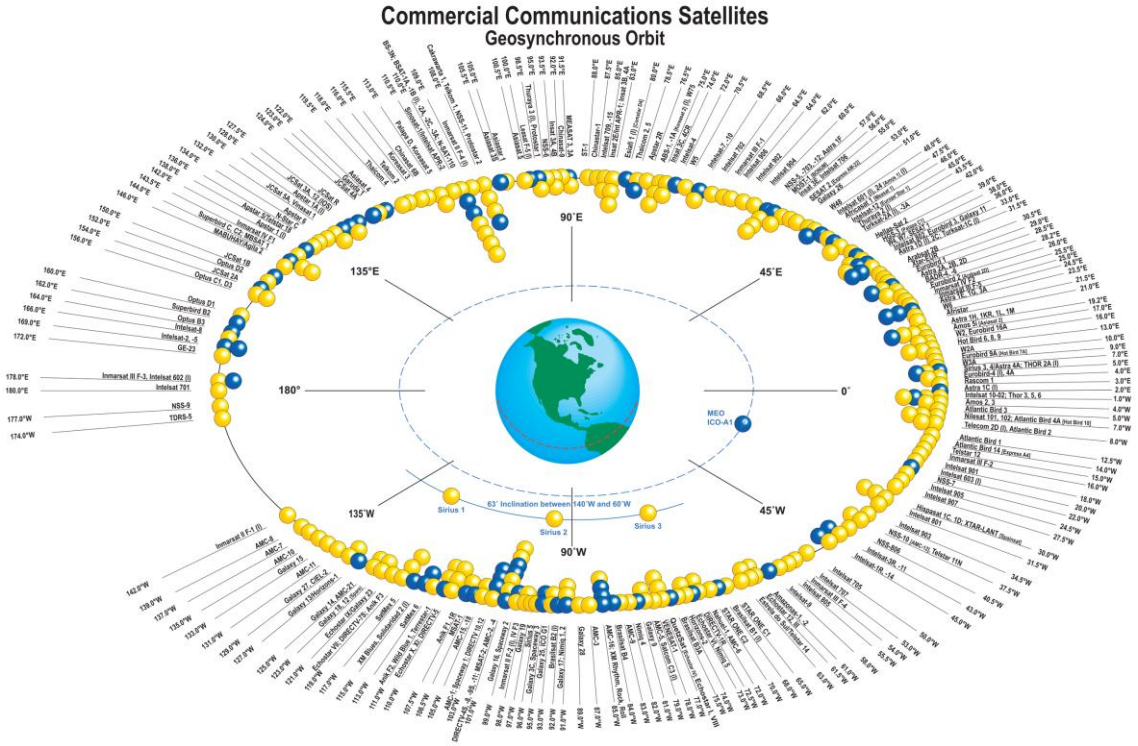

Figure. 1.6. List of satellites in Geostationary Earth Orbit (courtesy of Boeing).

1. 2. 2 Medium Earth Orbit

A Medium Earth Orbit, often called intermediate circular orbit (ICO), is the region of space around Earth above LEO and below Geostationary Earth Orbit (GEO). In terms of distance, satellites in the MEO are placed at a distance between 1400 km and 35786 km above the Earth. MEO satellites are much less used compared to LEO and GEO.

Compared to a LEO satellite, the surface covered by a satellite placed at MEO is larger due to the more important distance. Considering the Earth's rotation movement, it has been demonstrated in the past that a satellite placed at MEO in a polar orbit can cover the entire surface of the Earth within several days.

This orbit is above all used for global navigation satellite systems like Galileo (Europe), Glonass (Russia), Beidou (China) or GPS (USA). The MEO is used for navigation purposes as it is a compromise between LEO, which would require too many satellites to ensure constant visibility, and GEO, which do not cover the entire globe due to the inclinations of satellites.

Even though the signal delay is higher than the one in LEO, satellites placed at MEO are also used for Earth observation, military applications, and weather forecasting. However, applications that require a worldwide signal broadcast are not possible with MEO.

1. 2. 3 Low Earth Orbit

A Low Earth Orbit is an Earth-centered orbit at a distance between 160 and 1400 km above the Earth's surface. Satellites placed at LEO orbit in a circular pattern. The orbital period of a satellite at this orbit is 128 minutes

or less. To be able to track those satellites, it is necessary to have complex ground equipment as they are in constant movement.

This orbit allows the signal delay to be very small compared to MEO and HEO orbits as this orbit is closer to the Earth's surface. A LEO satellite requires less power to amplify the signal for communication systems compared to a GEO satellite. Hence, the foreseen applications of this orbit are the voice communication applications, where the signal delay is a crucial factor. Moreover, the satellites placed at LEO orbit can observe a particular point several times per day due to the low time to complete one orbit. Thus, this orbit is of particular interest for observation or military observation applications as with a network of satellites, it is possible to observe a surface's point any time of the day. This type of orbit is also used for human spaceflight, for example, the International Space Station is placed in LEO.

Nevertheless, satellites placed at this orbit only cover a small surface of the Earth, to allow a worldwide communication, it is necessary to have several LEO satellites. To be able to select an orbit, one must understand the problematic linked to the launch and the impact of space conditions on the different components. This is detailed in the next Section.

1. 3. Launch and Space Conditions

Space applications impose additional constraints on filters, multiplexers, and systems. Those constraints are mainly due to the unique aspects and conditions of satellite communications. Therefore, launch and space conditions led to more stringent specifications for microwave filters. Additionally, to the electrical behavior, specifications on temperature, pressure, vibrations, and shocks are required. These requirements drive the design trade-offs and qualification test protocol of microwave filters and multiplexers.

1. 3. 1 Vibrations and Shocks

A satellite is most of the time launched by a rocket. Vibration is a phenomenon usually induced during the launch of the satellite due to the combustion of motors and accelerations. The launches of the motors, and the separation of the different stages generated vibrations and shakes resulting in high mechanical tensions, high shock and can damage the components of the spacecraft. Therefore, the integration of microwave filters and multiplexers in the payload of a satellite must be designed taking into account those vibrations. This is why, vibration and shock tests are always performed on the microwave filter itself and on the overall satellite to ensure the reliability to space environment.

1. 3. 2 Temperature and Radiation

Space conditions rule satellites to operate in an adverse environment. In fact, depending on the position and orbit of the satellite, spacecraft can face abrupt temperature changes that can go from –160 °C to 150 °C. Nevertheless, for the payload components, thanks to the thermal shields, the operating temperature range is usually -20 °C to 60 °C. The RF devices of the satellite are influenced by the temperature changes and so are their electrical behavior. Hence, it is necessary for microwave filters and multiplexers to be flexible enough to

maintain the required electrical behavior while undergoing the unavoidable expansions due to temperature changes.

Additional design considerations due to radiation need to be taken into account for microwave filters and multiplexers. Radiation in space comes from fast-moving particles and X-rays. During solar storms, high-energy particles can penetrate into the satellite's metal skin. The energy brought by this particle can be absorbed by microscopic electrical components of a satellite and have a dramatic impact on the system. Consequently, the components of a satellite must demonstrate high reliability face to this extreme environmental stress.

1. 3. 3 Vacuum and Multipaction

In space environment, power generation is costly. In order to maximize the power efficiency of a satellite, low-loss filters and multiplexers is a key aspect during the design considerations. Nevertheless, to ensure a correct SNR (Signal Noise Ratio), the power levels of the signal must be sufficient. The absence of pressure added to important signal power level can create an RF breakdown phenomenon called Multipaction. The multipactor effect is a phenomenon where an electron resonance cumulated with very high incident energy creates an RF breakdown.

1. 4. Market Trends and Technology Impact

It is shown in Fig. 1.7 that the 2018 worldwide revenues generated by the space industry are 360 billion U.S. dollars [31]. The overall growth compared to 2017 is 3%. The global space economy is the union of the non-satellite space industry (82.5 B$) and the satellite space industry (277.4 B$). The non-satellite space industry is highly funded by the government budgets. The main application of the non-satellite space industry is mostly human spaceflight and exploration technologies: robotics and motor technologies, biosensors and chemical sensors, augmented reality devices and 3D tech, laser and imaging technology.

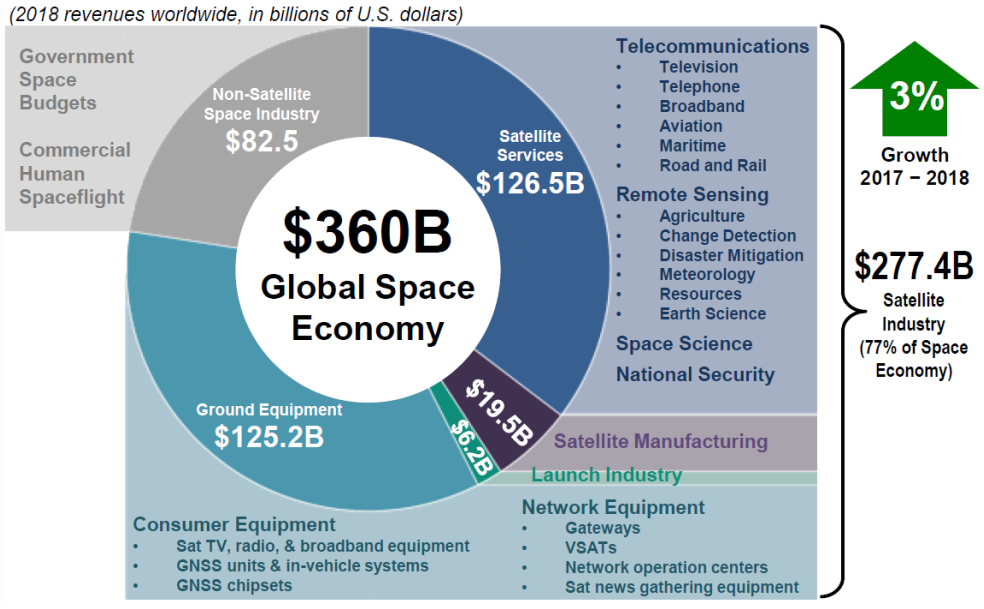

Figure. 1.7. Global satellite industry revenues (2018) [31].

The satellite space industry, representing 77% of the global space economy, is composed of the satellite manufacturing, launch industry, ground equipment, and telecommunications services. Fig. 1.8 represents the revenues of the fourth division of the satellite space industry. The largest segment is the satellite services despite a 1.7% decrease. This division is composed of consumer services (satellite television, radio, broadband), fixed satellite services (transponder agreements, managed network services), mobile satellite services, and earth observation services. This segment is highly depending on the provided consumer services as it represents almost 82% of the generated revenues. Another major segment is the ground equipment representing 45% of the satellite industry funding. Ground equipment is composed of network equipment (gateways, control stations, Very Small Aperture Terminals (VSATs)) and consumer equipment (satellite dishes, satellite radio equipment, satellite phones and mobile terminals). This segment revenues increased by 5%, especially thank to the growth in GNSS markets and network equipment. The last two segments represent the core of the space industrial base. In the present context, those segments undergo a significant development with a 26% and 34% growth for the satellite manufacturing and launch industry, respectively. This growth reflects the change of paradigm that the space industry is going through at the moment.

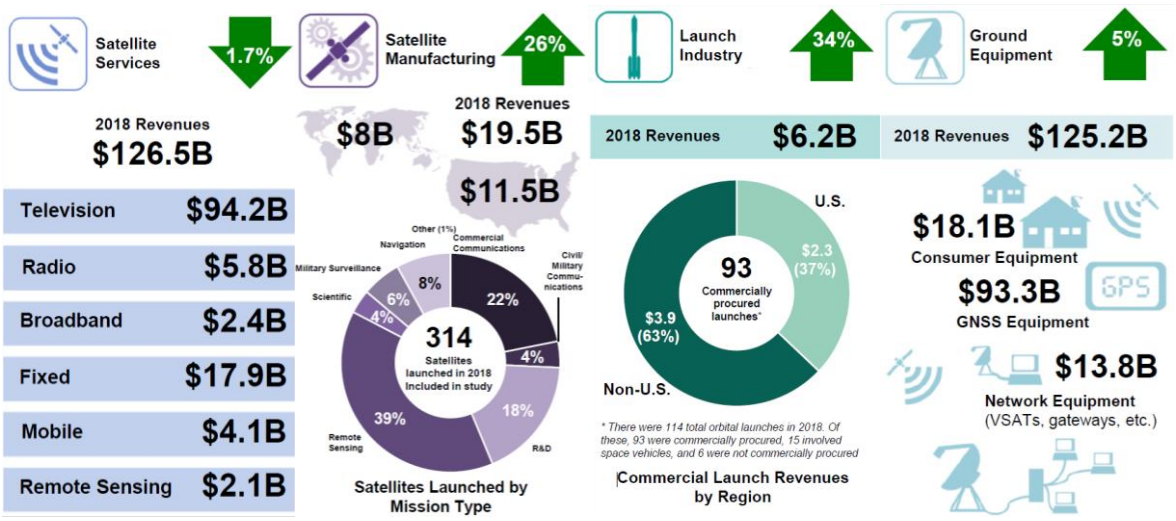

Figure. 1.8. Top-level global satellite industry findings [31].

1. 5. Satellite, Satellite Constellations and Frequency Bands

1. 5. 1 Satellite Constellations

With the emerging technological progress in the 1980s (multiple satellite launch, miniaturization of the components …) and the changes of the market needs (constant link, robustness in time of response), the space actors start thinking of implementing satellite constellations in low orbit. A satellite constellation is a system of satellites that work together to achieve a function. This type of system is usually implemented for applications that need constant contact with a point on the globe or instant global communication is needed. The first satellite of the first big caliber constellation was launched in 1986. These constellations are called Global Positioning System (GPS), and is composed of 24 satellites in MEO. Then, for telecommunication needs, other constellations have been studied and proposed. Among them, Skybridge (64 satellites) designed

by Alcatel Space Industries in 1998, Iridium (66 satellites) designed by Motorola, Télédésic (288 satellites) designed by Microsoft, GlobalStar (48 satellites) designed by Loral. The concept of LEO satellite constellations allows the implementation of lower price components, higher compactness, and makes the job easier when it comes to replacing satellites. Unfortunately, at that time, the economic constraints did not allow the implementation of those satellite constellations.

1. 5. 2 Satellite Mega-Constellations

The essential part of telecommunication satellite services is composed of GEO satellites. It is worthy to note that some non-GEO satellite constellation (Iridium, 66 satellites) ensures mobile communications. However, since 2015, the space market undergoes a change of paradigm as numerous satellite mega-constellation projects in LEO have risen. This type of constellation requires a more consistent number of satellites, typically hundreds to thousands, to cover the entire surface of the Earth whereas only 3 GEO satellites are enough. The change of paradigm to implement LEO satellite mega-constellation is essential to lower the time of latency for the customer. The principal problematic of the proposed concept is the cost of the launch and satellite itself. Another advantage of the LEO satellite mega-constellations is the versatility of the launch. Due to the high number of satellites, it is necessary to have several launches to put in place an entire constellation. Thus, this principle lowers the financial risk as the different launches can be adapted taking into account the success of the market. Finally, the satellite mega-constellation market is of high interest for private sectors as it has the potential to address the entire population on Earth.

1. 5. 3 Satellite Frequency Bands

The radio spectrum for satellite systems is listed in Table 1.2. These allocations are periodically addressed and revised by the ITU (International Telecommunication Union). Due to their low sensitivity to signal degradation, L- and S-band are mostly used for navigation applications such as the GPS. The C-band, largely developed in the 1980s, is used for radar applications, and communications satellites. The X-band is mostly dedicated to military applications. Finally, most of the satellite communication and the broadband applications are using Ku- and Ka-band. The different applications are illustrated in Fig. 1.9 [32].

TABLE 1.2
FREQUENCY ALLOCATIONS FOR SPACE APPLICATIONS [32]

Name	Frequency range (GHz)	Applications
L	1 – 2	GPS, satellite mobile services
S	2 – 4	Weather radar, surface ship radar
C	4 – 8	Satellite communications, satellite TV
X	8 – 12	Military satellites
Ku	12 - 18	Satellite communications
Ka	26 - 40	Satellite communications
Q	40 - 50	/
V	50 - 75	/

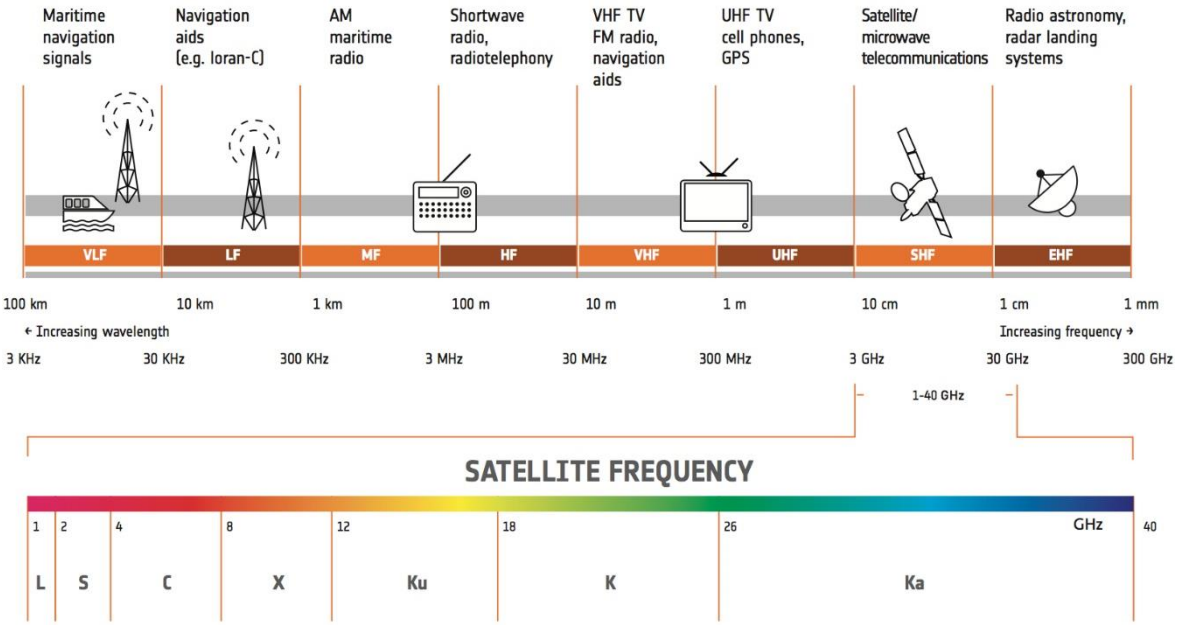

Figure. 1.9. Satellite frequency bands [32].

1. 5. 4 Communication Satellite Architecture

As previously stated, depending on the application, a satellite uses particular frequency allocations. The goal of a communication satellite is to relay the signal to different ground segments or satellites over allocated frequency bands. A communication satellite is in most of the cases composed of two main sections. The first one is the platform, which groups the different elements ensuring the good functionality of the communication satellite when placed in orbit. The second one is the payload. This section is composed of elements needed by the communication satellite to process the data and ensure the good behavior of the satellite. For the particular application developed in this thesis, only the payload section is detailed as the platform section has no microwave filter or multiplexer embedded (apart from the TMTC modules) [33].

The payload of a communication satellite is composed of antennas, receivers, and transmitters. Different payload configurations exist, Fig. 1.10 presents one of them. The different components of the payload, represented in Fig. 1.10, are used to relay a signal between satellites or ground segments. To do so, first the satellite receives a signal from the ground thanks to an input antenna. Then, an input filter, is used to select the desired band. This input filter is required to be as low loss as possible since the power level at this stage of the communication is at its lowest. It is then amplified with a low-noise amplifier (LNA). To address the correct transmission band, an oscillator is used to transpose the carrier frequency. Then, this received, filtered and amplified signal is separated into channels with the use of an IMUX (Input Multiplexer). The divided channels of the signal are then amplified through high-power amplifiers (HPA). The following step is to combine the signal, using an OMUX (Output Multiplexer) before the transmission to another ground segment thanks to the output antenna [33].

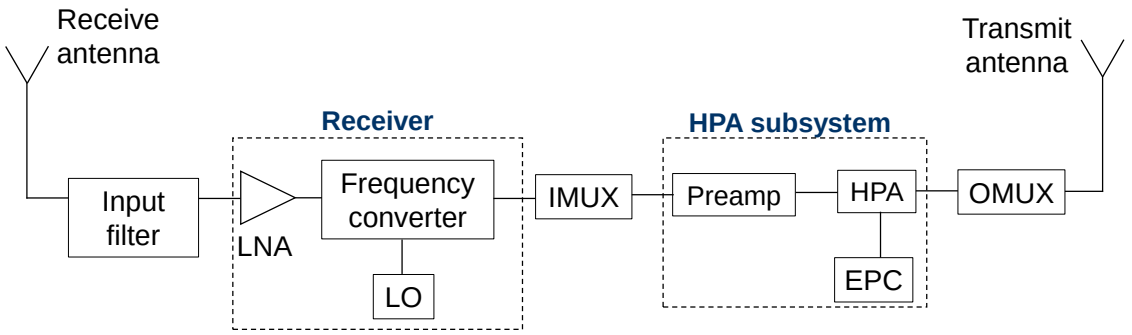

Figure. 1.10. Simplified diagram block of a satellite payload [33].

As it can be observed from Fig. 1.10, microwave and millimeter-wave filters, IMUXs, and OMUXs, play an important role in a satellite payload. The size and mass of those components are critical for the cost of the payload. Moreover, the commercial space industry is growing fast, and the past preserved satellite application market has now opened its doors to new actors. The development of satellites in terms of number, and size have saturated the present frequency allocations. Moreover, the future generation of mobile and high data speed internet is in crucial need for bandwidth, which is not suitable with the actual frequency allocations. Hence, the space actors are pushed towards the use of higher frequency bands, such as Q- and V-band. This frequency jump will allow the miniaturization of the microwave components, but it will also raise technological challenges. This is why, today, the space industry is investigating new technologies offering an optimal trade-off between size, weight, power, and cost (SWaP-C) for future implementation in space applications.

1. 6. Emerging Filter Technologies and Techniques

In this section, several technologies to implement microwave and millimeter-wave filters and multiplexers are presented. In the presented context, two major families of filter technologies are introduced, the non-planar family and the planar family. The selection of a technology depends on the foreseen application, taking into account different specifications, such as mass, volume, cost, electrical performance, and behavior to external environment. The recent advances in technologies and techniques are presented in the next section. It is obviously a hard work to sum up all the recent advances, it is tried to give an overview of the different paths for the future generation of microwave and millimeter-wave filters and multiplexers.

1. 6. 1 Non-Planar Technologies

The non-planar technologies are based on propagation inside a volume of air enclosed by a metallic cover. Depending on the geometry of the volume, basic and complex filter function can be achieved. In most of the case, the type of filter is based on a section of hollowed metallic waveguide (rectangular or circular), or dielectric resonator.

1. 6. 1. 1 Multi-Band Techniques

Most of the communication systems are designed to support different frequency bands. To separate these bands, a common technique is to use several filters. The use of multi-band filters can lead to a size, mass, and cost reduction in this context. A single multi-band filter can replace several single-band filter while maintaining the electrical performances. In satellite communication systems, the use of multi-band filter can substantially simplify the system architecture. Moreover, the concept of multi-band filter can be extended to multi-band diplexer, triplexer, and more generally to multiplexer. Different approaches were developed since the 1970s to implement multi-band in a single filter. The first one consists of using a wideband bandpass filter in which transmission zeros are implemented in the in-band of the filter [34]-[35]. A second one is based on the use of multimode resonators, in this case, each band of the multi-band filter corresponds to a propagation mode [36]-[37]. Another approach relies on using parallel connected filters [38]. Finally, it is also possible to implement a wideband bandpass filter in which notch reject filters are cascaded [39].

1. 6. 1. 2 Additive Manufacturing Techniques

The additive manufacturing technology, also called 3D printing, is a technique developed since the 1980s. The principle of the additive manufacturing is to fabricate mechanical elements in a single block which does not require any interconnection compared to conventional manufacturing process. During the last decades, substantial improvement has been made with the precision and the metallization techniques for 3D printing [40]. Thus the additive manufacturing technology allows a cost reduction, fast prototyping, and similar Q-factor to the conventional air-filled metallic waveguide technology [41]. In the current research, several additive manufacturing technologies exist [42]. One of the common technique is to directly print the desired component in metal with the use of laser melting technology [43]. Nevertheless, this technique is very costly and often offer a poor surface roughness. Another technique is to use the stereolithographic (SLA). This technique is much cheaper compared to laser melting technology, and allows the components to be lightweight and high resolution [44]. However, the drawback of this technique is the fragility of the components and also it needs an additional metallization process. The additive manufacturing is mainly used for non-planar components, yet, it is possible to use it to implement particular shaped planar components as demonstrated in [45].

The main advantage of the non-planar technologies is to present an extremely high *Q*-factor (> 1000) and very low insertion loss (< 1 dB). It also offers a high-power handling compared to other technologies thanks to the large dimensions. Moreover, as the propagation modes need to be enclosed by a metallic cover, the non-planar technologies are intrinsically self-shielded. Finally, this type of technology presents an acceptable thermal stability.

All the different aspects of the non-planar technologies justify their major implementation in most of the payload configurations. Indeed, those technologies are not only used for the emission part but also for the reception part. Nevertheless, this type of component exhibits a large footprint, is heavy, and expensive in the present market. Additionally, the fabricated filters and multiplexers based on the non-planar technologies are

complex to manufacture and require a tuning phase, which represents an increased cost in terms of money and time.

1. 6. 2 Planar Technologies

For applications requiring medium electrical performances, the planar technology is a good candidate to be implemented. The filters based on planar technologies offer a good compactness, footprint, and mass compared to non-planar technologies. Moreover, as most of the planar technologies are based on Printed Circuit Board (PCB) process, this type of technology can hit a high volume of production and address a mass production market. Thus, their implementation in the future satellite constellation market is of high interest. Finally, their implementation with other active or passive components, particularly active MMICs is easier and can introduce new concepts such as the so-called System on Substrate (SoS) [46].

1. 6. 2. 1 Micro-machined Technology

The micro-machined technology is based on the same principle as the microstrip and coplanar technology. The transmission line sections are implemented on a dielectric membrane of several micrometers. The dielectric layer is previously deposited on a thicker substrate. Then, the substrate is machined to be replaced by air [47]. Hence, an air-filled cavity is implemented under the coplanar transmission line. In some cases, a metal cavity is added above the transmission line to create an entirely shielded structure. By removing the dielectric, the transmission line has a pure TEM propagation mode [48]. This technology allows to reduce substantially the insertion loss and becomes of high interest for filter implementation. In fact, by removing the dielectric, the achievable *Q*-factor considerably increases. The literature reports several filter topologies taking advantage of micro-machined technology [49]-[53]. However, the high complexity of the fabrication process has slowed down the commercial acceptance, and complex filter geometry are not easily implementable. Moreover, the RF ports of the filter must be placed on the edge of the membrane and might lead to undesirous mode in the substrate and are hard to be integrated with planar components.

1. 6. 2. 2 Additive Micro-machined Technology

The additive micro-machined technology allows depositing multiple metal layers. In most of the case, this process uses a metal sacrificial layer removal. First, coplanar lines are defined to realize the filter function. Then, the support of the shielding structure is ensured by the deposit of a polymer. A metal layer is then deposited on the volume of the polymer. Finally, the polymer is removed to achieve a metallic shield on the top of the coplanar lines [54]-[56]. Extensive work has been done with the additive micro-machined technology. High *Q*-factor was achieved [57]-[58]. This technology benefits from the expertise of the industry world as microelectronic process has been used for companies for decades and are well mastered. Thus, additive micro-machined technology allows fabricating very small, high-performance components, and also “tuning free” filters. However, even if this technology enables to implement complex 3D structure, it requires a large number of layers to fabricate the entire component, and it is time costly. It should also be noted that it

becomes complex to fabricate components with high thickness with this technique and thus limiting the power-handling capability. Finally, even if this technology can address the mass production market and can be integrated with MMIC or standard SoS, its cost might be prohibitive for the implementation of the new space mega-constellation satellite.

1. 6. 2. 3 Substrate Integrated Waveguide Technology

The Substrate Integrated Waveguide (SIW) technology basis is to implement a waveguide structure in a substrate (planar structure) [59]. The major aspect of the SIW technology is to combine the advantages of the non-planar metallic waveguide technology with the advantages of planar technologies [60]. The sidewall of this planar waveguide is ensured by two rows of metallic cylinders or slots. The proposed concept is to achieve an integrated waveguide-like planar form using existing planar fabrication process techniques. The SIW technology exhibits similar propagation characteristics to the ones of non-planar rectangular metallic waveguide. This technology can be used with conventional fabrication process such as PCB or low-temperature covered ceramic (LTCC). Hence, the proposed SIW technology is well suited for mass production market, easy to integrate, and is cost-effective [61]. Moreover, this technology allows to introduce the concept of SiP (System in Package) which can be extended to the SoS concept [62]. SoS is of high interest to fabricate a cost-effective, easy manufacturing, and high-performance microwave and millimeter-wave platform. Nevertheless, when it comes to high frequency (> 20 GHz), the dielectric loss introduced by the substrate may become prohibitive for high performance specifications. In addition, the SIW technology is quite sensitive to external environment, such as temperature variation.

1. 6. 2. 4 Substrate Integrated Suspended Line Technology

The Substrate Integrated Suspended Line (SISL) technology is based on the Suspended Line (SL) technology. The SL technology requires a high fabrication cost, as it is based on a mechanical assembly. In the presented context, the SL technology is bulky, has heavy weight and present low integration possibilities. To overcome the drawbacks of SL technology, SISL was introduced [63]. SISL is a new technological platform introduced in 2014. It is based on standard multilayer PCB process to get rid of the additional metal cavity of SL technology. Thus, it offers compact size, lightweight, low fabrication cost, and self-packaging. It was introduced to counter effect the weakness of the SL technology.

1. 6. 2. 5 Air-Filled Substrate Integrated Waveguide Technology

The Air-Filled Substrate Integrated Waveguide (AFSIW) technology was introduced in 2014 [64]. It is based on a multilayer PCB process. In the most conventional form of AFSIW, a bottom and top substrate (substrate 1 and 3) are used to enclose an inner substrate (substrate 2) in which an air region has been manufactured. Hence, substrate 1 and 3 acts as electric broad-walls and substrate 2 is the propagation medium for the electromagnetic wave. The electric sidewalls of the AFSIW can be realized with two methods. The first one is to direct copper-platted the sidewalls, creating a direct waveguide-like structure. The second is to implement arrays of metallized via to ensure the electromagnetic boundaries. To fabricate those copper cylinders,

dielectric slabs on the sidewalls of the waveguide have to be kept [65]. By removing the dielectric in substrate 2, this structure allows to dramatically reduce the insertion loss as the dielectric loss are considered null. If the dielectric slabs are of small size (depending on the application frequency), the AFSIW technology supports TE_{10} fundamental mode [65]. Several components such as filters [66], [67] or antennas [68], [69] have already been introduced in the literature taking advantage of the technology. This work aims to extend the previous research.

1. 6. 3 Resonator Technologies

Microwave resonators represent an essential building block for the implementation of bandpass filters. The geometry of the resonator determines the field distribution of the electromagnetic wave. The major aspects of a microwave resonator are the size, unloaded *Q*-factor, power-handling capability, and cost. The unloaded *Q*-factor represents the intrinsic losses, depending on the technologies, materials, dimensions, of the resonator. The higher the *Q*-factor is, the smaller the losses are.

It can be observed from Fig. 1.11 that the AFSIW technology is in the middle between SIW and conventional air-filled metallic waveguide. The *Q*-factor range of AFSIW technology is considered to be from 800 to 3000. It is worthy to say that, higher *Q*-factor can be achieved, for example by stacking several layers of air to increase the total height of the resonator. However, it can be noticed that the AFSIW performance is closed to the non-planar technologies. The cost of the AFSIW remains low as it is based on standard multilayer PCB process. The size is directly established by the work frequency as the propagation is similar to conventional metallic waveguide. Nevertheless, Fig. 1.11 does not mention the ability of a technology to stack components. It is of particular interest, especially for space applications, to be able to stack components as the critical criteria is often the footprint. In this context, the planar structures, such as AFSIW, are more suitable to implement stacked components compared to non-planar structures due to their fabrication process.

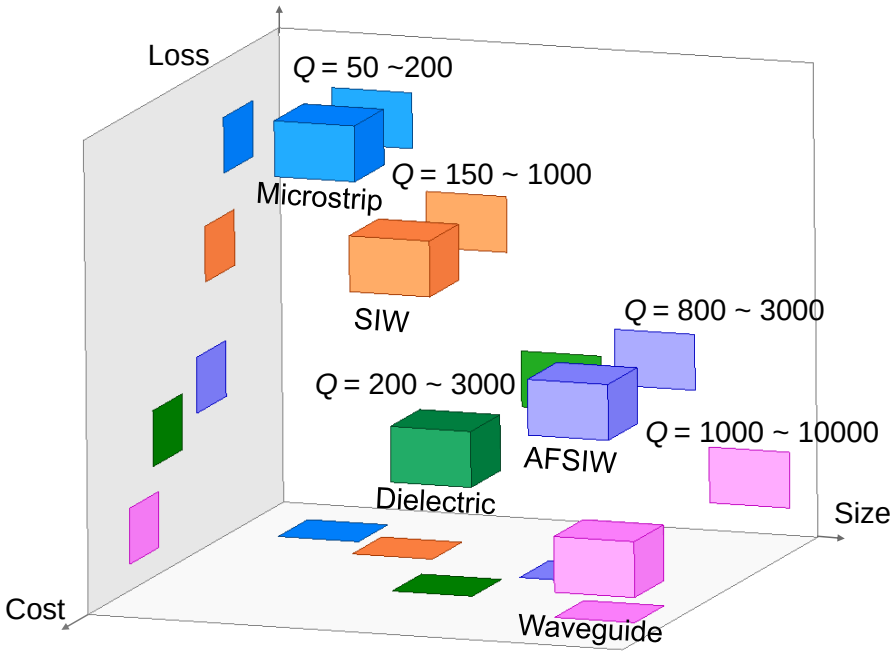

Figure. 1.11. Comparison of AFSIW resonator technology to conventional technologies.

1. 7. Conclusions

In this Chapter, a general context of the microwave applications has been discussed. A particular focus on space applications has been given. The context of new space has been explained and the need for future generations of satellites to benefit from an alternative technology is well highlighted with the economic context. Basic knowledge on space applications is explained, such as the different used orbits, satellite launch conditions, phenomena that a microwave filter can undergo in space. Different emerging technologies are presented. The high interest of the planar technologies is explained in terms of high integration degree. A particular attention has been given to the AFSIW technology as this thesis is going to use it. A comparison of the unloaded Q-factor, cost, and size of microwave resonators based on different technologies is given to allow the readers to understand the interest of the technology for the development of microwave and millimeter-wave filtering functions.

References

[1] D. M. Pozar, *Microwave Engineering*, 4th ed. John Wiley, 2012, ch. 6, pp. 272-316.

[2] Maxwell, J. (2010). A treatise on electricity and magnetism (Cambridge Library Collection - Physical Sciences). Cambridge: Cambridge University Press.

[3] F. E. Terman, "A brief history of electrical engineering education," *Proceedings of the IEEE*, vol. 86, no. 8, pp. 1792-1800, Aug. 1998.

[4] A. A. Oliner, "Historical perspectives on microwave field theory," *IEEE Transactions on Microwave Theory and Techniques*, vol. 32, no. 9, pp. 1022-1045, Sep. 1984.

[5] H. Sobol, and K. Tomiyasu, "Milestones of microwaves," *IEEE Transactions on Microwave Theory and Techniques*, vol. 50, no. 3, pp. 594-611, Mar. 2002.

[6] E. T. Jilg et al., 'The Intelsat IV spacecraft," *Comsat Technical Review*, vol. 2, no. 2, Fall 1972.

[7] C. Kudsia, R. Cameron, and W.-C. Tang, "Innovations in microwave filters and multiplexing networks for communications satellite systems," *IEEE Digest on Microwave Theory and Techniques*, vol. 40, pp. 1133-1149, Jun. 1992.

[8] S. B. Cohn, "Direct-coupled resonator filters," *Proc. IRE*, vol. 45, pp. 187-1976, Feb. 1957.

[9] C. M. Kudsia, and M. V. O'Donovan, "A light weight graphite fiber epoxy composite (GFEC) waveguide multiplexer for satellite application," *European Microwave Conference*, Montreux, Switzerland, 1974, pp. 585-589.

[10] J. E. Keigler, "RCA Satcom: An example of weight-optimized, satellite design for maximum communications capacity," *Acta Astronautics. New York: Pergamon*, 1978, vol. 5.

[11] W. G. Lin, "Microwave filters employing a single cavity excited in more than one mode," J. Appl. Phys., vol. 22, pp. 989–1001, Aug. 1951.

[12] B. L. Blacier and A. R. Champeau, "Dual-mode circular and/or square waveguide filters," U.S. Patent 3 697 898, issued Oct. 1972.

[13] A. E. Atia, and A. E. Williams, "New types of waveguides bandpass filters for satellite transponders," Comsat Technical Review, vol. 1, no. 1, pp. 21-43, Fall 1971.

[14] A. E. Atia, and A. E. Williams, "Narrow-bandpass waveguide filters," *IEEE Transactions on Microwave Theory and Techniques*., vol. 20, pp. 258-265, Apr. 1972.

[15] A. E. Atia, A. E. Williams, and R. W. Newcom, "Synthesis of dual-mode filters," *IEEE Transactions on Circuits and Systems*, vol. CAS-21, pp. 649–655, Sept. 1974.

[16] J. L. Dicks, and M. P. Brown Jr., "Intelsat IV-A satellite transmission design," *Proc. AIAA 5th Communications Satellite Systems Conf*., Los Angeles, CA, Apr. 1974.

[17] G. L. Matthaie, L. Young, and E. M. T. Jones, "Microwave filters, impedance matching networks, and coupling structures," Book Mart press, North Bergen, NJ, USA, Nov. 1985.

[18] W. C. Tang, and S. K. Chaudhuri, "A true elliptic-function filter using triple-mode degenerate cavities," *IEEE MTT-S Inr. Microwave Symp. Dig*., Boston, MA, May 31-June 3, 1983.

[19] R. R. Bonetti, and A. E. Williams, "Application of dual TM-modes to triple and quadruple mode filters," *IEEE Trans. Microwave Theory Tech*., vol. MTT-35, pp. 1143-1149, Dec. 1987.

[20] I. C. Hunter, L. Billonet, B. Jarry, and P. Guillon, "Microwave filters-applications and technology," *IEEE Transactions on Microwave Theory and Techniques*, vol. 50, no. 3, pp. 794-805, Mar. 2002.

[21] S. Kallianteris, and M. V. O'Donovan, "Technology advances in the realization of filter networks for communications satellites operating at frequencies above IO GHz," *Proc. AIAAKASI 6th Communications Satellite Systems Conf., Montreal*, Apr. 5-8, 1981.

[22] R. D. Richtmyer, "Dielectric resonators," *Journal of Applied Physics*, vol. 10, pp. 391-398, Jun. 1939.

[23] S. J. Fiedziuszko, "Dual-mode dielectric resonator loaded cavity filters," *IEEE Transactions on Microwave Theory and Techniques*, vol. MTT-30, pp. 1311–1316, Sept. 1982.

[24] M. J. Lancaster, Passive Microwave Device Applications of High Temperature Superconductors. Cambridge, MA: Cambridge Univ. Press, 1997.

[25] R. R. Mansour, "Microwave superconductivity," *IEEE Transactions on Microwave Theory and Techniques*, vol. 50, no. 3, pp. 750-759, Mar. 2002.

[26] R. R. Mansour *et al*., "Design considerations of superconductive input multiplexers for satellite applications," *IEEE Transactions on Microwave Theory and Techniques*, vol. 44, no. 7, pp. 1213-1228, Jul. 1996.

[27] R. R. Mansour *et al*., "A 60-channel superconductive input multiplexer integrated with pulse-tube cryocoolers," *IEEE Transactions on Microwave Theory and Techniques*, vol. 48, no. 7, pp. 1171-1180, Jul. 2000.

[28] https://www.thalesgroup.com/sites/default/files/database/d7/asset/document/Imux_Omux.pdf

[29] Constellations Telecom, Euroconsult, 2019

[30] UNOOSA, United Nations Official Document System, 2019.

[31] SIA, State of the Satellite Industry, 2019

[32] https://www.esa.int/spaceinimages/Images/2013/11/Satellite_frequency_bands

[33] T. M. Braun, *Satellite Communications Payload and System*, 1st ed. John Wiley, 2012.

[34] G. Macchiarella, and S. Tamiazzo, "Design techniques for dual-passband filters," *IEEE Transactions on Microwave Theory and Techniques*, vol. 53, no. 11, pp. 3265-3271, Nov. 2005.

[35] P. Lenoir, S. Bila, F. Seyfert, D. Baillargeat, and S. Verdeyme, "Synthesis and design of asymmetrical dual-band bandpass filters based on equivalent network simplification," *IEEE Transactions on Microwave Theory and Techniques*, vol. 54, no. 7, pp. 3090-3097, July 2006.

[36] L. Zhu, R. R. Mansour, and M. Yu, "Compact Waveguide Dual-Band Filters and Diplexers," *IEEE Transactions on Microwave Theory and Techniques*, vol. 65, no. 5, pp. 1525-1533, May 2017.

[37] L. Zhu, R. R. Mansour, and M. Yu, "Triple-Band Cavity Bandpass Filters," *IEEE Transactions on Microwave Theory and Techniques*, vol. 66, no. 9, pp. 4057-4069, Sept. 2018.

[38] G. Macchiarella, and S. Tamiazzo, "Dual-Band Filters for Base Station Multi-Band Combiners," *IEEE/MTT-S International Microwave Symposium*, Honolulu, HI, 2007, pp. 1289-1292.

[39] R. R. Mansour, and P. D. Laforge, "Multiband superconducting filters," *IEEE MTT-S International Microwave Symposium (IMS)*, San Francisco, CA, 2016, pp. 1-4.

[40] E. A. Rojas-Nastrucci, J. T. Nussbaum, N. B. Crane, and T. M. Weller, "Ka-band characterization of binder jetting for 3-D printing of metallic rectangular waveguide circuits and antennas," *IEEE Transactions on Microwave Theory and Techniques*, vol. 65, no. 9, pp. 3099-3108, Sept. 2017.

[41] C. Tomassoni, G. Venanzoni, M. Dionigi, and R. Sorrentino, "Compact quasi-elliptic filters with mushroom-shaped resonators manufactured with 3-D printer," *IEEE Transactions on Microwave Theory and Techniques*, vol. 66, no. 8, pp. 3579-3588, Aug. 2018.

[42] F. Calignano, D. Manfredi, E. P. Ambrosio, S. Biamino, M. Lombardi, E. Atzeni, A. Salmi, P. Minetola, L. Iuliano, and P. Fino, "Overview on additive manufacturing technologies," *Proceedings of the IEEE*, vol. 105, no. 4, pp. 593-612, Apr. 2017.

[43] O. A. Peverini, G. Addamo, M. Lumia, G. Virone, F. Calignano, M. Lorusso, and D. Manfredi, "Additive manufacturing of Ku/K-band waveguide filters: a comparative analysis among selective-laser melting and stereo-lithography," *IET Microwaves, Antennas & Propagation*, vol. 11, no. 14, pp. 1936-1942, 19 11 2017.

[44] M. Dionigi, C. Tomassoni, G. Venanzoni, and R. Sorrentino, "Simple high-performance metal-plating procedure for stereolithographically 3-D-printed waveguide components," *IEEE Microwave and Wireless Components Letters*, vol. 27, no. 11, pp. 953–955, Nov. 2017.

[45] E. Massoni, L. Silvestri, G. Alaimo, S. Marconi, M. Bozzi, L. Perregrini, and F. Auricchio, "3-D printed substrate integrated slab waveguide for single-mode bandwidth enhancement," *IEEE Microwave and Wireless Components Letters*, vol. 27, no. 6, pp. 536-538, Jun. 2017.

[46] Z. Li and K. Wu, "24-GHz frequency-modulation continuous-wave radar front-end system-on-substrate," *IEEE Transactions on Microwave Theory and Techniques*, vol. 56, no. 2, pp. 278-285, Feb. 2008.

[47] Chen-Yu Chi, and G. M. Rebeiz, "Planar millimeter-wave microstrip lumped elements using micro-machining techniques," *IEEE MTT-S International Microwave Symposium Digest*, San Diego, CA, USA, 1994, pp. 657-660 vol.2.

[48] N. I. Dib, and L. P. B. Katehi, "Impedance calculation for the microshield line," *IEEE Microwave and Guided Wave Letters*, vol. 2, no. 10, pp. 406-408, Oct. 1992.

[49] S. V. Robertson, L. P. B. Katehi, and G. M. Rebeiz, "Micromachined self-packaged W-band bandpass filters," *IEEE MTT-S International Microwave Symposium*, Orlando, FL, USA, 1995, pp. 1543-1546 vol.3.

[50] S. V. Robertson, L. P. B. Katehi, and G. M. Rebeiz, "Micromachined W-band filters," *IEEE Transactions on Microwave Theory and Techniques*, vol. 44, no. 4, pp. 598-606, Apr. 1996.

[51] Chen-Yu Chi, and G. M. Rebeiz, "A low-loss 20 GHz micromachined bandpass filter," *IEEE MTT-S International Microwave Symposium*, Orlando, FL, USA, 1995, pp. 1531-1534 vol.3.

[52] P. Blondy, A. R. Brown, D. Cros, and G. M. Rebeiz, "Low-loss micromachined filters for millimeter-wave communication systems," *IEEE Transactions on Microwave Theory and Techniques*, vol. 46, no. 12, pp. 2283-2288, Dec. 1998.

[53] M. Chatras, P. Blondy, D. Cros, O. Vendier, and J. L. Cazaux, "A surface-mountable membrane supported filter," *IEEE Microwave and Wireless Components Letters*, vol. 13, no. 12, pp. 535-537, Dec. 2003.

[54] F. David, M. Chatras, C. Dalmay, L. Lapierre, L. Carpentier, and P. Blondy, "Surface-micromachined rectangular micro-coaxial lines for sub-millimeter-wave applications," *IEEE Microwave and Wireless Components Letters*, vol. 26, no. 10, pp. 756-758, Oct. 2016.

[55] F. David, C. Dalmay, M. Chatras, A. Pothier, L. Carpentier, L. Lapierre, and P. Blondy, "3D micro-fabricated high-Q 140 GHz filter," *IEEE MTT-S International Microwave Symposium (IMS)*, Honololu, HI, 2017, pp. 1297-1299.

[56] Y. Wang, M. Ke, and M. J. Lancaster, "Micromachined 38 GHz cavity resonator and filter with rectangular-coaxial feed-lines," *IET Microw. Antennas Propag.*, vol. 3, Iss. 1, pp. 125-129, 2009.

[57] K. J. Vanhille, D. L. Fontaine, C. Nichols, D. S. Filipovic, and Z. Popovic, "Quasi-planar high-Q millimeter-wave resonators," *IEEE Transactions on Microwave Theory and Techniques*, vol. 54, no. 6, pp. 2439-2446, June 2006.

[58] K. J. Vanhille, D. L. Fontaine, C. Nichols, Z. Popovic, and D. S. Filipovic, "Ka-band miniaturized quasi-planar high-*Q* resonators," *IEEE Transactions on Microwave Theory and Techniques*, vol. 55, no. 6, pp. 1272-1279, June 2007.

[59] D. Deslandes, and K. Wu, "Integrated microstrip and rectangular waveguide in planar form," *IEEE Microwave and Wireless Components Letters*, Vol. 11, No. 2, pp. 68–70, Nov. 2001.

[60] D. Deslandes and K. Wu, "Single-substrate integration techniques for planar circuits and waveguide filters," *IEEE Transactions on Microwave Theory and Techniques*, Vol. 51, pp. 593-596, Feb, 2003.

[61] M. Bozzi, A. Georgiadis, and K. Wu, "Review of substrate Integrated waveguide (SIW) circuits and antennas," *IET Microwave Antennas and Propagation*, Vol. 5, No. 8, pp. 909–920, Jun. 2011.

[62] K. Wu, "Towards system–on–substrate approach for future millimeter–wave and photonic wireless applications," *Asia–Pacific Microwave Conference*, Yokohama, Japan, Dec. 12-15, 2006, pp. 1895–1900.

[63] Y. Wang, K. Ma, S. Mou, N. Yan and L. Li, "A low loss branch line coupler based on substrate integrated suspended line (SISL) technology and double-sided interconnected strip line (DSISL)," *Asia-Pacific Microwave Conference (APMC)*, Nanjing, 2015, pp. 1-3.

[64] F. Parment, A. Ghiotto, T. Vuong, J. Duchamp and K. Wu, "Broadband transition from dielectric-filled to air-filled Substrate Integrated Waveguide for low loss and high power handling millimeter-wave Substrate Integrated Circuits," *IEEE MTT-S International Microwave Symposium*, Tampa, FL, 2014, pp. 1-3.

[65] F. Parment, A. Ghiotto, T. Vuong, J. Duchamp and K. Wu, "Air-filled substrate integrated waveguide for low-loss and high power-handling millimeter-wave substrate integrated circuits," *IEEE Transactions on Microwave Theory and Techniques*, vol. 63, no. 4, pp. 1228-1238, Apr. 2015.

[66] F. Parment, A. Ghiotto, T.P. Vuong, J.M. Duchamp, and K. Wu, "Low-loss air-filled substrate integrated waveguide (SIW) band-pass filter with symmetric inductive posts," *European Microwave Conference (EuMC)*, Paris, 6-11 Sep. 2015.

[67] F. Parment, A. Ghiotto, T.P. Vuong, J.M. Duchamp, and K. Wu, "Ka-band compact and high performance bandpass filter based on multilayer air-filled SIW," *IET Electronics Letters*, vol. 53, no. 7, pp. 486-488, Mar. 2017.

[68] F. Parment, A. Ghiotto, T.P. Vuong, J.M. Duchamp, and K. Wu, "Millimetre-wave air-filled substrate integrated waveguide slot array antenna," *IET Electronics Letters*, vol. 53, no. 11, pp. 704-706, May 2017.

[69] A. Ghiotto, F. Parment, T.P. Vuong, and K. Wu, "Millimeter-wave air-filled SIW antipodal linearly tapered slot antenna," *IEEE Antennas and Wireless Propagation Letters*, vol. 16, pp. 768-771, Apr. 2017.

Chapter 2

AFSIW Technological Platform

This second Chapter is devoted to an overview of the AFSIW technological platform. Some basic microwave components such as a transmission line and a fourth-order bandpass filter using the AFSIW technology are presented. A mechanical structure, also called test fixture, is introduced to explain how the first prototype was measured. This test fixture is later used in this Chapter to perform power-handling tests on both the transmission line and filter. For the filter power-handling tests, a particular attention has been devoted to performing relevant test modeling the space environment. Thus, continuous wave power-handling in a vacuum chamber, multipactor test, and corona test have been performed. The intent of this thesis is not to detail those very complex phenomena. However, it was crucial to evaluate them to have an overall view of the technology capabilities.

2. 1. Air-Filled Substrate Integrated Waveguide Structure

The proposed AFSIW transmission line structure is illustrated in Fig. 2.1 and Fig. 2.2. It is based on the multilayer PCB process. The substrate 1 and 3, both enclosing substrate 2, are used as bottom and top electrical walls of the AFSIW, respectively. The substrate 2 implements an air-filled propagation channel. The electric sidewalls of substrate 2 can be implemented with continuously metallized sidewalls, or with arrays of metallized via as represented in Fig. 2.1(*a*) and Fig. 2.1(*b*), respectively.

Depending on the implementation of the electrical sidewalls of substrate 2, it is possible to determine the cutoff frequencies for the TE_{mn} mode. If the electric sidewalls are implemented with continuously metallized sidewalls, then the AFSIW structure is similar to an air-filled metallic rectangular waveguide of equal dimensions. Hence, the cutoff frequency for the TE_{mn} mode is given from the rectangular waveguide theory [1]:

$$f_{c_{mn}} = \frac{1}{2\pi\sqrt{\mu_0\varepsilon_0}}\sqrt{\left(\frac{m\pi}{a}\right)^2 + \left(\frac{n\pi}{b}\right)^2}, \tag{2.1}$$

where μ_0 is the vacuum permeability, ε_0 is the permittivity of free space, a is the width, and b is the height of the AFSIW section.

If the electric sidewalls are implemented with arrays of metallized via, dielectric slabs must be kept on the sidewalls of substrate 2 to be able to fabricate the metallized vias. If the width of the dielectric slabs is small, then (2.1) gives a good approximation for the cutoff frequency. It was demonstrated in [2] that the dielectric slabs can be taken into account to determine the cutoff frequency of the fundamental TE_{10} mode of an AFSIW structure with:

$$\tan\left(\frac{\pi f_{c_{10}}\sqrt{\varepsilon_r}(W_1-W_2)}{c}\right) = \sqrt{\varepsilon_r}\cot\left(\frac{\pi f_{c_{10}}W_2}{c}\right). \quad (2.2)$$

To solve (2.2), it is possible to use the Newton-Raphson method of iterations. Thus, the cutoff frequency of the TE_{10} mode of the AFSIW structure can be determined. Nevertheless, it is worthy to note that the dielectric slabs have a negligible impact on the cutoff frequency of the fundamental TE_{10} mode if their width remains small. The value depends on the electromagnetic properties and dimensions of the substrate. Indeed, as represented in Fig. 2.3, the E-field of the fundamental mode is at its maximum in the center of the structure and is weak near the sidewalls, where the dielectric slabs are implemented. Therefore, for AFSIW transmission line implementation, the dielectric slab widths can be neglected during the theoretical and simulation designs.

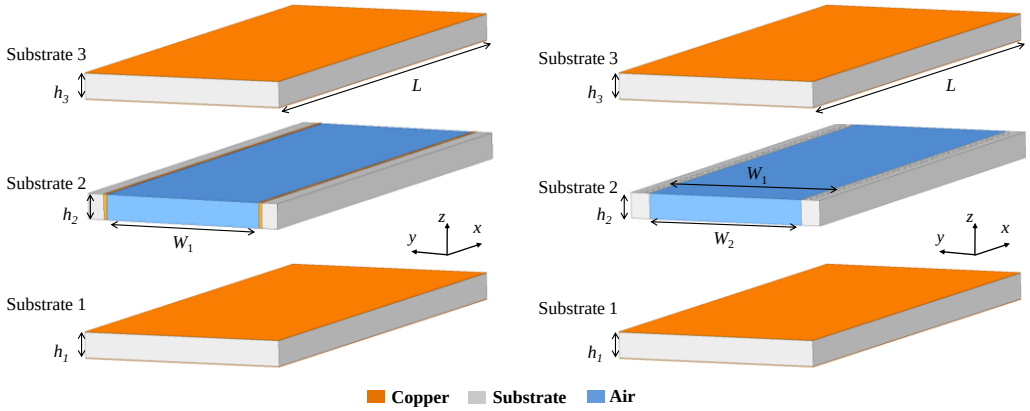

(*a*) (*b*)

Fig. 2.1. 3D views of the AFSIW structure with (*a*) direct copper platting and (*b*) arrays of metallized via.

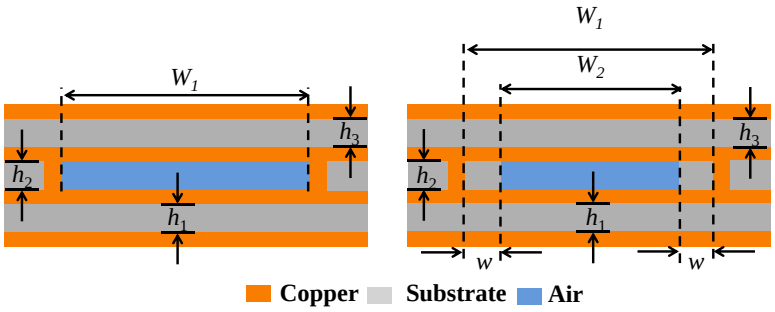

(*a*) (*b*)

Fig. 2.2. Cross-sectional views of the AFSIW structure with (*a*) direct copper platting and (*b*) arrays of metallized via.

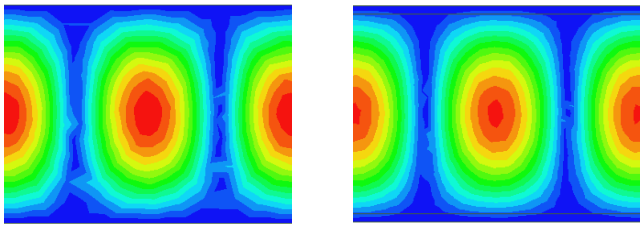

(*a*) (*b*)

Fig. 2.3. AFSIW E-fields of the TE10 mode with dielectric slabs width of (*a*) 0 mm and (*b*) 0.3 mm.

To detail the impact of the dielectric slabs on the AFSIW performances, a study of the unloaded *Q*-factor of an AFSIW cavity is presented. As it is stated in [3], the unloaded *Q*-factor of a resonator defines the sharpness of the resonance curve. It is defined as:

$$Q_{\mathrm{u}} = \omega_0 \frac{W_T}{P_{\mathrm{loss}}}, \tag{2.3}$$

where W_{T} is the average energy stored in the resonator, P_{loss} is the power dissipated in the resonator, and ω_0 is the radian resonance frequency. The power dissipated in the resonator is the sum of the power dissipated in the conducting walls P_{c} and the power dissipated in the dielectric P_{d}. Hence, the unloaded *Q*-factor can be rearranged into:

$$\frac{1}{Q_{\mathrm{u}}} = \frac{1}{Q_c} + \frac{1}{Q_d}, \tag{2.4}$$

where $Q_{\mathrm{c}} = \omega_0 W_{\mathrm{T}}/P_{\mathrm{c}}$ and $Q_{\mathrm{d}} = \omega_0 W_{\mathrm{T}}/P_{\mathrm{d}}$.

The study is based on the eigenmode simulations of the EM software ANSYS HFSS with copper as conductive metal. Two AFSIW cavities, implementing continuous sidewalls (directly copper platted) and discontinuous sidewalls (arrays of metallized via), respectively, are compared in terms of unloaded *Q*-factor. Both cavities, represented in Fig. 2.4 have a fixed width W_1 = 13 mm and the length *L* is adjusted so the cavity resonates at 21 GHz. Rogers RT/Duroid 6002 material, with a permittivity of 2.94 and a tanδ of 0.0012, is used for the particular case of discontinuous sidewalls. The diameter *d* of the vias is 0.4 mm and the distance between two center-to-center consecutive vias *p* is 0.8 mm. It can be observed in Fig. 2.5 that the unloaded *Q*-factor varies from 2496 (with w = 0 mm) to 2453 (with w = 0.4 mm), 1438 (with w = 0 mm) to 1415 (with w = 0.4 mm), 1005 (with w = 0 mm) to 995 (with w = 0.4 mm), for PCB standard thickness of 1.524 mm, 0.762 mm, and 0.508 mm, respectively. Therefore, it can be concluded that the dielectric slabs can be neglected in the design of such component. Moreover, if the dielectric slabs are not used to achieve a specific electric function, there is no need to implement them.

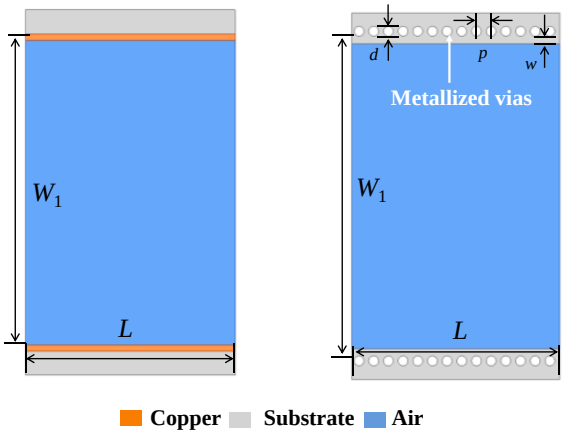

(*a*) (*b*)

Fig. 2.4. Top views of AFSIW cavities implementing (*a*) direct copper platting and (*b*) arrays of metallized via.

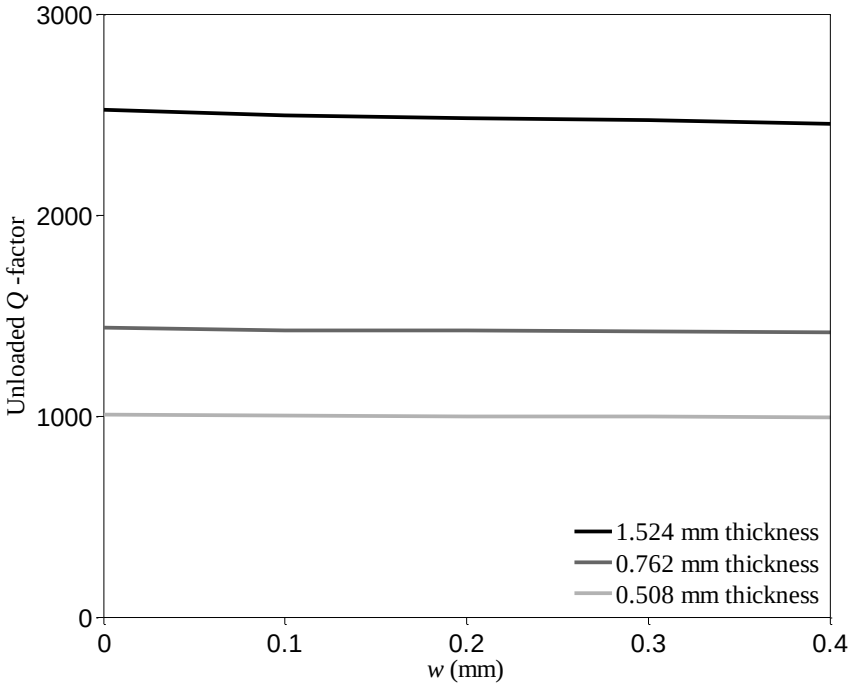

Fig. 2.5. Eigenmode simulations of the unloaded *Q*-factor of an AFSIW cavity loaded with dielectric slabs (width *w*) with different PCB standard thickness.

2. 2. Air-Filled Substrate Integrated Waveguide Transmission Line

To evaluate the intrinsic performances of the AFSIW technology, the simplest component to study is a transmission line. In this section, theoretical analyses, simulations using ANSYS HFSS electromagnetic (EM) software, and measurement results are presented. Due to the foreseen interest of the AFSIW technological platform for space applications, the proposed transmission line is studied and demonstrated in the Ka-band satellite communication frequency range (17.3 to 21.3 GHz) which is included in the WR-51 band. First, the loss mechanism in an AFSIW transmission line is briefly explained. Then, a transition from conventional rectangular waveguide (RWG) to AFSIW is detailed. This transition is then used in a test fixture to characterize an AFSIW transmission line. Finally, power-handling tests on the proposed component are carried out to evaluate the behavior of the technology.

2. 2. 1 Loss Mechanism

The AFSIW, as any propagation technology, is subjected to losses. Those losses impact the performance of the propagating structure and is an important aspect to consider. They can be classified into three categories, the conductor losses, dielectric losses, and radiation losses. The total attenuation α is expressed as:

$$\alpha = \alpha_d + K * \alpha_c + \alpha_r. \quad (2.3)$$

where α_c is the conductor loss attenuation, α_d is the dielectric loss attenuation, K is the surface roughness coefficient, and α_r is the radiation loss.

2. 2. 1. 1 Conductor Losses

The conductor losses come from the metals used to fabricate the propagating structure. Those metals present a certain surface resistivity R_s [4]:

$$R_s = \sqrt{\frac{\pi f \mu_0}{\sigma}}, \tag{2.4}$$

where μ_0 is the vacuum permeability, f is the work frequency, and σ is the conductivity of the metal.

Thus, when a power hits this metallic surface, collisions between atoms and electrons are created. The generated energy introduces conductor losses. The expression of the conductor losses is given by:

$$\alpha_c = \frac{R_s}{a^3 b \beta k \eta}(2b\pi^2 + a^3 k^2), \tag{2.5}$$

where a, and b are the width and height of the AFSIW transmission line, respectively. The coefficient k is the wave number, and β is the phase constant.

2. 2. 1. 2 Dielectric Losses

The dielectric losses are generated by the dissipation of the electromagnetic energy in a dielectric material. This loss mechanism depends on the nature of the material and on the operating frequency. The dielectric loss attenuation, in a filled dielectric waveguide, is given by [4]:

$$\alpha_d = \frac{k^2 \tan\delta}{2\beta}, \tag{2.6}$$

where δ is the skin depth.

2. 2. 1. 3 Surface Roughness Effect

Another loss mechanism is due to the surface roughness effect. This mechanism can significantly increase as the frequency increases due to the value of the skin depth getting closer to the value of the conductor surface roughness. Some efforts were put in place in order to develop an empirical formula to take into account the surface roughness effect. Extensive work has been done [5]-[8] in the field of surface roughness, and the coefficient $K_{\text{hammerstad}}$ is often used to evaluate this loss mechanism. The coefficient $K_{\text{hammerstad}}$ can be calculated using:

$$K_{Hammerstad} = 1+\frac{2}{\pi}\left(1.4 * \left(\frac{H_{rms}}{\delta}\right)\right), \tag{2.7}$$

where H_{rms} is the root mean square (RMS) conductor.

2. 2. 1. 4 Radiation Losses

In the particular case of this thesis, the components based on AFSIW with continuous sidewalls are self-shielded thanks to the structure of the technology. For the case of discontinuous sidewalls, the distance between two consecutive vias is small enough to neglect the radiation losses as it is demonstrated in [9], [10]. Thus, the radiation losses in both cases are considered null. Hence the total attenuation α becomes:

$$\alpha = \alpha_d + K_{Hammerstad} * \alpha_c. \tag{2.8}$$

To further highlight the interest of the technology as a propagation medium, a previous thesis has compared, theoretically and in simulations, the principal characteristics of an AFSIW transmission line compared to other planar technologies such as microstrip and conventional SIW [11]. The Table 2.1 summarizes the different results. All the technologies were compared with 0.508 mm thick substrates at 33 GHz. However, this frequency band is not the one of interest and thus it is necessary to study the technology in the desired frequency band. Moreover, in [2] and [11] the technologies are also compared theoretically in terms of power-handling capability. Nevertheless, this work did not address the power-handling effects linked to space applications, such as multipactor effect or corona effect, later explained in this Chapter. Hence, the following Sections will try to fill in the blanks of the AFSIW technology.

TABLE 2.1
SUMMARY OF THEORETICAL TOTAL LOSS FOR DIFFERENT TRANSMISSION LINE TECHNOLOGIES

Technology	Microstrip	SIW	SIW	AFSIW
Substrate	Rogers 5880	Rogers 5880	Rogers 6002	Rogers 6002
Total loss (dB/cm)	0.073	0.095	0.13	0.033

2. 2. 2. AFSIW to RWG Transition

To be able to characterize intrinsically the technology in terms of electrical performances, power-handling and thermal behavior, a transition from standard RWG to AFSIW must be designed. Hence, a compact five-section height-stepped RWG to AFSIW is detailed. The standard RWG section allows characterizing AFSIW circuits as this type of transition is not the limiting part, contrary to PCB integrated solutions.

The proposed transition is illustrated in Fig. 2.6. The AFSIW circuits can be seen as a nonstandard RWG. Thus, to design the transition, the easiest solution is to make a gradual change of section on several wavelengths. This solution is very costly, bulky, and not compact. To overcome those disadvantages, the transition can be designed using a series of discontinuities separated by a quarter-wavelength. This type of stepped impedance transformer has a wide bandwidth, as it keeps the same width while lowering the height.

The transition structure consists of an AFSIW section (13 x 1.524 mm²), 3 stepped impedance section, and a WR-51 section (13 x 6.48 mm²). The dimensions of the stepped impedance transformer are given in Fig. 2.6.

Fig. 2.7 shows the simulated S-parameters of the transition in the WR-51 band. It can be observed that the transition is well matched over the operating band. The insertion loss is equal to 0.04 dB over the work band. It is worthy to note that with the stepped impedance transformer, the length of the transition directly impacts the insertion loss. However, by minimizing the length of the transition, i.e., minimizing the number of sections, the impedance matching is harder to get over a wide band.

The designed transition is then implemented in a test fixture to be able to measure at low- and high-power levels. The test fixture is composed of two pairs of transition and their supports and one support for the AFSIW DUT (Device Under Test). The implementation of the test fixture is shown in Fig. 2.8.

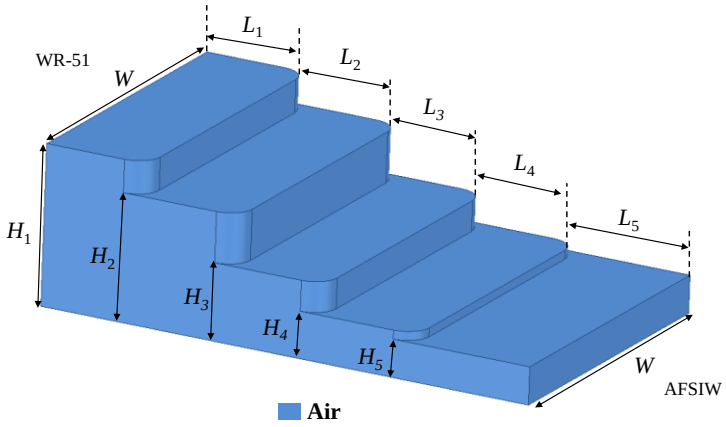

Fig. 2.6. Transition geometry with H_1 = 6.48 mm, H_2 = 5.15 mm, H_3 = 3.11 mm, H_4 = 1.88 mm, H_5 = 1.524 mm, L_1 = 4.34 mm, L_2 = 4 mm, L_3 = 3.72 mm, L_4 = 4 mm, L_5 = 4.34 mm, and W = 13 mm.

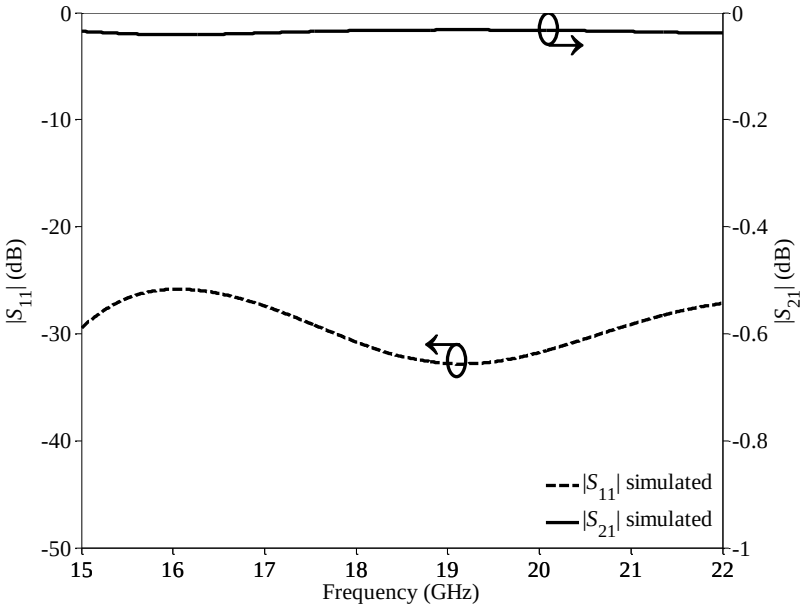

Fig. 2.7. Simulated S-parameters of the proposed transition from RWG WR-51 to AFSIW.

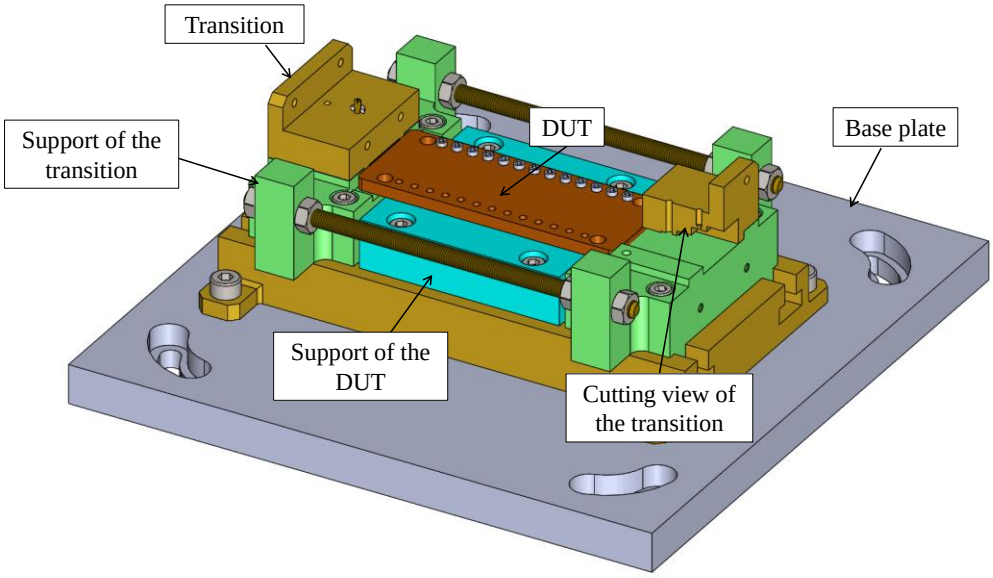

Fig. 2.8. 3D view of the proposed test fixture.

2. 2. 3. AFSIW Transmission Line

Based on Section 2. 1, an AFSIW transmission line is designed. To be able to operate in the WR-51 band, the AFSIW transmission line has a width of 13 mm, the height of the transmission line is chosen to be one of the PCB standard height, h_2 = 1.524 mm, and is equal to the AFSIW section height.

To be able to have the optimal performances, the electrical sidewalls of the transmission line were chosen to be copper platted. Hence, the dielectric losses are null and the AFSIW transmission line is similar to a WR-51 waveguide with a smaller height.

It is then possible to evaluate the principal characteristics of the AFSIW transmission line using the previous given formulas. With the chosen dimensions, the cutoff frequency of the TE_{10} mode is equal to 11.57 GHz using (2.1). Then, the lowest frequency band, which corresponds to 1.25*f_{c10} in order to avoid the high dispersive region occurring near the cutoff frequency [12], is equal to 14.46 GHz.

For demonstration purposes, an AFSIW transmission line is implemented using 1.524 mm thick Hi-*Tg* FR4 substrate for the three layers of the PCB. The transmission line has a length L = 70 mm and a width W = 13 mm. The fabricated inner substrate is shown in Fig. 2.9. Measurements were made using a N5225A PNA microwave network analyzer from Keysight with the WR-51 test fixture introduced previously. The effects of the cables, WR-51 waveguide and test fixture are de-embedded using a thru-reflect-line (TRL) AFSIW calibration kit. The AFSIW TRL kit has been designed and fabricated following the procedure explained in [14]. Reference planes are shown in Fig. 2.9. The theoretical, simulated, and measured transmission loss for the proposed structure is compared in Fig. 2.10. The theoretical loss mechanism of the AFSIW transmission line was calculated using (2.5) – (2.7) with a H_{rms} of 0.6 µm. Fig. 2.10 shows that the measured transmission loss varies from 0.02 dB/cm to 0.01 dB/cm over the band. The observed oscillation for the measured results comes from the incertitude of the TRL calibration. It can also be observed from Fig. 2.11 that the return loss of the fabricated AFSIW transmission line remains greater than 20 dB over the work band,

which demonstrates the good electrical behavior of the transmission line. To measure the transmission line, the test fixture previously presented is used. A photograph is given in Fig. 2.12.

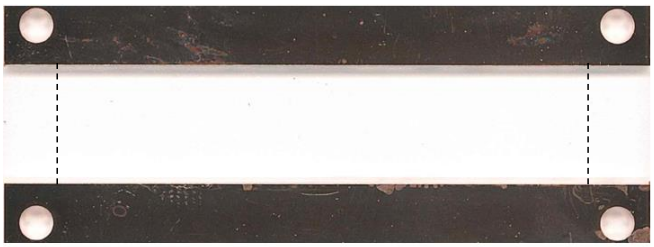

---- Reference planes

Fig. 2.9. Fabricated inner substrate of the AFSIW transmission line.

2. 2. 4. AFSIW Transmission Line Power-Handling

For microwave applications, it is important to evaluate the power-handling capability of a technology. Depending on the application, especially for space applications, the power limitation in terms of continuous wave signal can be a limiting effect. In a payload, interconnections between different components can be achieved using transmission line sections. Thus, evaluating the power-handling of an AFSIW transmission line can be useful for future implementations.

Therefore, to validate the power-handling capability of the AFSIW transmission line, experimental tests are carried out using Cobham Microwave high-power facilities. The experimental setup is shown in Fig. 2.13. To fully characterize the technology for space applications, the power-handling test is made using space environment conditions. Therefore, the DUT is placed in a vacuum chamber. The test flow is described below. First part of the test consists in reaching the partial vacuum (~10^{-5} mbar). This level of pressure is lower than the one requested for conventional tests under vacuum [13]. Once this pressure is established, the input power level is increased until the maximum power level available in Cobham facilities (190 W) in this frequency band. Then, the temperature in the vacuum chamber is increased to reach 90 °C. A higher temperature allows placing the DUT in a more stringent environment, as the conductivity of the metals and the electrical performances are degraded. Finally, the component behavior is observed in these conditions for a sufficient amount of time.

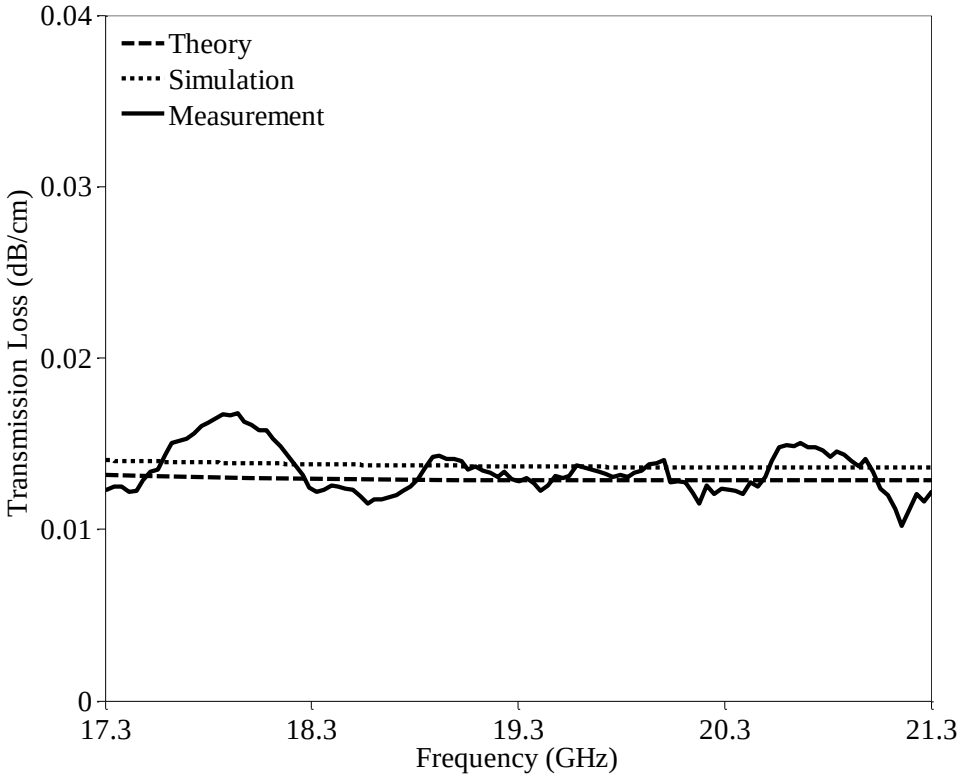

Fig. 2.10. Transmission loss of an AFSIW transmission line obtained in theory, simulation, and measurement.

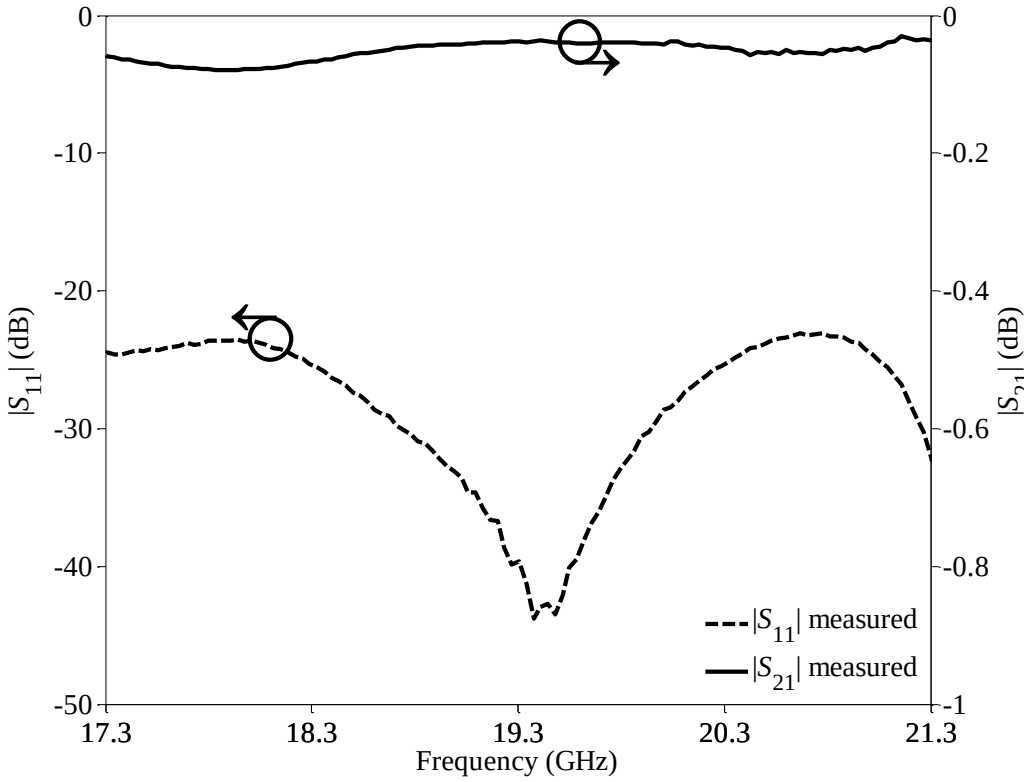

Fig. 2.11. Measured S-parameters of the AFSIW transmission line of length 70 mm.

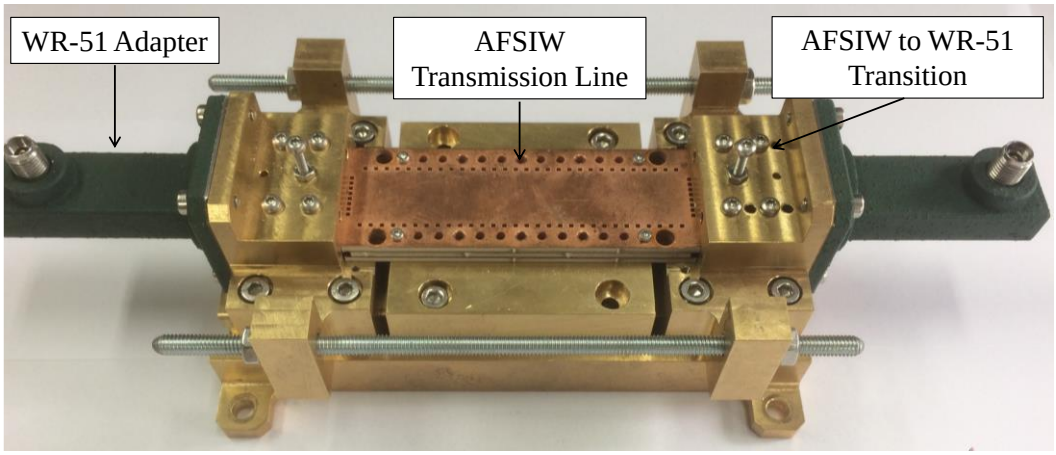

Fig. 2.12. Photographs of the AFSIW transmission line on the proposed test fixture.

The power-handling test is made at a single frequency point, here 20.9 GHz. It can be observed from Fig. 2.14 that the return loss of the transmission line remains greater than 20 dB during the whole test, thus demonstrating the good behavior of the component. Fig. 2.15 and Fig. 2.16 shows the behavior of the DUT in pressure and temperature. It can be observed in Fig. 2.15, that the pressure increases as the temperature is increased. This phenomenon is very current in the power-handling test under vacuum conditions and is called outgassing.

The power-handling test is well performed, and no sign of large decrease of return loss, large unexpected rapid decrease or increase of the temperature (except the ones created by power or thermal modifications) are observed. Thus, it can be concluded that the AFSIW transmission line can handle a minimum of 190 W under vacuum condition with a thermal set point of 90 °C.

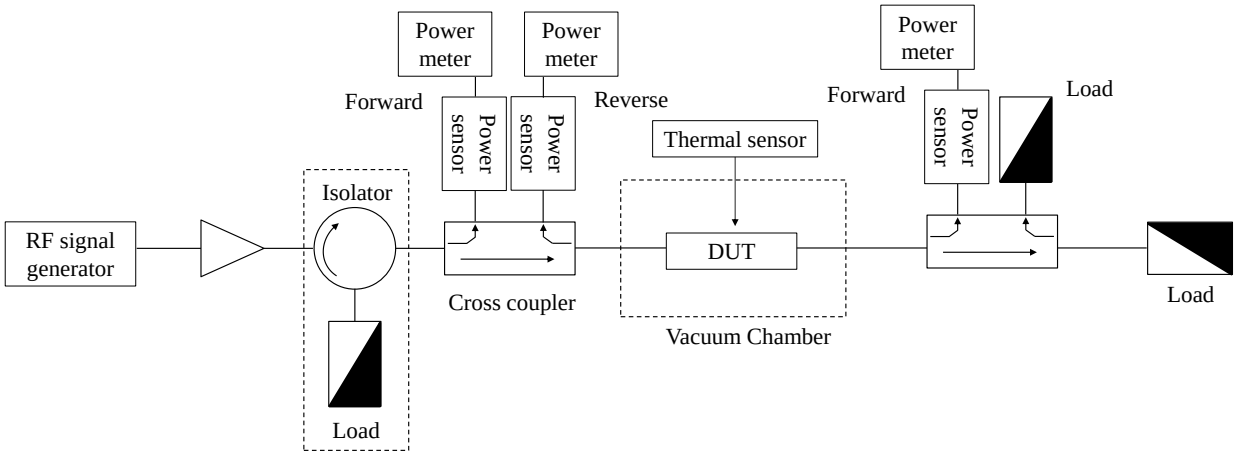

Fig. 2.13. Setup of the power-handling test with CW input in the vacuum chamber (10^{-5} mbar).

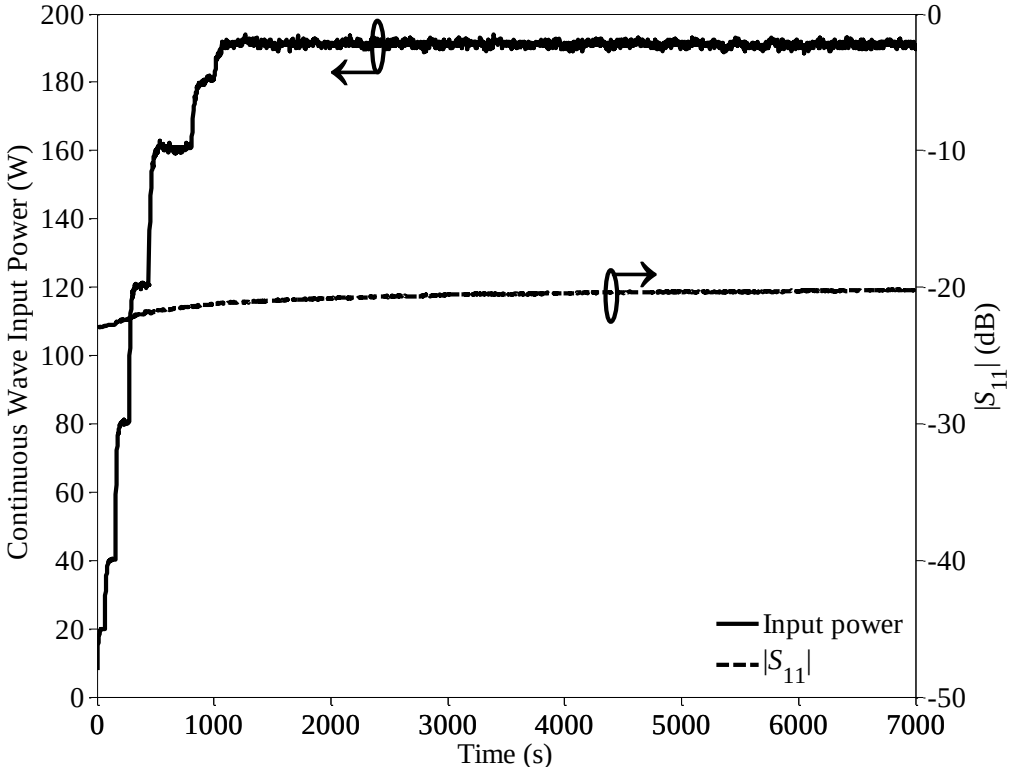

Fig. 2.14. Measured CW input power and return loss over time of the AFSIW transmission line in the vacuum chamber (10^{-5} mbar) at 20.9 GHz.

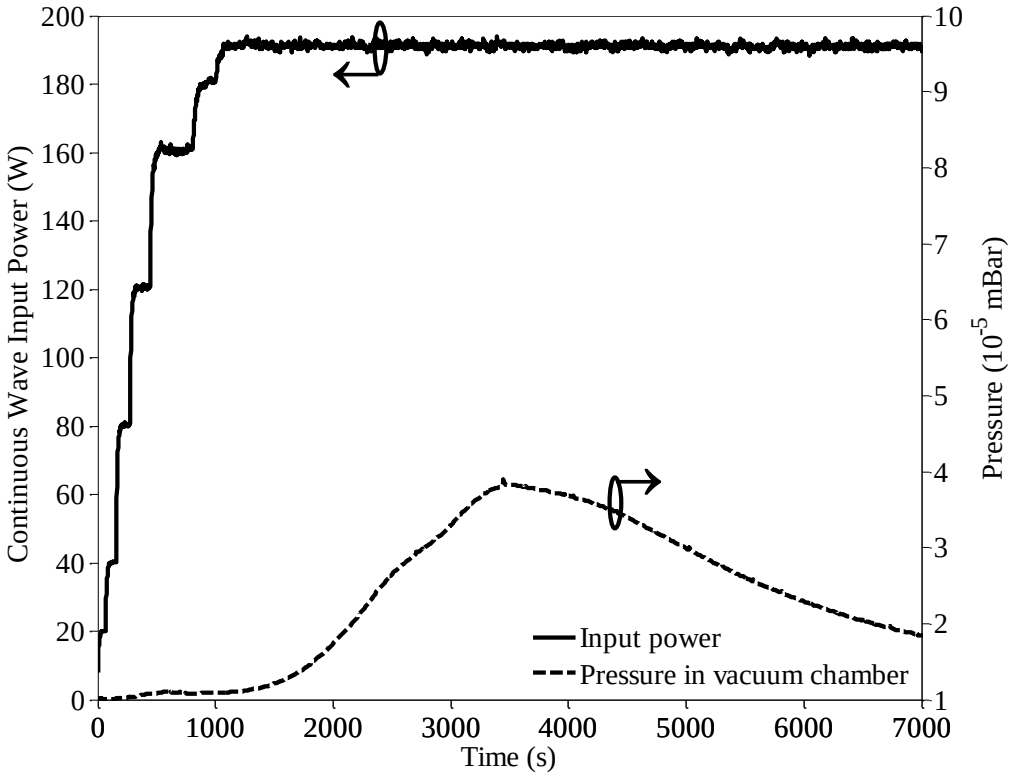

Fig. 2.15. Measured CW input power and pressure over time of the AFSIW transmission line in the vacuum chamber (10^{-5} mbar) at 20.9 GHz.

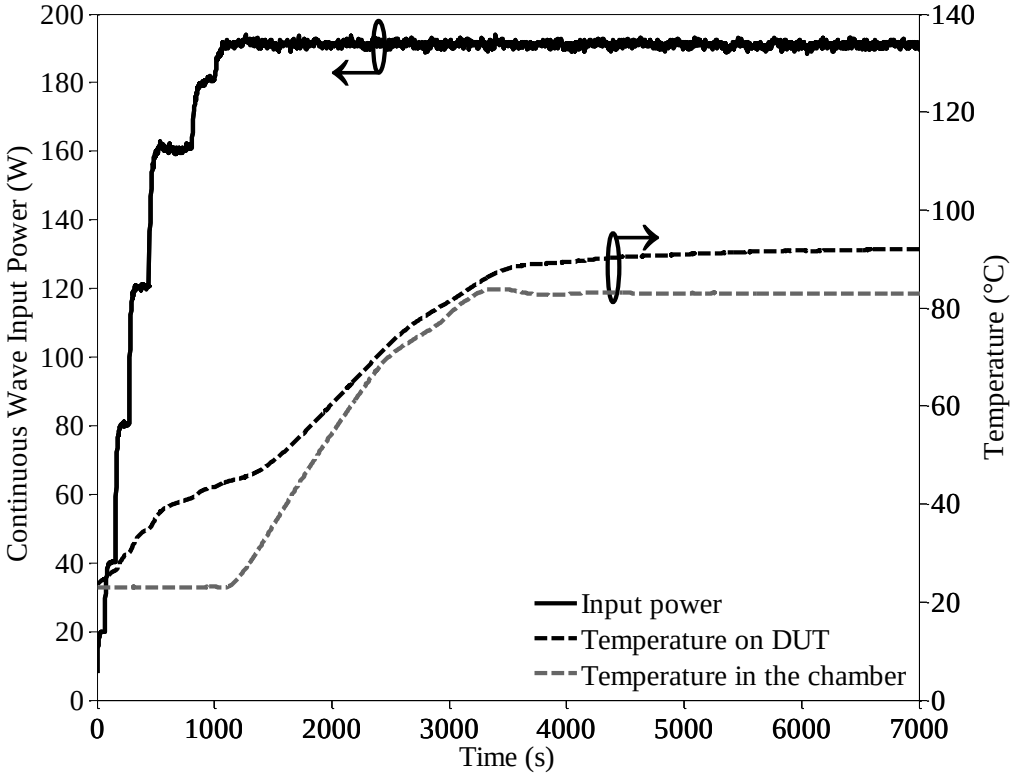

Fig. 2.16. Measured CW input power and temperature over time of the AFSIW transmission line in the vacuum chamber (10^{-5} mbar) at 20.9 GHz.

2. 3. Air-Filled Substrate Integrated Waveguide Filter

In the past decades, the emerging telecommunication applications such as telemetry, navigation, and remote control have tremendously stimulated the development of novel microwave and millimeter-wave components. The future generation of RF front-end, and payload systems have pushed the community to pursue high performance, high selectivity, low insertion loss, high power-handling performances. Among the microwave components, microwave filters have a crucial role in the communication chain.

A microwave filter is a two-port network component used to select a specific frequency band while rejecting other frequency bands. One of the crucial parameters of a filter technology is the *Q*-factor as it defines the achievable insertion loss. A promising feature of the AFSIW technology is to benefit from a high *Q*-factor while maintaining a high integration degree at a low cost. Microwave AFSIW filters can be synthesized by using classic design procedures for the conventional air-filled waveguide filters. Thus, the synthesis of AFSIW filters is similar to the synthesis of air-filled waveguide filters, although the sidewalls of an AFSIW can be implemented by using arrays of metallized via. In order to alleviate the time of simulation and to be able to use well-known synthesis methodologies, the sidewalls are often implemented as perfect electric conductors (PEC) in the simulation tools. Once the design is completed, it is possible, depending on the application, to implement the arrays of metallized via in order to fully simulate the total structure.

2. 3. 1 Filter Design

In order to validate the technology for filter applications, a specification of a filter operating in the Ka-band is proposed. An all-pole 4th order bandpass filter is proposed. The filter center frequency is located at 21 GHz, the -3 dB bandwidth of the filter is 300 MHz, giving a relative bandwidth of 1.43%. There are no specifications on the rejection level, insertion loss variation or group delay variation of the filter. There has been extensive work in the development of methodologies to design waveguide filters, and very good explanations can be found in [3].

First, the bandpass filter is designed by cascading four rectangular half-wavelength cavities (four rectangular resonators operating at fundamental mode TE_{10}) with inductive iris to couple them. The Chebyshev approximation is used to synthesis this type of filter. The design methodology of a Chebyshev filter implemented using thick inductive iris in an air-filled rectangular waveguide has been extensively studied in many publications [15]. Here, the used methodology is the one presented in [3]. The inductive irises are used as impedance inverters between two resonators. The fractional bandwidth ω_λ is calculated with the following equation:

$$\omega_\lambda = \frac{\lambda_{g_1} - \lambda_{g_2}}{\lambda_{g_0}}, \tag{2.9}$$

where λ_{g0}, λ_{g1} and λ_{g2} are the guided wavelength at the center, higher and lower frequency, respectively. Thus the impedance inverter values are obtained using the following equations:

$$\frac{K_{0,1}}{Z_0} = \sqrt{\frac{\pi}{2}\frac{\omega_\lambda}{g_0 g_1}}, \tag{2.10}$$

$$\left.\frac{K_{i,i+1}}{Z_0}\right|_{i=1:n-1} = \sqrt{\frac{\pi}{2}\frac{\omega_\lambda}{g_i g_{i+1}}}, \tag{2.11}$$

$$\frac{K_{n,n+1}}{Z_0} = \sqrt{\frac{\pi}{2}\frac{\omega_\lambda}{g_n g_{n+1}}}. \tag{2.12}$$

The equivalent circuit of the proposed bandpass filter is given in Fig. 2.17. Hence, the equivalent T network of the iris can be calculated using an EM simulator. An iris is represented by two series inductances denoted by X_a and a shunt inductance denoted by X_b [3]. Combining the *K*-inverter model with an EM simulator, the values of the equivalent circuit shown in Fig. 2.17 can be calculated with the following equations:

$$j\frac{X_b}{Z_0} = \frac{2S_{21}}{(1 - {S_{11}}^2) - {S_{21}}^2}. \tag{2.13}$$

$$j\frac{X_a}{Z_0} = \frac{1 + S_{11} - S_{21}}{1 - S_{11} + S_{21}}, \tag{2.14}$$

where S_{11} and S_{21} are the S-parameters of the dominant TE_{10} mode. The values X_a and X_b are related to K and ϕ as follows:

$$\frac{K}{Z_0} = \left|\tan\left(\frac{\phi}{2} + \tan^{-1}\frac{X_b}{Z_0}\right)\right|, \tag{2.15}$$

$$\phi = -\tan^{-1}\left(2\frac{X_a}{Z_0} + \frac{X_b}{Z_0}\right) - \tan^{-1}\frac{X_b}{Z_0}. \tag{2.16}$$

These functions are not explicit, and it is necessary to run the EM simulator for a range of iris widths to calculate S-parameters of the corresponding X_a, X_b, K, and ϕ. Knowing the value for K, it is possible to find the corresponding iris width. Then, the corresponding value ϕ is used to find the resonators' lengths using:

$$l_i = \frac{\lambda_{g0}}{2\pi}\left(\pi + \frac{1}{2}(\phi_i + \phi_{i+1})\right). \tag{2.17}$$

The methodology is used to design an all-pole fourth-order bandpass filter. The structure and the dimensions of the bandpass filter are shown in Fig. 2.18. The thickness of the inductive iris is fixed to 2 mm. As the proposed filter function is basic, the dielectric slabs were not required in this case, hence the electric sidewalls are directly implemented by copper platting. It is important to add that the filter is symmetric, meaning dimensions of cavities 1, 4, and cavities 2, 3 are equal ($L_1 = L_4$, $L_2 = L_3$). Obviously, the inductive iris follows the same logic.

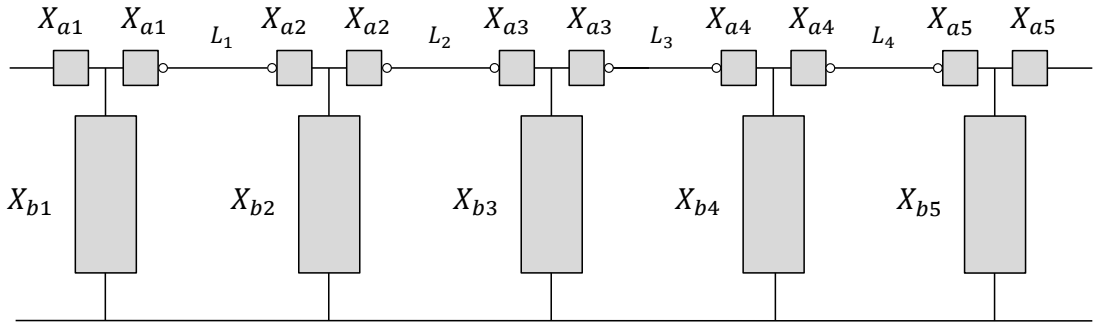

Fig. 2.17. Equivalent circuit of the proposed bandpass filter.

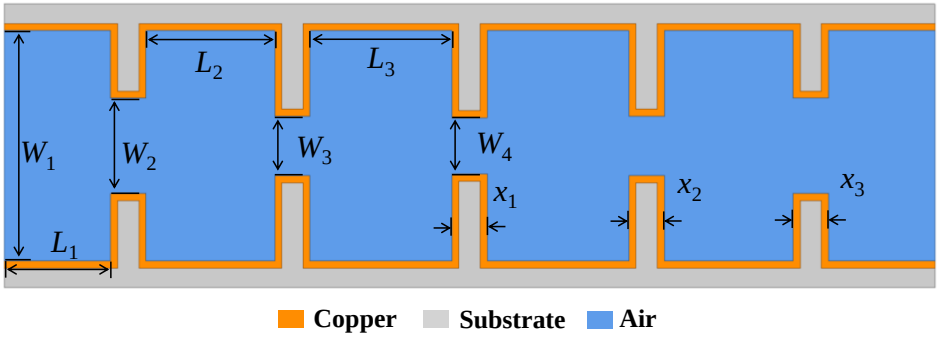

Fig. 2.18. Top view of substrate 2 with W_1 = 13 mm, W_2 = 5.37 mm, W_3 = 3.31 mm, W_4 = 3.07 mm, L_1 = 6 mm, L_1 = 7.25 mm, L_1 = 7.97 mm, x_1 = 2 mm, x_2 = 2 mm, and x_3 = 2 mm.

2. 3. 2 Experimental Results

For demonstration purpose, a fourth-order AFSIW filter, using an in-line arrow configuration, has been designed and fabricated. A photograph of the fabricated filter is shown in Fig. 2.19. The fabrication is based on a multilayer PCB process. The substrate used is FR4 with 1.524 mm thickness.

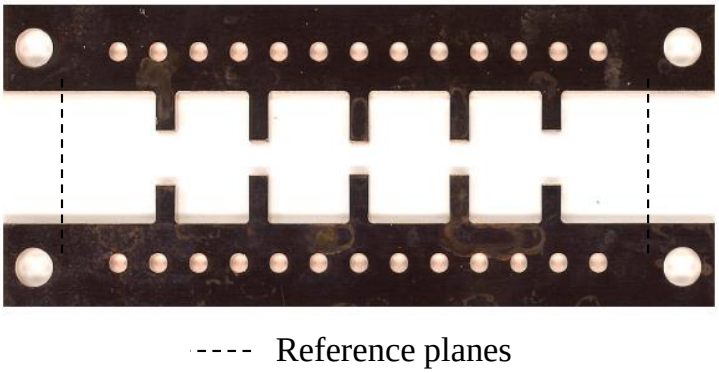

Fig. 2.19. Photographs of substrate 2 of the fabricated fourth-order AFSIW filter demonstrator.

A vector network analyzer, the test fixture introduced in previous Section, and an AFSIW TRL calibration kit are used for the measurement. Simulated and measurement S-parameters are shown in Fig. 2.20. The measured central frequency is 20.98 GHz. The measured -3 dB bandwidth is 305 MHz compared to 300 MHz in the simulation. The return loss of the filter is above 20 dB in the passband. The measured in-band insertion loss is 0.78 dB, very similar to the 0.72 dB obtained in the simulation. The obtained *Q*-factor, using a 1.524 mm thickness substrate, is 1560, determined using [16]:

$$Q_u \approx 4.343 \frac{N}{IL(\text{dB}) \frac{\Delta f_{3\text{dB}}}{f_0}}, \tag{2.18}$$

where N is the filter order, IL is the centre insertion loss, f_0 is the centre frequency, and $\Delta f_{3\text{dB}}$ is the -3 dB bandwidth.

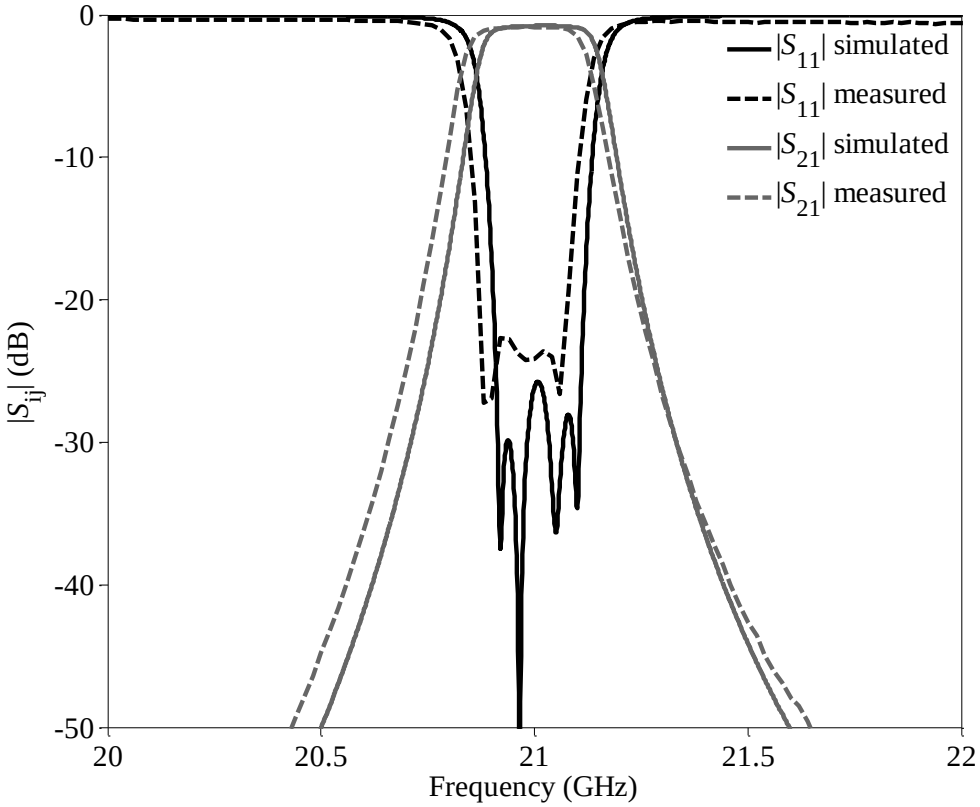

Fig. 2.20. Simulated and measured S-parameters of the in-line 4th order AFISW filter.

2. 3. 3. AFSIW Filter Power-Handling

For high-power operations, different effects must be taken into account. The first one is related to the thermal aspect and high-power breakdown, it is usually evaluated using a continuous wave test. The second one is the multipaction breakdown. Finally, the ionization breakdown, also known as corona effect, can also be detrimental in such applications. These different effects are evaluated for the AFSIW technological platform on the previously measured AFSIW filter demonstrator. It is worthy to add that another effect called passive intermodulation (PIM) is also important but is not studied in this work. The multipactor and corona tests were not performed on the AFSIW transmission line as it is not often a component subjected to those effects.

2. 3. 3. 1 Continuous Wave Test

To validate the power-handling capability of the AFSIW filter, experimental tests are carried out using Cobham Microwave high-power facilities. The experimental setup is the same as the one presented in Section 2. 2. 4. The test flow is similar to the one in the transmission line section except that the temperature of the vacuum chamber is not increased. Indeed, a filter is usually more lossy than a transmission line, operating at the same frequency and fabricated with the same technology. Under high-power conditions, those losses are responsible for a self-heating. Thus, to study the behavior of the filter, the temperature in the vacuum chamber was not increased.

The test is made at 20.9 GHz. Fig. 2.21 shows that the return loss of the filter remains greater than 20 dB during the time of the test. It is shown from Fig. 2.21 that the return loss is increasing during the test. As the temperature of the DUT is increasing, the physical dimensions of the filter expand causing the filter response to shift in frequency. As the test is performed on a single frequency point, the value of the RL is susceptible to change. This variation is continuous and shows no rapid change demonstrating the correct behavior of the component. It can be observed from Fig. 2.22 that the pressure of the test is 10^{-5} mbar during the whole test. Fig. 2.23 shows the input power, the temperature of the DUT and vacuum chamber versus time. As explained previously, it was not necessary to regulate the temperature in the vacuum chamber as the filter reach high temperature (120 °C) due to the losses. The filter is pressed on a brass support and the thermal sensor is placed on the top of the DUT.

It is demonstrated from the different responses that there is no sign of large decrease of return loss, large unexpected decrease or increase of any temperature (except the ones created by power or thermal modifications) are observed. Thus, it can be concluded that the AFSIW filter can handle a minimum of 190 W under vacuum condition. It is also worthy to observe that the filter behaves correctly with a measured stabilized temperature of 120 °C.

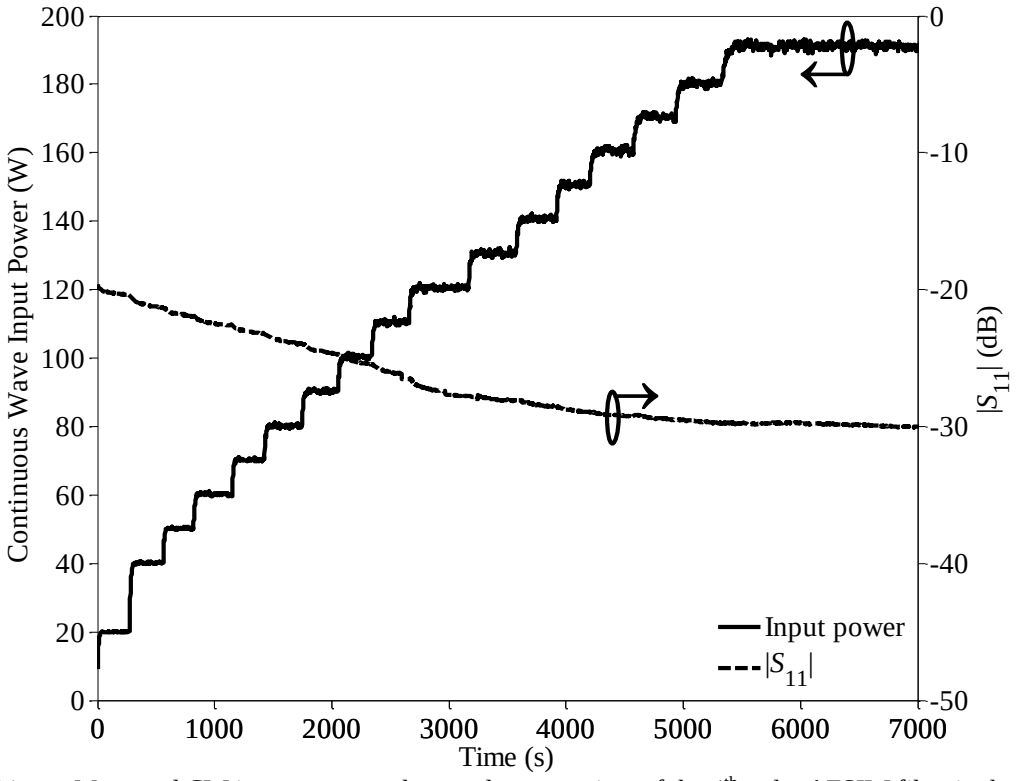

Fig. 2.21. Measured CW input power and return loss over time of the 4th order AFSIW filter in the vacuum chamber at 20.9 GHz.

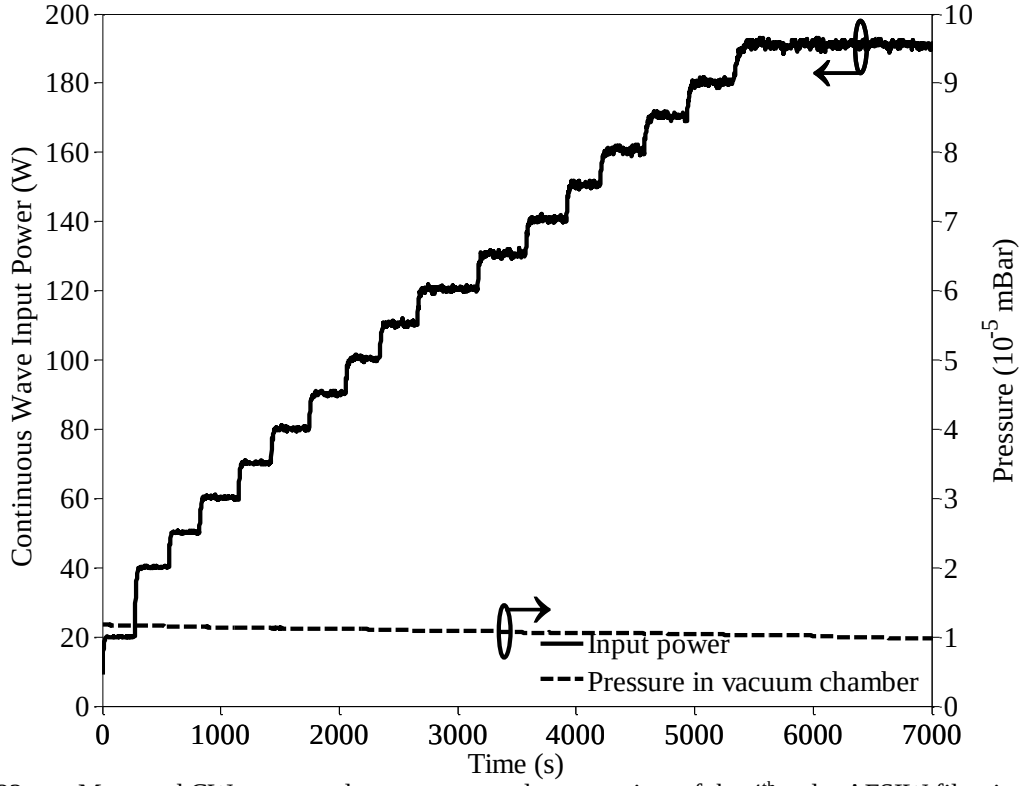

Fig. 2.22. Measured CW power and pressure return loss over time of the 4th order AFSIW filter in the vacuum chamber at 20.9 GHz.

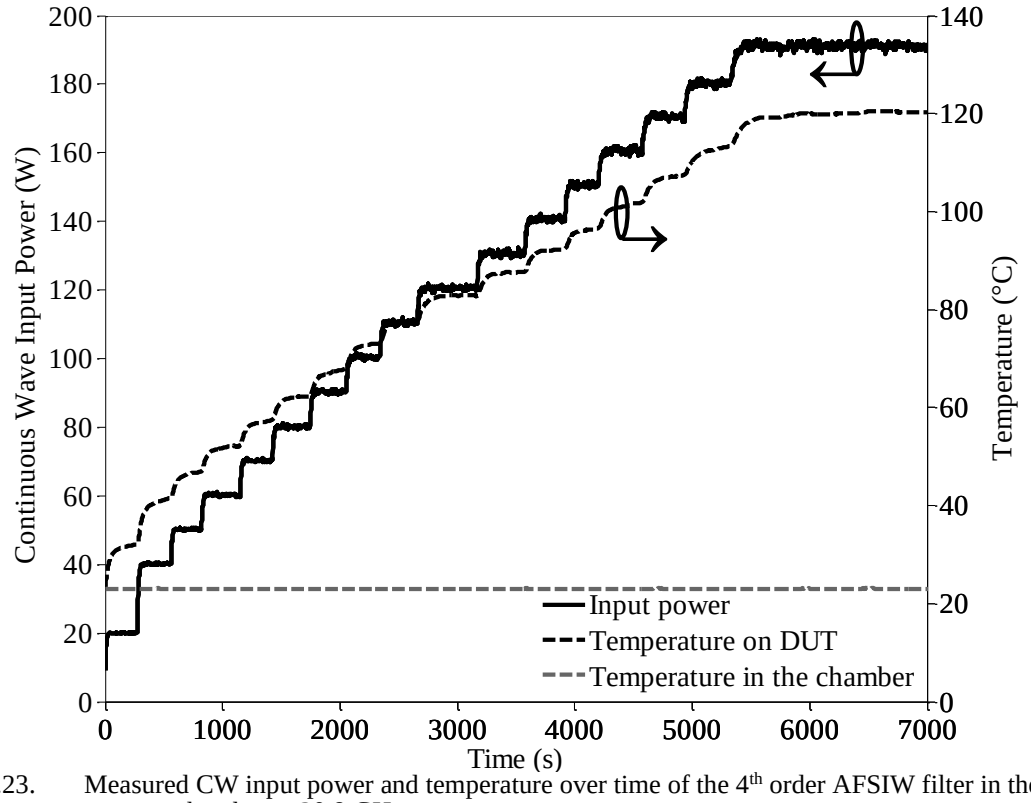

Fig. 2.23. Measured CW input power and temperature over time of the 4th order AFSIW filter in the vacuum chamber at 20.9 GHz.

2. 3. 3. 2 Multipactor Test

Multipactor breakdown is an electron avalanche discharge, happening under vacuum conditions and high-power RF electromagnetic fields [17]. This phenomenon can occur in satellite passive communication devices. The RF electromagnetic fields are susceptible to accelerate free electrons inside the component, those electrons, striking the metallic surfaces of the component can release secondary electrons. By a phenomenon of avalanche-like, a high electrical current can be created between the metallic surfaces, thus creating a short-circuit canceling the component function. Extensive work has been made to study the multipactor effect [18] and the intent of this thesis is to evaluate the power level the AFSIW technology can reach.

The interaction between the electron and the metallic surface can be modeled with the SEY (Secondary Electron Yield) function. The SEY model and formulas are described in [19] and [20]. Using the different data, a simulation of the multipactor effect was carried out using the software SPARK3D. The simulation shows no multipactor effect, using as input power the maximum available power in Cobham facilities (190 W).

In order to validate the simulation, an experimental test is carried out using Cobham Microwave high-power facilities. The experimental setup is shown in Fig. 2.24 and is the conventional one for multipactor measurements. A photograph of the electron gun position is given in Fig. 2.25. Contrary to the continuous wave input power-handling test, the multipactor test is made using pulsed input power in order to lower the self-heating of the filter. The applied signal has been pulsed with a carrier frequency of 20.9 GHz, a pulse width of 100 µs with a duty cycle of 10%. The pressure of the vacuum chamber is set at 5.5 10^{-6} mbar. Fig. 2.26 shows the return loss of the filter over the time range. It can be observed that the return loss is above 20 dB. Fig. 2.27 presents the pulsed input power, temperature of the DUT and vacuum chamber versus time.

To be sure to ignite the multipactor effect, if it is meant to occur, an electron gun is used during the test to saturate the gap of the two metal plates (critical multipactor area) in electrons. This electron gun needs to be pointed to a hole where the E-field is at its maximum, in our case, in the center of a resonance cavity. It is demonstrated from the different tests that there is no sign of large rapid increase or decrease of return loss or temperature. Thus, it can be concluded that the AFSIW filter can handle 190 W without multipactor effect occurring.

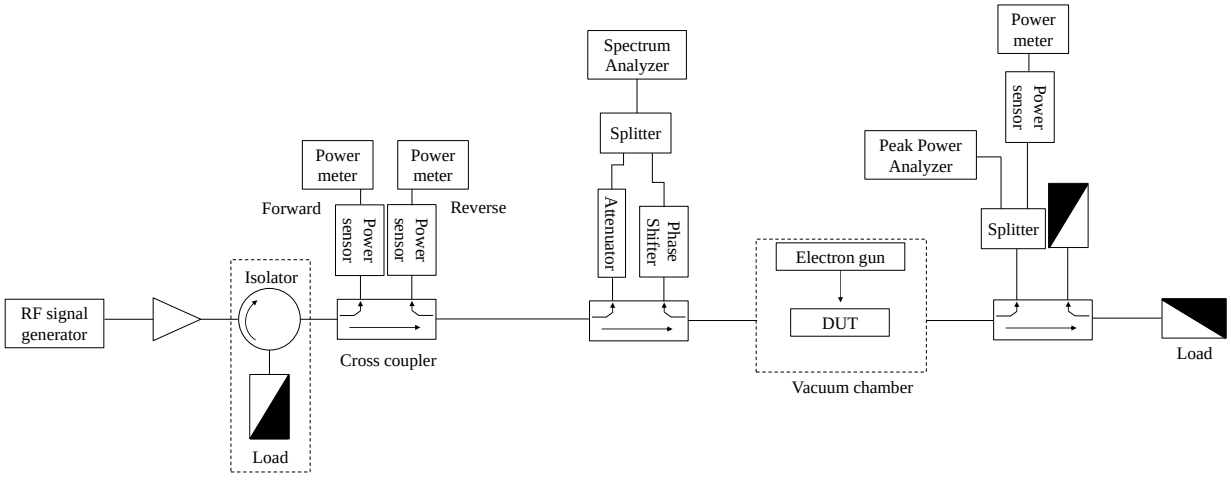

Fig. 2.24. Setup of the multipactor test with the detection systems.

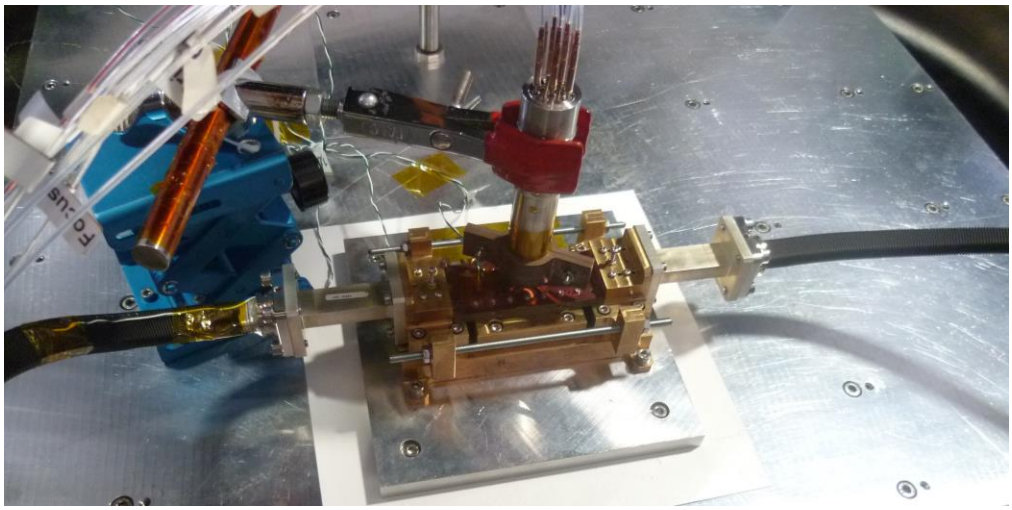

Fig. 2.25. Photographs of the multipactor test with the electron gun pointed to the DUT.

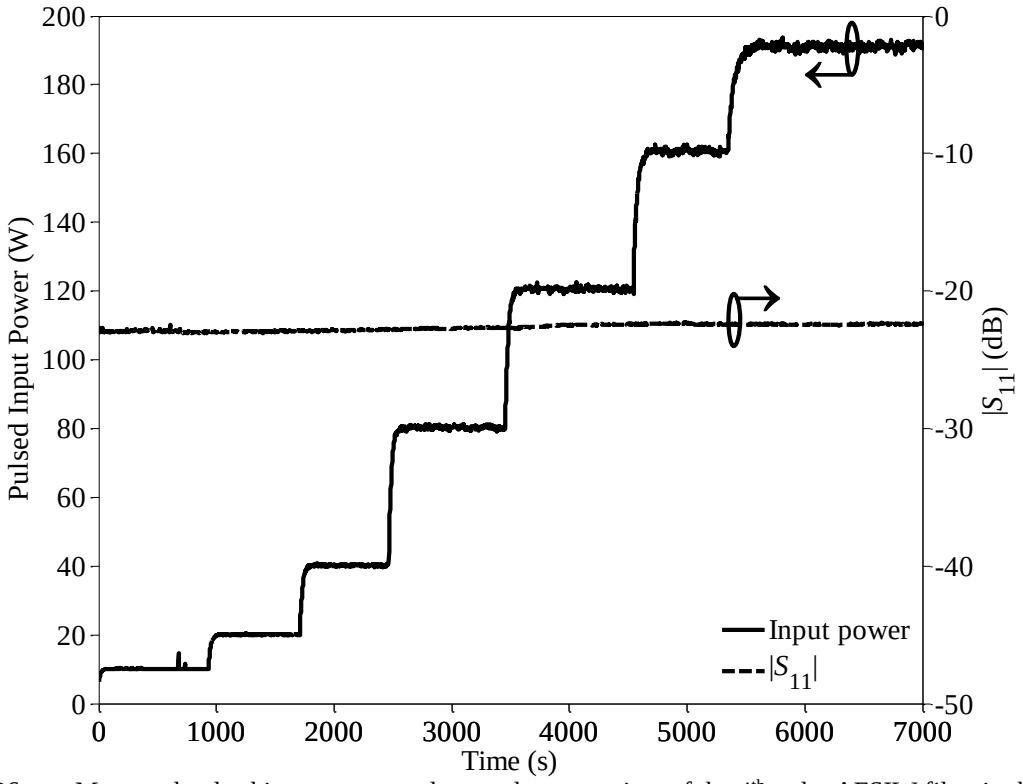

Fig. 2.26. Measured pulsed input power and return loss over time of the 4th order AFSIW filter in the vacuum chamber at 20.9 GHz.

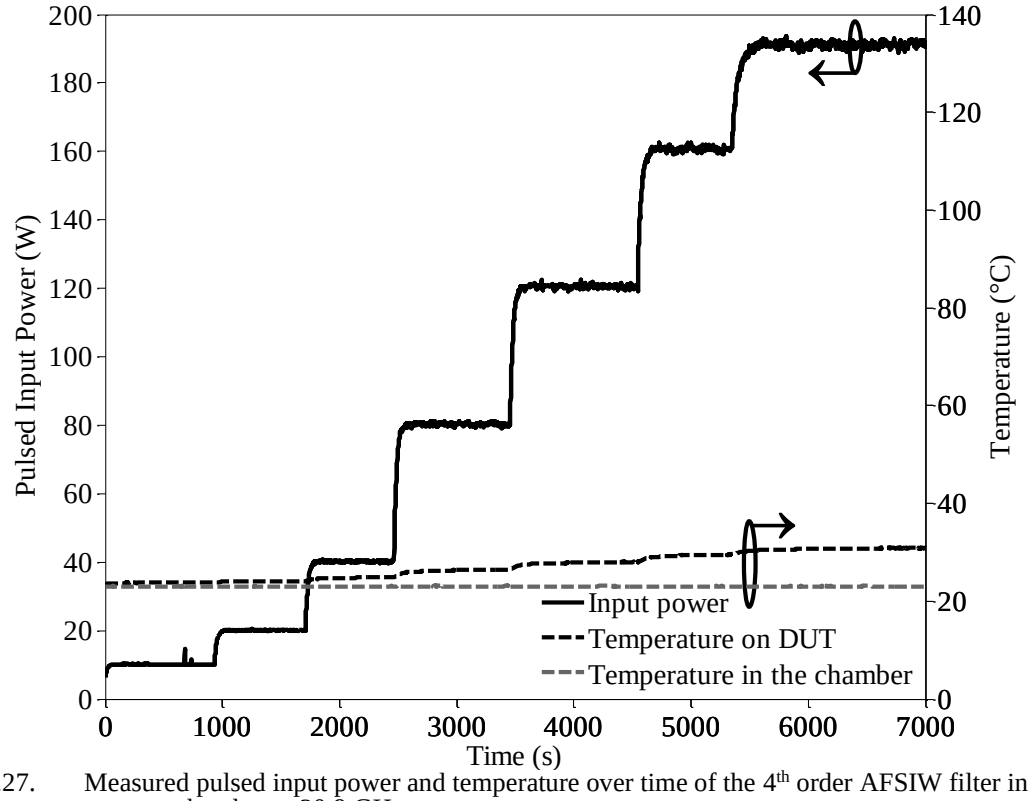

Fig. 2.27. Measured pulsed input power and temperature over time of the 4th order AFSIW filter in the vacuum chamber at 20.9 GHz.

2. 3. 3. 3 Corona Test

A corona discharge is an electrical discharge involving electron dynamics inside gases. When the electric field is strong enough, a chain reaction can be created. Electrons in the air can ionize atoms by colliding with them with enough energy transfer, resulting in releasing other electrons. Those electrons are susceptible to have the same behavior and thus create an avalanche-like reaction. To be able to ionize the two major constituents of air (N_2 and O_2), it is necessary to have high electric fields. If the avalanche-like process is ignited, it results in the formation of an electron plasma. This electron plasma is synonymous with a corona discharge and is a destructive phenomenon.

The AFSIW technology presents an important density of the electric field due to the small thickness of the substrates involved and the achieved *Q*-factor. Thus, filters using this technology are susceptible to present a corona discharge for high power applied signals. Ionization breakdown in microwave filters is an extremely complicated phenomenon to analyze. As for the other tests, the intent of this work is to present the results of the corona test. Readers are encouraged to consult the references that cover in more details the phenomenon [21]-[24].

To evaluate the input power and the critical pressure susceptible to create a corona discharge, the E-fields of the AFSIW filter are extracted from the EM simulator and inserted in the SPARK3D simulator. From SPARK3D, the critical pressure is evaluated as 26 mbar and a corona discharge occurs at 11 W. The critical pressure is the pressure at which the component has the lowest power-handling capability. The critical pressure is linked to the Paschen's law.

Therefore, to validate the simulated results, a corona test has been performed using Cobham Microwave high-power facilities. Fig. 2.28 shows a schematic diagram of the measurement setup. In this test,

a conventional method consisting in observing the RL behavior has been employed to detect corona discharge. The procedure for test consists in establishing the desired input power, then decrease the pressure until reaching the critical pressure, observe the DUT behavior for 30 minutes, then decrease again the pressure until $3\ 10^{-5}$ mbar, and finally observe the DUT behavior.

The input power was set to 9 W with a carrier frequency of 20.9 GHz. In Fig. 2.29 and Fig. 2.30, the measured return loss and temperature on the DUT are shown. As previously explained, it can be observed that the pressure is decreased from 1015 mbar to 26 mbar (critical pressure) at 451 s, and from 26 mbar to $3\ 10^{-5}$ mbar at 2100 s, as it is shown in Fig. 2.31. During the test, Fig 2.29 shows that the return loss of the filter remains greater than 20 dB, and Fig. 2.30 presents a stable temperature on the DUT.

It is demonstrated from the different responses that there is no sign of large decrease of return loss or temperature. Thus, it can be concluded that the AFSIW filter can handle 9 W at a critical pressure of 26 mbar.

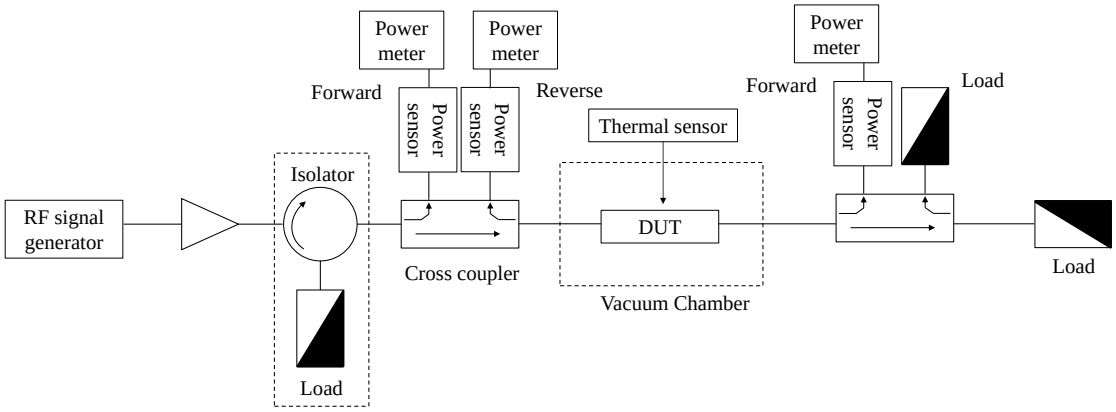

Fig. 2.28. Setup of the corona test.

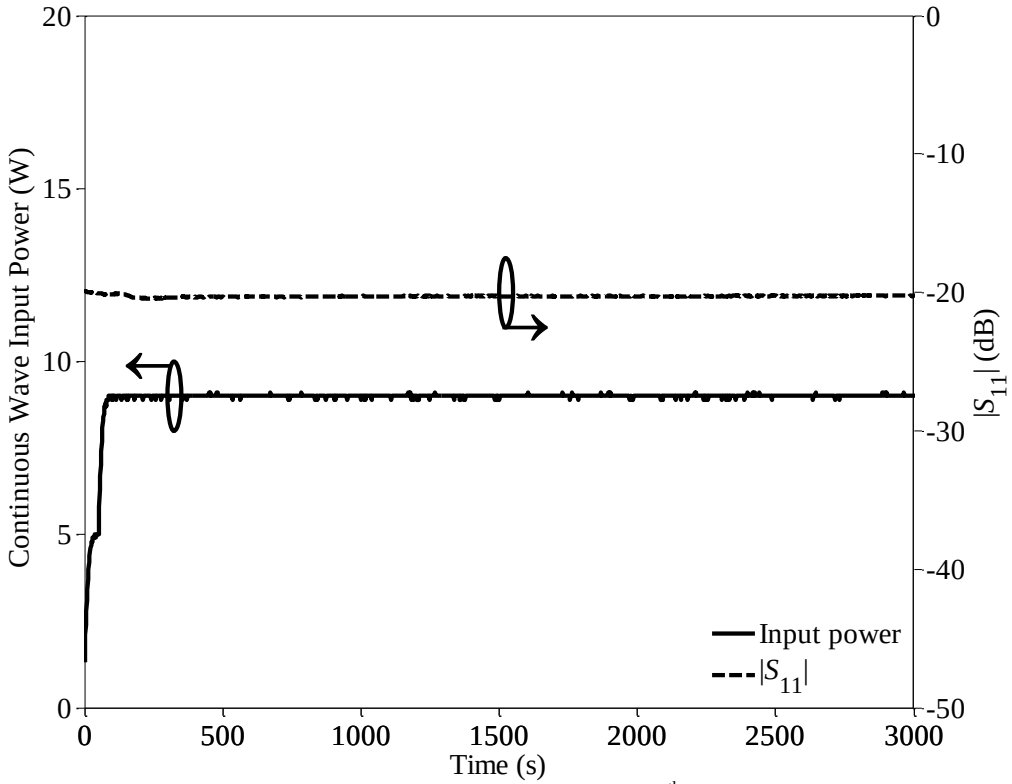

Fig. 2.29. Measured input power and return loss over time of the 4th order AFSIW filter in the vacuum chamber at 20.9 GHz.

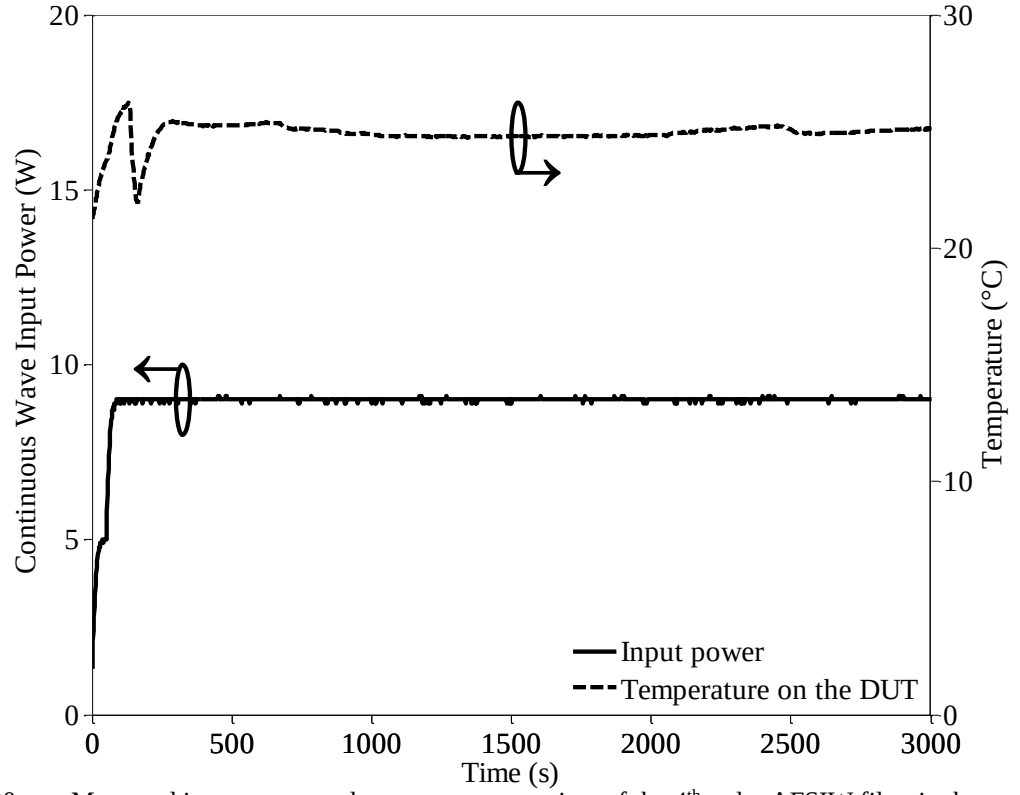

Fig. 2.30. Measured input power and temperature over time of the 4th order AFSIW filter in the vacuum chamber at 20.9 GHz.

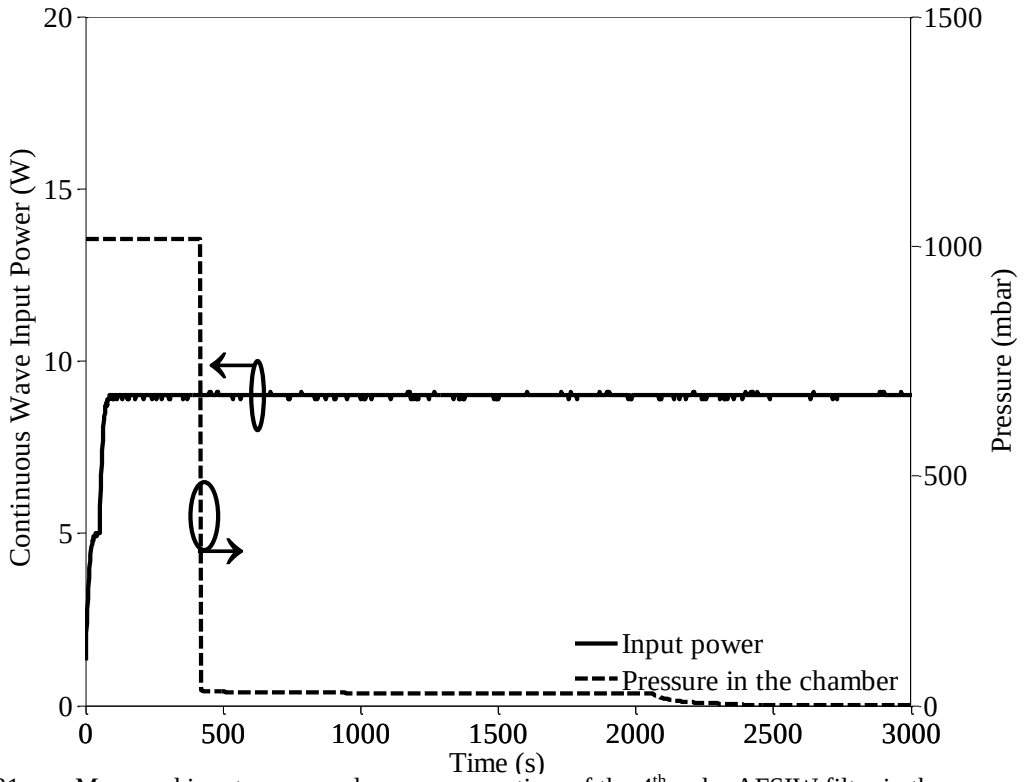

Fig. 2.31. Measured input power and pressure over time of the 4th order AFSIW filter in the vacuum chamber at 20.9 GHz.

To further investigate on the power handling capability of the fabricated filter, the same test is done with an input power of 10 W. The measured results are presented in Fig. 2.32 and Fig. 2.34. A large decrease of the return loss is observed at 685 s and a variation of the temperature on the DUT are observed. The variation of the temperature is not as pronounced as the return loss variation as the test is automatically stopped when detecting a variation of RL. If this security was not implemented, the creation of plasma would largely increase the temperature of the DUT and destroys it. The pressure profile is shown in Fig. 2.35. From the measured data, it can be concluded that a corona discharge occurs at 26 mbar with an input power of 10 W.

Table 1.2 summarizes the different measured performances obtained for the proposed Ka-band AFSIW components.

TABLE 1.2
SUMMARY OF MEASURED PERFORMANCES OF THE KA-BAND AFSIW COMPONENTS

Characteristics	Transmission Line	Filter
Small signal		
Return loss (dB)	> 20	> 20
Insertion loss (dB)	0.14	0.78
Center frequency (GHz)	/	20.98
-3 dB bandwidth (MHz)	/	305
-3 dB bandwidth (%)	/	1.45
Unloaded *Q*-factor	/	1560
High-power		
Continuous wave input power (W)	190	190
Multipactor (W)	/	190
Corona (W) @ 26 mbar (free)	/	9
Corona (W) @ 26 mbar (sparked)	/	10

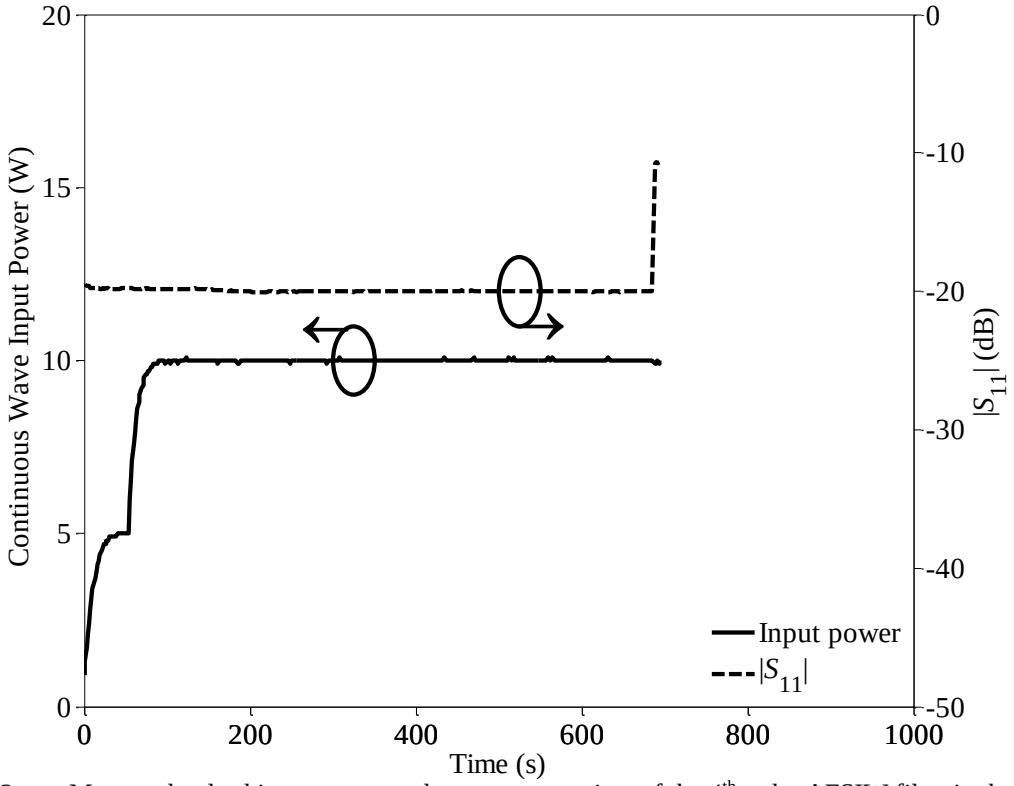

Fig. 2.32. Measured pulsed input power and pressure over time of the 4th order AFSIW filter in the vacuum chamber at 20.9 GHz.

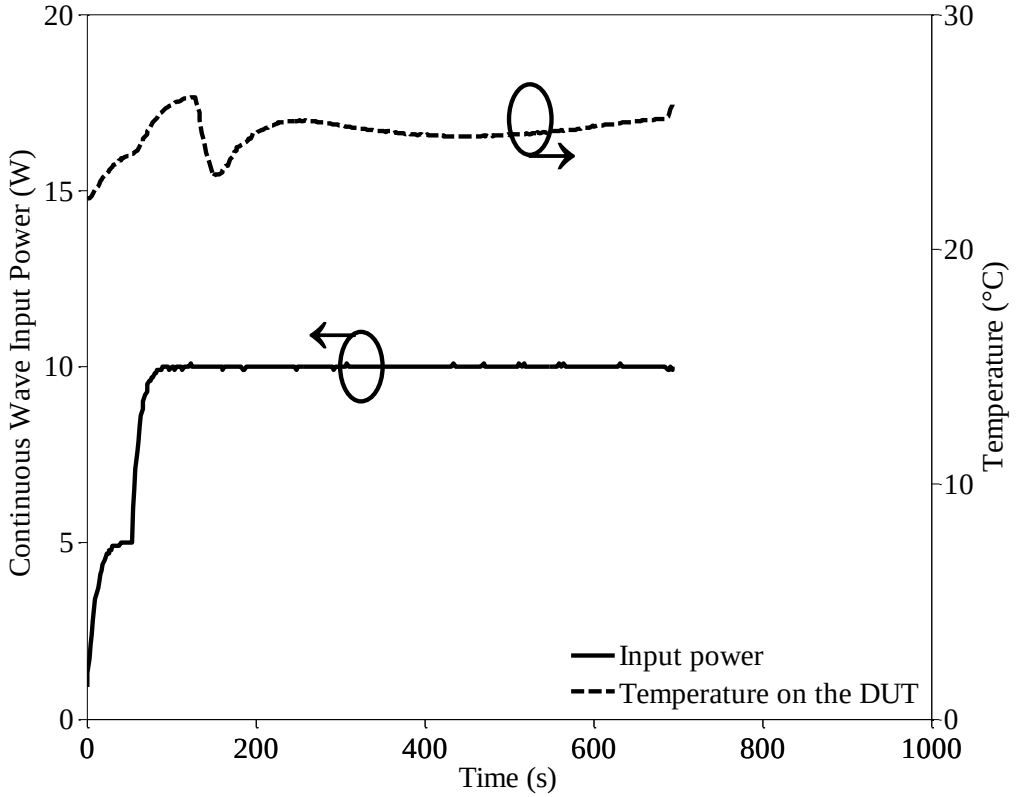

Fig. 2.33. Measured pulsed input power and pressure over time of the 4th order AFSIW filter in the vacuum chamber at 20.9 GHz.

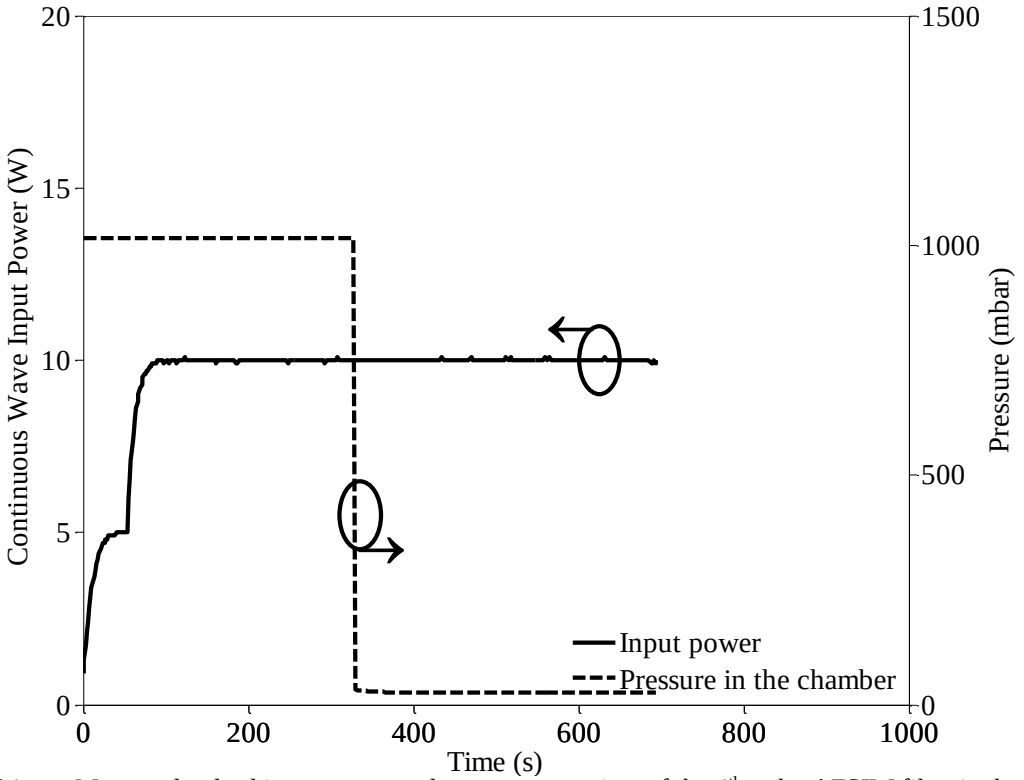

Fig. 2.34. Measured pulsed input power and pressure over time of the 4th order AFSIW filter in the vacuum chamber at 20.9 GHz.

2. 4. Conclusions

In this Chapter, the AFSIW technological platform is introduced. First, the structure of this technology is detailed as well as the implementation of the electric sidewalls. The loss mechanism of the technology is studied theoretically and compared to simulations and measurements. To be able to perform power-handling tests, a transition implemented in a test fixture is developed to be compliant with standard rectangular waveguide interconnections. To fully characterize the AFSIW transmission line behavior, a CW power-handling test was performed. The transmission line was tested under vacuum to be as close as possible of the space environment. The test was successfully done, and it was demonstrated that the AFSIW could handle a 190 W input power at 10^{-5} mbar for a set temperature of 90 °C. The proposed technology is then used to synthesize a Ka-band all-pole fourth-order bandpass filter operating at 21 GHz. The fabricated filter presents good results compared to simulations. To further study the implementation of AFSIW technological platform for filter functions, power-handling tests, including multipactor test and corona test are performed. The different power tests were in good agreement with the simulations. For the CW power-handling test, the filter handled a 190 W input power at 10^{-5} mbar. The multipactor test showed no multipactor effect with a pulsed input power of 190 °W. Finally, the corona test presented no corona discharge at a critical pressure of 26 mbar with a CW input power of 9 W. To evaluate the limit of the technology, another corona test was performed at the same critical pressure and with a CW input of 10 W, a corona discharge occurred and is closed to the 11 W obtained in the simulation. The AFSIW technological platform performances in the Ka-band were demonstrated in low- and high-power signal. In the next Chapter, the versatility of the technology will be discussed as well as the implementation of standard PCB process.

References

[1] N. Marcuvitz, Waveguide Handbook, Toronto, ON, Canada: McGraw-Hill, 1951, ch. 5, pp. 217-335.

[2] F. Parment, A. Ghiotto, T. Vuong, J. Duchamp, and K. Wu, "Air-filled substrate integrated waveguide for low-loss and high power-handling millimeter-wave substrate integrated circuits," *IEEE Transactions on Microwave Theory and Techniques*, vol. 63, no. 4, pp. 1228-1238, Apr.2015.

[3] R. J. Cameron, C. M. Kudsia, and R. R. Mansour, *Microwave Filters for Communication Systems*, Hoboken, NJ, USA: Wiley, 2007, ch. 14, pp. 501-530.

[4] D. M. Pozar, *Microwave Engineering*, 4th ed. John Wiley, 2012, ch. 6, pp. 272-316.

[5] E. Hammerstad and O. Jensen, "Accurate models for microstrip computer-aided design," *IEEE MTT-S International Microwave symposium Digest*, Washington, DC, USA, 1980, pp. 407-409.

[6] T. Liang, S. Hall, H. Heck, and G. Brist, "A practical method for modeling PCB transmission lines with conductor surface roughness and wideband dielectric properties," *IEEE MTT-S International Microwave Symposium Digest*, San Francisco, CA, 2006, pp. 1780-1783.

[7] S. Hall, S. G. Pytel, P. G. Huray, D. Hua, A. Moonshiram, G. A. Brist, and E. Sijercic, "Multigigahertz causal transmission line modeling methodology using a 3-D hemispherical surface roughness approach," *IEEE Transactions on Microwave Theory and Techniques*, vol. 55, no. 12, pp. 2614-2624, Dec. 2007.

[8] M. V. Lukic and D. S. Filipovic, "Modeling of 3-D surface roughness effects with application to μ-coaxial lines," *IEEE Transactions on Microwave Theory and Techniques*, vol. 55, no. 3, pp. 518-525, March 2007.

[9] Feng Xu and Ke Wu, "Guided-wave and leakage characteristics of substrate integrated waveguide," *IEEE Transactions on Microwave Theory and Techniques*, vol. 53, no. 1, pp. 66-73, Jan. 2005.

[10] M. Bozzi, L. Perregrini and K. Wu, "Modeling of conductor, dielectric, and radiation losses in substrate integrated waveguide by the boundary integral-resonant mode expansion method," *IEEE Transactions on Microwave Theory and Techniques*, vol. 56, no. 12, pp. 3153-3161, Dec. 2008.

[11] F. Parment, A. Ghiotto, T. Vuong, J. Duchamp and K. Wu, "Broadband transition from dielectric-filled to air-filled Substrate Integrated Waveguide for low loss and high power handling millimeter-wave Substrate Integrated Circuits," *IEEE MTT-S International Microwave Symposium (IMS2014)*, Tampa, FL, 2014, pp. 1-3.

[12] http://www.microwaves101.com/encyclopedias/waveguide-mathematics#cutoff

[13] Multipaction design and test, ECSS-E-20-01A Rev. 1, Mar. 2013.

[14] Engen, G.F., and Hoer, C.A.: "Thru-reflect-line: an improved technique for calibrating the dual six-port automatic network analyzer," *IEEE Trans. Microwave Theory Tech*., 1979, 27, (12), pp. 987–993.

[15] Shamsaifar, Khosro. "Designing iris-coupled waveguide filters using the mode-matching technique." *Microwave Journal*, Jan. 1992.

[16] V. Turgaliev, D. Kholodnyak, J. Mueller, and M. A. Hein, "Small-size low-loss bandpass filters on substrate-integrated waveguide capacitively loaded cavities embedded in low temperature co-fired ceramics," *J. Ceram. Sci. Technol*., vol. 6, no. 4, pp. 305–314, 2015.

[17] J. R. M. Vaughan, "Multipactor," *IEEE Trans. Electron Devices*, vol. 35, no. 7, pp. 1172–1180, Jul. 1988.

[18] "Multipaction design and test," European Space Agency, Noorwijk, The Netherlands, ECSS-E-20-01A, May 5, 2003.

[19] M. A. Furman and M. T. F. Pivi, "Simulation of secondary electron emission based on a phenomenological probabilistic model," Lawrence Berkeley Nat. Lab., Univ. California, Berkeley, CA, USA, Tech. Rep. LBNL-52807, Jun. 2003.

[20] J. de Lara et al., "Multipactor prediction for on-board spacecraft RF equipment with the MEST software tool," *IEEE Trans. Plasma Sci*., vol. 34, no. 2, pp. 476–484, Apr. 2006.

[21] A. D. MacDonald, *Microwave Breakdown in Gases*. New York: Wiley, 1966.

[22] T. Olsson, D. Anderson, U. Jordan, and M. Lisak, "Microwave breakdown in air-filled resonators," *IEEE MTT-S Int. Dig*., 1999, pp. 915–918.

[23] R. Woo, “Final report on RF voltage breakdown in coaxial transmission lines,” Jet Propulsion Lab, CA, U.S.A., Tech. Rep. 32-1500, Oct. 1970.

[24] M. Yu, “Power-handling capability for RF filters,” *IEEE Microwave Magazine*, vol. 8, no. 5, pp. 88-97, Oct. 2007.

Chapter 3

Configurable Perforated AFSIW Transmission Line

In this Chapter, the versatility of the AFSIW technology is presented. Original AFSIW filters based on the conventional PCB and the through-hole mounting (THM) process, with enhanced robustness to manufacturing tolerances, have been introduced in [1] and [3], opening new possibilities for the development of the AFSIW technological platform. Furthermore, [1] demonstrated a configurable AFSIW transmission line structure able to implement three determined functions: a transmission line and two specific bandpass filters. Compared to [1] and [3], the use of the THM process is extended much further in this work. For practical purposes, the THM process was implemented manually for all the proposed prototypes. A novel perforated AFSIW (PAFSIW) transmission line providing a high degree of configurability is introduced with theoretical and experimental studies. The proposed structure is based on perforated (discontinuous) broad walls (on top and/or bottom). Depending on the desired electrical function, sidewalls can be implemented with continuous and discontinuous electric walls. Applications of the proposed configurable PAFSIW for the generic implementation of fabrication-tolerant phase shifters, resonators and filters are demonstrated. PAFSIW sections can be implemented in systems-on-substrate [4], [5] to provide configurability and tunability thanks to its high versatility.

3. 1. PAFSIW Transmission Line

The proposed PAFSIW transmission line structure is illustrated in Fig. 3.1. It is based on the multilayer PCB process. The substrates 1 and 3, both enclosing substrate 2, are used for the bottom and top electric walls of the PAFSIW, respectively. Substrate 2 implements an air-filled propagation channel with continuously metallized sidewalls (which could be alternatively made of arrays of metallized vias [6]). Compared to conventional AFSIW [7], [8], substrate 1 and 3 are drilled (or perforated) to create an array of plated through holes (i.e., a via farm). The hole diameter d (obtained after platting) is determined to avoid signal leakage and to comply with electromagnetic compatibility (EMC) requirements [9]. Therefore, radiation losses are negligible. Furthermore, the plated through holes can contribute to venting in the case of a space application. The center to center distance p, between two consecutive holes, is selected to ensure the mechanical integrity of the top and bottom substrates while providing a high-density number of plated through holes. Compared to its AFSIW counterpart, the PAFSIW provides a weight reduction and can accommodate inductive posts mounted in its plated through holes using the THM process. The THM process consists of inserting metallic wire from the top to the bottom of the structure.

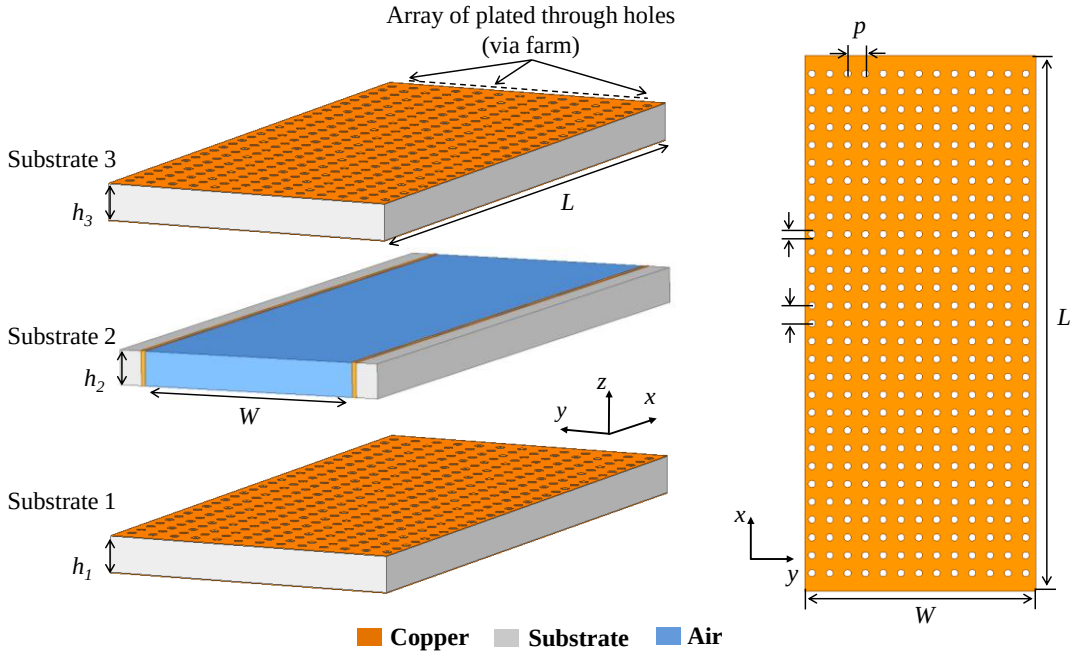

(*a*) (*b*)

Fig. 3.1. Perforated AFSIW structure: (*a*) 3D and (*b*) top view.

3. 1. 1. PAFSIW Loss Mechanisms

The theory of conventional rectangular waveguide is detailed in [10]. Among the electrical characteristics, the transmission loss is of high interest as it directly impacts the power-handling capability and the self-heating characteristics of a waveguide component. The attenuation constant α of a transmission line, neglecting radiation loss, is given by:

$$\alpha = \alpha_{\mathrm{d}} + K^{*}\alpha_{\mathrm{c}}, \tag{3.1}$$

where α_{d} is the attenuation due to dielectric loss, K is the surface roughness coefficient, and α_{c} is the attenuation due to ohmic loss.

Considering an AFSIW transmission line with continuous plated sidewalls (i.e., dielectric-less AFSIW) as illustrated in Fig. 3.1, the attenuation due to dielectric loss is null. Hence, considering the fundamental TE_{10} mode, the attenuation constant is given by:

$$\alpha_{\mathrm{AFSIW}} = \frac{P_l}{2P_{10}} = K\left(\frac{2\pi^2 R_{\mathrm{s}}}{W^3 k\beta\eta} + \frac{kR_{\mathrm{s}}}{h_2\beta\eta}\right), \tag{3.2}$$

where P_{10} is the power flowing through the waveguide for the TE_{10} mode defined as:

$$P_{10} = \frac{2\pi f\mu W^3 h_2 |A_{10}|^2}{4\pi^2}\mathrm{Re}(\beta), \tag{3.3}$$

and P_l is the power lost per unit length due to finite wall conductivity expressed as:

$$P_l = K\left[R_s \int_{y=0}^{h_2} |J_{sy}|^2 dy + R_s \int_{x=0}^{W} [|J_{sx}|^2 + |J_{sz}|^2] dx\right], \tag{3.4}$$

where f is the frequency, W and h_2 are the width and height of the AFSIW transmission line, respectively, k is the wave number, β is the phase constant, η is the intrinsic impedance of air, A_{10} is the amplitude constant, J_{sx}, J_{sy}, J_{sz} represents the surface currents and R_s is the surface resistivity defined by:

$$R_s = \sqrt{\frac{\pi f \mu_0}{\sigma}}, \tag{3.5}$$

where μ_0 is the free space permeability and σ is the conductor conductivity (here copper, with a conductivity of 58 x 10^6 S/m).

Considering a PAFSIW transmission line, the equivalent surface resistivity R_{seq} of the top and bottom walls are increased due to the presence of the array of plated through holes. Hence (3.4) becomes:

$$P_l = K\left[R_s \int_{y=0}^{h_2} |J_{sy}|^2 dy + R_{seq} \int_{x=0}^{W} [|J_{sx}|^2 + |J_{sz}|^2] dx\right]. \tag{3.6}$$

Considering a dense array of holes with d = 0.2 mm and p = 0.5 mm, it can be approximated that the equivalent surface resistance R_{seq} is homogeneously increased by a factor of 1.25 compared to the surface resistance R_s of a conventional AFSIW transmission line. Therefore, for PAFSIW, the conductor losses are increased compared to AFSIW. Neglecting radiation loss, the attenuation constant of the PAFSIW transmission line is:

$$\alpha_{AFSIW} = K\left(\frac{2\pi^2 R_s}{W^3 k\beta\eta} + \frac{kR_{seq}}{h_2\beta\eta}\right). \tag{3.7}$$

3. 1. 2. PAFSIW Versus AFSIW

In this study, the conventional dielectric-less AFSIW topology is compared with the proposed PAFSIW. For the perforated configuration, to fulfill the EMC requirements, the plated through hole diameter d is chosen to be smaller than a tenth of the guided wavelength λ_g ($d < \lambda_g/10$). Also, d is chosen such as to respect the PCB process through hole metallization rules (typically, $d > h_1/8$ and $d > h_3/8$, with h_1 and h_3 the height of the bottom and top substrates, respectively).

For comparison and demonstrations, the two topologies are implemented using 1.524 mm thick Hi-T_g FR4 substrate for the three layers of the PCB. Metallized via holes have a finish diameter d of 0.2 mm, a center-to-center distance p of 0.5 mm and an 18 µm copper platting thickness. As a demonstration, both AFSIW and PAFSIW transmission lines of equal length L = 70 mm and equal W = 13 mm to operate in the WR-51 band (15 to 22 GHz) are compared in terms of weight, transmission loss, return loss, average

power-handling capability (APHC) and self-heating in the downlink Ka-band satellite communication frequency range (17.3 to 21.3 GHz).

3. 1. 2. 1 Weight Comparison

Thanks to the arrays of plated vias, the PAFSIW results in a lower weight structure compared to its AFSIW counterpart. For the considered FR4 implementation, a measured weight reduction of 22% is achieved, which is not negligible considering a space application.

3. 1. 2. 2 Transmission Loss Comparison

Fig. 3.2 compares theoretical, simulated and measured transmission loss of the AFSIW and PAFSIW transmission lines, considering $K = 1.65$ for the theoretical and simulated results. The return loss of both transmission lines remains above 20 dB from 17.3 to 21.3 GHz. For the considered experimental implementation, as expected in theory, the transmission loss is increased for the PAFSIW compared to its AFSIW counterpart.

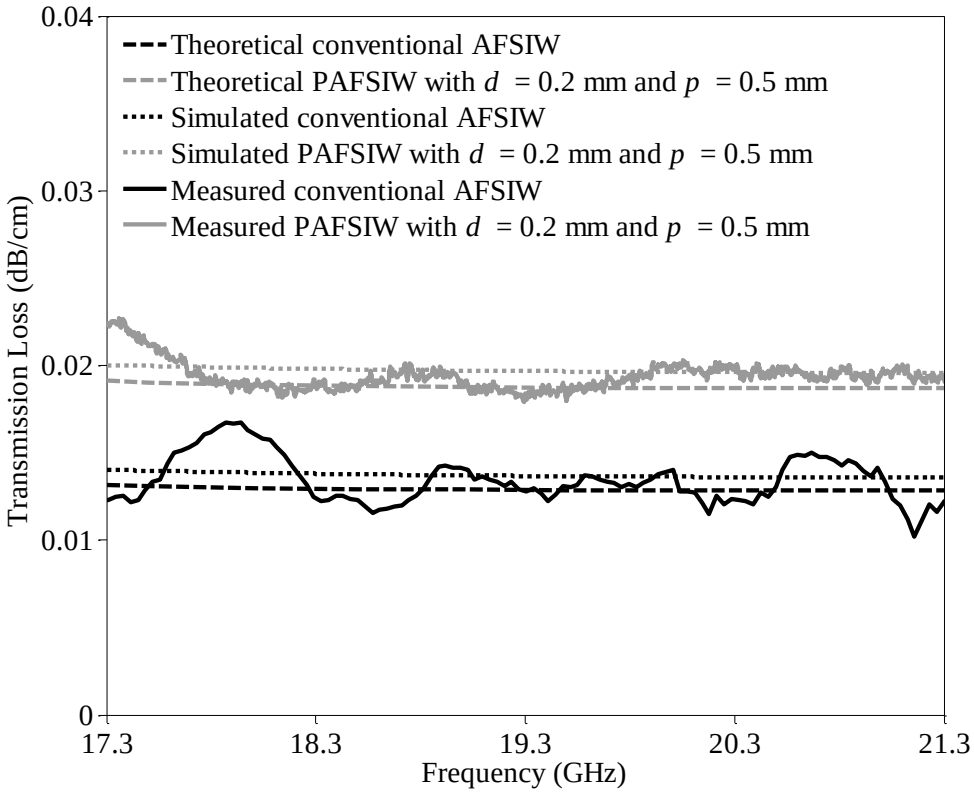

Fig. 3.2. Comparison of conventional and perforated AFSIW transmission loss obtained in theory, simulation, and measurement.

3. 1. 2. 3 Power-Handling and Self-Heating Comparison

For high performance applications, it is important to evaluate the power-handling capability and the self-heating of microwave and millimeter-wave components. In this Section, the self-heating of a transmission line based on PAFSIW and conventional AFSIW are compared. A schematic and a picture of the measurement setup are shown in Fig. 3.3 and Fig. 3.4, respectively. Power sensors are used to measure the input power applied to the device under test (DUT). A thermocouple sensor is placed on the input of both transmission lines to observe the self-heating.

The two FR4-based 70 mm long transmission lines are tested with a continuous wave (CW) signal at 20 GHz. The power is increased by steps of 20 W every 5 minutes until 120 W, then two steps of 30 W are done before reaching the maximum power input available at this frequency is reached (i.e., 190 W using the Cobham Microwave facilities). From 150 W, longer stages are performed in order to stabilize the DUT in terms of return loss and temperature. It can be observed in Fig. 3.5 that the return loss stays above 20 dB during the test for both structures, which ensures the correct electrical behavior of both circuits. For an input power of 190 W, it is shown in Fig. 3.6 that the conventional AFSIW transmission line heats up by 25 °C, compared to only 18 °C (with an ambient temperature of 23 °C) for its PAFSIW counterpart. It can also be concluded that both structures are able to handle more than 190 W of continuous wave input power.

As summarized in Table 3.1, compared to AFSIW, the PAFSIW is of interest to reduce weight and increase dissipation. However, PAFSIW results in higher transmission loss. Therefore, in the context of systems on substrate, the implementation of PAFSIW is of high interest in critical heat dissipation areas and also, as discussed in the following sections, to implement configurable or tunable sections, while other components and interconnections can be based on conventional AFSIW to optimize losses.

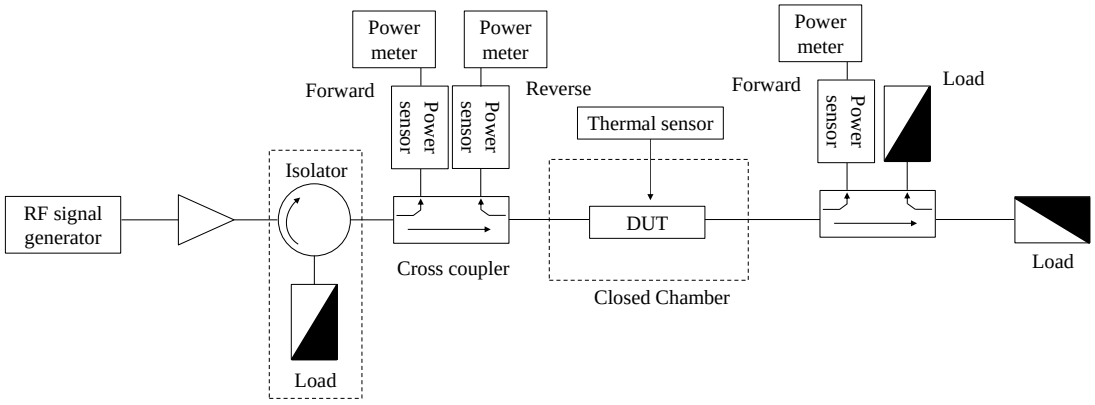

Fig. 3.3. Setup of the power-handling and self-heating test.

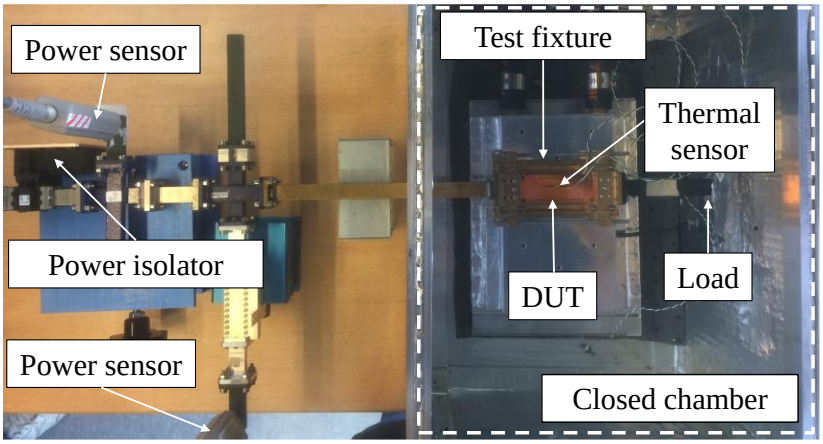

Fig. 3.4. Photographs of the power-handling and self-heating experiment.

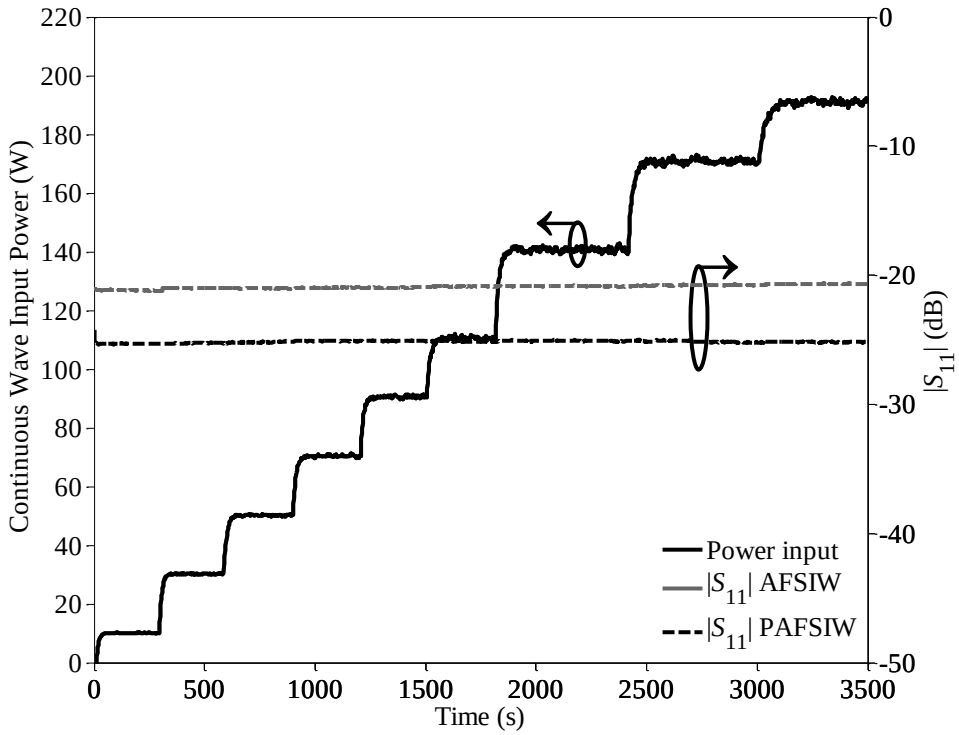

Fig. 3.5. Measured input power and return loss over time of the PAFSIW and conventional AFSIW transmission lines at 20 GHz.

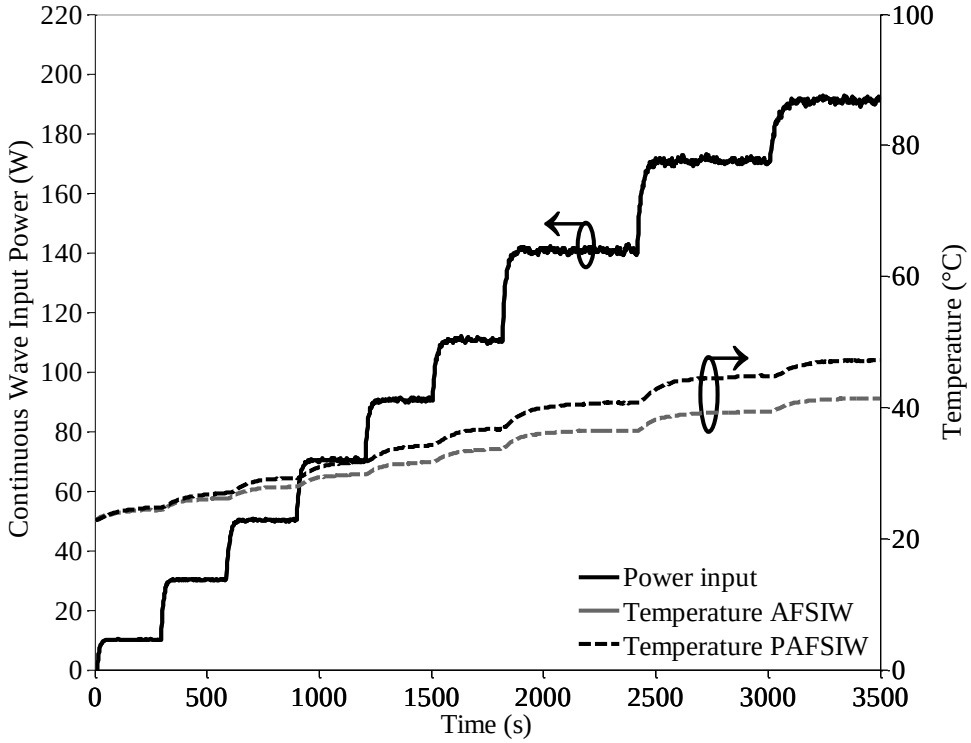

Fig. 3.6. Measured input power and temperature over time of the PAFSIW and conventional AFSIW transmission lines at 20 GHz.

TABLE 3.1
COMPARISON BETWEEN CONVENTIONAL AND PERFORATED AFSIW TRANSMISSION LINE OPERATING IN THE 17.3 TO 21.3 GHZ FREQUENCY RANGE (W = 12.95 MM, L = 70 MM, H_1=H_2=H_3 = 1.52 MM, D = *0.2 MM AND* P = *0.5 MM*)

Performances	Weight (g)	Theoretical transmission loss (dB/cm)	Simulated transmission loss (dB/cm)	Measured transmission loss (dB/cm)	Measured return loss (dB)	APHC (W)	Measured self-heating ΔT (@ 20 GHz & 190 W) (°C/W)
Conventional AFSIW	20.96	< 0.016	< 0.015	< 0.017	> 20	> 190	0.125
PAFSIW	16.22	< 0.019	< 0.019	< 0.021	> 20	> 190	0.09

3. 2. Configurable PAFSIW Phase Shifters

Phase shifters are extensively used in feeding networks implemented for example in phased array antennas which require a proper division, both in amplitude and phase, of the signals feeding each elementary radiator. Thus, configurable and tunable PAFSIW phase shifters are of high interest.

3. 2. 1. Theory and Design

The proposed configurable PAFSIW phase shifting structure consists of metallic posts mounted using the THM process in determined plated through holes of the PAFSIW via farm, which form an array composed of *m* columns along the PAFSIW length and *n* lines along the PAFSIW width. A single column realize a unitary

PAFSIW section of length $\Delta L_{\text{eff}} = p$. Assembling metallic posts on the sides of the PAFSIW section, equal-length unequal-width phase shifters [11] can be implemented. The metallic posts can be mounted on a single side or both sides of the PAFSIW, in a symmetrical or asymmetrical manner. As an illustration, Fig. 3.7(*a*) and Fig. 3.7(*b*) show symmetrical implementations. In Fig. 3.7(*a*), two unitary sections ($m = 2$) of effective width $W_{\text{eff}} = W_{\text{eff1}} = W_{\text{eff2}}$ implements metallic posts on the first lines of both sides of the AFSIW plated through hole array. In Fig. 3.7(*b*), four unitary sections ($m = 4$) implement metallic posts with a stepped number of metallic posts on both sides to increase the phase shifting. The phase-shifting PAFSIW transmission line section of total length $L_{\text{eff}} = m\,\Delta Leff$ can be decomposed in m single unitary sections of effective width W_{effi} (with $i = 1$ to m), which can be determined using the well-known formula for the effective width determination of SIW [12]. The implementation of metallic posts on the sides reduces the unitary section effective width W_{effi} and therefore its propagation constant β_{i} of the fundamental TE_{10} mode. The total phase obtained using this principle is compared to the phase of a reference conventional AFSIW transmission line of the same width W and length $L = L_{\text{eff}}$, having propagation constant β_{ref}. The total phase difference $\varphi(f)$ of the proposed phase shifter is given by:

$$\phi(f) = \Delta L_{\text{eff}} \sum_{i=1}^{m} (\beta_{\text{i}}(f) - \beta_{\text{ref}}(f)), \tag{3.8}$$

with the propagation constants expressed as:

$$\beta_{\text{i}}(f) = \sqrt{\left(\frac{2\pi f}{c}\right)^2 - \left(\frac{\pi}{W_{\text{effi}}}\right)^2}, \tag{3.9}$$

and

$$\beta_{\text{ref}}(f) = \sqrt{\left(\frac{2\pi f}{c}\right)^2 - \left(\frac{\pi}{W}\right)^2}, \tag{3.10}$$

where c the velocity of light.

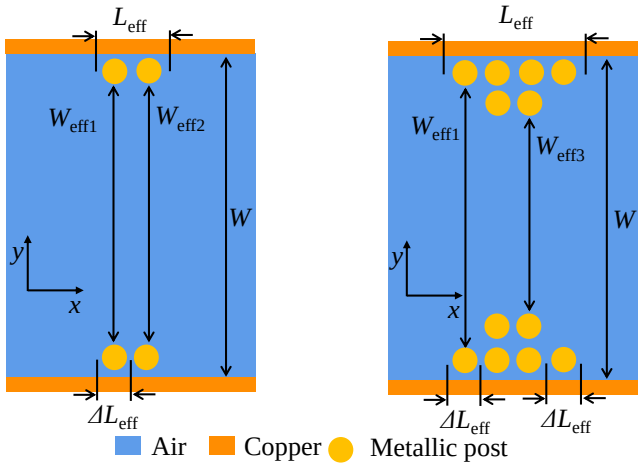

Fig. 3.7. Examples of PAFSIW phase shifters implementation: (*a*) a two unitary section ($m = 2$) phase shifter implementing metallic posts on the first lines on both sides and (*b*) a four unitary section ($m = 4$) phase shifter implementing a stepped number of metallic posts on both sides.

3. 2. 2. Experimental Validation

For demonstrations and experimental validation, symmetrical phase shifters based on the proposed configurable PAFSIW structure are designed and implemented on a multilayer PCB consisting of three 1.524 mm thick FR4 substrates. The arrays of plated through holes have a finished diameter *d* of 0.2 mm and a center-to-center pitch *p* of 0.5 mm.

Firstly, the S-parameters of the reference PAFSIW transmission line are determined both from simulations and measurement before implementing the phase-shifting posts. Simulated and experimental results are shown in Fig. 3.8. The fabricated PAFSIW achieves a return loss above 20 dB with an insertion loss lower than 0.07 dB over the 17.3 to 21.3 GHz frequency range. A good agreement between simulation and measurement results is obtained.

Secondly, the posts, consisting of 0.2 mm diameter silver plated wires, are inserted using the THM process to fabricate the phase shifters. S-parameters are then measured to determine the phase difference φ(f) and amplitude imbalance compared to the reference PAFSIW transmission line. Fig. 3.9 shows a good agreement between theoretical, simulated and measured phase differences of three-unitary-section phase shifters implementing single, double and triple lines of posts on both sides, as illustrated in Fig. 3.9(*a*), (*b*), and (*c*), respectively. Over the frequency band of interest, it can be observed that those three phase shifters implement phase shifts of -1°±0.012°, -3.7°±0.9° and -8.4°±1.4°, respectively. Fig. 3.10 shows the measured amplitude imbalance. The obtained amplitude imbalances are as low as 0±0.012 dB, 0±0.026 dB and 0±0.03 dB, respectively, from 17.3 to 21.3 GHz.

The PAFSIW phase shifting structure allows a high degree of freedom to implement phase shifters as different combinations of metallic post loaded unitary sections can be implemented. As other examples, Fig. 3.11 (*d*), (*e*) and (*f*) illustrate three other alternative phase shifter implementations. The comparison between theoretical, simulated and measured phase shifts are shown in Fig. 3.11. Those alternative phase shifters implement -0.4°±0.03°, -2°±0.5° and -5.8°±1° phase differences, respectively. Fig. 3.12 shows the theoretical, simulated and measured amplitude imbalance of the three alternative phase shifters. It can be observed that the amplitude imbalances are as low as 0±0.011 dB, 0±0.034 dB and 0±0.031 dB, respectively.

Considering designs based on only three unitary sections (m = 3) and the implementation of posts only in the first three lines to avoid mismatches, there is as much as 81 and 324 possible combinations, for symmetrical and asymmetrical phase shifter implementations, respectively. Those combinations allow implementing phase shifters providing phase shifts between 0 and 8.4°±1.4° with a very low amplitude imbalance.

This large number of possible implementations makes the proposed PAFSIW of high interest for the fine-tuning of feeding network. Furthermore, it is worthy to note that using a higher number of unitary sections and/or a higher number of lines, higher values of the phase shift can be achieved to implement configurable and tunable phase shifters.

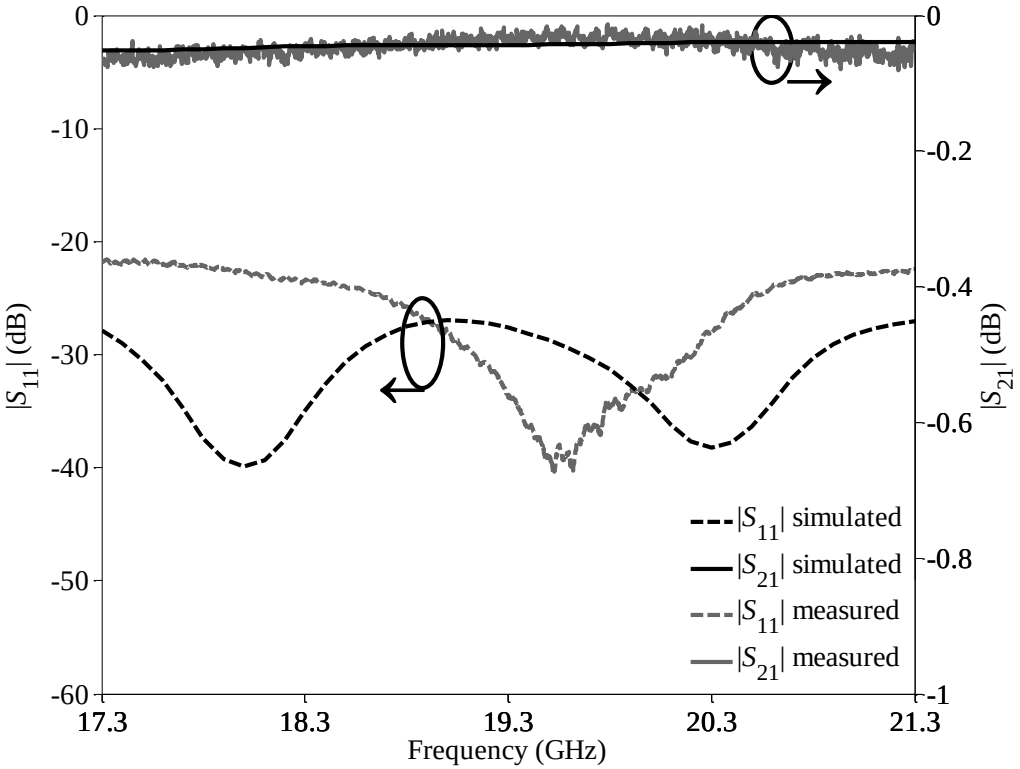

Fig. 3.8. Simulated and measured S-parameters of the PAFSIW configurable phase shifter without inserted metallic posts.

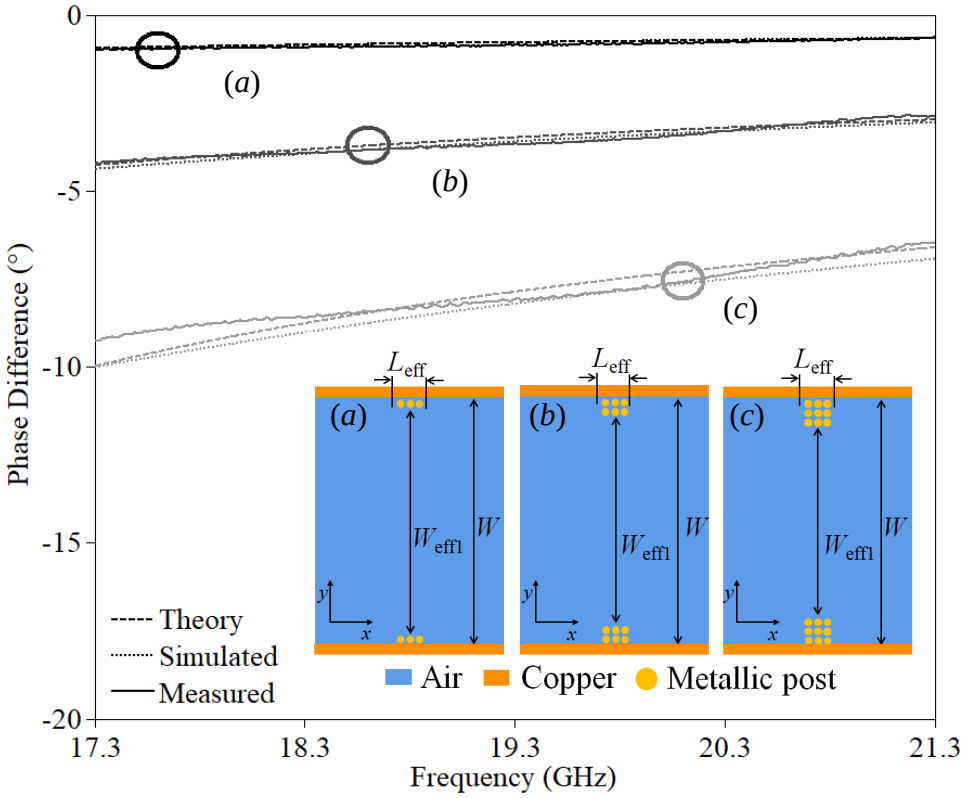

Fig. 3.9. Theoretical, simulated and measured phase difference of symmetrical three-unitary-section phase shifters implementing (*a*) single, (*b*) double and (*c*) triple lines of posts on both sides.

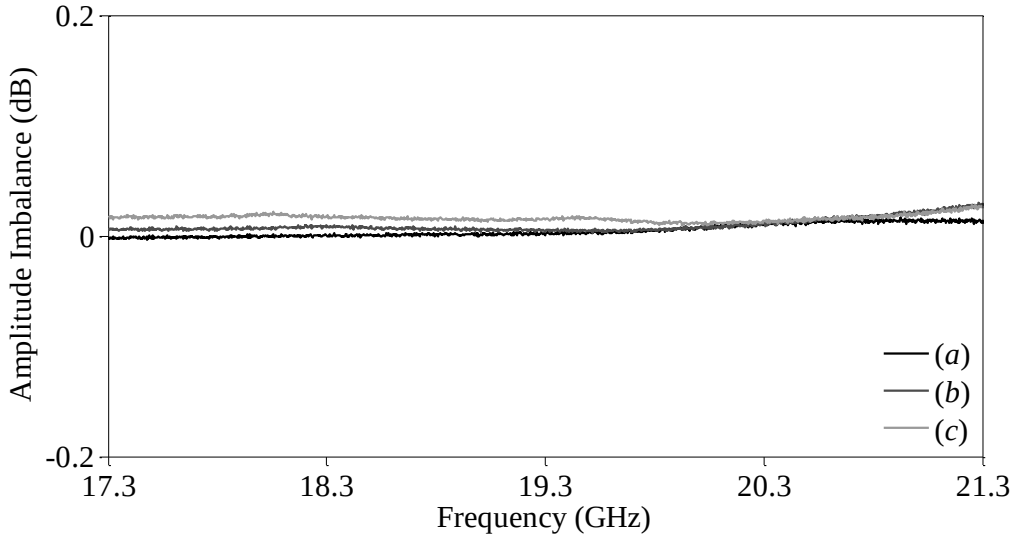

Fig. 3.10. Measured amplitude imbalances of the Fig. 3.9(*a*), (*b*) and (*c*) prototypes.

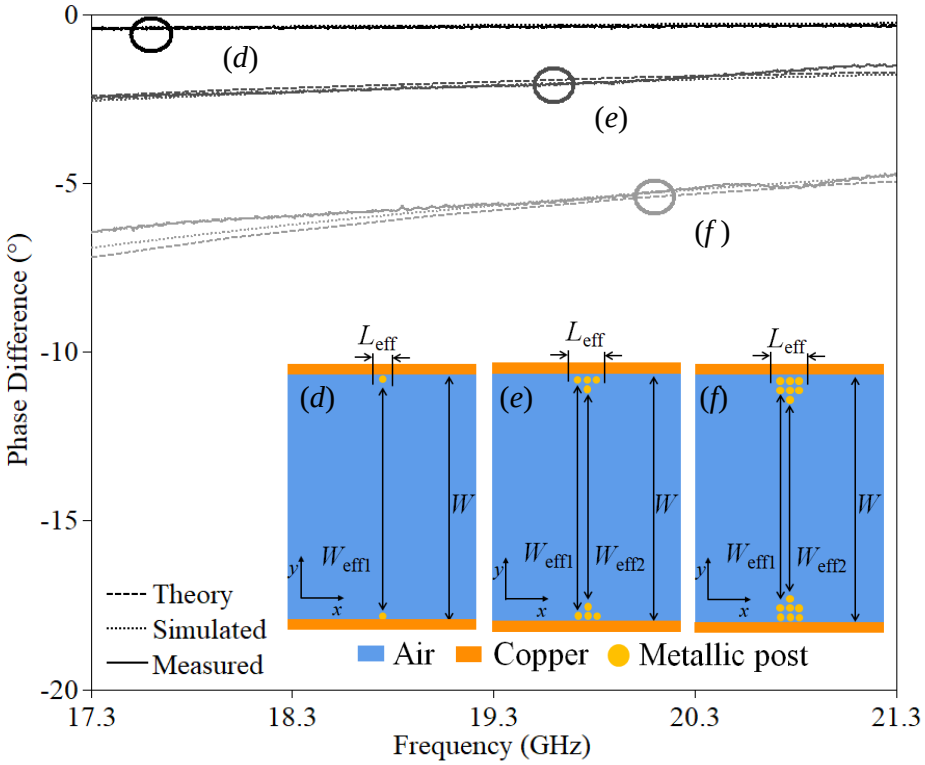

Fig. 3.11. Theoretical, simulated and measured phase difference of symmetrical phase shifters with (*d*) a single unitary section of a single metallic post on both sides, (*e*) three unitary sections with a stepped number of metallic posts on both sides going from one to two posts, and (*f*) three unitary sections with a stepped number of metallic posts on both sides going from two to three posts.

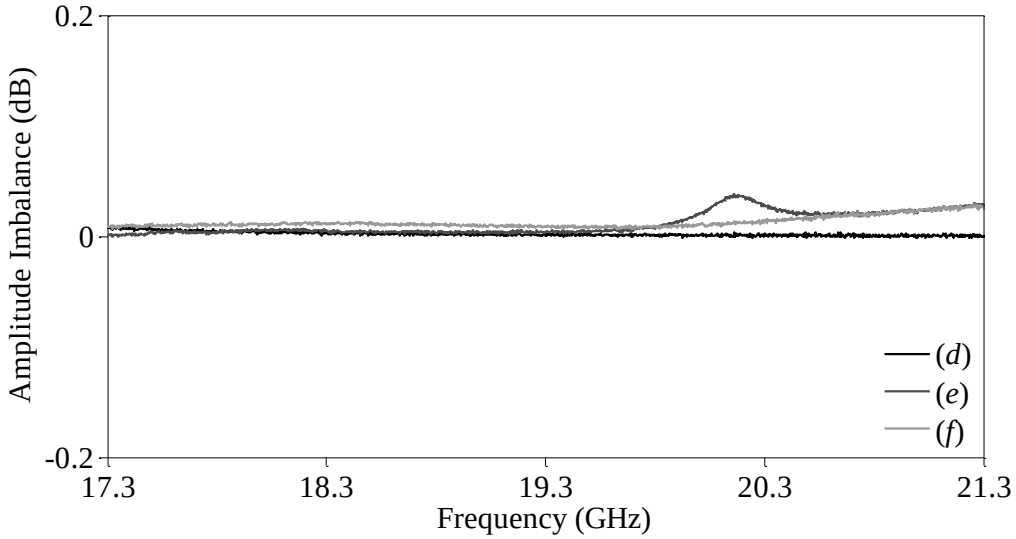

Fig. 3.12. Measured amplitude imbalances of the Fig. 3.11(*a*), (*b*) and (*c*) prototypes.

3. 3. Configurable PAFSIW Resonators

In this Section, the implementation and frequency dependence of a single PAFSIW resonator is studied, as, for instance, it is essential for the design of configurable PAFSIW filters. The geometry of a PAFSIW resonator of edge-to-edge length *L* and width *W* is shown in Fig. 3.13 with a symmetrical implementation of posts in four columns (from c_1 to c_4) and twelve lines (from l_1 to l_{12}) on the sidewalls. The metallic post used is this study have the same characteristics as the ones presented in the previous Section.

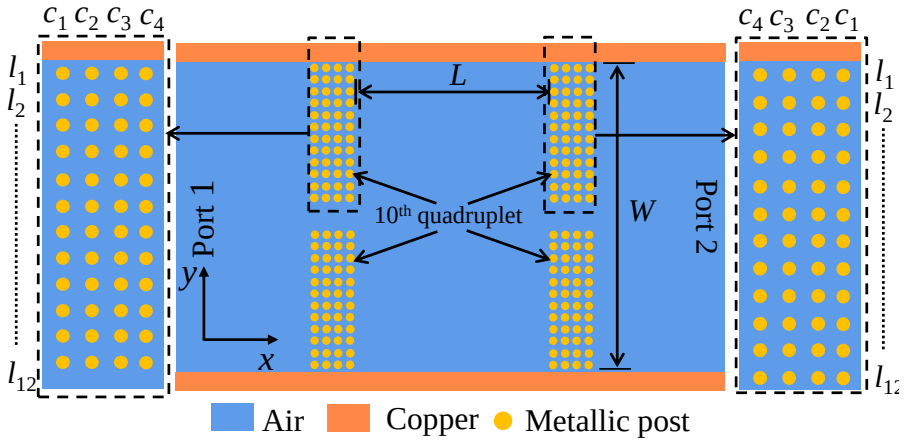

Fig. 3.13. Illustration of a PAFSIW resonator.

For comparison purposes and a proof of concept, a conventional and a perforated AFSIW resonator are fabricated. They are shown in Fig. 3.14 (*a*) and (*b*), respectively. For this proof of concept, only the plated through holes of interest have been drilled for the PAFSIW resonator prototype. Both resonators have a width *W* of 13 mm and a length *L* determined with the conventional waveguide theory [13] and SIW equivalent width formula for the PAFSIW resonator[12], to obtain a TE_{10} resonant frequency of 21 GHz.

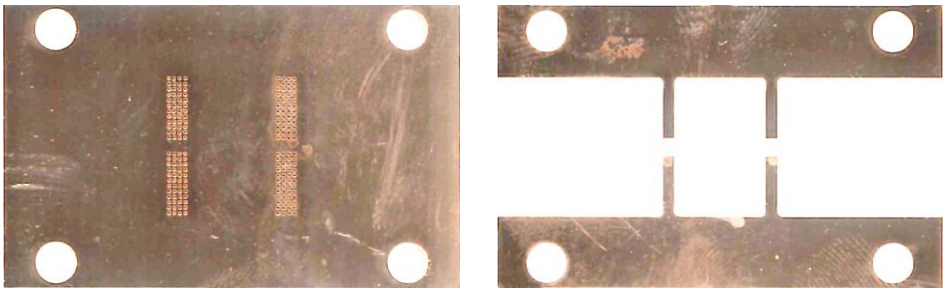

(*a*) (*b*)

Fig. 3.14. Fabricated (*a*) top substrate (substrate 3) of the PAFSIW resonator and (*b*) inner substrate (substrate 2) of the AFSIW iris resonator, with L = 8.418 mm and 8.43 mm for the PAFSIW and AFSIW resonators, respectively.

The input and output of the resonators have small openings to decouple the input and output couplings. Furthermore, after mounting the metallic posts on the PAFSIW resonator, it is demonstrated in Fig. 3.15 that the two resonators have a similar measured resonant frequency (20.996 GHz for the PAFSIW resonator compared to 20.999 GHz for the AFSIW resonator), which proves the equivalency between the two structures. The slight shift of the resonant frequency obtained in measurement is mainly due to the fabrication tolerances and the assembling process.

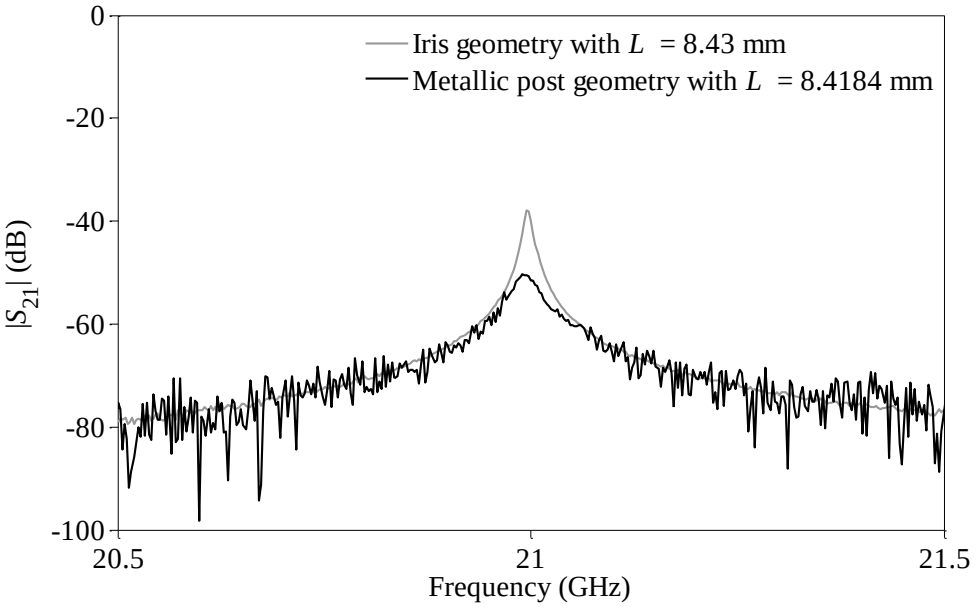

Fig. 3.15. Measured $|S_{21}|$ of the PAFSIW and AFSIW resonators.

As demonstrated in the previous Section, the perforated topology allows a high degree of design and fine-tuning capability. Hence, a frequency configurability study is carried out. One possibility to tune the resonant frequency is to consider the removal of a quadruplet of posts of the c_4 inner columns (considering the particular example of Fig. 3.13), which is formed by 4 metallic posts which are symmetrically arranged in reference to the resonator center and the x and y axes. As an illustration, and better understanding, the 10th quadruplet is shown in Fig. 3.13.

Fig. 3.16 shows the simulated and measured frequency shift due to the removal of a single quadruplet i (with i = 1 to 12). A frequency shift of up to -250 MHz is achieved by removing the 12th quadruplet. A weak coupling is considered in this study to avoid the impact of the input and output couplings on the cavity resonant frequency.

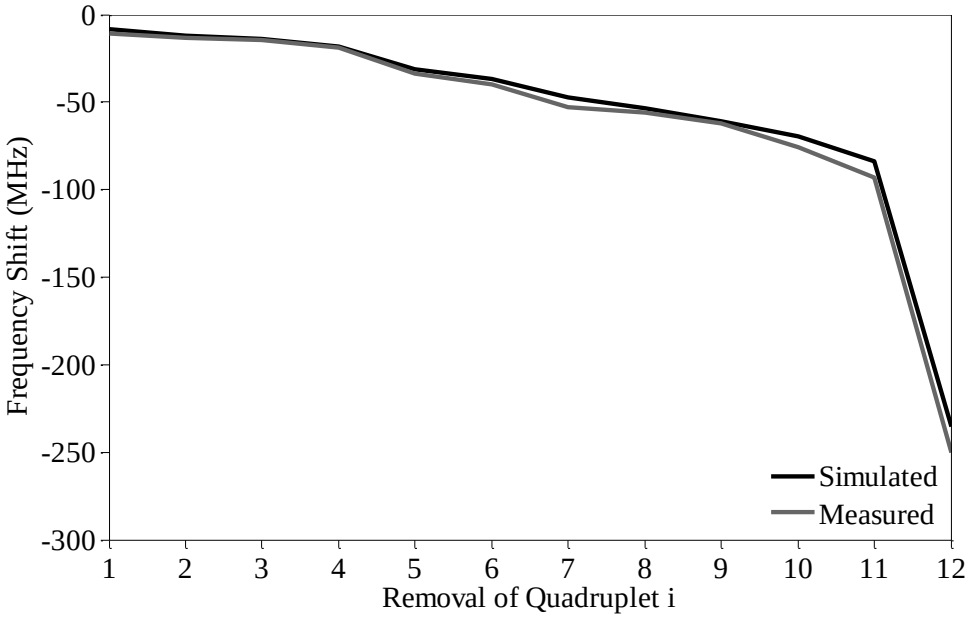

Fig. 3.16. AFSIW resonator frequency shift depending on the removal of a quadruplet of metallic posts.

For demonstration purposes, this study only considered the removal of a quadruplet of metallic posts. It is worthy to take into account that a lot of combinations are possible to obtain a desired resonant frequency. Numerous symmetrical and asymmetrical arrangements can be considered, providing a high degree of freedom. Here, the removal of posts in the coupling windows has been proposed to reduce the resonant frequency. Furthermore, the resonant cavity frequency can be increased by inserting post on the sidewalls of the cavities.

3. 4. Configurable PAFSIW Resonator Couplings

In this Section, the coupling between two PAFSIW resonators is studied, as it is also essential for the design of filters. This Section demonstrates the high robustness of the through-hole mounted metallic post coupling compared to the conventional iris coupling against the standard PCB fabrication process. Then, an equivalency between the through-hole mounted metallic post coupling and conventional iris coupling topologies is demonstrated in measurement, before establishing the limitation in obtainable coupling coefficient of discretized iris couplings based on mounted metallic posts fitting a determined PAFSIW plated through-hole array. Finally, the genericity and versatility of the PAFSIW structure are emphasized by introducing modified discretized iris coupling configurations to increase the set of achievable coupling coefficients, allowing the design of filters with stringent specifications.

3. 4. 1. Monte Carlo Analysis

It has been detailed in [3] that standard tolerance of the milling and drilling process in the PCB industry are ±0.1 mm and ±0.025 mm, respectively. Thus, as the PAFSIW iris geometry is based on the drilling process, the proposed PAFSIW topology shows an enhanced fabrication robustness compared to its AFSIW counterpart.

To evaluate the effect of the fabrication tolerances on the internal coupling, a Monte Carlo analysis is made for both internal coupling topologies. It is shown from Monte Carlo simulations that the dispersion is higher using the milling process, represented in Fig. 3.17, compared to using the drilling process, shown in Fig. 3.18.

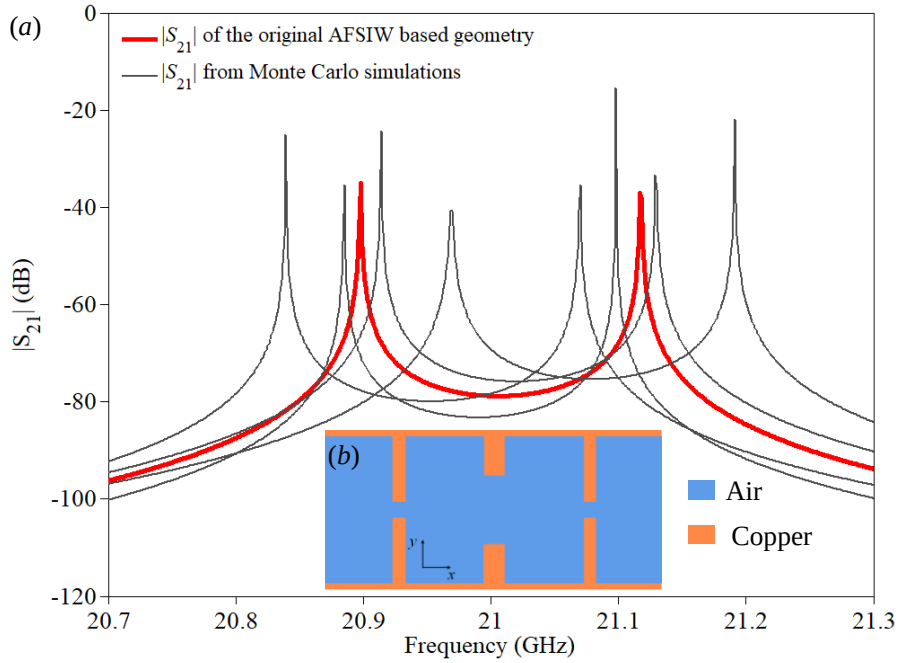

Fig. 3.17. (*a*) Monte Carlo analysis of AFSIW internal coupling made with milled inductive iris and (*b*) its geometry.

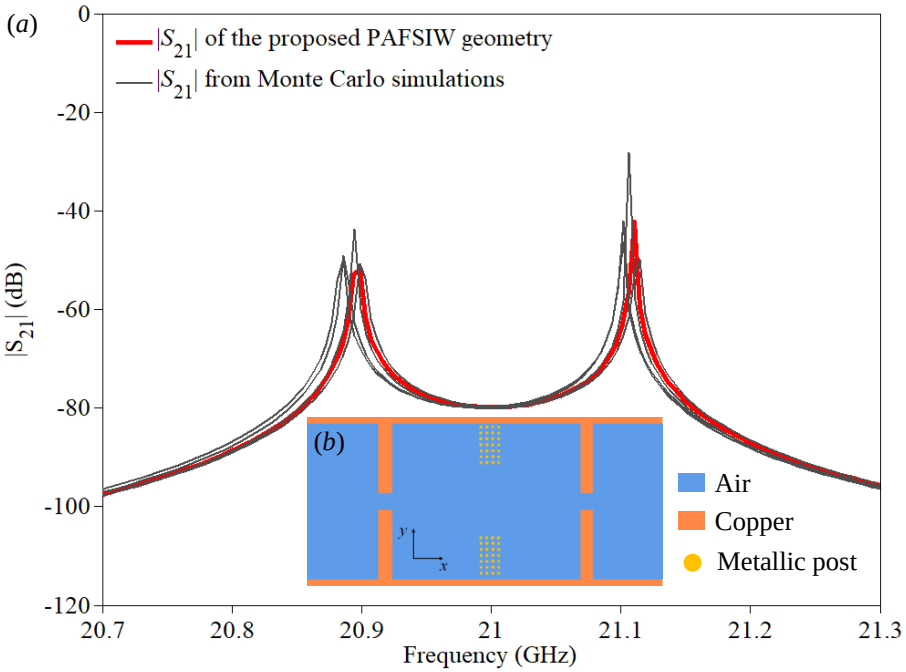

Fig. 3.18. (*a*) Monte Carlo analysis of PAFSIW internal coupling made with drilled inductive iris and (*b*) its geometry.

3. 4. 2. Coupling Equivalence

A study to demonstrate the equivalence between the through-hole mounted metallic post coupling and the rounded-iris couplings is carried out. The two considered geometries are illustrated in Fig. 3.19.

The studied rounded-iris coupling is based on two cavities of width W = 13 mm and length L adjusted such that the coupling is centered at f_c = 21 GHz. The coupling window has an edge-to-edge width $l_{opening}$ = 7.314 mm and a length L_{iris} = 2 mm. The corners of the window are rounded with a radius R_{iris} = 0.1 mm.

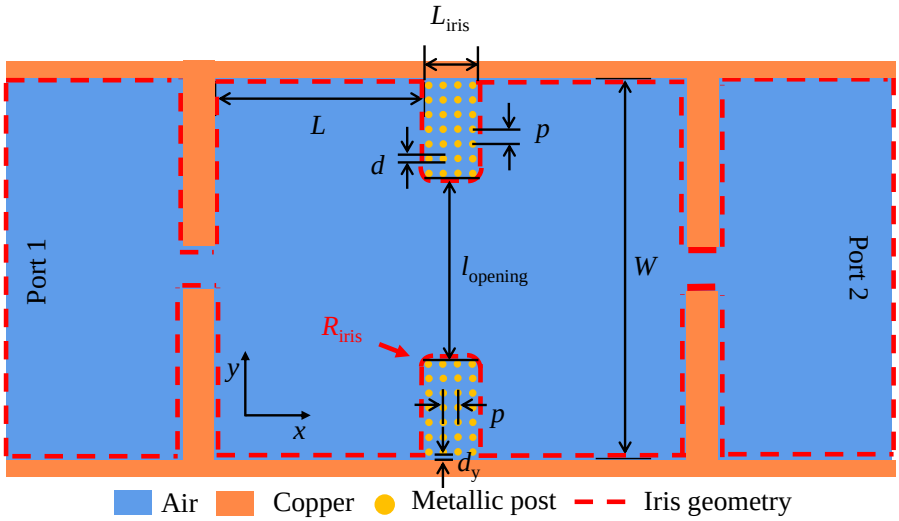

Fig. 3.19. Illustration of internal couplings made with through-hole mounted metallic post and rounded iris.

The studied through-hole mounted metallic post coupling is based on the same two cavities also adjusted such that the coupling is centered at f_c = 21 GHz. The metallic posts used in this study have the same characteristics as the ones presented in the previous Sections. The length L_{iris} is corresponding to the width of 4 metallic post columns. The width $l_{opening}$ of the PAFSIW coupling window has an edge-to-edge dimension of 7.3 mm.

For demonstration purposes, the two topologies have been designed, fabricated and measured. To avoid the input and output coupling effects, the two resonant peaks of the resonators are observed below -40 dB. Fig. 3.20 (*a*) and (*b*) shows the fabricated prototypes. For this measurement, only the plated through holes of interest have been drilled for the through-hole mounted metallic post coupling resonator prototypes.

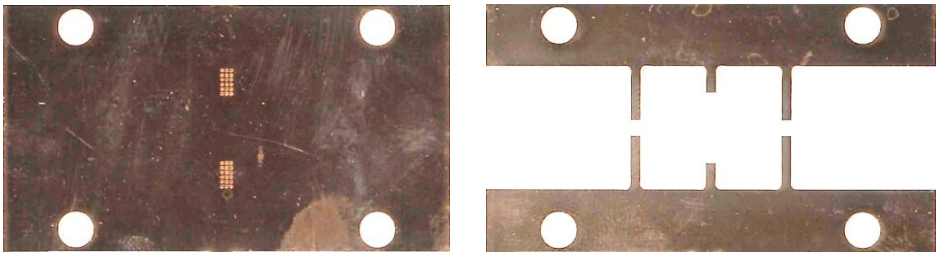

(*a*) (*b*)

Fig. 3.20 Fabricated (*a*) top substrate (substrate 3) of the through-hole mounted metallic post coupling and (*b*) inner substrate (substrate 2) of the iris-based AFSIW coupling with $l_{opening}$ = 7.3 mm and 7.314 mm, respectively.

It can be observed from measurement, in Fig. 3.21, that the through-hole mounted metallic post coupling window is equivalent to a rounded-iris window. The measured two resonant peaks for the conventional iris geometry are located at 18.53 GHz and 23.35 GHz compared to 18.48 GHz and 23.3 GHz for the metallic post geometry. The slight shift of the resonant frequencies obtained in measurement is mainly due to the fabrication tolerances and the multilayer assembly process.

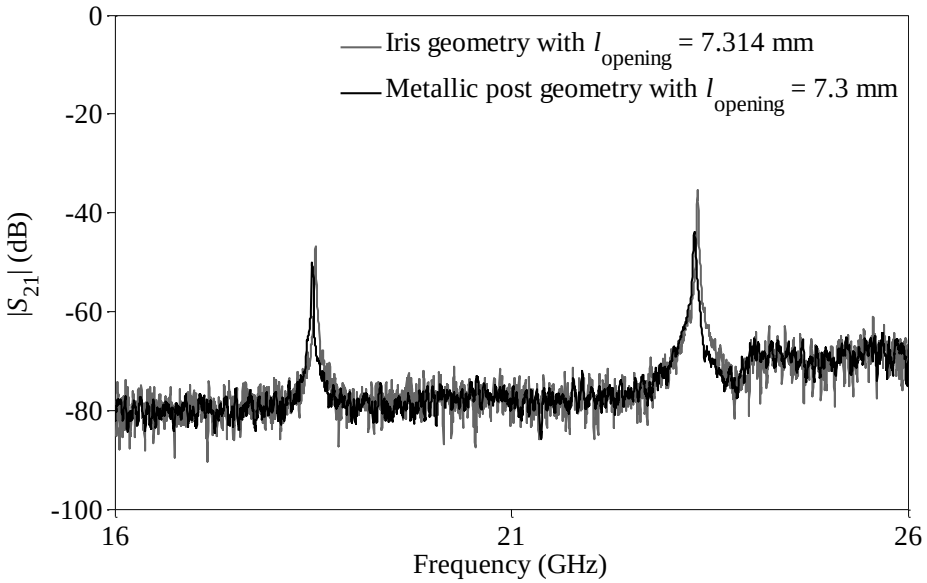

Fig. 3.21. Measured $|S_{21}|$ of the through-hole mounted metallic post and rounded-iris coupling topologies.

The demonstrated equivalency can be used to directly convert conventional rectangular waveguide iris filter designs, obtained using any well-known filter synthesis method, to through-hole mounted metallic post designs. Thus, a fabrication-tolerant PAFSIW filtering structure can be synthesized and fabricated without additional design time.

However, it is important to notice that for direct conversion from the conventional rectangular waveguide designs to the through-hole mounted metallic post designs, the length d_y (shown in Fig .3.19) between the metallic posts and the sidewalls is adjusted such that the metallic post geometry matches the iris geometry. Thus, it is not a generic solution as the perforated array of plated through holes is adapted for each new design. In the following Section, discretized iris and modified discretized-iris coupling configurations based on a PAFSIW with a fixed array of metallized through holes with diameter d of 0.2 mm, center-to-center pitch p of 0.5 mm and d_y dimension equal to 0.3 mm, are introduced and studied to provide genericity.

3. 4. 3. Through-Hole Mounted Metallic Post Discretized Iris Couplings

When using a configurable PAFSIW structure having a fixed array of metalized through holes, synthesized iris coupling geometries cannot be directly converted using the previously demonstrated equivalency. Instead a specific set of geometries, or through-hole mounted metallic post discretized iris, can be implemented, corresponding to post implemented in *m* columns of *n* sidewall lines, as illustrated in Fig. 3.22.

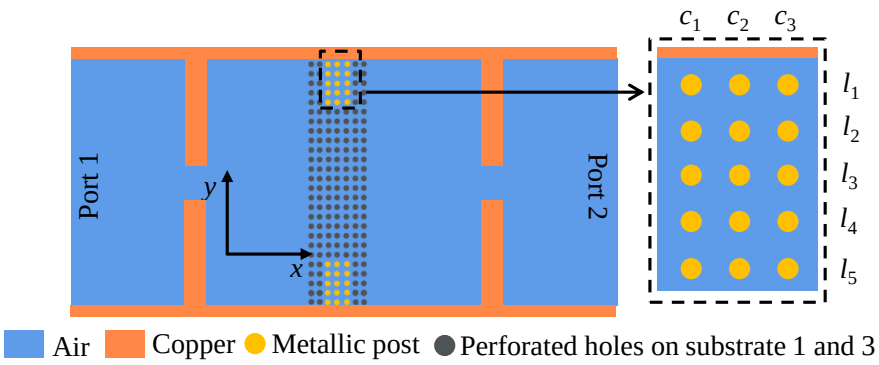

Fig. 3.22. Illustration of a PAFSIW discretized-iris coupling consisting of a three-column (m = 3) and five-sidewall-line (n = 5) post implementation.

The parameters used to determine the coupling coefficients are the length of the two resonators tuned to keep constant the central frequency f_c between the two resonances and the number of implemented metallic post columns (m) and lines (n). Thus, the coupling study is discrete and not continuous, due to the fixed array of plated through holes. Fig. 3.22 illustrates an example of coupling implementation with m = 3 and n = 5. For all the possible configurations, the coupling coefficient k can be calculated using the following equation [14]:

$$k = \frac{{f_1}^2 - {f_2}^2}{{f_1}^2 + {f_2}^2}, \tag{3.11}$$

where f_1 and f_2 are the higher and lower resonant frequencies, respectively. Considering the achievable coupling coefficients for the different configurations implementing metallic posts in m columns of n sidewall lines of the PAFSIW plated through-hole array, the coupling coefficient abacus shown in Fig. 3.23 is obtained. However, as it can be seen in Fig. 3.23, such specific set of discretized-iris couplings provide a limited set of k values. In the following part, to provide a higher degree of freedom, modified discretized iris coupling configurations are introduced.

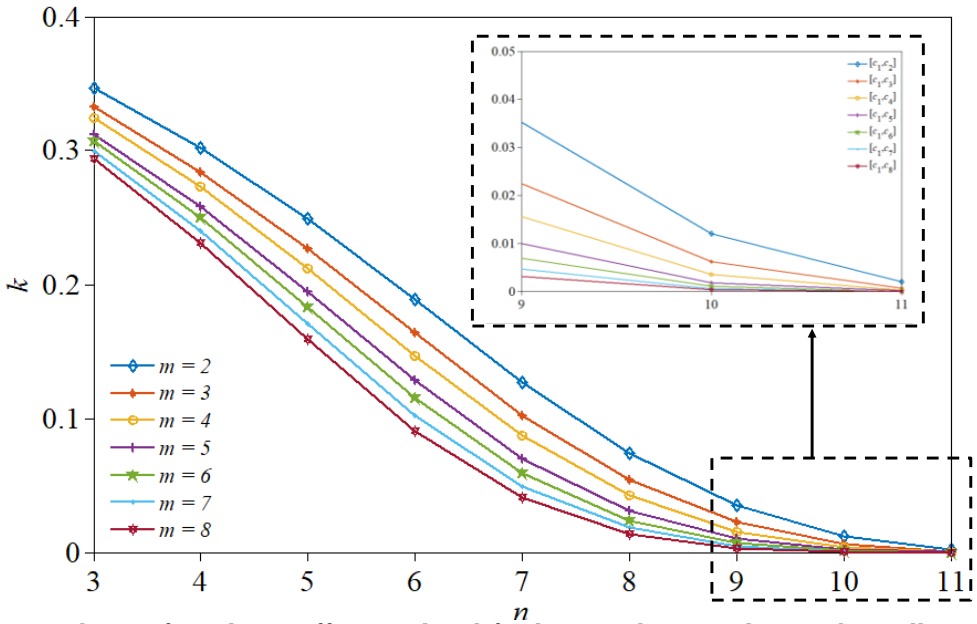

Fig. 3.23. Abacus of coupling coefficient values k for discretized-iris couplings with metallic posts implemented in m columns of n sidewall lines obtained from simulation results (with f_c = 21 GHz and W = 12.954 mm).

3. 4. 4. Modified Through-Hole Mounted Metallic Post Discretized Iris Couplings

From the abacus shown in Fig. 3.23, it can be concluded that the steps between two consecutive coupling coefficient values are too high to allow the design of filters, especially for narrowband filter designs. However, additionally to the fabrication-tolerant aspect, the PAFSIW structure also suggests a high number of internal coupling coefficients considering the high number of possible coupling topologies that can be implemented.

Starting from a conventional rectangular shaped through-hole mounted metallic post discretized-iris coupling introduced in the previous Section, it is possible to fine-tune the coupling coefficient by removing and/or inserting metallic posts, especially in the proximity of the coupling window. Fig. 3.24 (*a*) shows an example of discretized iris coupling configuration which achieves a coupling coefficient of 0.0042. It is demonstrated that, by inserting or removing metallic posts, the coupling coefficient can be controlled. Fig. 3.24 (*b*) to Fig. 3.24 (*j*) shows some examples of possible modification of the original discretized iris coupling of Fig. 3.24(*a*). Those examples of alternative configurations provide coupling coefficients in the range of 0.0043 to 0.0094. Through this approach, it is possible to obtain a large set of coupling coefficient values, allowing the implementation of stringent coupling coefficient requirements.

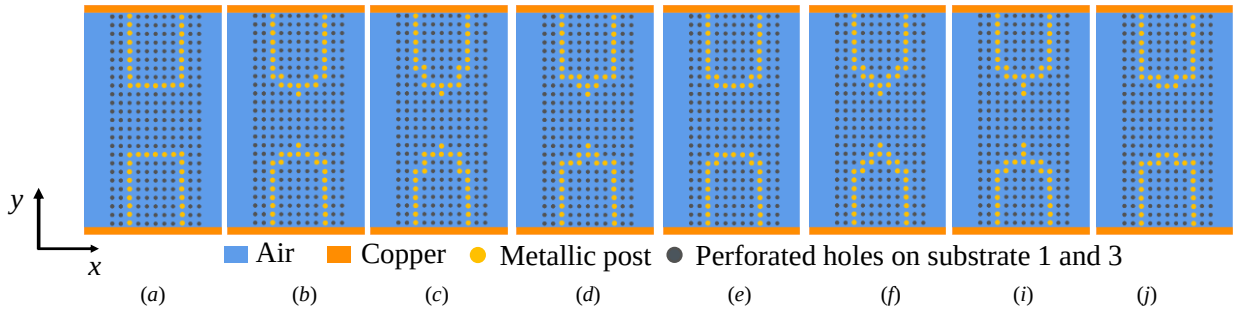

Fig. 3.24. Examples of 7 columns coupling geometries providing coupling coefficient *k* equal to (*a*) 0.0042, (*b*) 0.0043, (*c*) 0.0051, (*d*) 0.0057, (*e*) 0.0068, (*f*) 0.0074, (*i*) 0.0088 and (*j*) 0.0094.

In this Section, the high degree of freedom provided by the PAFSIW structure has been demonstrated and exploited to obtain configurable coupling coefficients. Some examples of couplings based on 7 column metallic post implementations were shown for the demonstration. It is worth noting that coupling implementations based on smaller and higher number of columns will provide some more *k* values.

Finally, the discretized iris couplings study (providing a coarse discretization of a conventional iris waveguide design), can be used to obtain a coarse design from any well-known filter design synthesis method. Then, slight modifications of the discretized-iris couplings can be obtained inserting and/or removing posts to obtain the desired coupling coefficients. It is worth noting that, in this paper, only symmetrical implementations have been considered. This work can be extended with asymmetrical implementations providing even more versatility. Moreover, all the studied couplings are based on iris-like topologies. However, inductive coupling topologies, such as the one introduced in [3], can also be implemented, giving even higher design flexibility.

3. 5. Configurable PAFSIW Filters

For demonstrations, in this Section, the configurability and genericity of the PAFSIW transmission line is used to design, fabricate and implement two different filters. The two filters are fourth order filters operating in the

Ka-band. They are designed and fabricated with the same perforated AFSIW transmission line structure (i.e., having the same array of plated through holes). Two different metallic post arrangements are determined to achieve the two desired filter specifications. The metallic posts and via farm used is this study have the same characteristics as the ones presented in the previous Sections.

3. 5. 1. Theory and Design

The two designed filter demonstrators based on the generic PAFSIW structure operate at 20 GHz (filter A) and 21 GHz (filter B) with a 500 MHz (2.5 %) and 350 MHz (1.66 %) bandwidth, respectively. First, the coupling matrix, for both filters, is determined to achieve the desired center frequency, bandwidth, and a return loss better than RL = 20 dB. The values of the coupling matrix are given by the following equations presented in [15]:

$$R_1 = \frac{1}{g_0 g_1}, \tag{3.12}$$

$$R_{\mathrm{n}} = \frac{1}{g_4 g_5}, \tag{3.13}$$

and

$$M_{\mathrm{i,i+1}} = \frac{1}{\sqrt{g_{\mathrm{i}} g_{\mathrm{i+1}}}}, \tag{3.14}$$

where the g_{i} are the low pass prototype Chebyshev parameters, $M_{\mathrm{i,i+1}}$ are the coupling elements and R_1 and R_{n} are the source and load impedances.

Then, the physical k_{ij} coupling coefficients are obtained from the normalized M_{ij} coupling coefficients using:

$$k_{\mathrm{ij}} = \frac{BW}{f_0} M_{\mathrm{ij}}, \tag{3.15}$$

where *BW* is the filter bandwidth.

From the abacus introduced in Section 3. 4, the discretized iris coupling implementations providing the coupling values closest to the calculated k_{ij} values are selected to implement a coarse initial filter design. Then, the metallic post arrangement is fine-tuned using the principles introduced in Section 3. 4 and 3. 5 to achieve the required specifications. Few steps of optimization, consisting in removing and/or inserting metallic posts are required to obtain the desired response from the initial design. It is important to notice that to control the cavity resonant frequencies, almost independently from the coupling coefficients, the plated through holes located near the sidewalls are used.

The fabricated filters are based on a multilayer PCB consisting of three Hi-T_{g} FR4 substrates with $h_1 = h_2 = h_3 = 1.524$ mm. The configurations of the filter A and B metallic post arrangement are illustrated in

Fig. 3.25(*a*) and Fig. 3.25(*b*), respectively. A total of 222 and 244 metallic posts are inserted for filter A and B, respectively, in a total of 2486 perforated holes. For the given specifications, as no weak couplings are needed, holes in the center of the PAFSIW transmission line were not drilled.

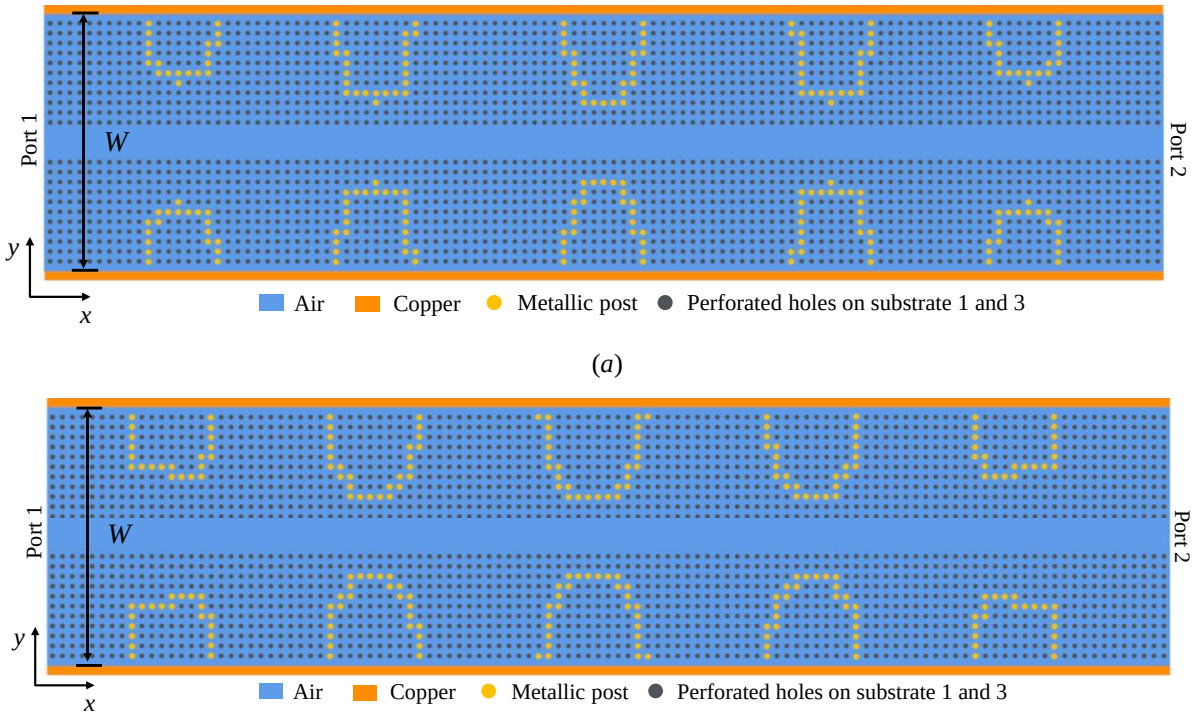

Fig. 3.25. Filter (*a*) A and (*b*) B metallic post arrangement with d = 0.2 mm and p = 0.5 mm.

3. 5. 2. Fabrication and Experiment

For demonstration purpose, two identical configurable PAFSIW transmission line have been fabricated. Their dimensions are 70.37 x 24.52 x 4.5 mm^3. One of them is shown in Fig. 3.26, without metallic post, on the WR-51 test fixture introduced in the previous Chapter and used for measurement. It is worthy to note that without metallic post, the structure achieves a transmission line function.

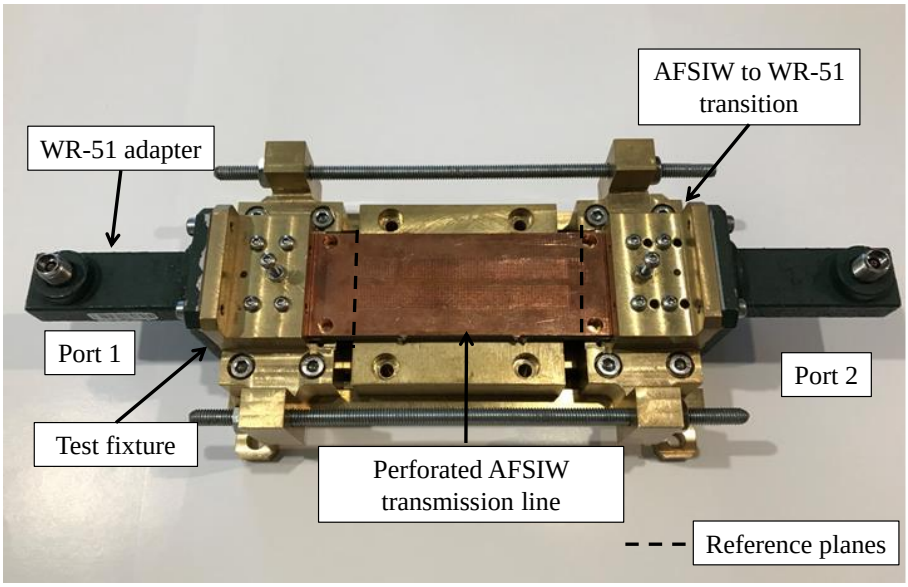

Fig. 3.26. Fabricated PAFSIW transmission line structure mounted on the test fixture.

Fig. 3.27(*a*) and Fig. 3.28(*b*) show the simulated and measured S-parameters of filter A and B, respectively. The measurements have been obtained after assembling and soldering the through-hole mounted metallic posts according to the filter A or B configurations. A good agreement between simulation and measurement is obtained. Simulated and measured results are summarized in Table 3.2, for both filters.

It can be noticed that holes in the center of the PAFSIW transmission line were not drilled as weak couplings were not needed to achieve the targeted specifications for both demonstrators. Therefore, the number of holes is reduced, leading to a shorter fabrication time. Also, the loss of the filter is slightly, but not significantly, reduced.

TABLE 3.2
SUMMARY OF MEASURED AND SIMULATED RESULTS

Characteristics	Filter A Measured / Simulated	Filter B Measured / Simulated
Return loss (dB)	> 23 / > 25	> 20 / > 25
Insertion loss (dB)	0.9 / 0.7	1.03 / 0.8
Center frequency (GHz)	19.99 / 20	20.97 / 21
-3 dB bandwidth (MHz)	510 / 500	360 / 350
-3 dB bandwidth (%)	2.7 / 2.5	1.72 / 1.67
Unloaded *Q*-factor	756	982

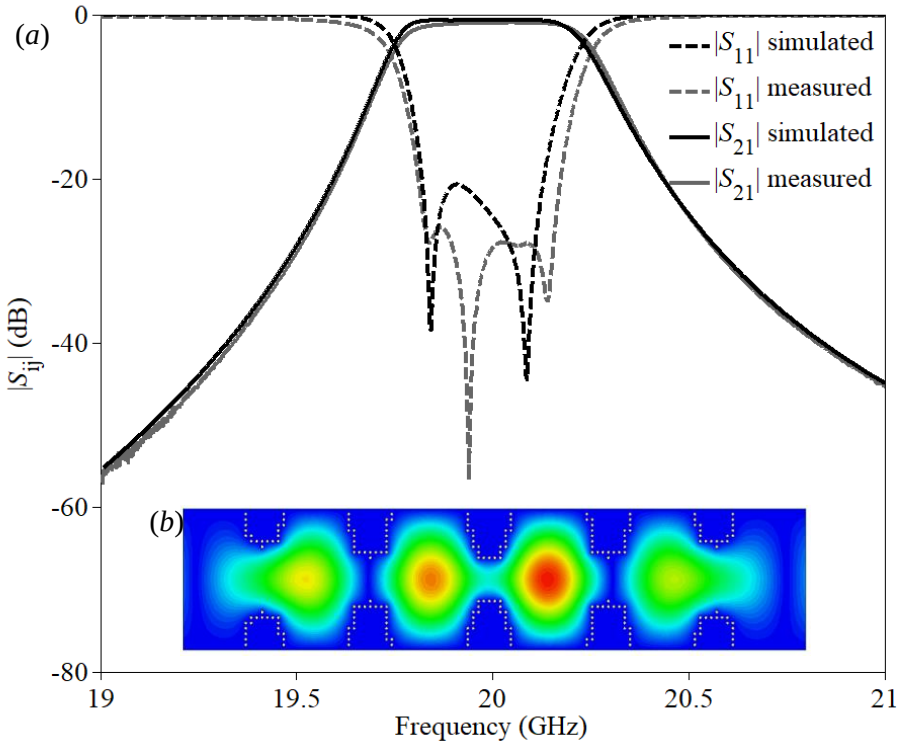

Fig. 3.27. (*a*) Simulated and measured S-parameters of the PAFSIW filter A and (*b*) simulated E-field magnitude distribution at 20 GHz for a given phase.

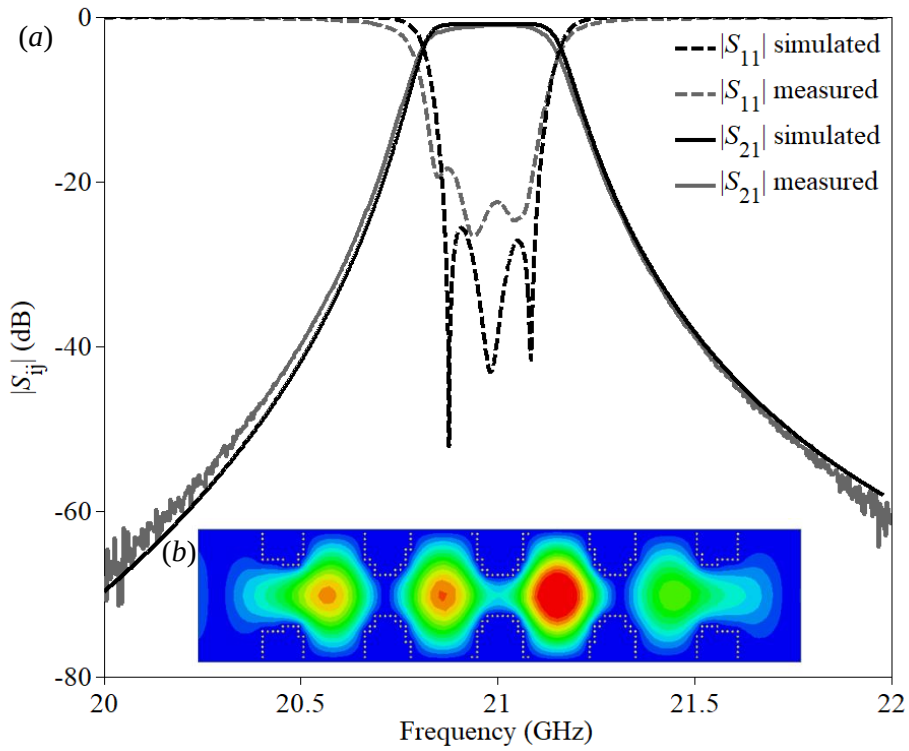

Fig. 3.28. (*a*) Simulated and measured S-parameters of the PAFSIW filter B and (*b*) simulated E-field magnitude distribution at 21 GHz for a given phase.

3. 6. Self-Heating of Filters Based on PAFSIW

In the previous Sections, the principle of configurable filters based on PAFSIW structure was detailed and demonstrated. Nevertheless, the PAFSIW structure is not only implementable on configurable filters but is also suitable for conventional structures. In this Section, a power-handling capability and self-heating comparison is made on inductive iris filters based on PAFSIW and AFSIW.

3. 6. 1. Filter Design

The self-heating of a filter is an important aspect to take into account before implementing this component in a microwave or millimeter-wave system. Indeed, in many high-power handling applications, the limiting aspect of a filter is due to the self-heating. This self-heating can cause a high frequency shift, leading the filter to be non-compliant with the specifications. Moreover, the insertion loss can be dramatically increased due to self-heating, causing the system to fail. Finally, the high temperature at stake can also degrade the assembly of a filter, especially with filters based on PCB or using low-*Tg* solder.

Therefore, the PAFSIW structure can be of high interest as it allows the filter to dissipate the heat more efficiently compared to conventional AFSIW structure. In this study, it is proposed to implement the PAFSIW structure on a conventional iris type filter and to compare it with its AFSIW counterpart. The proposed implementation of the PAFSIW with an inductive iris filter is shown in Fig. 3.29. It is based on a multilayer PCB process, substrates 1 and 3 are perforated to create an array of platted through-holes above and below the geometric configuration of substrate 2. In this particular case, $h_1 = h_2 = h_3 = 1.905$ mm, the diameter d of the holes is 0.35 mm, and the distance between two consecutive holes p is 0.6 mm.

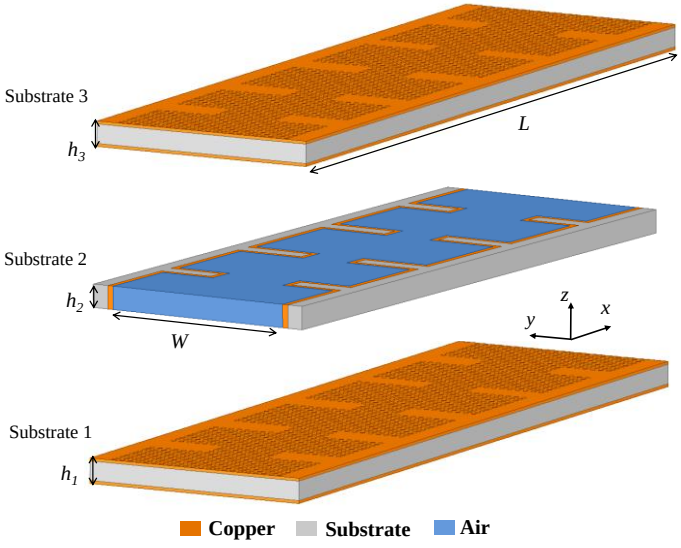

Fig. 3.29. Perforated AFSIW structure implemented on a fourth-order filter.

To demonstrate the proposed concept, a PAFSIW inductive iris filter is compared to an AFSIW inductive filter. The proposed filters have been designed to have a central frequency of 21 GHz with a fractional bandwidth of 1.43% (300 MHz). The Chebyshev approximation is used to synthesis those filters. Both filters

are fabricated using FR4 Hi-*Tg* material. The geometric configuration of the structures is illustrated in Fig. 3.30 and the geometric parameters are given in Fig. 3.30.

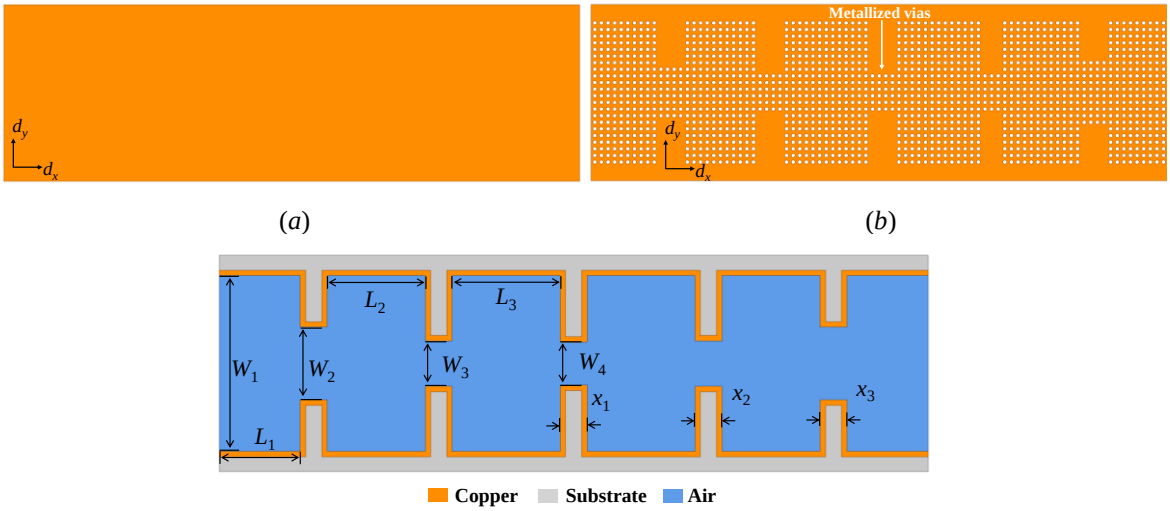

(*a*) (*b*)

(*c*)

Fig. 3.30. Top view of substrates 1 and 3 for (*a*) conventional AFSIW, and (*b*) PAFSIW implementation, and (*c*) substrate 2 identical for both structures with W_1 = 13 mm, W_2 = 5.37 mm, W_3 = 3.31 mm, W_4 = 3.07 mm, L_1 = 6 mm, L_1 = 7.25 mm, L_1 = 7.97 mm, x_1 = 2 mm, x_2 = 2 mm, and x_3 = 2 mm.

3. 6. 2. Experimental Results

For demonstration purpose, the PAFSIW and AFSIW filters have been fabricated. A photograph of the fabricated filters is shown in Fig. 3.31.

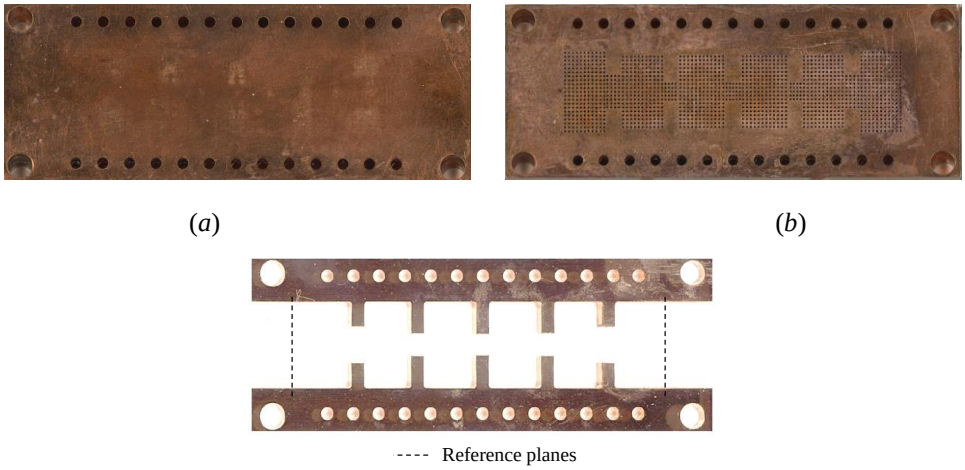

(*a*) (*b*)

(*c*)

Fig. 3.31. Photographs of substrates 1 and 3 for (*a*) conventional AFSIW, and (*b*) PAFSIW, and (*c*) substrate 2 of the fabricated filter demonstrators. The dimensions of the fabricated filter are 70 x 26.7 x 5.72 mm^3.

A vector network analyzer and a test fixture are used to measure both filters. To de-embed the effects of the connectors, cables, and transitions, a thru-reflect-line (TRL) calibration kit is also used. Fig. 3.32 and Fig. 3.33 show the simulated and measured S-parameters for both filters.

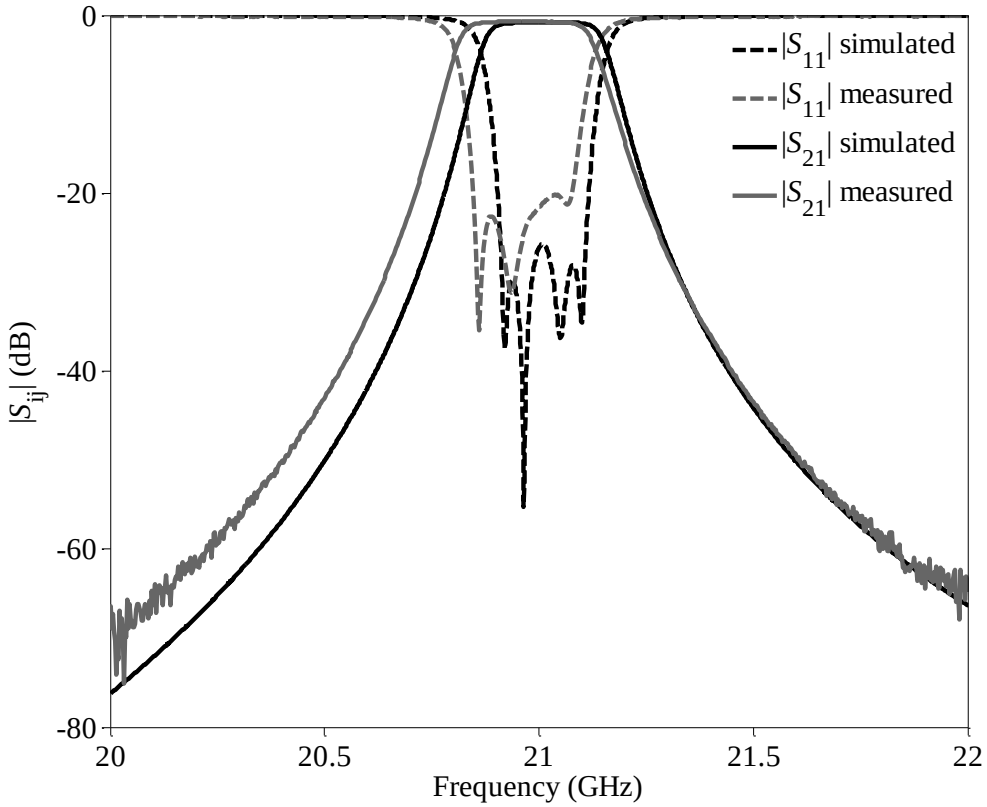

Fig. 3.32. Simulated and measured S-parameters of the AFSIW inductive iris filter.

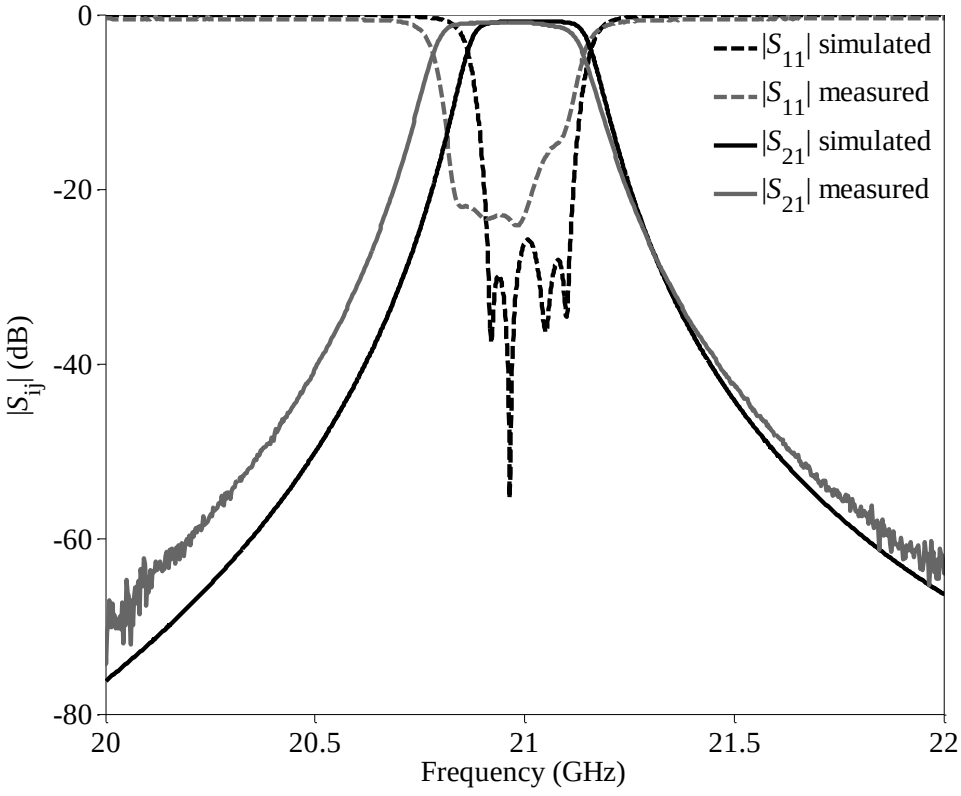

Fig. 3.33. Simulated and measured S-parameters of the PAFSIW inductive iris filter.

The measured results are in good agreement with the simulations. A slight frequency shift is observed on the central frequency of the AFSIW (30 MHz) and PAFSIW (40 MHz) filter. The return loss remains greater than 17 dB for both filters. Finally, the measured insertion loss is in good accordance with the simulated results. It is demonstrated in measurement that the via farm causes the insertion loss to increase by 34% in this particular case (even if the bandwidth of both filters is not exactly the same, this gives an idea of the impact of via farm). A summary of the measured and simulated results is given in Table 3.3.

TABLE 3.3
SUMMARY OF MEASURED AND SIMULATED RESULTS

Characteristics	AFSIW Filter Measured / Simulated	PAFSIW Filter Measured / Simulated
Return loss (dB)	> 20 / > 25	> 17 / > 25
Insertion loss (dB)	0.72 / 0.68	0.93 / 0.91
Center frequency (GHz)	20.97 / 21	20.95 / 21
-3 dB bandwidth (MHz)	324 / 300	348 / 300
-3 dB bandwidth (%)	1.54 / 1.43	1.66 / 1.43
Unloaded *Q*-factor	1561	1127

3. 6. 3. Power-Handling and Self-Heating Comparison

The two prototyped filters are then compared in terms of self-heating. The measurement setup is the same as the one presented in Section. 3. 1. To evaluate the self-heating of the filters, two power sensors are used on the input and output of both filters. For practical reasons, the thermal sensors are placed on the top substrate of the structure. The filters are tested using the test fixture presented in previous Sections but are not reported on any base plate. Hence, the self-heating of both filters are evaluated only by their behavior in temperature.

The two FR4-based filters are tested with a CW signal at 20.8 GHz. The power is increased by steps of 20 W every 5 until a maximum power of 120 W. Then, when the maximum power is reached, a stabilization stage is applied. The results are given in Fig. 3.34 and Fig. 3.35. As it can be observed from Fig. 3.34, the return loss of both filters remains greater than 18 dB. The fluctuation of the return loss observed in Fig. 3.34 is common in power-handling test. As the temperature changes, as shown in Fig. 3.35, the return loss of the DUT changes due to the single frequency point for measurements. For an input power of 120 W, it is shown in Fig. 3.35 that the conventional AFSIW filter heats up by 65 °C, compared to 53 °C for its PAFSIW counterpart.

Thus, the proposed structure can be of good interest in application where self-heating is important. The authors also think that the perforated structure can be implemented locally on pre-identified “high thermal risk” areas, such as resonators in filters.

In those tests, the DUT was not reported on any metal support. It is important to add that by introducing this metal support, the holes would act as heat pipes, thus increasing the thermal dissipation of the circuit. Unfortunately, due to a lack of time and power-handling test facility availability, these tests could not be performed in time.

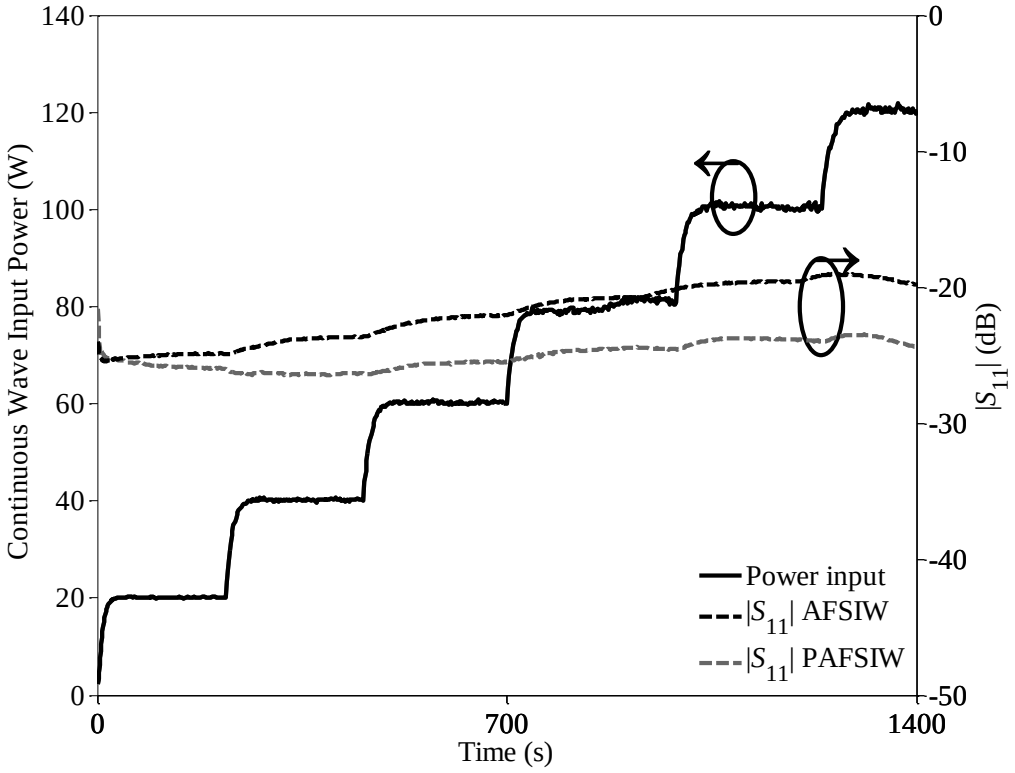

Fig. 3.34. Measured input power and return loss over time of the PAFSIW and conventional AFSIW filters at 20.8 GHz.

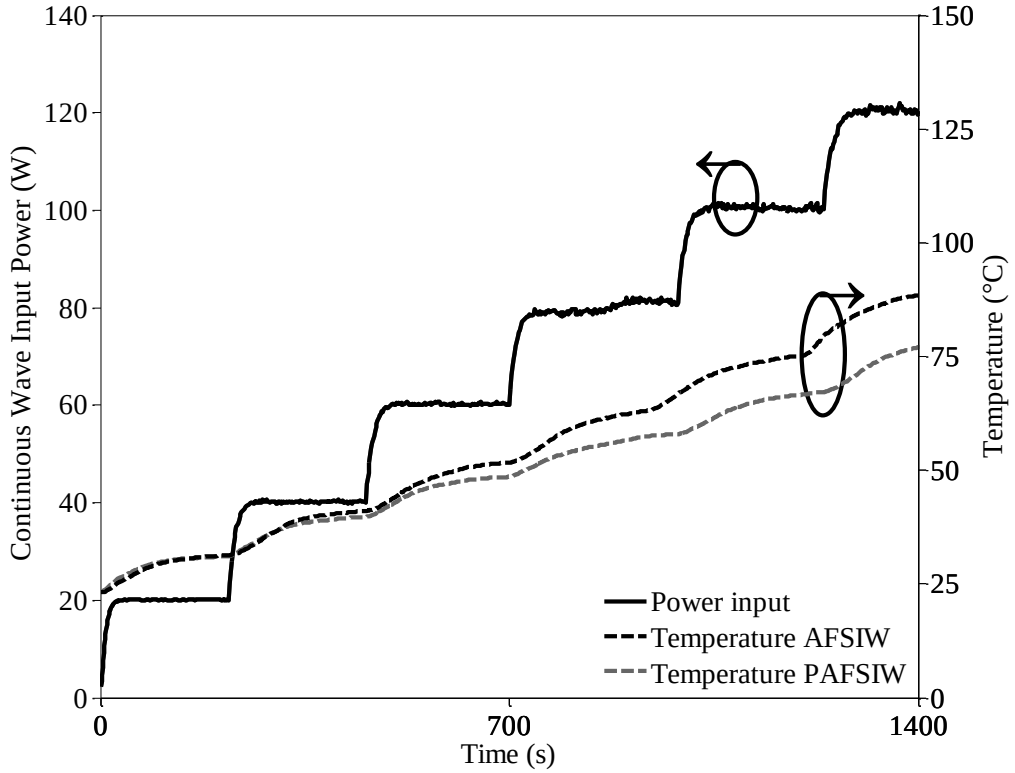

Fig. 3.35. Measured input power and temperature over time of the PAFSIW and conventional AFSIW filters at 20.8 GHz.

3. 7. Conclusions

In this Chapter, the PAFSIW has been introduced. A theoretical study of the PAFSIW transmission line properties has been presented and validated with simulated and experimental results. Moreover, a power-handling measurement has been carried out to further evaluate the enhanced thermal dissipation and average power handling capabilities of the proposed topology compared to its AFSIW counterpart. Then, the design of configurable phase shifters, resonators, and filters based on a PAFSIW transmission line section have been introduced with experimental demonstrations. All presented theoretical, simulated and measured results are in good agreements. This technology, using the through-hole mounting (THM) process, is envisioned to be implemented in the design of configurable and fabrication-tolerant components and circuits with enhanced thermal dissipation and power handling, including phase shifters, cavities and filters. The implementation of high performance and versatile PAFSIW sections in systems on substrates can provide a high degree of configurability and tunability, which are both highly desired for the emerging microwave and millimeter-wave applications. The proposed technique could also be conjugated with other conventional PCB standard process, such as surface mountable [17], to leverage the high versatility of the technology

References

[1] A. Doghri, A. Ghiotto, T. Djerafi, and K. Wu, "Compact and low cost substrate integrated waveguide cavity and bandpass filter using surface mount shorted stubs," *IEEE MTT-S Int. Microw. Symp.*, Montreal, 17-22 June 2012.

[2] T. Martin, A. Ghiotto, F. Lotz, and T.P. Vuong, "Fabrication-tolerant reconfigurable AFSIW filters based on through-hole mounted metallic posts for versatile high performance systems," *IEEE MTT-S Int. Microw. Symp.*, Philadelphia, PA, Jun. 2018.

[3] T. Martin, A. Ghiotto, T.P. Vuong, and F. Lotz, "Fabrication-tolerant AFSIW filters based on quadruplet through-hole mounted inductive posts," *Eur. Microw. Conf. (EuMC)*, Madrid, 2018.

[4] Ke Wu, "Towards system-on-substrate approach for future millimeter-wave and photonic wireless applications," *Asia-Pacific Microwave Conference*, Yokohama, 2006, pp. 1895-1900.

[5] Z. Li and K. Wu, "24-GHz frequency-modulation continuous-wave radar front-end system-on-substrate," *IEEE Transactions on Microwave Theory and Techniques*, vol. 56, no. 2, pp. 278-285, Feb. 2008.

[6] T. Martin, A. Ghiotto, T.P. Vuong, and F. Lotz, "Self-temperature-compensated air-filled substrate integrated waveguide (AFSIW) cavities and filters," *IEEE Trans. Microw. Theory Techn*., vol. 66, no. 8, pp. 3611-3621, Aug. 2018.

[7] F. Parment, A. Ghiotto, T.P. Vuong, J.M. Duchamp, and K. Wu, "Broadband transition from dielectric-filled to air-filled substrate integrated waveguide for low loss and high power handling millimeter-wave substrate integrated circuits," *IEEE MTT-S Int. Microw. Symp*., pp. 1-4, Jun. 2014.

[8] F. Parment, A. Ghiotto, T. Vuong, J. Duchamp, and K. Wu, "Air-filled substrate integrated waveguide for low-loss and high power-handling millimeter-wave substrate integrated circuits," *IEEE Transactions on Microwave Theory and Techniques*, vol. 63, no. 4, pp. 1228-1238, Apr.2015.

[9] Electromagnetic compatibility, ECSS-E-ST-20-07C Rev. 1, Feb. 2012.

[10] D. M. Pozar, *Microwave Engineering*, 4th ed. John Wiley, 2012, ch. 6, pp. 272-316.

[11] F. Parment, A. Ghiotto, T. P. Vuong, J. M. Duchamp, and K. Wu, "Double dielectric slab-loaded air-filled SIW phase shifters for high-performance millimeter-wave integration," *IEEE Trans. Microw. Theory Techn*., vol. 64, no. 9, pp. 2833-2842, Sept. 2016.

[12] M. Bozzi, A. Georgiadis, and K. Wu, "Review of substrate-integrated waveguide circuits and antennas," *IET Microw., Antennas Propag*., vol. 5, no. 8, pp. 909–920, Jun. 2011.

[13] N. Marcuvitz, *Waveguide Handbook*, Toronto, ON, Canada: McGraw-Hill, 1951, ch. 5, pp. 217-335.

[14] J.-S. Hong and M. J. Lancaster, *Microstrip Filter for RF/Microwave Applications*, New York, NY, USA: Wiley, 2001, ch. 8, pp. 235-272.

[15] R. J. Cameron, C. M. Kudsia, and R. R. Mansour, *Microwave Filters for Communication Systems*, Hoboken, NJ, USA: Wiley, 2007, ch. 14, pp. 501-530.

[16] T. Martin, A. Ghiotto, A. Marque, T.P. Vuong, F. Lotz, P. Monteil, and L. Carpentier, "Broadband air-filled SIW to waveguide transition for interconnect, instrumentation and measurement applications," *IEEE MTT-S International Microwave Workshop Series on Advanced Materials and Processes for RF and THz Applications (IMWS-AMP)*, Pavia, 2017, pp. 1-3.

[17] A. Doghri, A. Ghiotto, T. Djerafi, and K. Wu, "Compact and low cost substrate integrated waveguide cavity and bandpass filter using surface mount shorted stubs," *IEEE MTT-S Int. Microw. Symp.*, Montreal, 17-22 June 2012.

Chapter 4

Advanced Filter Responses

In this Chapter, the implementation of transmission zeros using the AFSIW technological platform is discussed. The AFSIW multilayer aspect was at first glance seen as a disadvantage since the top and bottom layers had no other purposes than mechanical supports. However, a post-process technique [1] and a fabrication tolerant configurable transmission line have been developed taking advantage of the top and bottom layer [2]-[4], as explained in the previous Chapter. In this Chapter, the multilayer aspect of the AFSIW technology is profitably used to create transmission zeros in AFSIW filter by using an SIW transmission line in the bottom substrate to cross-couple non-adjacent cavities.

4. 1. Third-Order Cross-Coupled AFSIW Filter

In this Section, the first advanced filtering response in AFSIW technology is presented. The filter configuration is a third-order in-line arrow topology. It implements a cross-coupling between non-adjacent resonators 1 and 3, which allows the introduction of a transmission zero (Tz) in the upper- or lower- band of the filter depending on the nature of the cross-coupling.

4. 1. 1. Filter Topology

The coupling diagram of the proposed structures is represented in Fig. 4.1. For the conventional third-order filter, there is a unique signal path (path 1-2-3). The proposed third-order with a cross-coupling between resonators 1 and 3 implement two signal paths (path 1-2-3) and (path 1-3). This configuration is of high interest because the selectivity of the upper- or lower- near-band of the filter is improved. It was first reported in [5]. The introduction of Tz can be explained by studying the phase relationships of the building blocks of a bandpass filter.

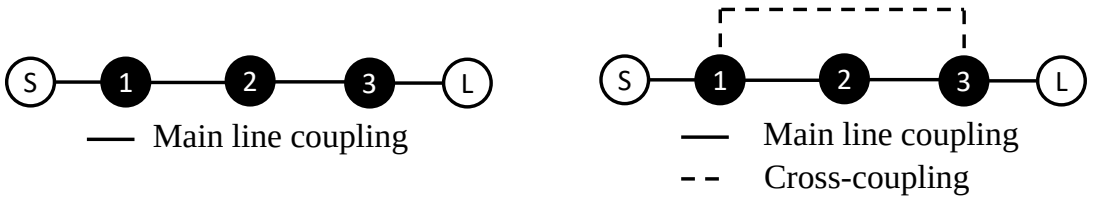

(*a*) (*b*)

Fig. 4.1. Coupling diagram of (*a*) the conventional third-order filter and (*b*) the third-order cross-coupled filter, both with in-line arrow configuration.

Fig. 4.2 represents the prototype equivalent circuit for a waveguide filter. The resonators of the filter are represented by capacitor/inductor pairs. The couplings between the different resonators are represented by inductor as the AFSIW topology is similar to a conventional rectangular metallic waveguide technology. It was

demonstrated in [6] that if the series inductor is considered as a two-port device, a signal traveling from port 1 to port 2 will undergo a phase shift. This phase shift tends toward -90° for series inductors, and 90° for series capacitors. For the particular case of the resonator, the phase shift of the signal is depending on the resonance frequency of the resonator. Hence, as stated in [6], the phase shift below resonance will tend toward 90° and -90° above resonance.

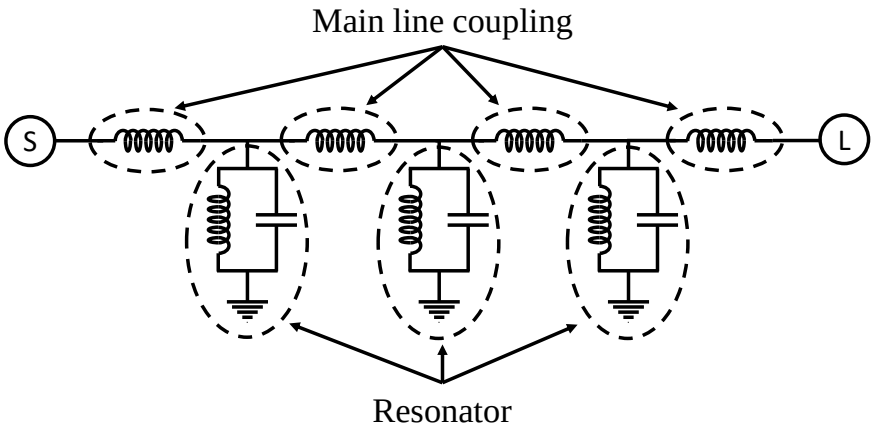

Fig. 4.2. Equivalent circuit for conventional third-order waveguide filter.

Based on the coupling diagrams shown in Fig. 4.3 (using conventional AFSIW technology), it is possible to study the phase relationships of the different paths in the proposed structure. Since both paths share a common starting and ending point, only the internal elements between resonators 1 and 3 are necessary to study the phase relationships. Depending on the requirements on the near rejection, the cross-coupling can be implemented as a capacitive or inductive coupling. To demonstrate the flexibility of the advanced filter responses, theoretical demonstration with both types of coupling is made. Considering the different nature of the elements in both coupling paths, the total phase shifts are reported in Table 4.1. The first configuration of the filter (with a capacitive cross-coupling) causes the signal to be out of phase below resonance and in phase above resonance. This causes a signal cancellation, which creates a transmission zero on the lower rejection skirt. The second configuration of the filter (with an inductive cross-coupling) causes the signal to be in phase below resonance and out of phase above resonance. This implies a signal cancellation, resulting in the creation of a transmission zero on the upper rejection skirt.

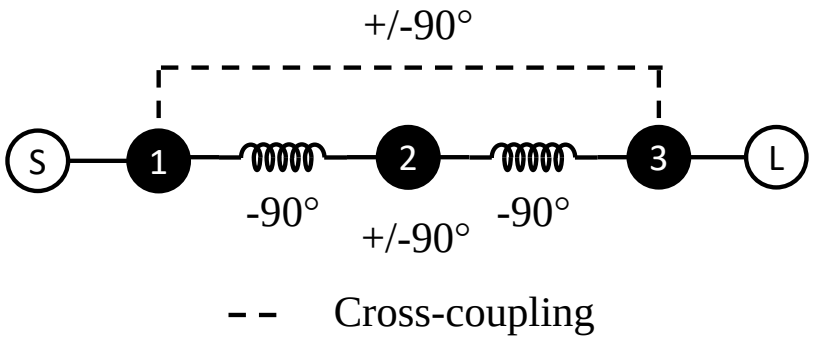

Fig. 4.3. Coupling diagram of the third-order 1-3 cross-coupled filter with phase relationships of building elements.

The implementation of Tz is of high interest for filter designers as it increases the selectivity of the filter. Depending on the application, a filter is susceptible to have an upper-band transmission zero, or a

lower-band transmission zero. To demonstrate the impact of Tz on the filter response, Fig. 4.4 represents the selectivity (S_{21}) of the three filters configuration previously discussed. It can be observed from Fig. 4.4 that the implementation of a 1-3 inductive cross-coupling enables the filter to have a sharper near-band selectivity on the upper-band of the filter compared to the conventional three poles. It can also be noticed that for this particular topology, the selectivity on the lower-band of the filter is degraded compared to the conventional three poles. For the implementation of a 1-3 capacitive cross-coupling, the opposite behavior can be observed. Depending on the required specifications, the optimal filter configuration can be chosen.

TABLE 4.1
TOTAL PHASE SHIFTS OF THIRD ORDER CROSS-COUPLED AFSIW FILTER FOR BOTH PATHS WITH TWO CROSS-COUPLING NATURES

Total phase shift	Below resonance	Above resonance
Path 1-2-3	-90°+90°-90° = -90°	-90°-90°-90 = -270°
Path 1-3 (capacitive coupling)	+90°	+90°
Result	Out of phase (creation of Tz)	In phase
Path 1-3 (inductive coupling)	-90°	-90°
Result	In phase	Out of phase (creation of Tz)

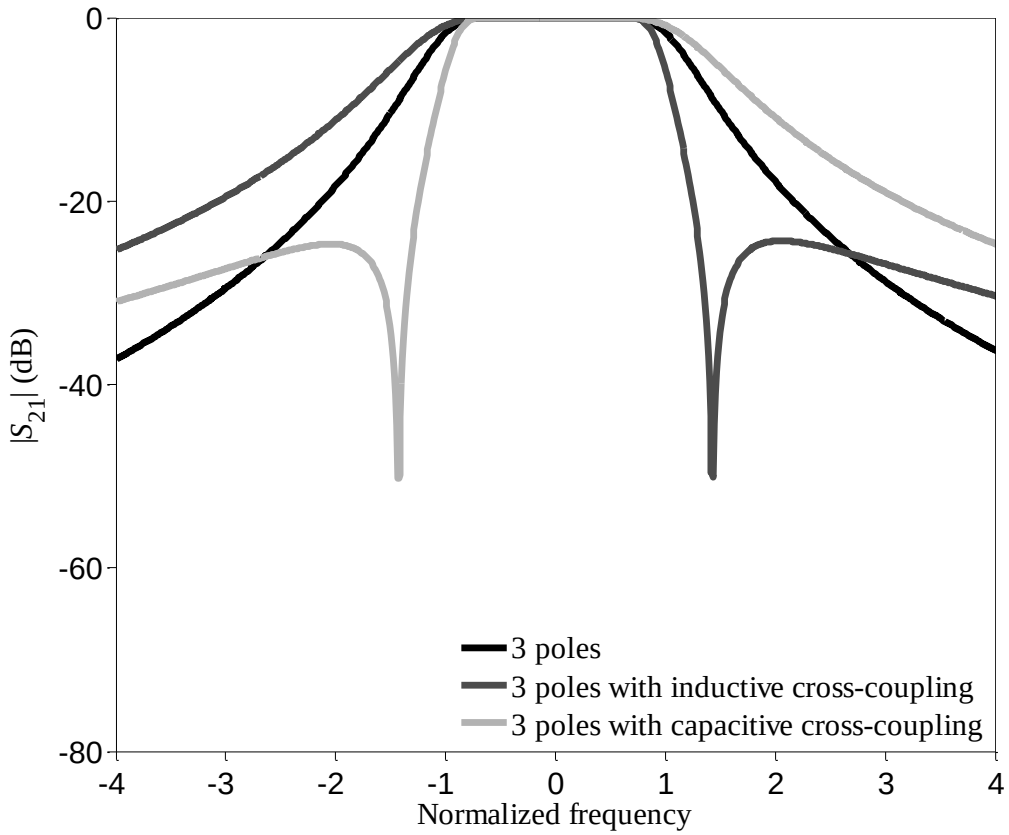

Fig. 4.4. S_{21} parameters of the three filter topologies.

4. 1. 2. Cross-Coupling Implementation Using AFSIW

To implement a cross-coupling in AFSIW technology, it is possible to take advantage of the multilayer aspect of the technology. A secondary path can be created using the top or bottom substrate. To do so, standard PCB processes, such as etching, is used.

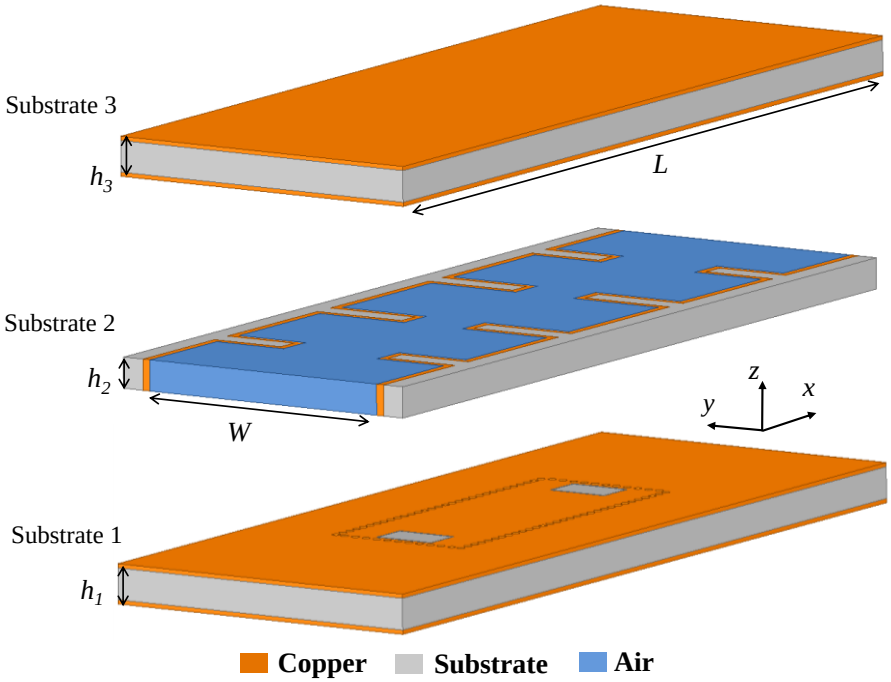

Fig. 4.5. 3D view of the third-order in-line arrow with 1-3 cross-coupling AFSIW filter.

Fig. 4.5 shows the proposed third-order in-line arrow configuration implementing a 1-3 cross-coupling filter. Path 1-2-3 is the primary path, located in substrate 2. The cross-coupling is implemented in the bottom layer of the structure. To allow the signal propagation in the SIW transmission line, the top of substrate 1 is etched with inductive iris, thus creating the secondary signal path (path 1-3). Considering this type of cross-coupling, it is important to take into account the electrical length of the SIW transmission in the total phase shift in addition to the nature of the cross-coupling. In this particular case, the coupling diagram represented in Fig. 4.3 becomes the one shown in Fig. 4.6.

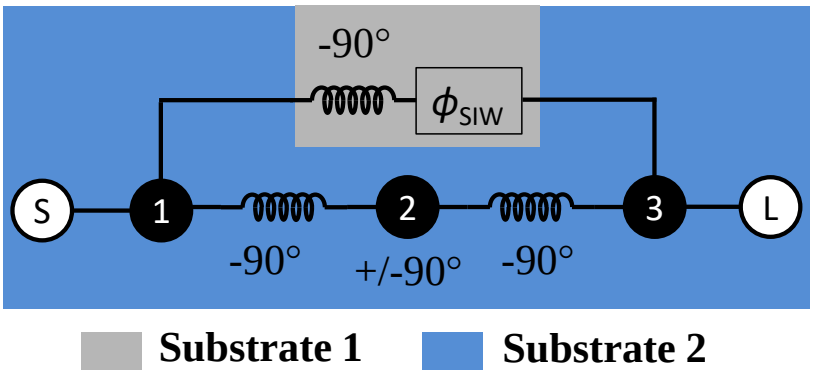

Fig. 4.6. Coupling diagram, with source/load coupling, of the third-order cross-coupled filter implemented in AFSIW technology using a SIW transmission line.

TABLE 4.2
TOTAL PHASE OF THIRD-ORDER 1-3 CROSS-COUPLED AFSIW FILTER SHIFTS FOR BOTH PATHS USING SIW TRANSMISSION LINE

Total phase shift	Below resonance	Above resonance
Path 1-2-3	-90°+90°-90°= -90°	-90°-90°-90° = -270°
Path 1-3	$-90°+\phi_{SIW}$	$-90°+\phi_{SIW}$
Result with $\phi_{SIW} = 360°$	In phase	Out of phase (creation of Tz)
Result with $\phi_{SIW} = 180°$	Out of phase (creation of Tz)	In phase

As it is shown in Table 4.2, depending on the electrical length ϕ_{SIW} of the SIW transmission line, the two presented types of coupling can be achieved. The electrical length ϕ_{SIW} must be chosen to be a multiple of a half wavelength. It is of common knowledge that a half wavelength provides a 180° phase shift. Thus, by playing with the additional phase shift created by the SIW transmission line, it is possible to have an equivalent overall inductive cross-coupling (with $\phi_{SIW} = 360°$ or a multiple), thus creating a transmission zero on the upper-band of the bandpass. On the other hand, if the electrical length of the SIW transmission is set to $\phi_{SIW} = 180°$ or a multiple, the equivalent overall coupling is capacitive, hence creating a transmission zero on the lower-band of the filter. The position of the transmission zero can be controlled by increasing or decreasing the coupling between resonators 1 and 3 by changing the etched inductive coupling window dimensions.

4. 1. 3. Filter Design

In order to improve the near-band selectivity, the proposed principle is implemented on a third-order with 1-3 equivalent overall inductive cross-coupling. First, the filter is designed based on Chebyshev approximation without the cross-coupling implementation. The proposed filter has been designed to operate at 21 GHz with a fractional bandwidth of 1.43% (i.e., 300 MHz). Then the cross-coupling between resonators 1 and 3 is implemented with a weak level using an SIW transmission line and an etched inductive iris. The correct phase of the transmission line is obtained with W_4 and L_4 parameters. Finally, depending on the required specifications, the coupling between resonators 1 and 3 is adjusted with the etched inductive iris. Few steps of optimization are necessary to obtain the correct response for the cross-coupled filter design from the first filter design. The filter is based on a multilayer PCB consisting of three Rogers RT/Duroid 6002 substrate with thickness $h_1 = h_3 = 0.508$ mm and $h_2 = 1.524$ mm. The geometric configuration of the structure is shown in Fig. 4.7. All the dimensions are reported in Table 4.3.

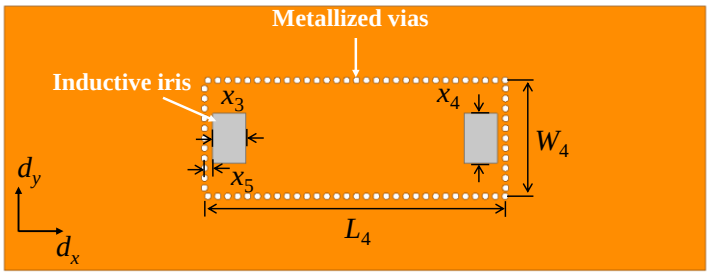

(*a*)

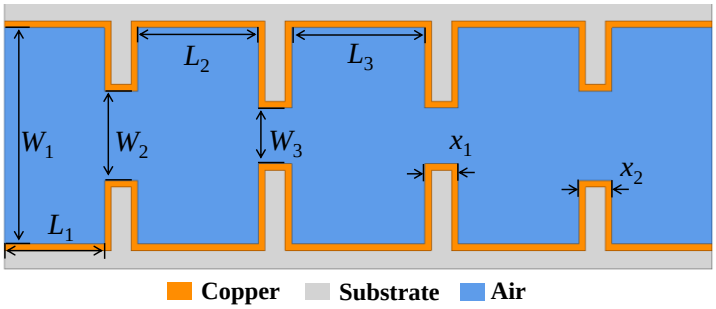

(*b*)

Fig. 4.7. Top views of (*a*) substrate 1, implementing the secondary path with the cross-coupling, and (*b*) substrate 2 implementing the primary path with the three resonators.

TABLE 4.3
DIMENSIONS OF THE DESIGNED 1-3 CROSS-COUPLED AFSIW FILTER

Dimension	$i = 1$	$i = 2$	$i = 3$	$i = 4$	$i = 5$
L_i (mm)	6	7.465	7.955	24.42	/
x_i (mm)	2	2	3.2	3	0.45
W_i (mm)	13	5.32	3.16	7	/

4. 1. 4. Robustness Against PCB Manufacturing Tolerances

In industry, a manufacturing process tolerance analysis is required to determine the yield of a filter topology. For this reason, robustness against the standard PCB process milling tolerances (+/- 30 mils, approximately +/- 0.0762 mm), the substrate permittivity uncertainty (+/- 0.04 considering Rogers RT/Duroid 6002) and the standard multilayer PCB process substrate to substrate misalignment (+/- 30 mils, approximately +/- 0.0762 mm), are evaluated. It should be noticed that more advanced PCB process class can be used to provide lower tolerances, but at the expense of a higher cost.

A well-known approach to determine the sensitivity of a filter to dimensional random variations is to perform a Monte Carlo analysis. For this purpose, the FEST3D simulator, using a +/- 0.0762 mm variation on physical dimensions, has been used. Results are reported in Fig. 4.8(*a*). A variation of only +/- 1 MHz on the rejection frequency location can be observed with a negligible impact on the center frequency and bandwidth. Furthermore, the return loss remains above 15 dB.

As the cross-coupling of the proposed topology is made using an SIW transmission line in the bottom substrate, a study of the substrate dielectric constant uncertainty is also needed. The datasheet of the particular used substrate gives the uncertainty of the dielectric constant (+/ 0.04). Fig. 4.8(*b*), reporting S-parameters of the filter obtained with the ANSYS HFSS simulator, shows that the variation of the dielectric constant has almost no impact on the transmission zeros frequencies and other characteristics of the filter.

Finally, a study of the substrate to substrate misalignment is carried out. A suitable approach is to evaluate the filter response to the worst cases of alignment using a full-wave simulator, here ANSYS HFSS. In the proposed structure, the misalignment of substrate 1 and substrate 2 implies a misalignment of the etched coupling windows. The results are shown in Fig. 4.8(*c*). It can be observed that with a worst case of 0.152 mm misalignment in *x* and *y* directions, the frequency response is very slightly impacted.

The three studies highlight the high robustness of the proposed structure to PCB manufacturing tolerances, and therefore its high interest for implementation.

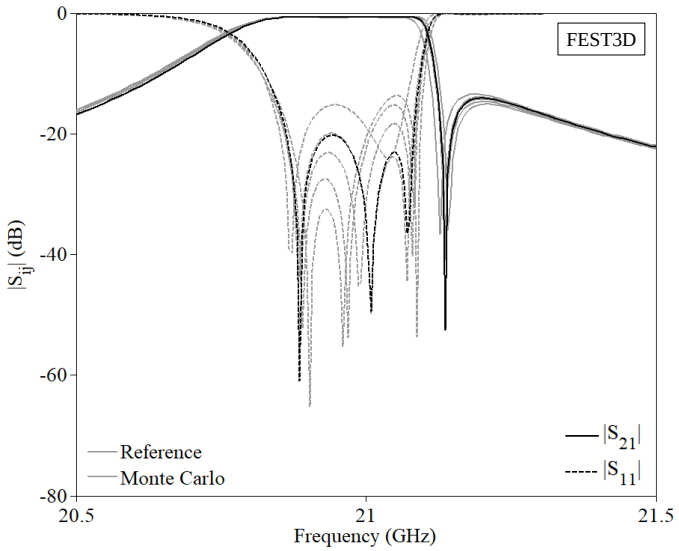

(*a*)

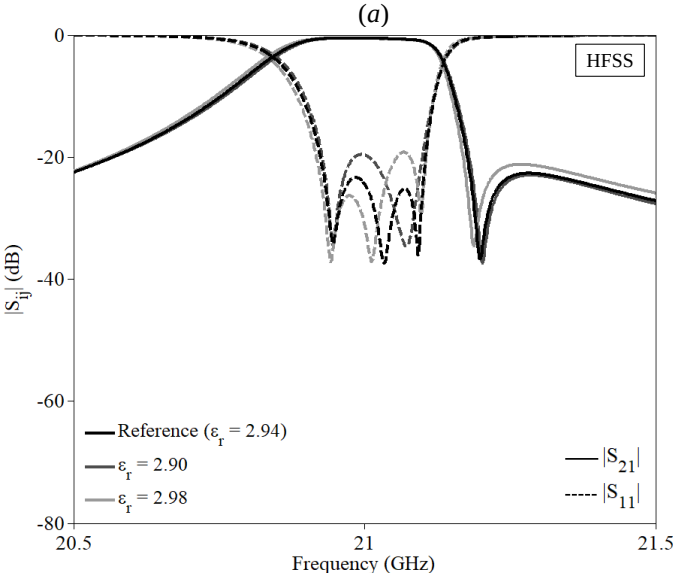

(*b*)

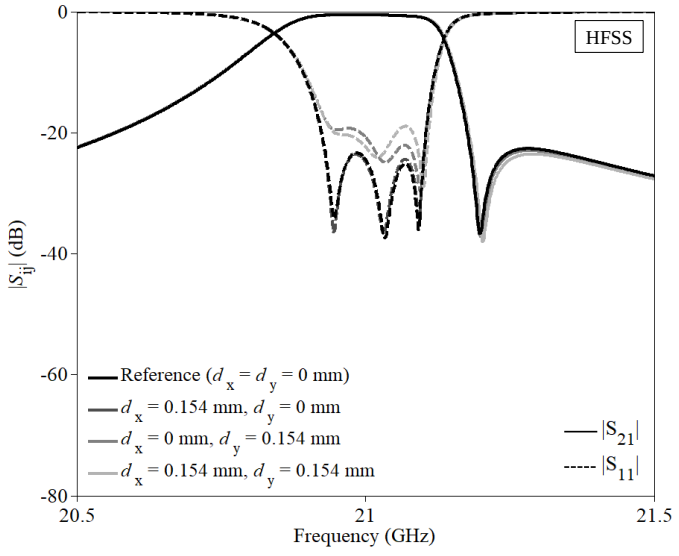

(*c*)

Fig. 4.8. Robustness analysis against (*a*) milling and drilling tolerances based on a Monte Carlo analysis using FEST3D, (*b*) dielectric constant variation using HFSS and (*c*) multilayer misalignment using HFSS.

4. 1. 5. Experimental Results

For demonstration purposes, a third-order with 1-3 cross-coupling AFSIW filter, using an in-line arrow configuration, has been designed and fabricated. The arrays of metallized via holes of substrate 1 have a diameter *d* of 0.8 mm and a center-to-center pitch *p* of 1.2 mm. A photograph of the fabricated filter is shown in Fig. 4.9.

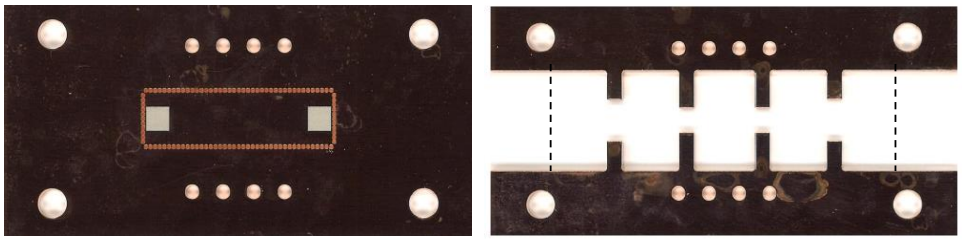

(*a*) (*b*)

Fig. 4.9. Photographs of (a) substrate 1 and (b) substrate 2 of the fabricated third-order 1-3 cross-coupling AFSIW filter demonstrator. The dimensions of the fabricated filter are 61.8 x 31.15 x 2.54 mm^3.

A vector network analyzer and a test fixture with a thru-reflect-line (TRL) calibration kit to de-embed the effects of connectors and transition have been used. Fig. 4.10 shows the simulated and measured S-parameters. The measured frequency response is similar to the simulated counterpart with a 40 MHz (0.19%) frequency shift. The measured -3 dB bandwidth has a small variation of about 10 MHz (3.3%) compared to the simulated results. The measured and simulated rejection frequencies are in good agreement with the simulations. The rejection is located at 21.18 GHz for a simulation location at 21.17 GHz. The measured in-band insertion loss is 0.66 dB which is slightly higher than the 0.54 dB obtained in the simulation. The measured *Q*-factor is equal to 1429 using the formula described in Chapter 2 and the different results are presented in Table 4.4. Table 4.5 presents a comparison with similar planar filter topologies.

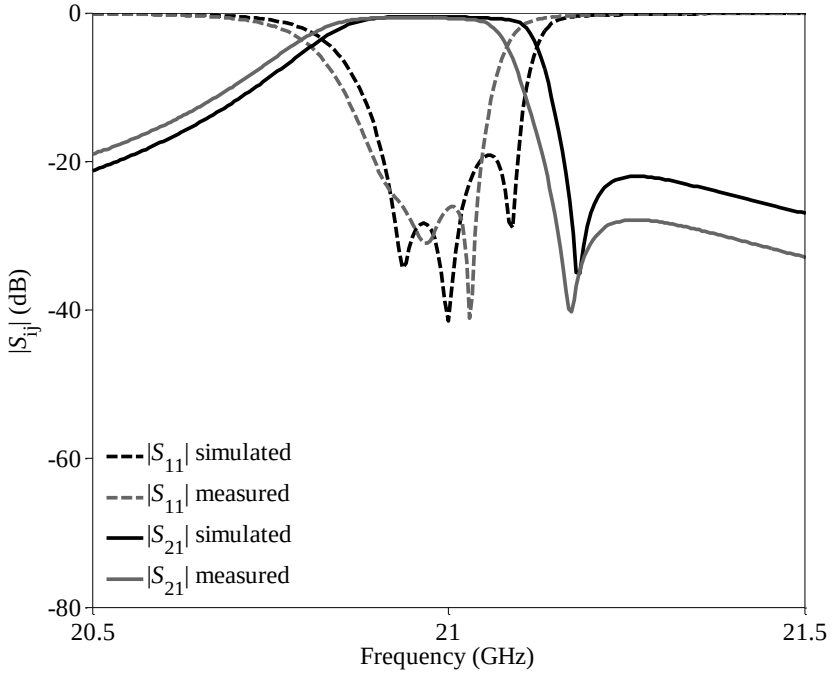

Fig. 4.10. Simulated and measured S-parameters of the fabricated third-order 1-3 cross-coupled AFSIW filter demonstrator.

TABLE 4.4
COMPARISON OF SIMULATED AND MEASURED RESULTS OF THIRD-ORDER AFSIW CROSS-COUPLED FILTER

Characteristics	Simulated (HFSS)	Measured
Return loss (dB)	> 22	> 22
Insertion loss (dB)	0.54	0.66
Center frequency (GHz)	21	20.96
Rejection frequency (GHz)	21.17	21.18
-3 dB bandwidth (MHz)	300	290
-3 dB bandwidth (%)	1.43	1.38
Unloaded *Q*-factor	1689	1429

TABLE 4.5
COMPARISON WITH SUBSTRATE INTEGRATED 1-3 CROSS-COUPLED FILTERS

Specifications	[8]	[9]	[10]	**Proposed filter**
Process	PCB	PCB	PCB	**PCB**
Technology	Combline SIW	SIW	SIW	**AFSIW**
PCB substrate material	Rogers 4003	Rogers 5880	Rogers 6002	**Rogers 6002**
Filter order	3rd	3rd	4th	**3rd**
Total height (mm)	1.524	0.762	0.508	**2.54**
Area (mm^2)	1880	561	121	**1925**
Center frequency (GHz)	5.3	13.35	35	**20.96**
-3 dB bandwidth (%)	4.9	8.99	8	**1.38**
Insertion loss (dB)	1.8	1.25	1.2	**0.66**
Rejection frequencies (GHz)	5.68	14.2	36.2	**21.18**
Unloaded *Q*-factor	147	115	180	**1429**

4. 2. Quasi-Elliptic Fourth-Order In-Line Configuration AFSIW Filter

In this Section, based on the previous demonstration of an advanced filtering response using AFSIW technology, a fourth-order quasi-elliptic AFSIW filter is presented. The filter configuration is a fourth-order in-line arrow topology. In the proposed structure, a cross-coupling between non-adjacent resonators 1 and 4 is implemented. The implementation of a 1-4 negative cross-coupling (in opposition to the sign of the coupling between adjacent resonators) in a fourth-order filter allows the generation of two transmission zeros, above and below the filter passband. This structure is of particular interest when the passband of the filter needs to be highly isolated from other bands. A typical example is channel filters of a multiplexer.

4. 2. 1. Filter Topology

The proposed structure coupling diagram is represented in Fig. 4.11. The conventional fourth-order filter allows only a single signal path (path 1-2-3-4), whereas the quasi-elliptic structure enables a secondary path (path 1-4). The introduction of Tz can be explained by studying the phase relationships of the building blocks of a bandpass filter as described in Section 4. 1.

The study on the phase relationships of the two paths is carried out. The coupling diagram of the proposed structure using the AFSIW technology is represented in Fig. 4.12. The phase of the internal elements to study is resonators 2 and 3 and also the couplings between resonators 1-2, 2-3, and 3-4.

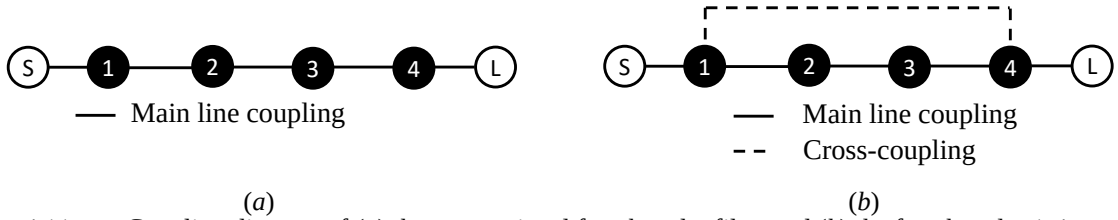

(*a*) (*b*)

Fig. 4.11. Coupling diagram of (*a*) the conventional fourth-order filter and (*b*) the fourth-order 1-4 cross-coupled filter, both with in-line arrow topologies.

The achievable responses of the proposed structure are studied depending on the nature of the cross-coupling. The total phase shifts are reported in Table 4.6. The first configuration of the filter (with inductive cross-coupling) causes the signal to be in phase both below and above resonance. This configuration is of high interest to create imaginary transmission zeros to flatten the group delay. The second configuration of the filter (with capacitive cross-coupling) allows the two signal paths to be out of phase below and above the resonance. Hence, transmission zeros are created below and above the passband, substantially improving the near-band selectivity of the filter.

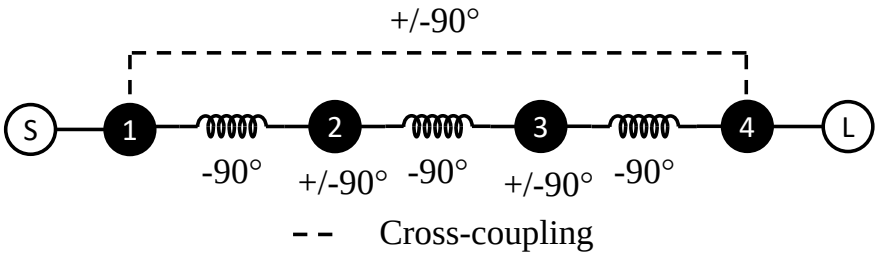

Fig. 4.12. Coupling diagram of the fourth-order 1-4 cross-coupled filter with phase relationships of building elements.

TABLE 4.6
TOTAL PHASE SHIFTS OF QUASI-ELLIPTIC AFSIW FILTER FOR BOTH PATHS WITH TWO CROSS-COUPLING NATURES

Total phase shift	Below resonance	Above resonance
Path 1-2-3-4	-90°+90°-90°+90°-90° = -90°	-90°-90°-90 -90°-90°= -450°
Path 1-4 (capacitive coupling)	+90°	+90°
Result	Out of phase (creation of Tz)	Out of phase (creation of Tz)
Path 1-4 (inductive coupling)	-90°	-90°
Result	In phase	In phase

The quasi-elliptic structure allows implementing two transmission zeros below and above the passband. At first glance, the generation of transmission zeros is of high interest for the selectivity of the filter. Nevertheless, it can also be seen as a way to significantly reduce the size of the filter while maintaining the same in- and near-band performances. To demonstrate this effect, Fig. 4.13 represents the selectivity (S_{21}) of conventional fourth-order, quasi-elliptic fourth-order, and sixth-order filters. It can be observed from Fig. 4.13 that the implementation of the 1-4 cross-coupling in the fourth-order filter allows the filter to have similar selectivity levels in the near-band as a sixth-order filter, while maintaining the compactness of a fourth-order. In other words, the same near-band electrical performances can be achieved while minimizing the volume of the filter by 2 resonators and 2 coupling elements. It is also worthy to note that the implementation of the

quasi-elliptic fourth-order topology tends to lower the insertion loss of the filter compared to a conventional fourth-order filter with the same specifications.

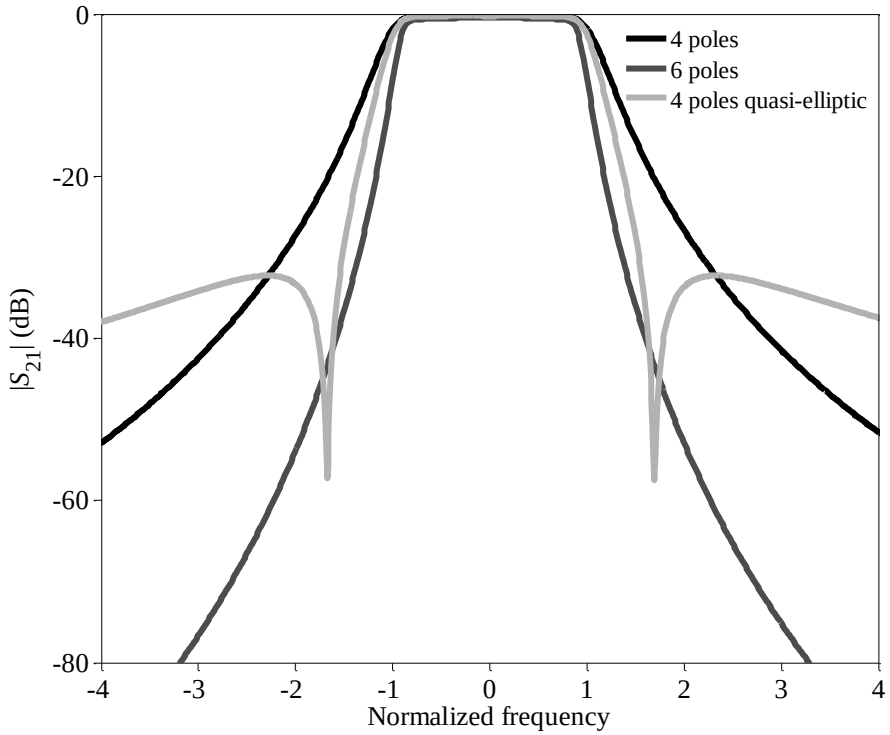

Fig. 4.13. S_{21} parameters of the conventional fourth- and sixth-order, and quasi-elliptic filter topologies.

4. 2. 2. Cross-Coupling Implementation Using AFSIW

Again, the proposed structure takes advantage of the AFSIW multilayer aspect. The cross-coupling is implemented following the same idea as explained in Section 4. 1. The SIW transmission line is also implemented in the bottom substrate of the structure to link two non-adjacent resonators.

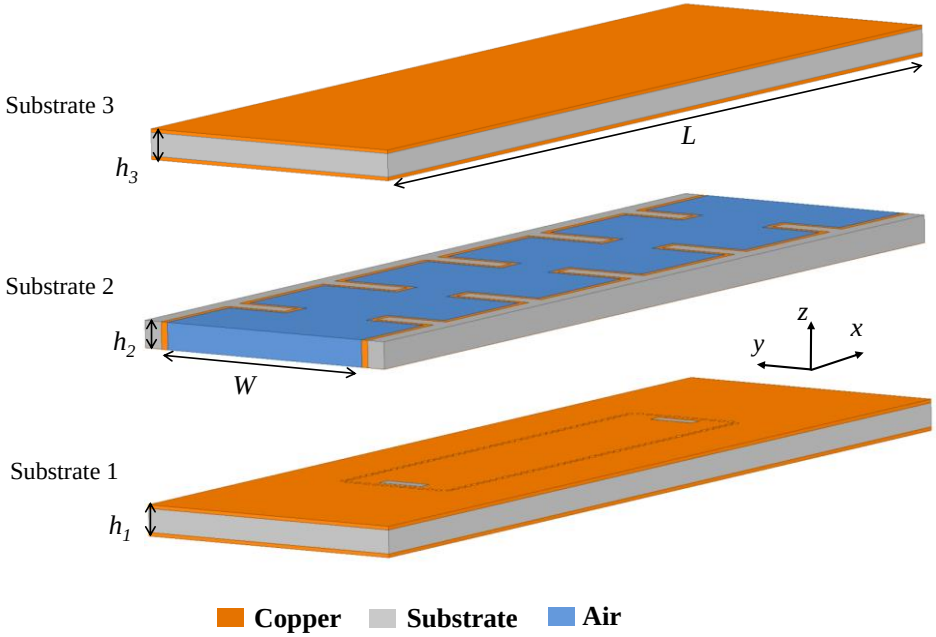

Fig. 4.14. 3D view of quasi-elliptic fourth-order in-line arrow AFSIW filter.

Fig. 4.14 shows the proposed quasi-elliptic fourth-order in-line arrow AFSIW filter. The primary path is generated by resonator 1-2-3-4. The secondary path is implemented using an SIW transmission line coupling the non-adjacent resonators 1 and 4. The nature of the cross-coupling is given by property of the iris, which is inductive in this particular implementation. Then, the electrical length ϕ_{SIW} is taken into account to obtain the equivalent overall sign of the cross-coupling. The coupling diagram of the proposed structure taking into account the electrical length of the transmission line is given in Fig. 4.15.

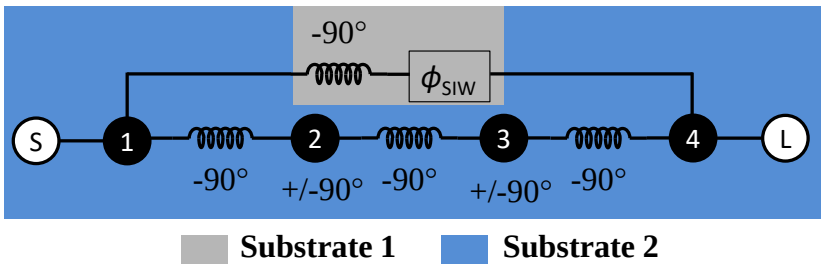

Fig. 4.15. Coupling diagram of the quasi-elliptic fourth-order filter implemented in AFSIW technology using a SIW transmission line.

TABLE 4.7
TOTAL PHASE SHIFTS OF QUASI-ELLIPTIC AFSIW FILTER FOR BOTH PATHS USING SIW TRANSMISSION LINE

Total phase shift	Below resonance	Above resonance
Path 1-2-3	-90°+90°-90°+90°-90° = -90°°	-90°-90°-90 -90°-90°= -450°
Path 1-4	-90°+ϕ_{SIW}	-90°+ϕ_{SIW}
Result with $\phi_{SIW} = 360°$	In phase	In phase
Result with $\phi_{SIW} = 180°$	Out of phase (creation of Tz)	Out of phase (creation of Tz)

The Table 4.7 shows the total phase shifts of the two paths with different equivalent overall cross-coupling natures. It is stated that if the electrical length ϕ_{SIW} of the SIW transmission line is equal to 360° or a multiple, the two paths are in phase, hence creating imaginary transmission zeros below and above the resonance, allowing flattening the group delay. On the other hand, if the electrical length ϕ_{SIW} of the SIW transmission line is equal to 180° or a multiple, a signal cancellation occurs and creates a transmission zero on the lower (below resonance) and upper (above resonance) skirt. This is due to the equivalent overall coupling being capacitive. The transmission zeros positions can be controlled by increasing or decreasing the coupling by adjusting the coupling window.

4. 2. 3. Filter Design

To demonstrate the proposed quasi-elliptic principle, an equivalent overall capacitive 1-4 cross-coupling is implemented on a conventional fourth-order AFSIW filter. Using a Chebyshev approximation, it is possible to synthesize the fourth-order AFSIW filter without the cross-coupling. The proposed filter has been designed to have a central frequency of 21 GHz with a fractional bandwidth of 1.67% (i.e., 350 MHz). Following, the implementation of the 1-4 cross-coupling is made with a weak level. The correct phase of the SIW transmission line is controlled by the physical dimensions W_5 and L_4. Depending on the required specifications, the coupling level is increased while maintaining the resonance frequencies of the resonators. Few steps of optimization are necessary to obtain the correct response for the cross-coupled filter design from the first filter design. The filter

is based on the same process as presented in Sections 4. 1 and 4. 2 with the same materials and thickness. All the dimensions of the designed filter are given in Table 4.8. The geometric implementation of the filter is given in Fig. 4.16.

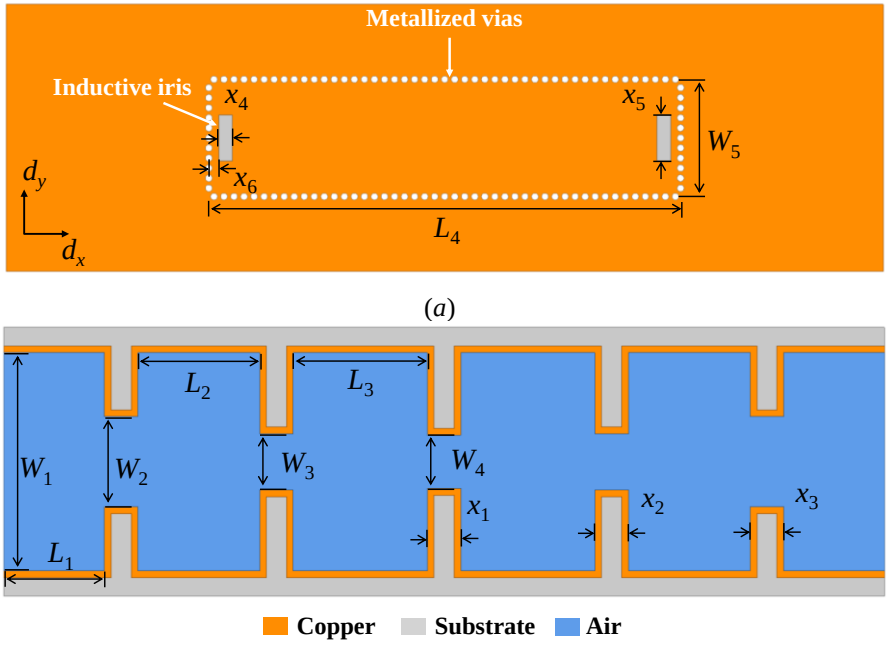

Fig. 4.16. Top views of (*a*) substrate 1, implementing the secondary path with the 1-4 cross-coupling, and (*b*) substrate 2 implementing the primary path with the four resonators.

TABLE 4.8
DIMENSIONS OF THE DESIGNED QUASI-ELLIPTIC AFSIW FILTER

Dimension	i = 1	i = 2	i = 3	i = 4	i = 5	i = 6
L_i (mm)	6	7.226	7.964	28.154	/	/
x_i (mm)	2	2	2	0.8	2.75	0.3
W_i (mm)	13	5.356	3.334	3.161	7	/

4. 2. 4. Robustness Against PCB Manufacturing Tolerances

For the same reasons as explained in Section 4. 1. 4, robustness against the PCB process milling tolerances (+/- 0.0762 mm), the substrate permittivity uncertainty (+/- 0.04 considering Rogers RT/Duroid 6002) and the standard multilayer PCB process substrate to substrate misalignment (+/- 0.0762 mm), are evaluated.

The results of the Monte Carlo analysis using the FEST3D simulator with a +/- 0.0762 mm variation on physical dimensions is shown in Fig. 4.17(*a*). A variation of +/- 2 MHz on the rejection frequencies locations is observed. It has a negligible impact on the center frequency and the bandwidth of the structure.

The study of the substrate dielectric constant uncertainty is carried out. The same datasheet given by Rogers is used to obtain the dielectric constant uncertainty. Then, using a full-wave simulator, here ANSYS HFSS, the impact of this uncertainty is studied on the proposed structure. Fig. 4.17(*b*) reports S-parameters of the filter with a variation of +/- 0.04 of the dielectric constant of the SIW transmission line. It can be observed that it has no impact on the location of the transmission zeros.

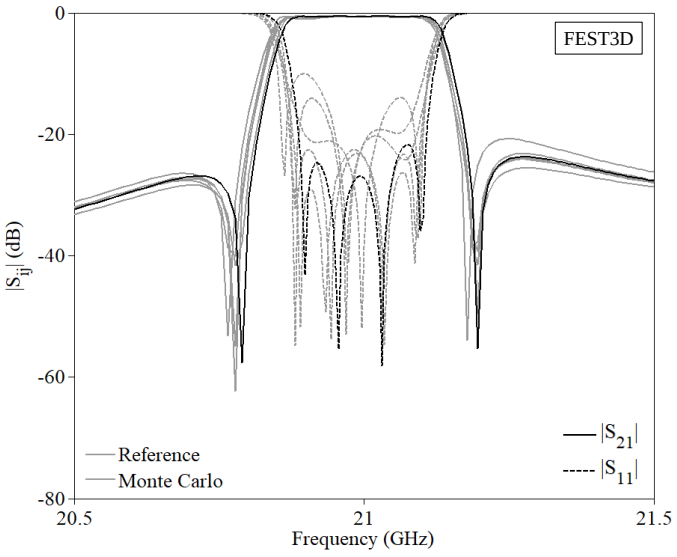

(*a*)

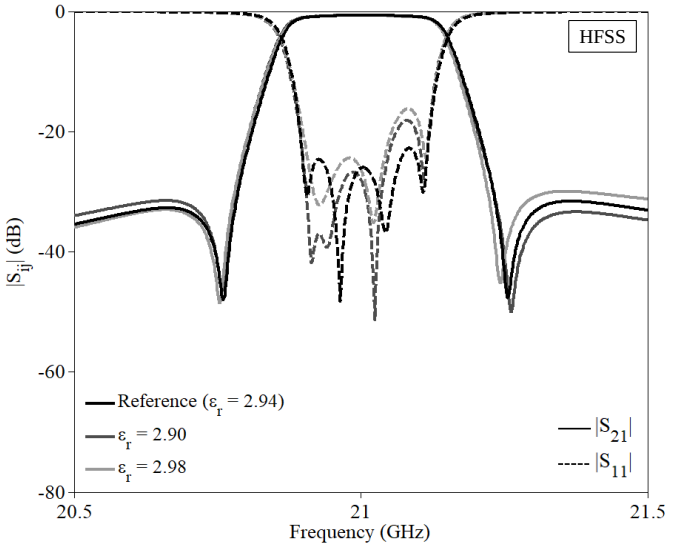

(*b*)

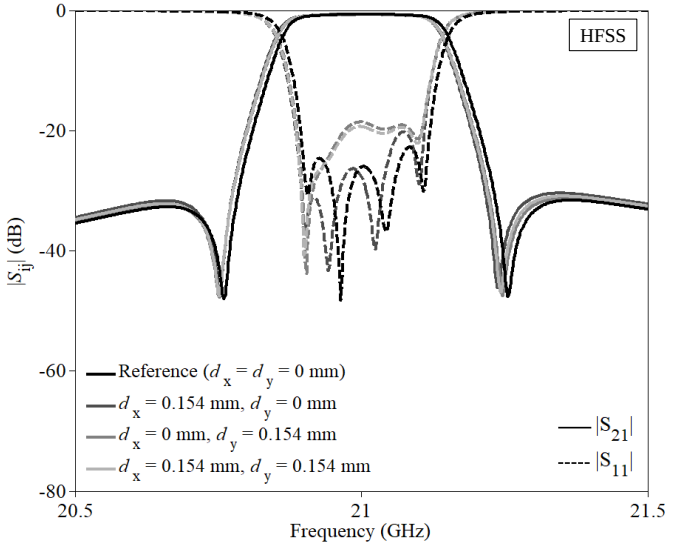

(*c*)

Fig. 4.17. Robustness analysis against (*a*) milling and drilling tolerances based on a Monte Carlo analysis using FEST3D, (*b*) dielectric constant variation using HFSS and (*c*) multilayer misalignment using HFSS.

The last study concerns the substrate to substrate misalignment. The same approach as in Section 4. 1 is used. The misalignment of substrates 1 and 2 is studied using the full-wave ANSYS HFSS simulator. The results are shown in Fig. 4.17(*c*). It can be observed that with a worst case of 0.152 mm misalignment in *x* and *y* directions, the frequency response is very slightly impacted.

The three studies show the high robustness of the proposed structure to PCB manufacturing tolerances, substrate dielectric constant uncertainty, and substrate to substrate misalignment.

4. 2. 5. Experimental Results

For demonstration purpose, a quasi-elliptic fourth-order with 1-4 cross-coupling AFSIW filter, using an in-line arrow configuration, has been designed and fabricated. The arrays of metallized via holes have the same dimensions as detailed previously. A photograph of the fabricated filter is given in Fig. 4.18.

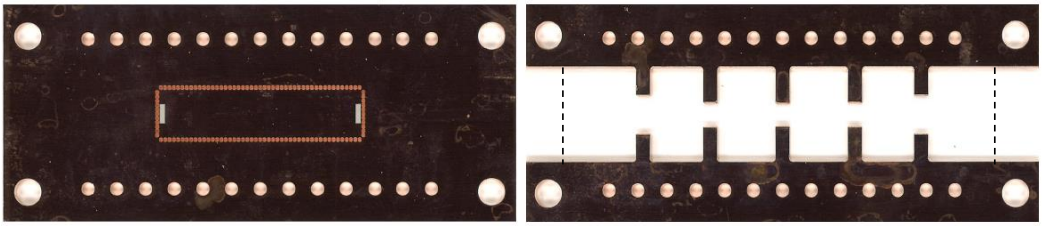

---- Reference planes

(*a*) (*b*)

Fig. 4.18 Photographs of (*a*) substrate 1 and (*b*) substrate 2 of the fabricated quasi-elliptic fourth-order AFSIW filter demonstrator. The dimensions of the fabricated filter are 71.4 x 31.15 x 2.54 mm^3.

The measurement of the fabricated prototype has been achieved using the same flow (vector network analyzer, test fixture, and TRL calibration kit). The comparison between simulated and measured results is given in Fig. 4.19. The measured center frequency is 20.99 GHz compared to 21 GHz in simulations. The measured bandwidth of the filter is 280 MHz, slightly smaller than the 300 MHz of the simulated results. The measured rejection frequencies are located at 20.77 GHz and 21.22 GHz. The return loss of the measured filter remains greater than 20 dB. Finally, the measured in-band insertion loss is 0.78 dB. The obtained *Q*-factor of the measured filter is evaluated to 1613. All the measured results are presented in Table 4.9.

TABLE 4.9
COMPARISON OF SIMULATED AND MEASURED RESULTS OF QUASI-ELLIPTIC AFSIW

Characteristics	Simulated (HFSS)	Measured
Return loss (dB)	> 22	> 22
Insertion loss (dB)	0.7	0.78
Center frequency (GHz)	21	20.99
Rejection frequencies (lower/upper) (GHz)	20.72 / 21.24	20.77 / 21.22
-3 dB bandwidth (MHz)	300	280
-3 dB bandwidth (%)	1.43	1.34
Unloaded *Q*-factor	1737	1613

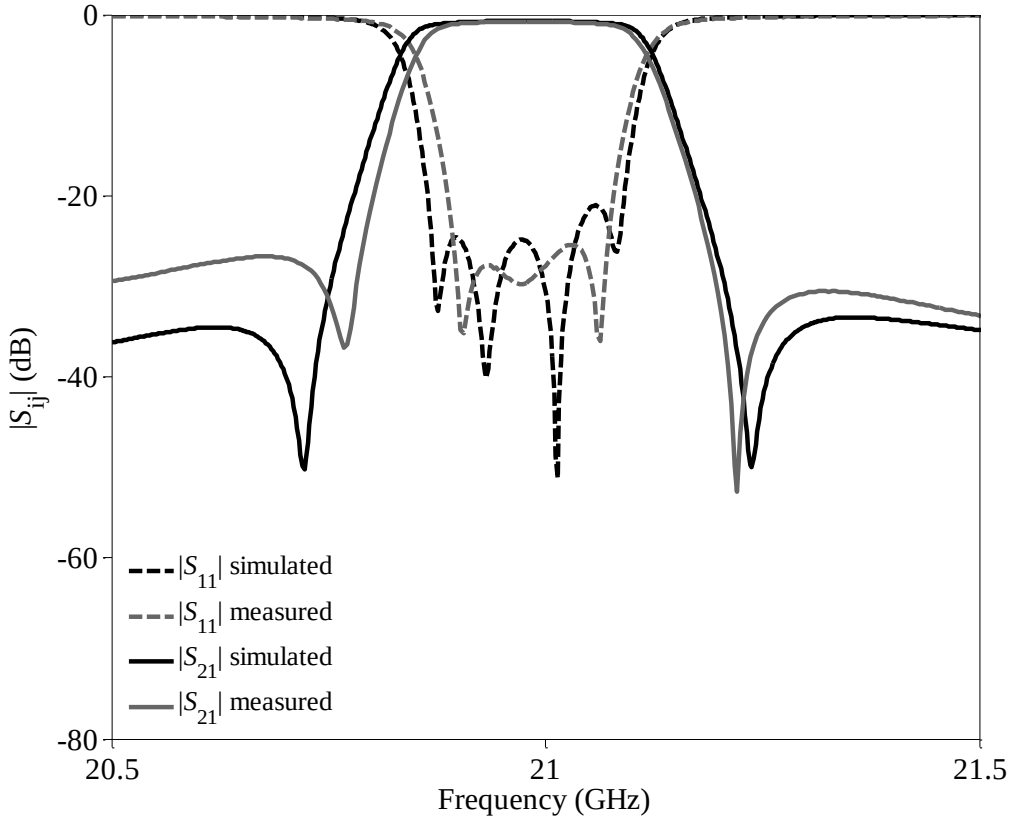

Fig. 4.19. Simulated and measured S-parameters of the fabricated quasi-elliptic AFSIW filter demonstrator.

4. 2. 6. Drawbacks of the In-Line Configuration

As previously explained, the implemented cross-coupling is not purely inductive or capacitive. Indeed, the total phase contribution consists of the nature of the cross-coupling plus the SIW transmission line electrical length. This will cause the signal to be periodically out of phase or in phase depending on the frequency. This causes periodical resonance peak all along the propagation frequency range.

Those spurious resonances degrade the wideband response of the filter. Fig. 4.20 represents the wideband response of the two fabricated prototypes. It can be observed that spurious resonances are located below and above the passband, preventing the filter to have a high-wideband isolation. The frequency shift of the resonance peaks is due to a fabrication process error. The inductive iris allowing the implementation of the secondary path was etched on the top and bottom copper layers of substrate 1, instead of only the top copper layer. Thus, an electromagnetic shield was implemented manually to prevent the signal from leaking.

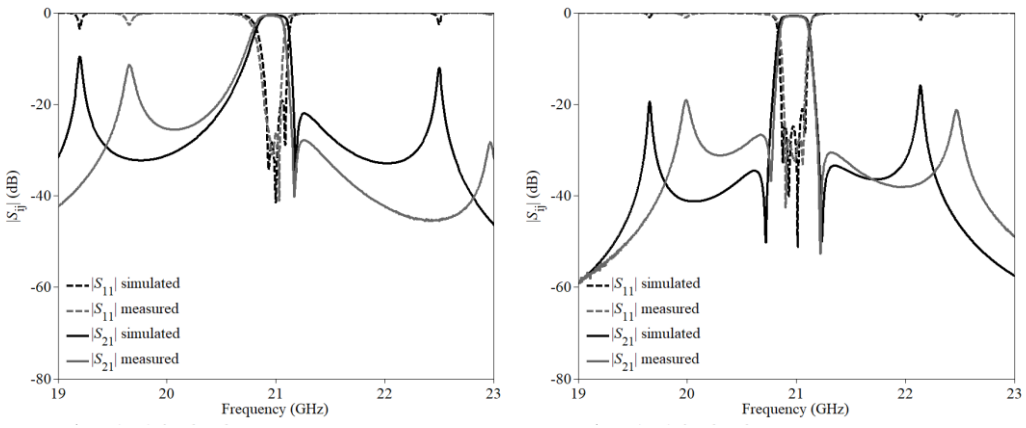

(*a*) (*b*)

Fig. 4.20. Simulated and measured S-parameters of (*a*) the third-order 1-3 cross-coupled and (*b*) the fourth-order 1-4 cross-coupled in-line configuration filters.

4. 3. Quasi-Elliptic Fourth-Order Folded Configuration AFSIW Filter

In this Section, taking into consideration the different drawbacks of the in-line arrow configuration, a quasi-elliptic fourth-order filter with a folded configuration is presented. The folded configuration allows minimizing the electrical length of the cross-coupling, hence minimizing the periodicity of its resonance.

4. 3. 1. Filter Topology

The coupling diagram of the folded structure is shown in Fig. 4.21(*a*). The coupling diagram using the AFSIW technology is given in Fig. 4.21(*b*). The study on the phase relationships is the same as the one presented in Section 4. 2 (i.e., primary path 1-2-3-4 and secondary path 1-4).

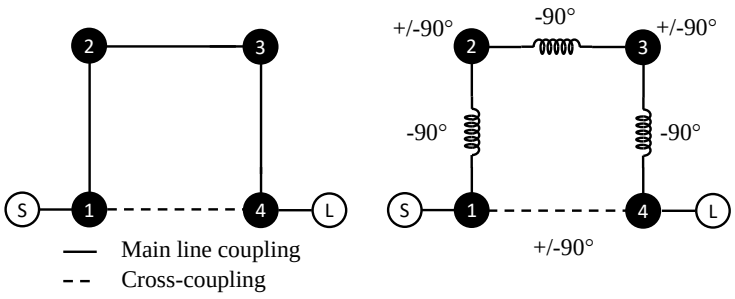

(*a*) (*b*)

Fig. 4.21. Coupling diagram of (*a*) the conventional fourth-order filter and (*b*) the fourth-order 1-4 cross-coupled filter, both with folded topologies.

4. 3. 2. Cross-Coupling Implementation Using AFSIW

Similarly, to the previous Sections, the cross-coupling between the non-adjacent resonators 1 and 4 is implemented using the bottom substrate of the multilayer structure. The 3D view of the proposed structure is shown in Fig. 4.22.

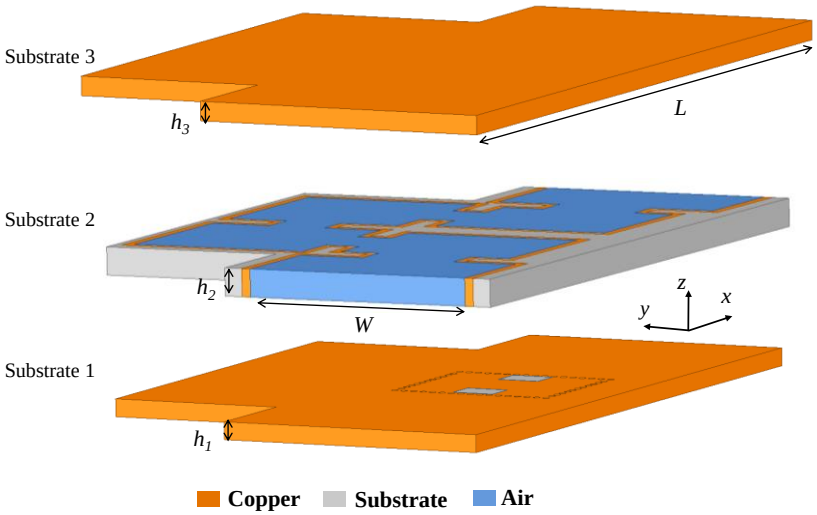

Fig. 4.22. 3D view of quasi-elliptic fourth-order folded AFSIW filter.

Fig. 4.23 shows the proposed quasi-elliptic fourth-order folded AFSIW filter coupling diagram implementation. The primary path is generated by resonator 1-2-3-4. The secondary path is implemented using a SIW transmission line coupling non-adjacent resonators 1 and 4. The folded configuration of the filter allows minimizing the length and thus electrical length of the SIW transmission line. Indeed, the folded configuration enables resonators 1 and 4 to be closer (1 coupling) than the in-line arrow configuration (3 couplings and 2 resonators).

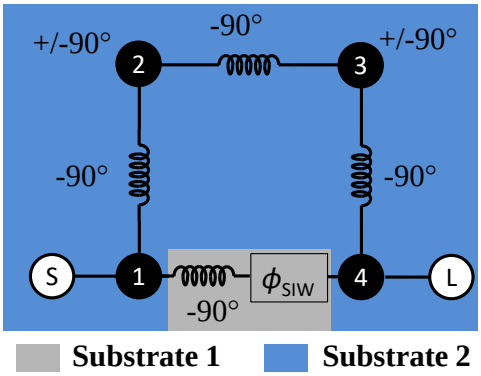

Fig. 4.23. Coupling diagram of the quasi-elliptic fourth-order filter implemented in AFSIW technology using a SIW transmission line.

TABLE 4.10
TOTAL PHASE SHIFTS OF QUASI-ELLIPTIC FOLDED AFSIW FILTER FOR BOTH PATHS USING SIW TRANSMISSION LINE

Total phase shift	Below resonance	Above resonance
Path 1-2-3	-90°+90°-90°+90°-90° = -90°°	-90°-90°-90 -90°-90°= -450°
Path 1-4	-90°+ϕ_{SIW}	-90°+ϕ_{SIW}
Result with $\phi_{SIW} = 360°$	In phase	In phase
Result with $\phi_{SIW} = 180°$	Out of phase (creation of Tz)	Out of phase (creation of Tz)

Table 4.10 shows that to obtain a quasi-elliptic function, it is necessary to implement a SIW transmission line with an electrical length ϕ_{SIW} equal to 180°. Hence, the equivalent overall nature of the cross-coupling is capacitive and transmission zeros below and above the passband of the filter are created.

4. 3. 3. Filter Design

To demonstrate the proposed quasi-elliptic folded principle, a filter with the same specifications as the one presented in Section 4. 2 is designed. The geometry of the filter is shown in Fig. 4.24. The correct phase of the SIW transmission line is controlled by the physical dimensions W_6 and L_5. The position of the transmission zeros can be controlled by playing with the inductive coupling between resonators 1 and 4. The dimensions of the designed filter are given in Table 4.11.

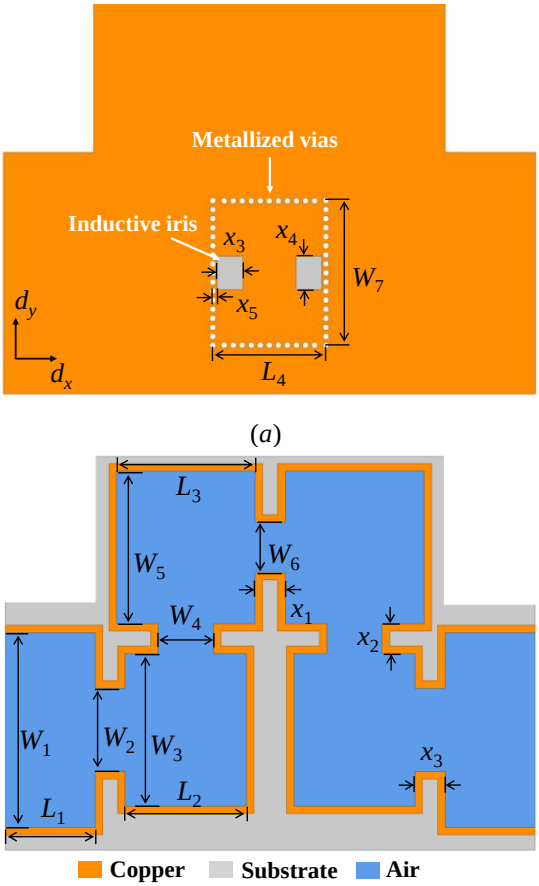

Fig. 4.24. Top views of (*a*) substrate 1, implementing the secondary path with the 1-4 cross-coupling, and (*b*) substrate 2 implementing the primary path of the quasi-elliptic folded filter.

TABLE 4.11
DIMENSIONS OF THE DESIGNED QUASI-ELLIPTIC FOLDED AFSIW FILTER

Dimension	$i = 1$	$i = 2$	$i = 3$	$i = 4$	$i = 5$	$i = 6$
L_i (mm)	6	8.042	9.202	6.9	/	/
x_i (mm)	2	2	2	1.7	2.2	/
W_i (mm)	13	5.547	10.16	3.684	10.16	3.33

4. 3. 4. Robustness Against PCB Manufacturing Tolerances

Studies similar to the ones described in Section 4. 1 are carried out to determine the yield of the proposed structure. The same conclusions concerning the PCB manufacturing tolerances, substrate dielectric constant uncertainty, and substrate to substrate misalignment can be made. Those studies prove the high interest of the proposed structure to implement high performance, compact, and high selectivity AFSIW filters.

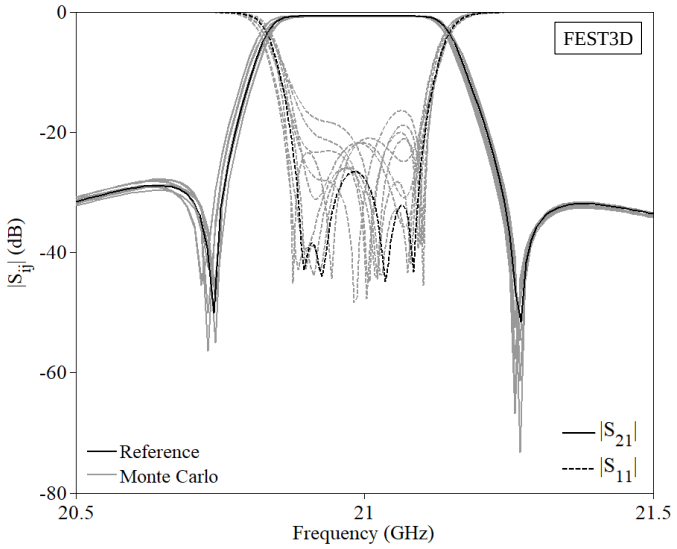

(*a*)

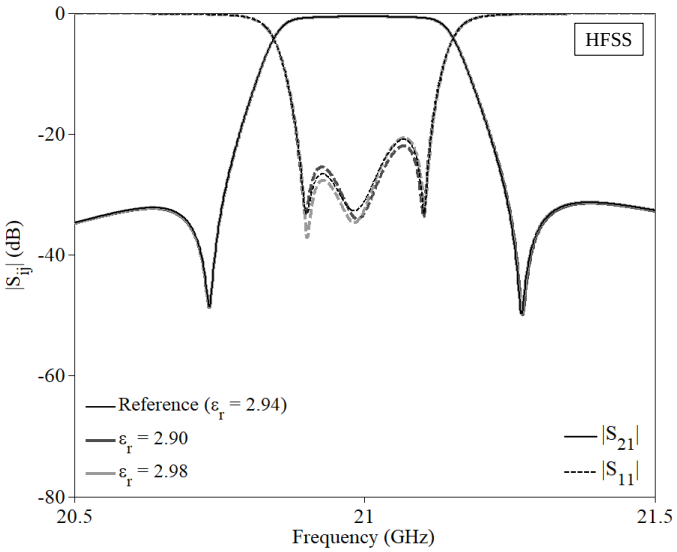

(*b*)

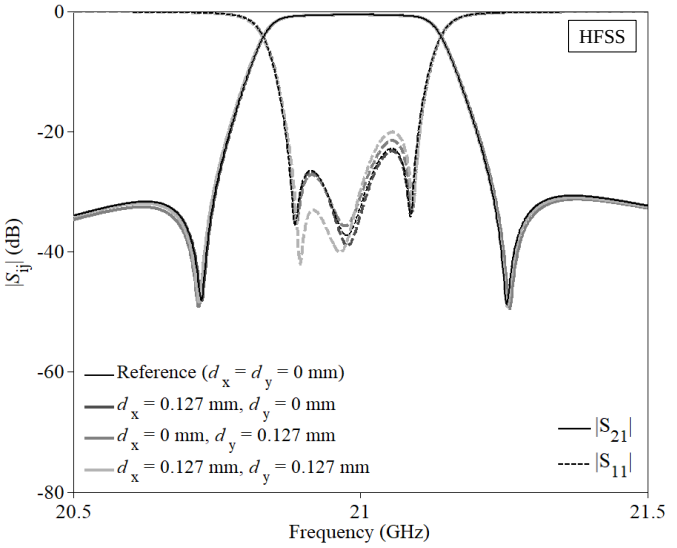

(*c*)

Fig. 4.25. Robustness analysis against (*a*) milling and drilling tolerances based on a Monte Carlo analysis using FEST3D, (*b*) dielectric constant variation using HFSS and (*c*) multilayer misalignment using HFSS.

4. 3. 5. Experimental Results

For demonstration purpose, a quasi-elliptic fourth-order with 1-4 cross-coupling AFSIW filter, using folded configuration, has been designed and fabricated. The arrays of metallized via have the same dimensions as the ones detailed previously. A photograph of the fabricated filter is shown in Fig. 4.26.

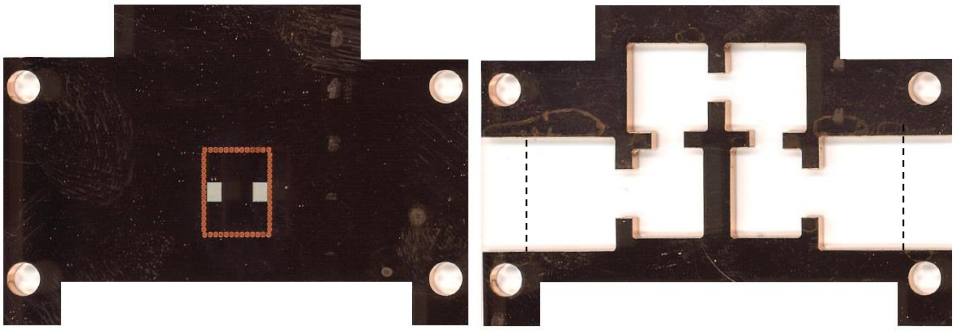

(*a*) (*b*)

Fig. 4.26. Photographs of (*a*) substrate 1 and (*b*) substrate 2 of the fabricated quasi-elliptic fourth-order folded AFSIW filter demonstrator. The dimensions of the fabricated filter are 54.2 x 37.3 x 2.54 mm^3.

The measurement flow is the same as the one described in Section 4. 1. Comparison between simulation and measurement is shown in Fig. 4.27. The measured centre frequency is 20.9 GHz. The measured -3 dB bandwidth of the filter is 360 MHz, presenting an increase of 10 MHz compared to the simulation. The transmission zeros frequencies are located at 20.63 GHz and 21.25 GHz, very similar to the simulated locations. The return loss of the filter remains greater than 18 dB in the passband. The measured in-band insertion loss is 0.7 dB, similar to the 0.6 dB obtained in simulations with a measured *Q*-factor of 1478. As it is demonstrated in Fig. 4.28, the wideband response of the filter is clean of spurious peaks until 23 GHz. A comparison between simulated and measured results is given in Table 4.12. A comparison to quasi-elliptic filters based on planar technologies is given in Table 4.13.

TABLE 4.12
COMPARISON OF SIMULATED AND MEASURED RESULTS OF THE QUASI-ELLIPTIC FOLDED AFSIW FILTER

Characteristics	Simulated (HFSS)	Measured
Return loss (dB)	> 22	> 21
Insertion loss (dB)	0.6	0.7
Center frequency (GHz)	20.9	20.89
Rejection frequencies (lower/upper) (GHz)	20.64 / 21.25	20.63 / 21.25
-3 dB bandwidth (MHz)	350	360
-3 dB bandwidth (%)	1.66	1.71
Unloaded *Q*-factor	1745	1478

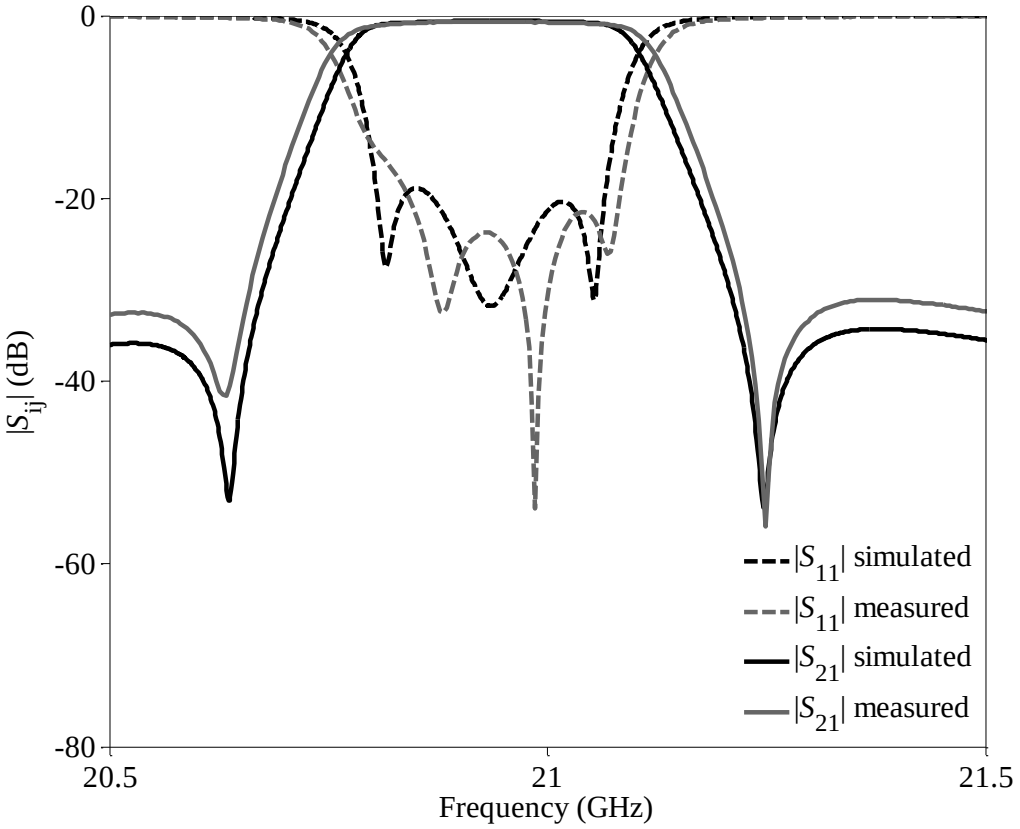

Fig. 4.27. In-band simulated and measured S-parameters of the fabricated quasi-elliptic folded AFSIW filter demonstrator.

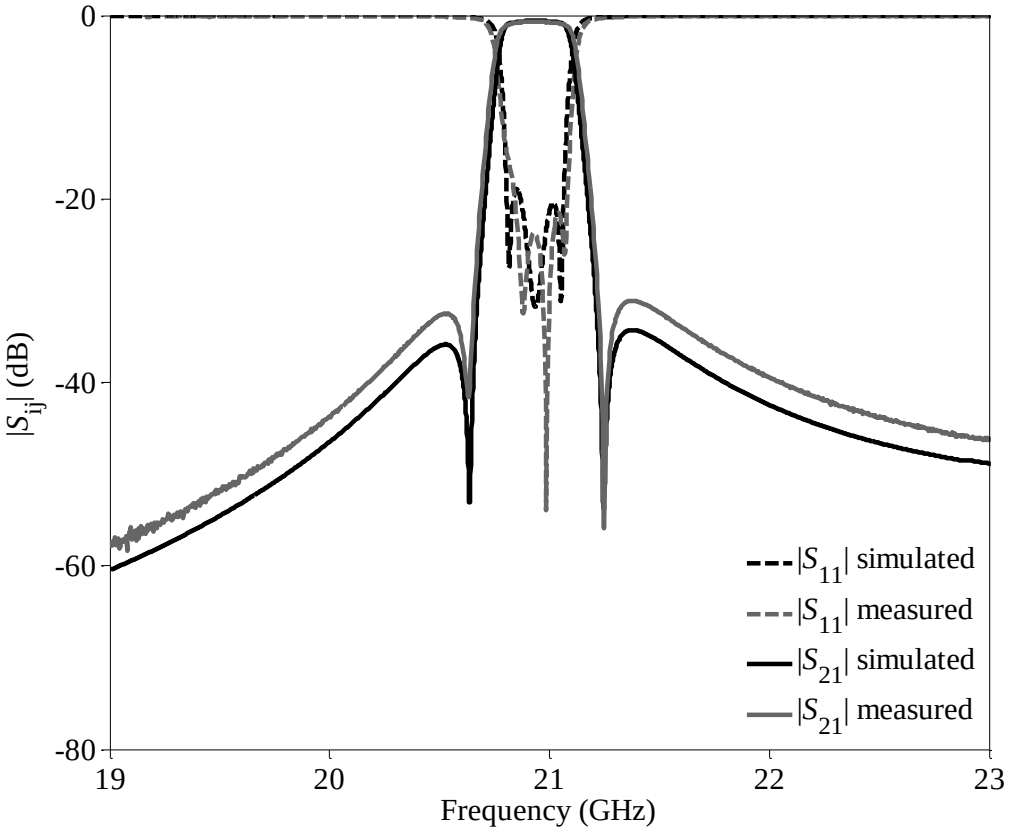

Fig. 4.28. Wideband simulated and measured S-parameters of the fabricated quasi-elliptic folded AFSIW filter demonstrator.

TABLE 4.13
COMPARISON WITH SUBSTRATE INTEGRATED QUASI-ELLIPTIC FILTERS

Specifications	[11]	[12]	[13]	**Proposed filter**
Process	PCB	PCB	PCB	**PCB**
Technology	Combline SIW	SIW	SIW	**AFSIW**
PCB substrate material	Rogers TMM4	Rogers 5880	Taconic TLY-5	**Rogers 6002**
Filter order	4th	4th	4th	**4th**
Total height (mm)	3.175	0.508	0.508	**2.54**
Area (mm²)	450	350	100	**1560**
Center frequency (GHz)	5.68	20.5	27	**20.99**
-3 dB bandwidth (%)	1.8	3.41	7.41	**1.71**
Insertion loss (dB)	3.6	0.9	2.1	**0.71**
Rejection frequencies (GHz)	5.56 / 5.8	19.6 / 21.4	25.6 / 28.4	**20.63 / 21.25**
Unloaded *Q*-factor	225	520	116	**1478**

4. 4. Higher Order Filter

In order to extend the principle of cross-couplings, a potential implementation, benefiting from the high *Q*-factor, compactness, and self-packaging characteristic of AFSIW, is studied. The application requires a set of realistic specifications, leading to the design of a seventh-order AFSIW bandpass filter operating in the satcom uplink Ku-band. The filter implements the proposed cross-coupling principle.

4. 4. 1. Filter Specifications

In most of the emerging telecommunication applications, highly compact and easily integrated microwave filter is highly desired. The foreseen application, using the cross-coupling principle, is the implementation of an IMUX operating in the Ku-band. The cross-coupling allows the introduction of transmission zeros below and above the passband of a filter which greatly increases the isolation of the different channels. It also allows the reduction of the guard bands, hence leading to an optimized utilization of the frequency spectrum. For the implementation of an IMUX, the channel filters must have very strong near rejection, flat insertion loss and group delay responses, high *Q*-factor, be compact and self-packaged.

Therefore, a specification of a channel filter operating in the Ku-band is studied. The filter requirements are very stringent on the near rejection and insertion loss variation. It is highly desired to minimize the insertion loss. Finally, the filter must be compact compared to the presently used technologies.

The frequency mask of the channel filter of the Ku-band is given in Fig. 4.29. A detailed list of the required specifications is given in Table 4.14.

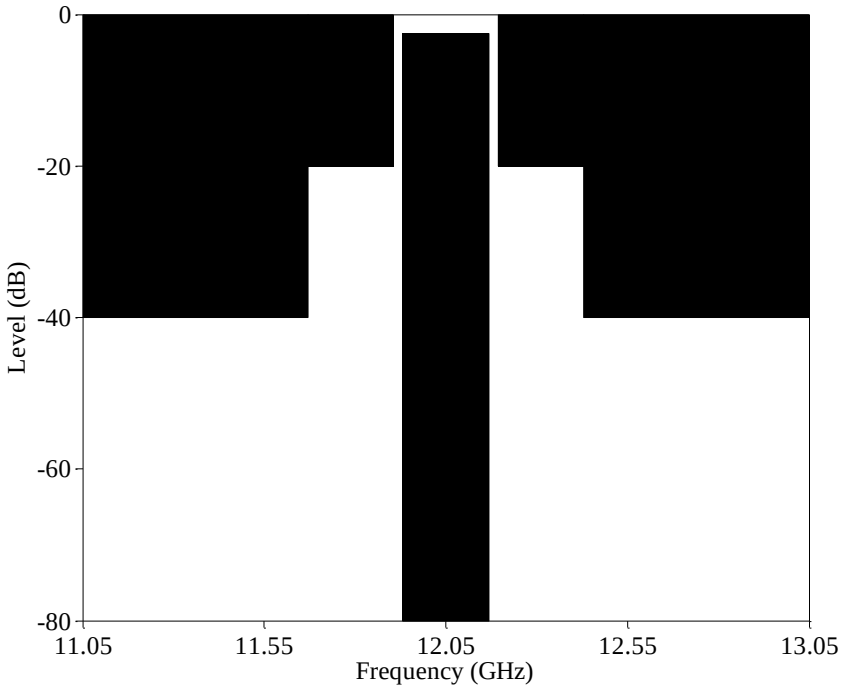

Fig. 4.29. Frequency mask of the Ku-band filter.

TABLE 4.14
SPECIFICATION OF THE REQUIRED KU-BAND FILTER

Specification		
Return loss (dB)	> 20	
Insertion loss (dB)	< 3	
Center frequency (GHz)	12.05	
Near rejection	$f_0 \pm 144$ MHz	20 dB
	$f_0 \pm 380$ MHz	40 dB
	$f_0 \pm 430$ MHz	40 dB
Insertion loss variation	$f_0 \pm 60$ MHz	0.3 dBpp
	$f_0 \pm 100$ MHz	0.5 dBpp
	$f_0 \pm 118$ MHz	1.1 dBpp
Group delay variation	$f_0 \pm 60$ MHz	3 nspp
	$f_0 \pm 100$ MHz	6 nspp
	$f_0 \pm 118$ MHz	20 nspp
-3 dB bandwidth (MHz)	260	

4. 4. 2. Filter Design

In order to be compliant with the near-rejection specifications and size limitations, the proposed solution for satisfying the requirements is a seventh-order filter with two transmission zeros located below and above the passband. This solution is a trade-off between size and performance to ensure a good rejection level with low insertion loss. To achieve the transmission zeros, the proposed principle detailed in the previous Section is used. Taking into considerations the previous Sections, the filter topology is implemented in an in-line folded configuration in order to minimize the length of the SIW transmission lines. The filter topology is given in Fig. 4.30. The filter is designed, without the cross-couplings, to operate at 12.05 GHz with a -3 dB bandwidth equal to 260 MHz (2.16%). Then the cross-couplings between resonators 1 and 4, and resonators 3 and 6, are implemented with a weak level using a SIW transmission line and an etched inductive iris as described in previous Sections. The correct phase of the transmission line is obtained with the width and length of the

transmission line. Finally, depending on the required specifications, the coupling between resonators 1 and 4, and resonators 3 and 6 is adjusted with the etched inductive iris. The filter is based on a multilayer PCB consisting of two Rogers RT/Duroid 6002 substrate with thickness $h_1 = h_3 = 0.508$ mm and a Rogers RT/Duroid 6010 with $h_2 = 1.905$ mm. The geometric configuration of the structure is shown in Fig. 4.31. All the dimensions are reported in Table 4.15. The group delay variation specifications are not too severe and thus do not need to be flattened using imaginary transmission zeros.

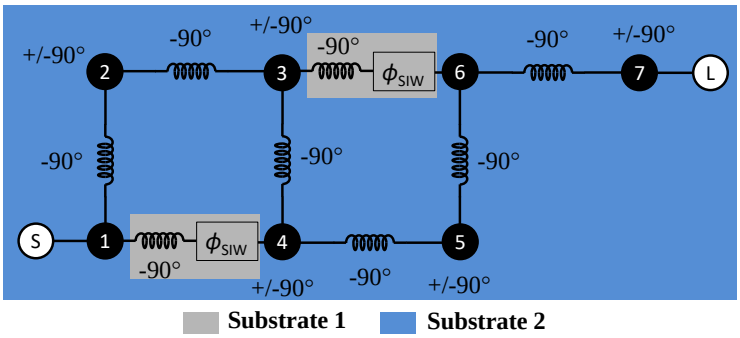

Fig. 4.30. Coupling diagram of the quasi-elliptic seventh-order filter implemented in AFSIW technology using two SIW transmission lines.

The quasi-elliptic response is implemented using two cross-couplings, between resonators 1 and 4, and resonators 3 and 6 as illustrated in Fig. 4.31. The minimal path rule allows the seventh-order filter to implement a maximum of 2 transmission zeros. It is worthy to note that two cross-couplings were implemented in our case, but it is also possible to introduce a single cross-coupling (with a stronger coupling) to achieve the same response. The transmission zeros can be controlled, with the etched coupling window, to achieve the desired near rejection levels and thus reach the desired near rejection level.

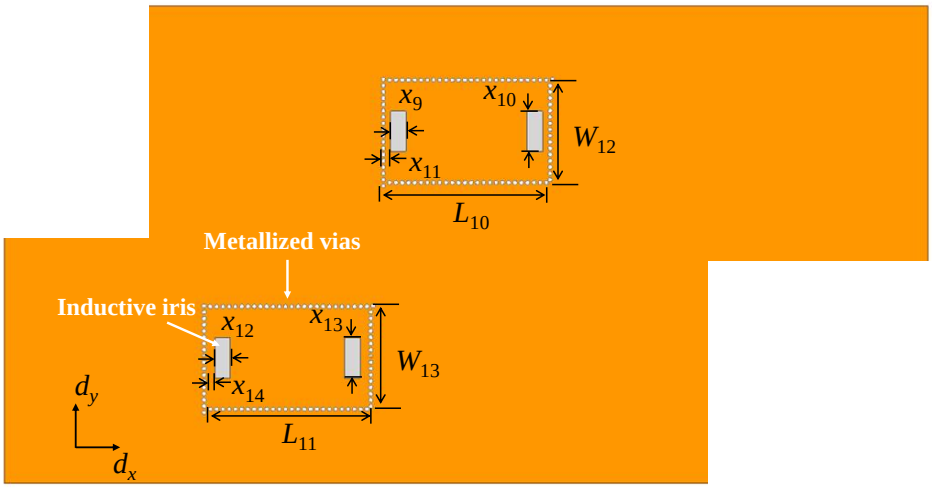

(*a*)

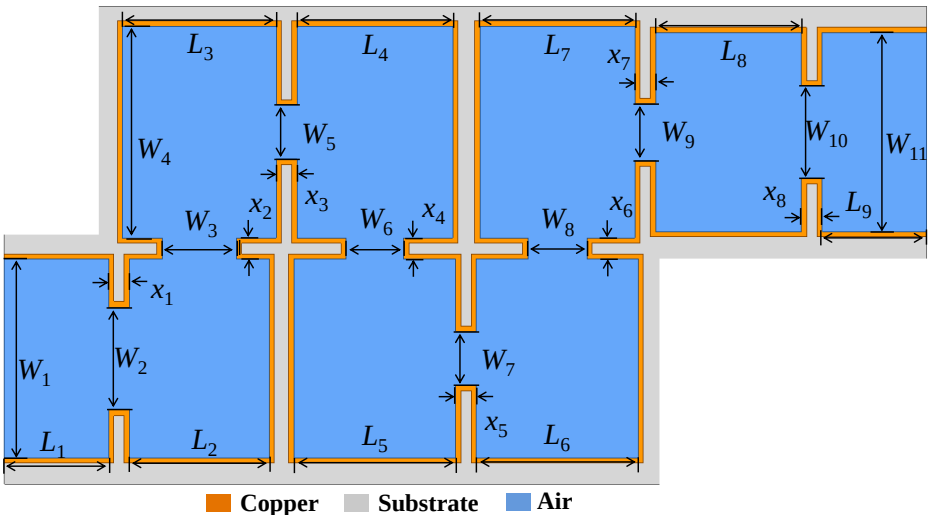

(*b*)

Fig. 4.31. Top views of (*a*) substrate 1, implementing the secondary path with the 1-4 and 3-6 cross-couplings, and (*b*) substrate 2 implementing the primary path of the quasi-elliptic folded filter.

TABLE 4.15
DIMENSIONS OF THE DESIGNED KU-BAND SEVENTH-ORDER AFSIW FILTER

Dimension	$i = 1$	$i = 2$	$i = 3$	$i = 4$	$i = 5$	$i = 6$	$i = 7$	$i = 8$	$i = 9$	$i = 10$	$i = 11$	$i = 12$	$i = 13$	$i = 14$
L_i (mm)	10	13.985	14.838	15.496	15.486	14.921	14.726	13.39	10	15.953	15.953	/	/	/
x_i (mm)	2	2	2	2	2	2	2	2	1.5	3.813	1.02	1.5	3.813	1.02
W_i (mm)	19.05	8.898	5.469	20.3	5.652	5.177	5.51	5.51	7.103	9.782	19.05	9.82	9.82	5.652

4. 4. 3. Experimental Results

For demonstration purpose, a quasi-elliptic seventh-order with 1-4 and 3-6 cross-couplings AFSIW filter, using an in-line folded configuration, has been designed and fabricated. The arrays of metallized via have the same dimensions as in previous Sections. A photograph of the fabricated filter is given in Fig. 4.32.

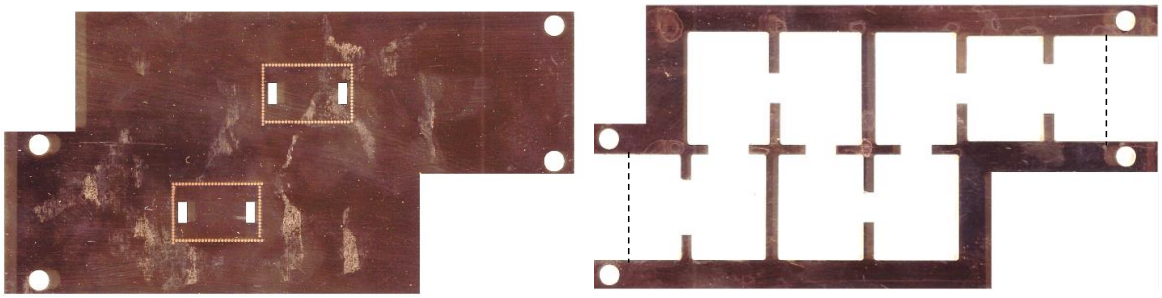

(*a*) (*b*)

Fig. 4.32. Photographs of (*a*) substrate 2 and (*b*) substrate 1 of the fabricated Ku-band AFSIW filter. The dimensions of the fabricated filter are 107.3 x 52.4 x 5.95 mm^3.

A vector network analyzer and a test fixture with a thru-reflect-line (TRL), operating at the Ku-band, calibration kit to de-embed the effects of connectors and transition have been used. The simulated and measured S-parameters are shown in Fig. 4.33. It can be observed that the response has a frequency shift equal to 48 MHz (0.4%). The measured -3 dB bandwidth is 253 MHz similar to the 260 MHz in the simulation. The measured rejection levels are in good agreement with the simulations but the frequency shift. The measured in-band

insertion loss is 0.78 dB which is slightly higher than the 0.76 dB obtained in the simulation. The measured *Q*-factor is equal to 1945. The measured results are given in Table 4.16.

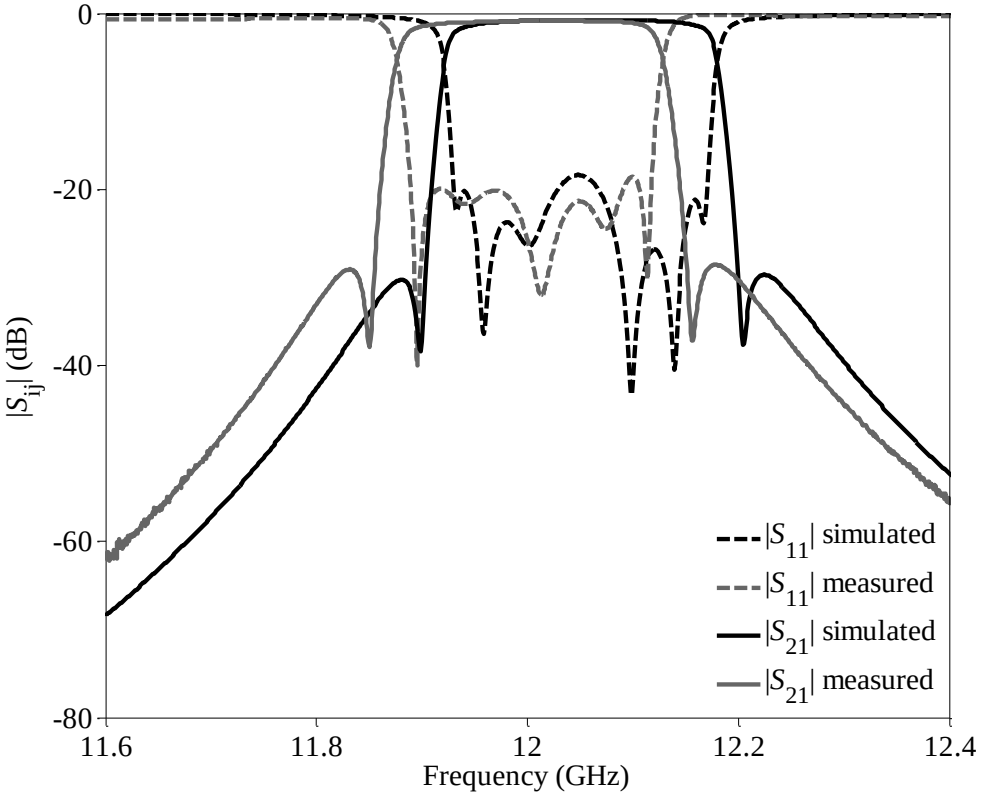

Fig. 4.33. Simulated and measured S-parameters of the fabricated seventh-order AFSIW filter demonstrator.

TABLE 4.16
COMPARISON OF SIMULATED AND MEASURED RESULTS OF KU-BAND SEVENTH-ORDER QUASI-ELLIPTIC FOLDED AFSIW FILTER

Characteristics	Simulated (HFSS)	Measured
Return loss (dB)	> 22	> 20
Insertion loss (dB)	0.72	0.76
Center frequency (GHz)	12.05	12.0
Rejection frequencies (lower/upper) (GHz)	11.9 / 12.21	11.85 / 12.16
-3 dB bandwidth (MHz)	260	253
-3 dB bandwidth (%)	2.16	2.1
Unloaded *Q*-factor	1957	1945

For comparison purposes, the measured results of the seventh-order filter were shifted in frequency to be able to compare the measured results with the required specifications. Thus, Fig. 4.34 shows the measured results of the filter shifted by 50 MHz. The rejection mask is represented in Fig. 4.34. It can be observed that the filter is compliant with the required near rejection specifications. The measured return loss remains greater than 20 dB, which was also a required specification. The measured insertion loss is 0.78 dB, which is compliant with the required 3 dB.

For the insertion loss variation, the first required specification of 0.3 dBpp (peak to peak) ± 60 MHz from the central frequency is compliant, so is the second and third specification of 0.5 dBpp ± 100 MHz, and

1.1 dBpp ± 118 MHz from f_0. The measured results are compared to the simulations and specifications mask in Fig. 4.35.

Concerning the group delay variation, Fig. 4.36 shows the comparison between simulation and measurement of the group delay. The three specifications of 3 ns ± 60 MHz, 6 ns ± 100 MHz, and 20 ns ± 118 MHz are fulfilled.

The required specifications are listed in Table 4.17. The status of the filter (compliant or not compliant) is also listed in this table. It is demonstrated in this Section that all the required electrical specifications have been fulfilled for a high order filter using the proposed cross-coupling principle.

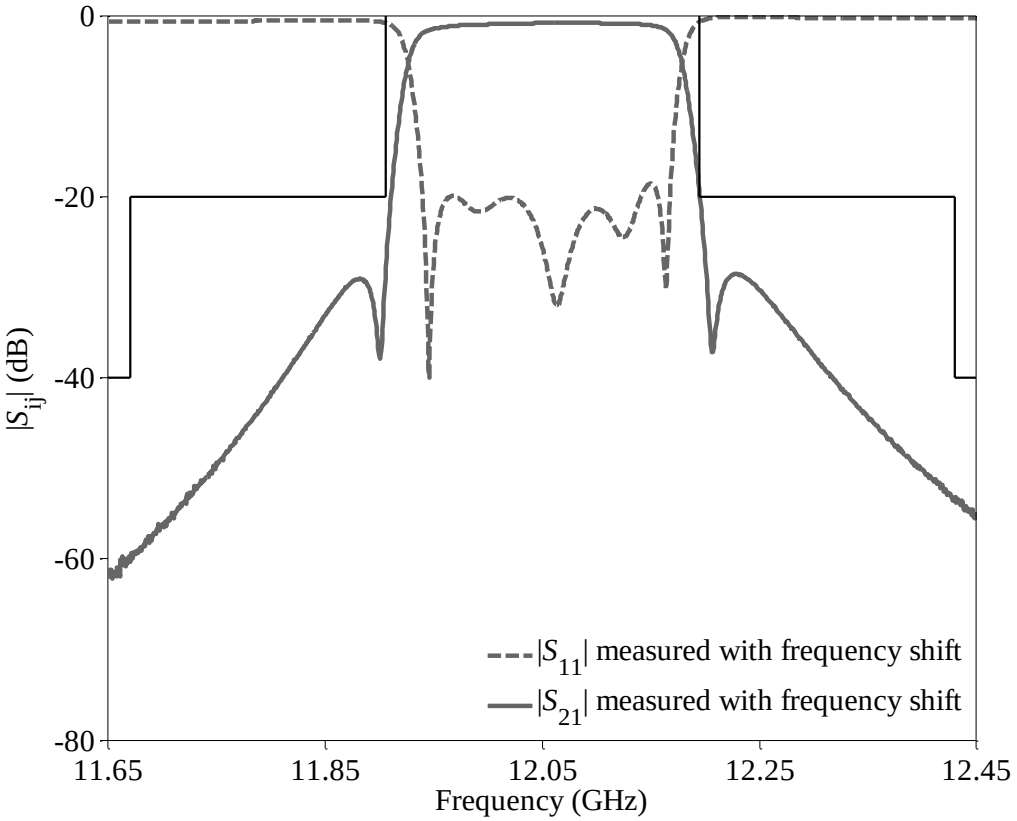

Fig. 4.34. Measured S-parameters, with the applied frequency shift (50 MHz), of the fabricated seventh-order AFSIW filter demonstrator with the specifications mask.

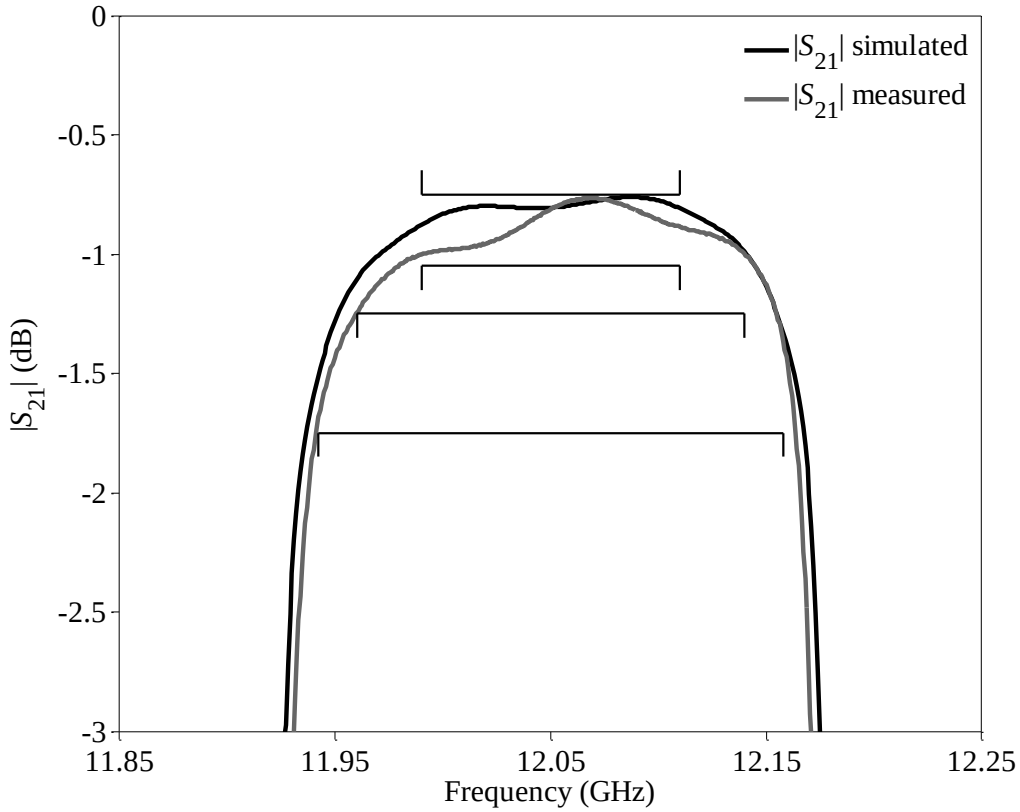

Fig. 4.35. Simulated and measured insertion loss variation, with the applied frequency shift (50 MHz), of the fabricated seventh-order AFSIW filter demonstrator with the specifications mask.

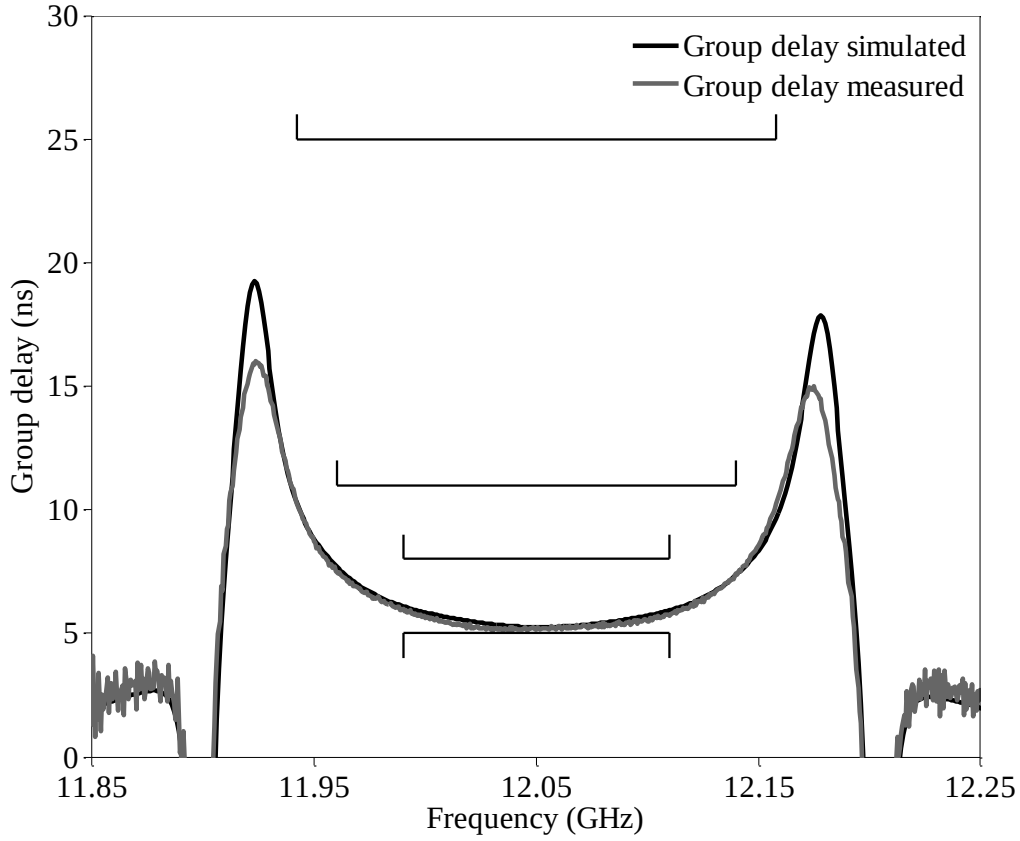

Fig. 4.36. Simulated and measured group delay variation, with the applied frequency shift (50 MHz), of the fabricated seventh-order AFSIW filter demonstrator with the specifications mask.

TABLE 4.17
SPECIFICATIONS OF THE MEASURED KU-BAND FILTER WITH 50 MHZ FREQUENCY SHIFT

Specification			Status
Return loss (dB)	> 20		Compliant
Insertion loss (dB)	< 3		Compliant
Center frequency (GHz)	12.05		Compliant
Near Rejection	$f_0 \pm 144$ MHz	20 dB	Compliant
	$f_0 \pm 380$ MHz	40 dB	Compliant
	$f_0 \pm 430$ MHz	40 dB	Compliant
Insertion loss variation	$f_0 \pm 60$ MHz	0.3 dBpp	Compliant
	$f_0 \pm 100$ MHz	0.5 dBpp	Compliant
	$f_0 \pm 118$ MHz	1.1 dBpp	Compliant
Group delay variation	$f_0 \pm 60$ MHz	3 nspp	Compliant
	$f_0 \pm 100$ MHz	6 nspp	Compliant
	$f_0 \pm 118$ MHz	20 nspp	Compliant
-3 dB bandwidth (MHz)	260		253

4. 5. Conclusions

In this Chapter, a novel technique to introduce transmission zeros in filters based on AFSIW technology is theoretically studied and demonstrated from simulations and measurements. The proposed technique takes advantage of the multilayer aspect of the technology to implement a secondary path into the bottom substrate. By playing with the phase of the different paths, a signal cancellation creating a transmission zero can be created. The proposed technique can be implemented in conventional filter configurations (in-line arrow, folded, in-line folded…). For demonstration purposes, the principle was implemented in the Ka-band on a third- and fourth-order in-line arrow configuration, and fourth-order folded configuration. The fabricated filters present good results compared to simulations. To further extend the work, the proposed principle was implemented on a higher order filter. The design was faced to real specifications for operation in the satcom uplink Ku-band. Hence, a seventh-order AFSIW filter with a double cross-coupling was fabricated. The filter shows very good results and is compliant with almost the full list of specifications. The proposed principle is foreseen to be implemented in an IMUX operating in the Ku-band. The transmission zeros allow a reduction of the guard band and increase the compactness of the device. To be able to operate in space conditions, it is necessary to study the impact of the external environment on the filter response. This problematic will be studied in the next Chapter.

References

[1] T. Martin, A. Ghiotto, T.P. Vuong, F. Lotz, and P. Monteil, "High performance air-filled substrate integrated waveguide filter post-process tuning using capacitive post," *IEEE MTT-S Int. Microw. Symp*., Hawaii, HI, Jun. 2017, pp. 196-199.

[2] T. Martin, A. Ghiotto, F. Lotz, and T.P. Vuong, "Fabrication-tolerant reconfigurable AFSIW filters based on through-hole mounted metallic posts for versatile high performance systems," *IEEE MTT-S Int. Microw. Symp*., Philadelphia, PA, Jun. 2018, pp. 319-322.

[3] T. Martin, A. Ghiotto, T.P. Vuong, and F. Lotz, "Fabrication-tolerant AFSIW filters based on quadruplet through-hole mounted inductive posts," *Eur. Microw. Conf. (EuMC)*, Madrid, 2018.

[4] T. Martin, A. Ghiotto, T.P. Vuong, and F. Lotz, "Configurable perforated air-filled substrate integrated waveguide (AFSIW) for generic high-performance systems on substrate," *IEEE Transactions on Microwave Theory and Techniques*, to be published.

[5] R. M. Kurzrok, "General three-resonator filters in waveguide," *IEEE Transactions on Microwave Theory and Techniques*, vol. 14, no. 1, pp. 46-47, Jan. 1966.

[6] J. B. Thomas, "Cross-coupling in coaxial cavity filters - a tutorial overview," *IEEE Transactions on Microwave Theory and Techniques*, vol. 51, no. 4, pp. 1368-1376, Apr. 2003.

[7] R. Levy, "Filters with single transmission zeros at real or imaginary frequencies," *IEEE Transactions on Microwave Theory and Techniques*, vol. 24, no. 4, pp. 172-181, Apr. 1976.

[8] J. D. Martínez, S. Sirci and V. E. Boria, "Compact SIW filter with asymmetric frequency response for C-band wireless applications," *IEEE International Wireless Symposium (IWS)*, Beijing, 2013, pp. 1-4.

[9] S. Deng, F. Xu and L. Yang, "A compact bandpass filter with transmission zero based on SIW triangular cavities," *IEEE International Conference on Ubiquitous Wireless Broadband (ICUWB)*, Nanjing, 2016, pp. 1-3.

[10] X. Chen and K. Wu, "Self-packaged millimeter-wave substrate integrated waveguide filter with asymmetric frequency response," *IEEE Transactions on Components, Packaging and Manufacturing Technology*, vol. 2, no. 5, pp. 775-782, May 2012.

[11] S. Sirci, F. Gentili, J. D. Martínez, V. E. Boria, and R. Sorrentino, "Quasi-elliptic filter based on SIW combline resonators using a coplanar line cross-coupling," *IEEE MTT-S Int. Microw. Symp*., Phoenix, AZ, 2015.

[12] X. Chen and K. Wu, "Substrate integrated waveguide cross-coupled filter with negative coupling structure," *IEEE Transactions on Microwave Theory and Techniques*, vol. 56, no. 1, pp. 142-149, Jan. 2008.

[13] K. Gong, W. Hong, Y. Zhang, P. Chen, and C. J. You, "Substrate integrated waveguide quasi-elliptic filters with controllable electric and magnetic mixed coupling," *IEEE Transactions on Microwave Theory and Techniques*, vol. 60, no. 10, pp. 3071-3078, Oct. 2012.

Chapter 5

Self-Temperature-Compensated AFSIW Cavities and Filters

This fifth Chapter is devoted to an overview of the developed technique to achieve a temperature compensation of AFSIW filters. The first technique is based on the use of dielectric slab on a sidewall of an AFSIW cavity. It can be implemented on any filter configuration (in-line arrow, in-line folded, folded …) as the slab is implemented on a single sidewall. The proposed technique is associated to the implementation of transmission zero (Tz) previously explained in Chapter 4 and is demonstrated in the Ku-band. The second technique consists of inserting two dielectric slabs on the opposite sidewalls of an AFSIW cavity and is demonstrated in the Ka-band. For demonstration purposes, the two techniques have been applied on two conventional temperature ranges -20 °C/+70 °C and -40 °C/+80 °C, respectively.

5. 1. Background

In most communication applications, the temperature drift is an essential aspect of the filter design, as the specified performances are expected to operate over a wide temperature range, usually from -40 °C to 80 °C. Air-filled metallic waveguides have been widely used in many microwave and millimeter-wave applications taking benefit of their very low insertion loss and high power-handling characteristics. To ensure thermal stability, a common technique is to consider sufficient error margin during the design phase to provide the filter specifications over the desired temperature range. Another technique is to fabricate the filter with materials having high thermal stability, in terms of physical dimensions and electrical characteristics, such as Invar (1.2 ppm/°C) [1], [2]. Nevertheless, this type of material is difficult to machine, expensive and substantially heavier than conventional materials. In some designs, composite materials are used instead of Invar because of their lightweight properties [3]. However, manufacturing issues make their implementation prohibitive. An alternative technique consists of choosing an appropriate material inserted in a resonator to minimize the frequency shift versus the temperature. In [4], [5], a bimetal topology is used to adjust resonant frequencies and achieve temperature compensation. Extensive work addressing the temperature compensation of resonators and filters using different technologies have been reported [6], [7]. However, all those technologies are not suitable for the foreseen mass market of the satellite constellations due to their prohibitive cost, high-weight, and large size.

In the proposed work, a dielectric material is inserted into an AFSIW resonator. The key point is to choose a material that has an opposite impact on the resonant frequency compared to dimension dilatations. This technique is of high interest has it is compliant with the standard manufacturing process of the PCB.

5. 2. Single Slab Self-Temperature-Compensated AFSIW Cavities and Filters

In the presented context, the use of the AFSIW technological platform seems to be of high interest for communication satellite applications. To fulfill the space requirements, a novel temperature compensation technique for AFSIW cavities, filters, multiplexers, and any AFSIW components based on resonant cavities is proposed and demonstrated. By choosing an appropriate material, the resonance frequency drift caused by the dimensional variations of the cavity can be compensated The proposed technique is implemented on an in-line folded filter configuration. Moreover, the temperature compensation of transmission zeros (Tzs), together with the thermal variation effects of the coupling is discussed. The proposed temperature compensation technique is demonstrated in the downlink Ku-band satellite communication frequency range for the need of the ESA (European Space Agency) and the CNES (Centre National d'Études Spatiales).

5. 2. 1 Theory of Single Slab Self-Temperature-Compensated AFSIW Cavities

In this Section, a multiphysics model based on the transmission line theory is developed to determine the resonance frequency of an AFSIW cavity loaded with a single dielectric slab taking into considerations the thermal effects on the dimensional expansions and relative permittivity of the materials. Then, this model is compared and validated with eigenmode simulation results.

5. 2. 1. 1 Single Slab Air-Filled SIW Cavity Equivalent Multiphysics Transmission Line Model

In this work, a theoretical analysis, based on a transmission line equivalent model, inspired from [8]-[10], is developed to study the resonance frequency of an AFSIW cavity loaded with a single dielectric slab. The multiphysics model is developed based on an equivalent transmission line model and allows the study of the thermal behavior of the resonance frequency of single slab AFSIW cavities considering the dimensional expansions and relative permittivity variation of the materials. This model is then used to synthesis single slab self-temperature-compensated AFSIW cavities. The transmission line theory is used to determine a characteristic equation between the fundamental TE_{101} mode resonant frequency, the single dielectric slab AFSIW cavity dimensions, and the electromagnetic properties of the materials.

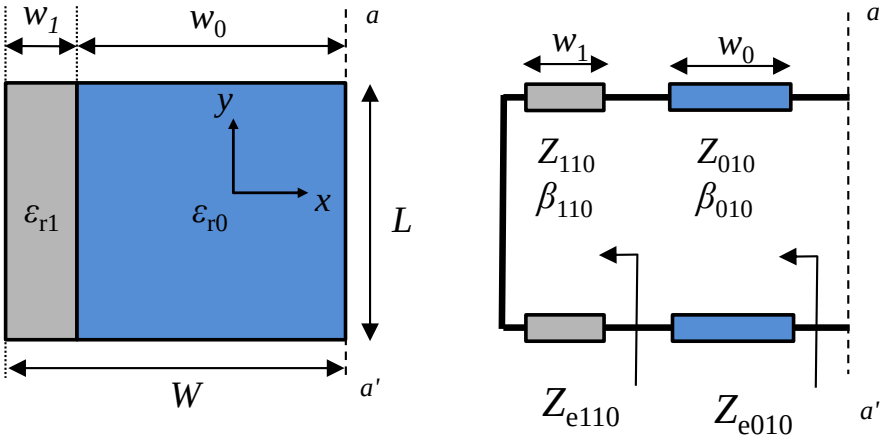

Fig. 5.1. Single slab AFSIW cavity (*a*) top view and (*b*) equivalent transmission line model.

A single slab AFSIW cavity of width W, length L, and height h_2 = 1.905 mm top view is shown in Fig. 5.1(*a*). The proposed cavity is composed of an air-filled region of relative permittivity $\varepsilon_{r0} = 1$ of width w_0 loaded with a single dielectric slab of relative permittivity ε_{r1} of width w_1. Fig. 5.1(*b*) represents the equivalent transmission line model. The (*aa*') plane represents a short circuit. All the given dimensions are considered at ambient temperature T_a = 23 °C. The air-filled region supports the dominant TE_{101} propagation mode and is represented with guide impedance Z_{010} and propagation constant β_{010}. The dielectric slab region is represented by the transmission line of length w_1. It also supports the dominant TE_{101} propagation mode and is represented with guide impedance Z_{110} and propagation constant β_{110}. Thus, the transmission lines of the model have guided impedances Z_{i10} and propagation constants β_{i10} at T_a which can be calculated using the following equations:

$$\beta_{i10} = \sqrt{\left(2\pi f\sqrt{\mu_0\varepsilon_0\,\varepsilon_{ri}}\right)^2 - \left(\frac{\pi}{L}\right)^2}, \tag{5.1}$$

and

$$Z_{i10} = \sqrt{\frac{\mu_0}{\varepsilon_0\varepsilon_{ri} - \left(\frac{1}{2Lf\sqrt{\mu_0}}\right)^2}}, \tag{5.2}$$

where f is the frequency, ε_0 is the vacuum permittivity and μ_0 is the vacuum permeability.

A variation of the temperature implies a dimensional expansion and a change of the electromagnetic properties of the materials. With a temperature change ΔT (compared to ambient temperature T_a), the dielectric slab permittivity, and the cavity dimensions, considering essentially linear variations, are given by:

$$w_i^{T+\Delta T} = (1+\delta_x\Delta T)w_i, \tag{5.3}$$

$$L^{T+\Delta T} = (1+\delta_y\Delta T)L\,, \tag{5.4}$$

and

$$\varepsilon_{r1}{}^{T+\Delta T} = (1+\delta_e \Delta T)\varepsilon_{r1}, \tag{5.5}$$

where the PCB substrate material coefficient of thermal expansion (CTE) in the *x* and *y* directions is represented by δ_x, and δ_y, respectively, and δ_e is the single dielectric slab material thermal coefficient of permittivity (TCP).

(5.5) suggests an interesting assessment, that is to say, a material with a negative TCP should provide a temperature compensation for AFSIW cavities; the dielectric slab material TCP providing an effect opposite to the substrate CTE on the cavity resonant frequency. Thus, to counteract the dimension expansions with a temperature change expressed by (5.3) and (5.4), the proposed compensation technique is based on the insertion of a single dielectric slab on one sidewall to be able to implement the proposed technique in any filter or multiplexer configuration. Hence, considering a temperature change of ΔT, (5.1) and (5.2) becomes:

$$\beta_{010}{}^{T+\Delta T} = \sqrt{\left(2\pi f^{T+\Delta T}\sqrt{\mu_0\varepsilon_0\varepsilon_{r0}}\right)^2 - \left(\frac{\pi}{(1+\delta_x\Delta T)L}\right)^2}, \tag{5.6}$$

$$\beta_{110}{}^{T+\Delta T} = \sqrt{\left(2\pi f^{T+\Delta T}\sqrt{\mu_0\varepsilon_0(1+\delta_e\Delta T)\varepsilon_{r1}}\right)^2 - \left(\frac{\pi}{(1+\delta_x\Delta T)L}\right)^2}, \tag{5.7}$$

$$Z_{010}{}^{T+\Delta T} = \sqrt{\frac{\mu_0}{\varepsilon_0\varepsilon_{r0} - \left(\frac{1}{2(1+\delta_x\Delta T)Lf^{T+\Delta T}\sqrt{\mu_0}}\right)^2}}, \tag{5.8}$$

and

$$Z_{110}{}^{T+\Delta T} = \sqrt{\frac{\mu_0}{\varepsilon_0(1+\delta_e\Delta T)\varepsilon_{r1} - \left(\frac{1}{2(1+\delta_x\Delta T)Lf^{T+\Delta T}\sqrt{\mu_0}}\right)^2}}. \tag{5.9}$$

Then, the $Z_{e110}{}^{T+\Delta T}$ equivalent impedance shown in Fig. 5.1(*b*) can be determined from transmission line theory:

$$Z_{e110}{}^{T+\Delta T} = jZ_{110}{}^{T+\Delta T}\tan(\beta_{110}{}^{T+\Delta T}w_1{}^{T+\Delta T}). \tag{5.10}$$

Thus, the equivalent impedance $Z_{e010}{}^{T+\Delta T}$ at the cavity short circuit plane (*aa*') is:

$$Z_{e010}{}^{T+\Delta T} = Z_{010}{}^{T+\Delta T}\frac{Z_{e110}{}^{T+\Delta T} + jZ_{010}{}^{T+\Delta T}\tan(\beta_{010}{}^{T+\Delta T}w_0{}^{T+\Delta T})}{Z_{010}{}^{T+\Delta T} + jZ_{e110}{}^{T+\Delta T}\tan(\beta_{010}{}^{T+\Delta T}w_0{}^{T+\Delta T})}. \tag{5.11}$$

For the TE_{101} mode, at the cavity resonance frequency $f = f_{TE101}{}^{T+\Delta T}$, the imaginary part of (5.11) is:

$$\mathrm{Im}(Z_{e010}{}^{T+\Delta T}) = 0. \tag{5.12}$$

Thus, the Newton-Raphson method, implemented in [8], can be used to determine the cavity resonance frequency $f_{TE101}{}^{T+\Delta T}$.

5. 2. 1. 2 Theoretical Analysis

The proposed theoretical model is applied with a single dielectric slab of RT/Duroid 6010LM substrate material with a relative permittivity of ε_{r1} = 10.2. In the -50°C to 170 °C temperature range, this material has a TCP of δ_e = -425 ppm/°C and CTE in *x* and *y* dimensions of $\delta_x = \delta_y$ = 24 ppm/°C.

Based on the previously presented theoretical transmission line model, the resonant frequency of the single slab loaded AFSIW cavity can be determined solving (5.12). Considering space application specifications, the theoretical resonance frequencies f_{Tc}, f_{Ta} and f_{Th} are calculated at T_c = -20 °C, T_a = 23 °C, and T_h = 70 °C, respectively. Fig. 5.2 shows the theoretical resonance frequencies of a single slab AFSIW cavity versus the dielectric slab width w_1, for a fixed L = 15.805 mm and W = 19.05 mm. Fig. 5.2 also illustrates the frequency shift Δf defined by:

$$\Delta f = 100 \left| 2 \frac{f_{T_c} - f_{T_h}}{f_{T_c} + f_{T_h}} \right| \tag{5.13}$$

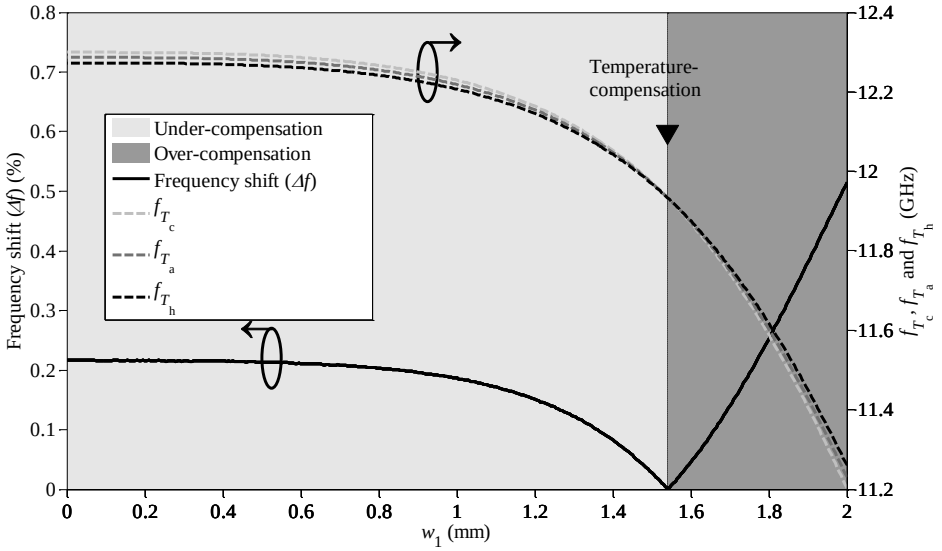

Fig. 5.2. Theoretical frequency shift of the single slab AFSIW cavity calculated in the -20 °C to 70 °C temperature range and theoretical single slab AFSIW cavity resonance frequency, with L = 15.805 mm, W = 19.05 mm at T_c = -20 C, T_a = 23 C and T_h = 70 C versus the dielectric slab width w_1.

In Fig. 5.2, it is theoretically demonstrated that for values of w_1 below 1.54 mm, Δf decreases with an increase of w_1. Thus, an under-compensation of the single slab AFSIW cavity is obtained. For values of w_1 above 1.54 mm, the frequency shift Δf increases with an increase of w_1. Hence, an overcompensation of the single slab AFSIW cavity is achieved. Finally, for a single dielectric slab of width w_1 = 1.54 mm, a perfect temperature compensation of the resonance frequency is obtained.

Fig. 5.3 represents the resonant frequency of the single slab AFSIW cavity at T_a with the frequency shift obtained in the -20 °C to 70 °C temperature range, versus the single dielectric slab width w_1 and the cavity length L, for a fixed cavity width W = 19.05 mm.

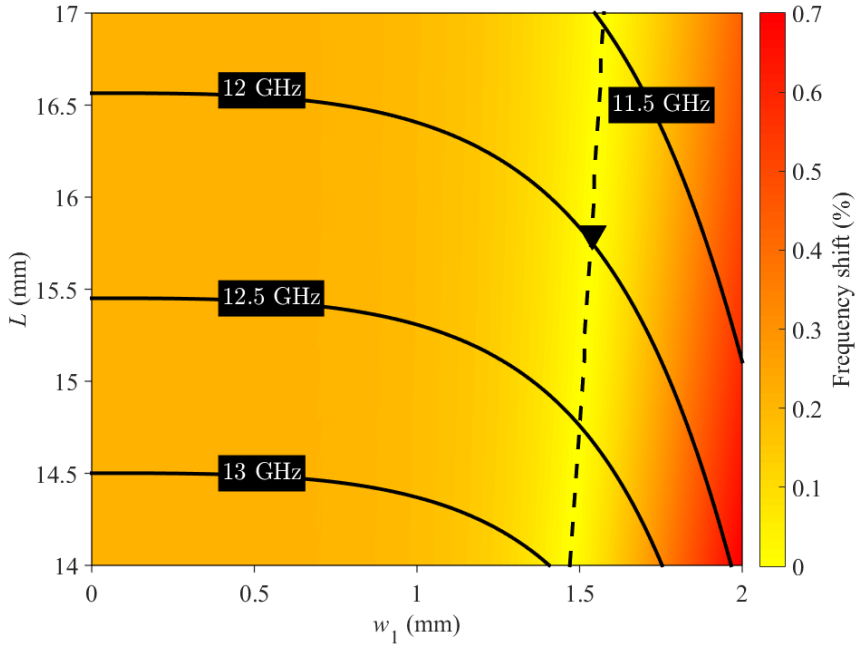

Fig. 5.3. Theoretical frequency shift of the single slab AFSIW cavity versus the single dielectric slab width w_1 and the cavity length L (with W = 19.05 mm). The black dotted line corresponds to the optimal thermal compensation. The black straight lines represent the isocurves of the resonance frequency at T_a of the single slab AFSIW cavity. Those theoretical results are obtained in the -20 °C to 70 °C temperature range.

It can be observed that the proposed temperature compensation technique allows controlling the resonance frequency of the single slab AFSIW cavity with L and w_1, simultaneously, while maintaining a perfect temperature compensation. For the particular application described in the introduction, the ▼ marker, represented in Fig. 5.2 and Fig. 5.3, corresponds to a single slab self-temperature-compensated AFSIW cavity resonating at 11.975 GHz, which dimensions are L = 15.805 mm, W = 19.05 mm and w_1 = 1.54 mm.

5. 2. 1. 3 Theoretical and Eigenmode Results Comparison

The proposed multiphysics equivalent model is used to determine the resonance frequency and the thermal stability of a single slab self-temperature-compensated AFSIW cavity and a temperature-uncompensated AFSIW cavity. The obtained results are compared with eigenmode simulations taking into account the dimensional expansion and relative permittivity of the materials at T_c = -20 °C, T_a = 23 °C, and T_h = 70 °C. The configurations of both cavities are illustrated in Fig. 5.4. The different dimensions and material properties, at T_a, are reported in Table 5.1.

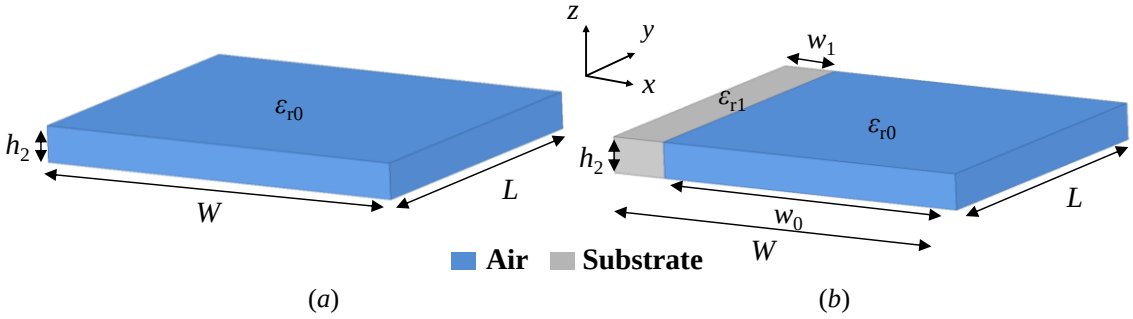

Fig. 5.4. Geometry of the (*a*) air cavity resonator and (*b*) single slab air-filled cavity resonator.

TABLE 5.1
DIMENSIONS AND MATERIAL PROPERTIES OF THE AIR AND SINGLE SLAB AIR-FILLED CAVITIES

	W (mm)	L (mm)	w_0 (mm)	w_1 (mm)	ε_{r0}	ε_{r1}
Air cavity	19.05	16.626	/	/	1	/
Single slab AFSIW cavity	19.05	15.805	17.51	1.54	1	10.2

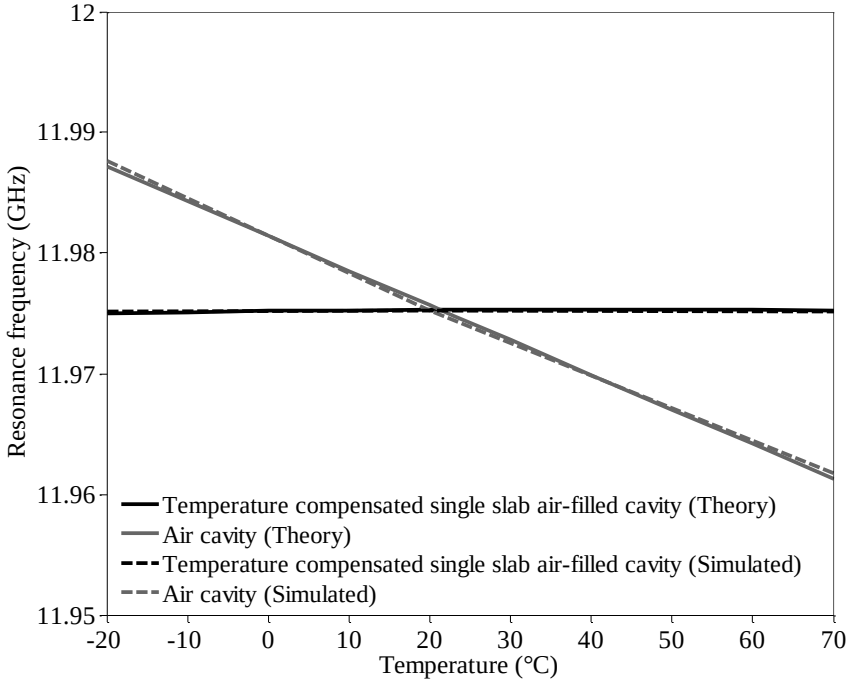

Fig. 5.5. Theoretical and simulated resonance frequencies of the air cavity and the self-temperature-compensated air-filled cavity versus temperature.

Fig. 5.5 shows the comparison of the resonance frequencies obtained theoretically with the equivalent model and from simulations using the ANSYS HFSS electromagnetic (EM) software eigenmode solver. It is demonstrated that a very good agreement between theory and simulation is obtained for both cavities over the -20 °C to 70 °C temperature range. The air cavity presents a theoretical frequency drift of 12.3 MHz at -20 °C and -13.5 MHz at 70 °C, compared to a simulated frequency drift of 12.4 MHz at -20 °C and -13.45 MHz at 70 °C. The single slab self-temperature-compensated AFSIW cavity has a theoretical frequency drift of -0.2 MHz at -20 °C and 0.1 MHz at 70 °C, compared to a simulated frequency drift of -0.1 MHz at -20 °C and 0 MHz at 70 °C. Therefore, the theoretical model is in very good agreement with the eigenmode simulations to evaluate the frequency drift due to the temperature variations. In terms of thermal stability, the air cavity exhibits a theoretical thermal stability of -23.8 ppm/°C at -20 °C and -23.9 ppm/°C at 70 °C. While the single slab self-temperature-compensated AFSIW cavity shows a theoretical frequency resonance stability of 0.4 ppm/°C at -20 °C and 0.2 ppm/°C at 70 °C.

5. 2. 1. 4 Metallized Via-Hole Single Slab Self-Temperature-Compensated AFSIW Cavity Equivalent Width

The multiphysics model previously developed is based on continuous electric sidewalls. However, the implementation of a single slab AFSIW cavity would require an additional step to insert and fix the

compensating dielectric material. Instead, to take maximum advantage of the PCB process and avoid any costly additional step, the inner substrate of the AFSIW multilayer stack, can consist in the compensating material (Rogers RT/Duroid 6010LM in our case). Then, using discontinuous electrical sidewalls based on metallized via holes, allows to simultaneously fabricate the cavity and the sidewall single slab.

The effective width W_{eff} of a dielectric-filled SIW cavity with metallized via holes of diameter d, center-to-center distance between two consecutive via p, and center-to-center distance between the two via rows W_{via} is given by [11]:

$$W_{\text{eff}}=W_{\text{via}}-\frac{d^2}{0.95p}. \tag{5.14}$$

This relation has been validated for the case of AFSIW in simulation, comparing dispersion characteristics. A single slab self-temperature-compensated AFSIW cavities can therefore be synthesized using the theoretical model described in Section 5. 2. 1. Then, its via rows center-to-center width W, can be determined using (5.14).

5. 2. 2 Single Slab Self-Temperature-Compensated Quasi-Elliptic AFSIW Filters

5. 2. 2. 1 Expansion of Inductive Iris and Coupling Drift

In this Section, the impact of the dimensional expansion of an inductive iris on its M coupling coefficient drift is investigated. It was demonstrated in [12] and later in [13], that for a given rectangular iris geometrical ratio b/a, the term M/a^3 is constant, where a and b are the width and length of the iris, respectively. Therefore, assuming a linear expansion of the material, the term M/a^3 remains constant versus the temperature variations (as b/a). Thus, as stated in [14], it is possible to study the coupling coefficient variation versus the temperature when considering a perfect temperature compensation for the resonators. The coupling coefficient $M^{T+\Delta T}$, considering a ΔT temperature variation, can be expressed as:

$$\frac{M^{T+\Delta\text{T}}}{(a^{T+\Delta\text{T}})^3}=\frac{M^{T+\Delta\text{T}}}{(a^T(1+\delta\Delta\text{T}))^3}=\frac{M^T}{(a^T)^3}, \tag{5.15}$$

where δ is the CTE of the iris material. The coupling coefficient drift is thus given by:

$$\frac{M^{T+\Delta\text{T}}}{M^T}=(1+\delta\Delta T)^3. \tag{5.16}$$

It can be noticed in (5.16), that the coupling coefficient drift is not dependent on the iris geometry.

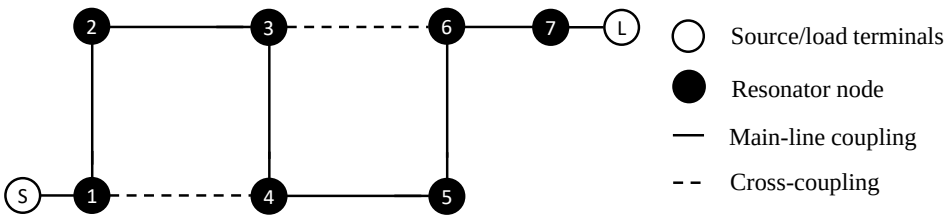

Fig. 5.6. Coupling and routing schematic.

$$M_1 = \begin{pmatrix} 0 & 1.045 & 0 & 0 & 0 & 0 & 0 & 0 & 0 \\ 1.045 & 0 & 0.855 & 0 & -0.11 & 0 & 0 & 0 & 0 \\ 0 & 0.8550 & 0 & 0.68 & 0 & 0 & 0 & 0 & 0 \\ 0 & 0 & 0 & 0 & 0.53 & 0 & -0.11 & 0 & 0 \\ 0 & -0.11 & 0.68 & 0.53 & 0 & 0.68 & 0 & 0 & 0 \\ 0 & 0 & 0 & 0 & 0.68 & 0 & 0.58 & 0 & 0 \\ 0 & 0 & 0 & -0.11 & 0 & 0.58 & 0 & 0.845 & 0 \\ 0 & 0 & 0 & 0 & 0 & 0 & 0.845 & 0 & 1.035 \\ 0 & 0 & 0 & 0 & 0 & 0 & 0 & 1.035 & 0 \end{pmatrix}$$

Fig. 5.7. Coupling matrix M_1 of the specified filter.

$$M_2 = \begin{pmatrix} 0 & 1.0486 & 0 & 0 & 0 & 0 & 0 & 0 & 0 \\ 1.0486 & 0 & 0.8579 & 0 & -0.1104 & 0 & 0 & 0 & 0 \\ 0 & 0.8579 & 0 & 0.6823 & 0 & 0 & 0 & 0 & 0 \\ 0 & 0 & 0 & 0 & 0.5318 & 0 & -0.1104 & 0 & 0 \\ 0 & -0.1104 & 0.6823 & 0.5318 & 0 & 0.6823 & 0 & 0 & 0 \\ 0 & 0 & 0 & 0 & 0.6823 & 0 & 0.582 & 0 & 0 \\ 0 & 0 & 0 & -0.1104 & 0 & 0.582 & 0 & 0.8479 & 0 \\ 0 & 0 & 0 & 0 & 0 & 0 & 0.8479 & 0 & 1.0385 \\ 0 & 0 & 0 & 0 & 0 & 0 & 0 & 1.0385 & 0 \end{pmatrix}$$

Fig. 5.13. Coupling matrix M_2 of the specified filter considering perfectly temperature-compensated cavities and coupling coefficient drift of 0.34%.

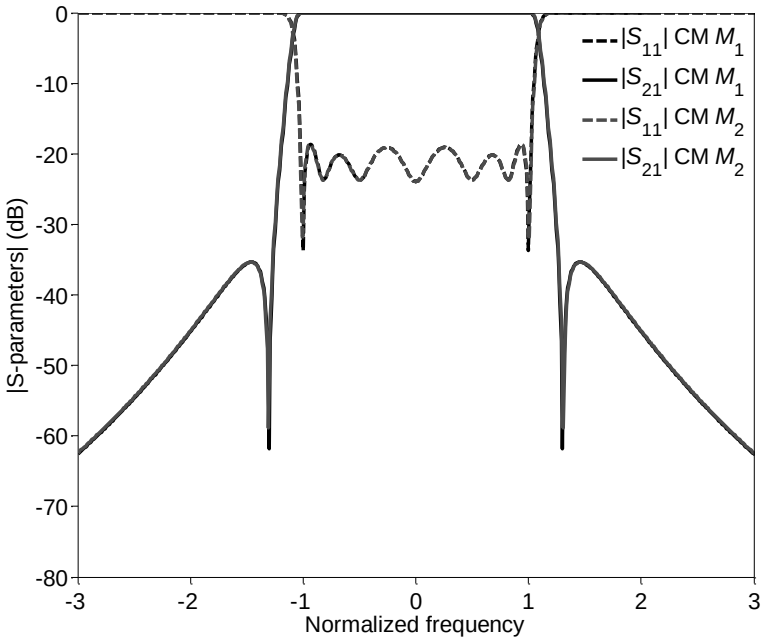

Fig. 5.9. S-parameters of the seventh-degree quasi-elliptic filter coupling matrix M_1 and M_2.

The coupling coefficient drift is then calculated considering the CTE of the RT/Duroid 6010LM (δ = 24 ppm/°C), which is the material of the inductive iris. Solving (5.16), considering a temperature increase of 47 °C from the ambient temperature (T_a = 23 °C), a coupling coefficient drift of 0.34% is obtained. Then, it is possible to quantify the effect of the coupling coefficients drift on the frequency response of a filter.

As an example, the coupling matrix M_1, of a quasi-elliptic seventh-order filter with in-line folded configuration and cross-coupling implementation on non-adjacent resonators 1-4 and 3-6, is determined with the procedure described in [15]. The coupling and routine schematic of the filter are shown in Fig. 5.6, while the coupling matrix M_1 is given in Fig. 5.7. The cross-couplings of the non-adjacent resonators are implemented with inductive iris and a SIW (substrate integrated waveguide) transmission line as reported in [16]. Thus, the cross-couplings are subjected to the same coupling drift behavior.

Applying a 0.34% coupling coefficient drift to the input/output resistance and to the coupling coefficients of M_1, the coupling matrix M_2 is thus obtained. It is given in Fig. 5.8. It is theoretically demonstrated in Fig. 5.9, showing the S-parameters of M_1 and M_2, that the coupling coefficient variations due to temperature imply a drift of the filter lower band-edge of 0.86 ppm/°C, upper band-edge of 0.97 ppm/°C, lower band transmission zero of 1.05 ppm/°C, and upper band transmission zero of 1.1 ppm/°C.

Thus, it can be concluded that the temperature variation has a negligible impact on the coupling coefficients, considering both adjacent and non-adjacent couplings, compared to the impact of the resonance frequency of uncompensated cavity resonators. Therefore, the inductive iris of the internal resonators and cross-couplings do not need to be thermally compensated in the design of single slab self-temperature-compensated filters with all pole or quasi-elliptic response, in which all the resonators of the filter are thermally compensated using the single slab temperature compensation technique.

5. 2. 2. 2 Design of a Single Slab Self-Temperature-Compensated Seventh-Order AFSIW Filter Demonstrator

For demonstration purposes, a temperature-uncompensated (without dielectric slab) in-line seventh-order quasi-elliptic filter (presented in Chapter 4), is designed, fabricated and measured to evaluate the frequency drift due to dimensional expansions with temperature variations. Then, using the previous Sections, a single slab self-temperature-compensated in-line seventh-order quasi-elliptic AFSIW filter is also designed, fabricated and measured. Both filters are designed with the same specifications, to operate at 12.05 GHz with a 236 MHz (1.96%) –3 dB bandwidth.

The two filters are fabricated with three different layers, substrate 2 and 3 are RT/Duroid 6010LM with thickness $h_2 = h_3 = 1.905$ mm, and substrate 1 is Rogers 6002 with thickness $h_1 = 0.508$ mm. The implemented metallized via holes in substrate 1 and 2 have a diameter $d = 0.4$ mm. The distance between two consecutive center-to-center vias is $p = 0.6$ mm. The iris length (b) for both filters is fixed to 2 mm. First, a pre-design is made using the theoretical model introduced in Section 5. 2. 1. Then, the filter final dimensions are optimized taking into consideration the internal couplings with a 3D electromagnetic software (ANSYS HFSS). For the single slab self-temperature-compensated AFSIW filter, for fabrication simplicity, the dielectric slabs implemented in the resonators have equal width $w_9 = 1.5$ mm. Also, the resonator width is all fixed to $W_r = 20.3$ mm. As shown in Fig. 5.3, there is sufficient design freedom to obtain self-temperature-compensation while fixing the AFSIW resonator cavity width and dielectric slab width. Both

fabricated prototypes are shown in Fig. 5.10 and Fig. 5.11, respectively, with dimensions reported in the figure titles.

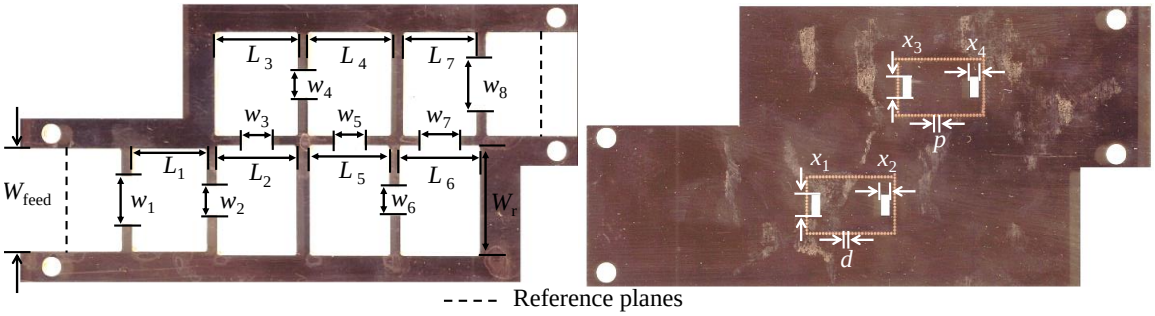

(*a*) (*b*)

Fig. 5.10. Photograph of (*a*) substrate 2 and (*b*) substrate 1 of the fabricated temperature-uncompensated dielectric in-line seventh-order filter (with W_{feed} = 19.05 mm, W_r = 20.3 mm, L_1 = 13.39 mm, L_2 = 14.726 mm, L_3 = 14.921 mm, L_4 = 15.486 mm, L_5 = 15.496 mm, L_6 = 14.838 mm, L_7 = 13.985 mm, w_1 = 9.782 mm, w_2 = 7.103 mm, w_3 = 5.204 mm, w_4 = 5.51 mm, w_5 = 5.177 mm, w_6 = 5.652 mm, w_7 = 5.469 mm, w_8 = 8.898 mm, x_1 = 3.813 mm, x_2 = 1.5 mm, x_3 = 3.813 mm, x_4 = 1.5 mm, d = 0.4 mm, and p = 0.6 mm).

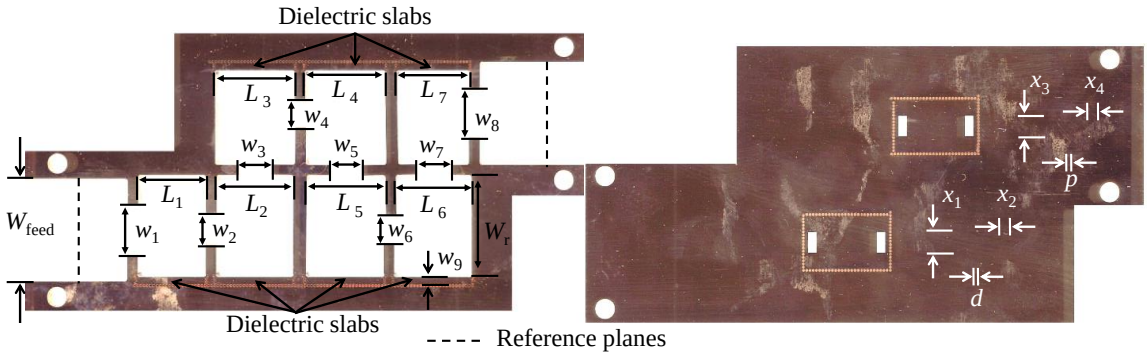

(*a*) (*b*)

Fig. 5.11. Photograph of (*a*) substrate 2 and (*b*) substrate 1 of the fabricated temperature-uncompensated dielectric in-line seventh-order filter (with W_{feed} = 19.05 mm, W_r = 20.3 mm, L_1 = 13.423 mm, L_2 = 14.378 mm, L_3 = 14.453 mm, L_4 = 14.851 mm, L_5 = 14.829 mm, L_6 = 14.279 mm, L_7 = 12.667 mm, w_1 = 8.93 mm, w_2 = 6.802 mm, w_3 = 5.146 mm, w_4 = 5.845 mm, w_5 = 5.208 mm, w_6 = 6.143 mm, w_7 = 5.811 mm, w_8 = 9.518 mm, w_9 = 1.5 mm, x_1 = 3.766 mm, x_2 = 1.5 mm, x_3 = 3.766 mm, x_4 = 1.5 mm, d = 0.4 mm, and p = 0.6 mm).

5. 2. 2. 3 Experimental Results at Ambient Temperature

For comparison purposes, both fabricated filters are measured at ambient temperature T_a and compared to the simulation results in Fig. 5.12 and Fig. 5.13. It can be observed that a good agreement between simulated and measured results is obtained for both filters. Measurements were done using a N5225A PNA microwave network analyzer from Keysight, with a WR-75 test fixture, similar to the WR-51 test fixture introduced in [17]. A thru-reflect-line (TRL) AFSIW calibration kit is used to characterize the filters at the reference planes illustrated in Fig. 5.10 and Fig. 5.11. The experimental responses of both filters are shifted in frequency by 50 MHz (0.41%) compared to the simulation. This frequency shift is mainly due to fabrication errors. Reflection coefficients in the pass band of both fabricated filters are greater than 18 dB.

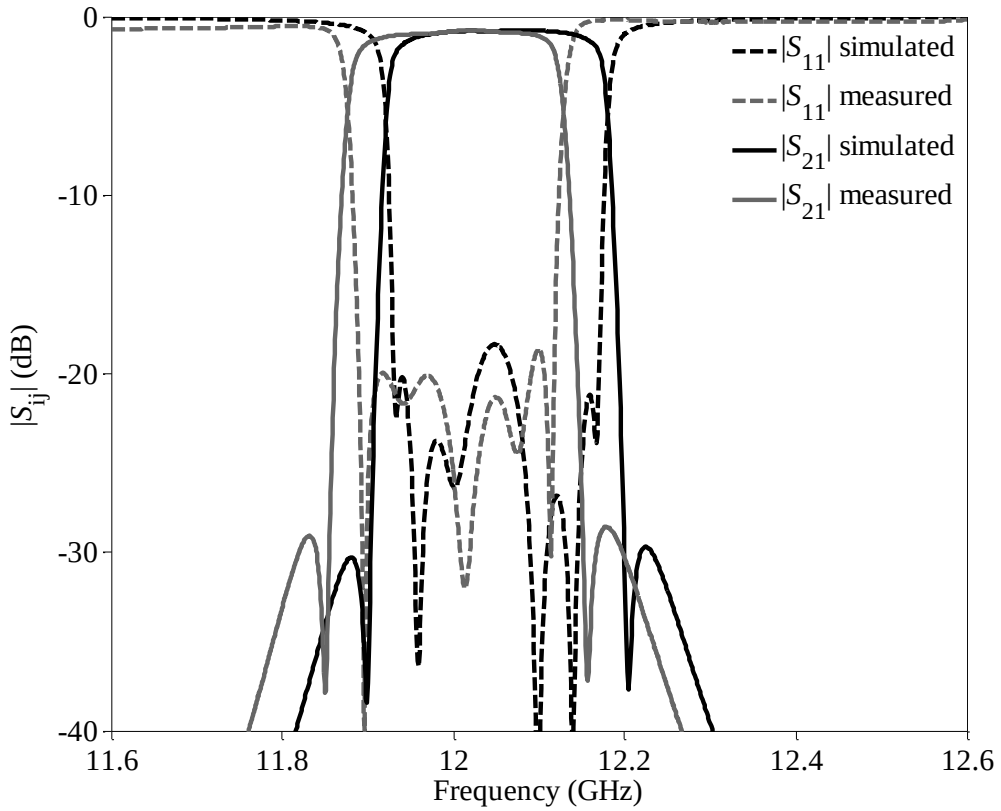

Fig. 5.12. Simulated and measured temperature-uncompensated dielectric-less in-line seventh-order filter S-parameters at ambient temperature (T_a).

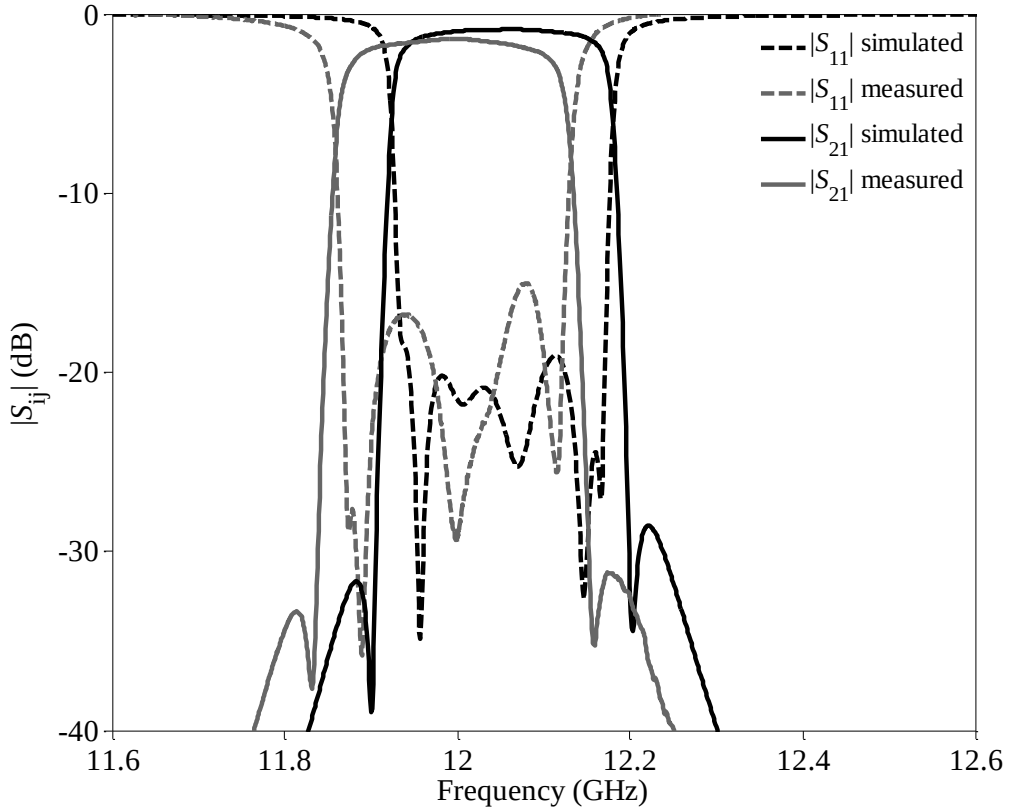

Fig. 5.13. Simulated and measured single slab self-temperature-compensated in-line seventh-order filter S-parameters at ambient temperature (T_a).

The temperature-uncompensated filter achieves a 0.76 dB insertion loss, while the single slab self-temperature-compensated filter has an insertion loss of 1.38 dB. The measured insertion loss is higher than in the simulation. This is due to the fabrication problem as well as the assembly process. Indeed, after investigation, the electrical contact in the filter was not as good as previous ones. Simulated and measured results are compared in Table 5.2.

TABLE 5.2
COMPARISON OF SIMULATED AND MEASURED PERFORMANCES AT AMBIENT TEMPERATURE OF THE PROTOTYPED IN-LINE SEVENTH-ORDER FILTERS

Performances ($@T_a$)	Uncompensated filter		Compensated filter	
	Simulated	Measured	Simulated	Measured
Return loss (dB)	> 20	> 19	> 20	> 18
Insertion loss (dB)	0.72	0.76	0.9	1.38
-3 dB bandwidth (MHz)	260	253	260	272

5. 2. 2. 4 Experimental Results Versus Temperature Variation

Finally, a WK3-600 climatic chamber from Weiss Umwelttechnik GmbH, is used to characterize both filters in the -20 °C to 70 °C temperature range. Each filter is measured at different temperatures, T_c = -20 °C, T_a = 23 °C, and T_h = 70 °C, with a thermal stabilization step of 2 hours for each temperature. The temperature in the climatic chamber is controlled using a thermocouple sensor positioned on the device under test (DUT). Samples are sequentially measured at T_a, T_h, T_c and then again at T_a. The measurement is considered valid only if both T_a measurements are identical.

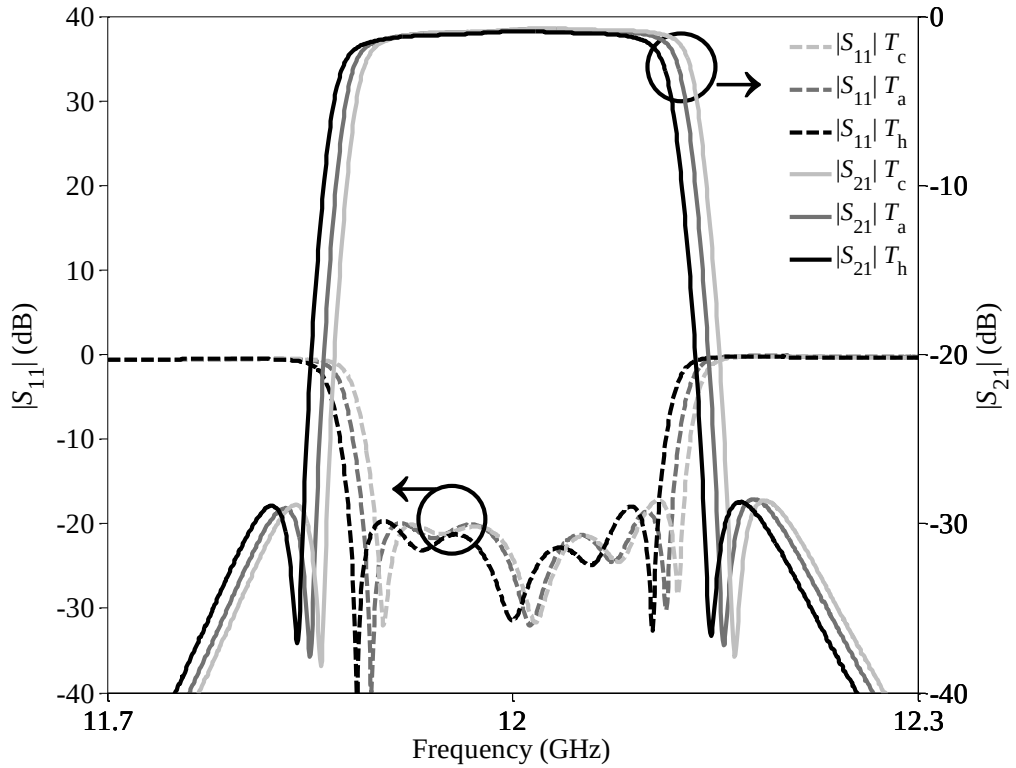

Fig. 5.14. Simulated and measured temperature-uncompensated dielectric-less in-line seventh-order filter S-parameters at T_c, T_a, and T_h.

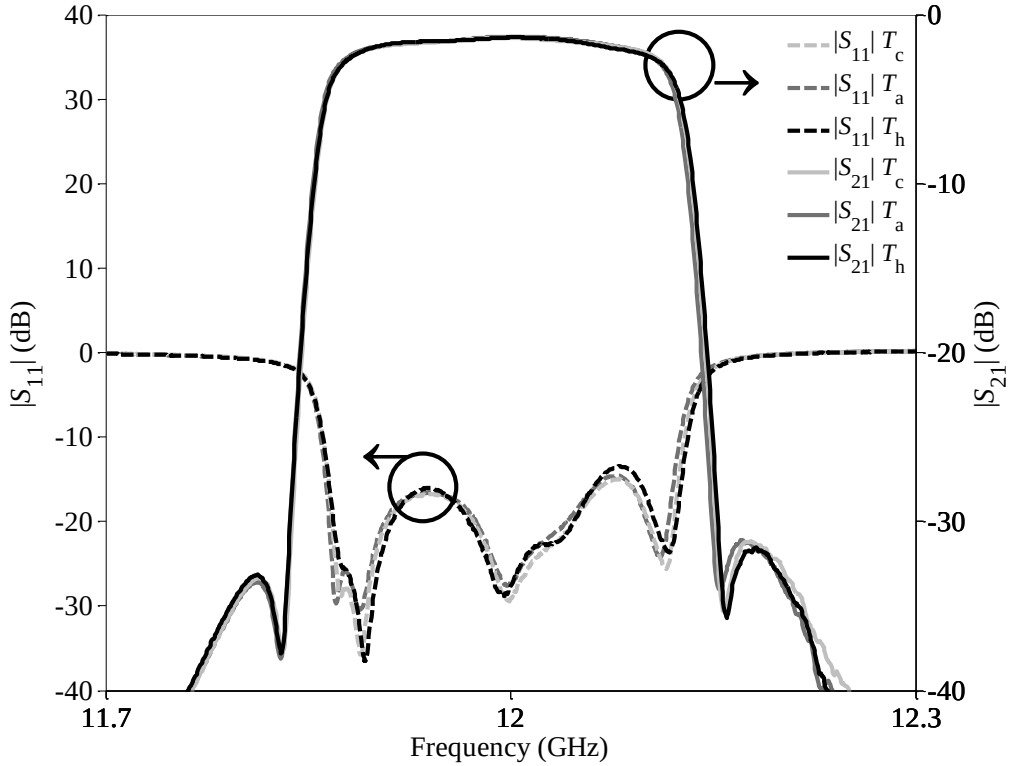

Fig. 5.15. Simulated and measured single slab self-temperature-compensated in-line seventh-order filter S-parameters at T_c, T_a, and T_h.

Measured S-parameters at T_c, T_a, and T_h are shown in Fig. 5.14 and Fig. 5.15, for the uncompensated and self-compensated filters, respectively. It can be observed that the reflection coefficient remains greater than 16 dB for both filters at the three temperatures.

All the measured and simulated results are reported in Table 5.3. The single slab self-temperature-compensated in-line seventh-order filter demonstrates a thermal stability of the lower band-edge of 0.53 ppm/°C at -20 °C and a thermal stability of the upper band-edge of 0.88 ppm/°C at 70 °C. The center frequency of the compensated filter has a thermal stability of 0.58 ppm/°C at -20 °C and a thermal stability of 0.89 ppm/°C at 70 °C. Furthermore, the lower band and upper band transmission zeros have a thermal stability of 2.55 ppm/°C and 2.3 ppm/°C at -20 °C, and 2.34 ppm/°C and 4.37 ppm/°C at 70 °C, respectively.

Additionally, the temperature-uncompensated dielectric-less filter shows a thermal stability of the lower band-edge of 14.12 ppm/°C at -20 °C and a thermal stability of the upper band-edge of 15.89 ppm/°C at 70 °C. The center frequency of the uncompensated filter has a thermal stability of -15.5 ppm/°C at -20 °C and a thermal stability of -17.73 ppm/°C at 70 °C. Moreover, the lower band and upper band transmission zeros have a thermal stability of -15.9 ppm/°C and -15.5 ppm/°C at -20 °C, and -16.88 ppm/°C and -17.5 ppm/°C at 70 °C, respectively. The unloaded quality factor is evaluated using [18]:

$$Q_u \approx 4.343 \frac{N}{\mathrm{IL(dB)} \frac{\Delta f_{3dB}}{f_0}}, \tag{5.17}$$

where f_0 is the resonant frequency, N is the order of the filter, IL represents the insertion loss in dB, and Δf_{3dB} is the -3 dB bandwidth.

The center frequency thermal stability is expressed in parts-per-million per degree Celsius and is calculated using:

$$\delta_f = \frac{f_{T_a+\Delta T} - f_{T_a}}{\Delta T f_{T_a}}. \tag{5.18}$$

TABLE 5.3
MEASURED PERFORMANCES OF THE PROTOTYPED SEVENTH-ORDER FILTERS

Performances	Uncompensated filter			Compensated filter		
Temperature	T_c	T_a	T_h	T_c	T_a	T_h
Centre frequency (GHz)	12.011	12.003	11.993	11.995	11.995	11.995
Centre frequency drift (MHz)	8	0	-10	-0.3	0	0.5
Centre frequency thermal stability, δ_f (ppm/°C)	-15.5	/	-17.73	0.58	/	0.89
Centre frequency shift, Δf (%) between -20 and +70°C	0.15			0.008		
Lower band Tz (GHz)	11.858	11.85	11.841	11.83	11.831	11.83
Lower band Tz thermal stability (ppm/°C)	-15.9	/	-16.88	2.55	/	2.34
Upper band Tz (GHz)	12.164	12.156	12.146	12.156	12.157	12.16
Upper band Tz thermal stability (ppm/°C)	-15.5	/	-17.5	2.3	/	4.37
-3 dB bandwidth (MHz)	252	252	252	271	272	274
Return loss (dB)	> 20	> 20	> 20	> 16	> 16	> 15
Insertion loss (dB)	0.72	0.76	0.89	1.3	1.38	1.4
Q_u	2053	1945	1661	1057	992	970

5. 3. Double Slab Self-Temperature-Compensated AFSIW Cavities and Filters

The single slab temperature compensation technique is demonstrated and validated. It is then intuitive for this research to extend the asymmetrical case of a single slab to a symmetrical case of double slabs. The temperature compensation technique is based on the same electromagnetic properties. To further demonstrate the versatility of the AFSIW technology, the proposed temperature compensation technique is applied to cavities and filters operating in the Ka-band. Moreover, to validate the performance of the proposed temperature compensation technique, the temperature range for this double slab case is fixed to -40 °C to 80 °C. Finally, a post-process tuning method is demonstrated to allow fine-tuning.

5. 3. 1 Theory of Double Slab Self-Temperature-Compensated AFSIW Cavities

In this Section, a double slab AFSIW cavity temperature compensation technique is studied based on a similar theoretical multiphysics model as presented in Section 5. 2. To extend the study, a post-process temperature compensation technique is introduced to counterbalance potential fabrication errors and/or allow fine-tuning.

5. 3. 1. 1 Double Slab Air-Filled SIW Cavity Equivalent Multiphysics Transmission Line Model

A theoretical model based on transmission theory similar to the one presented in Section 5. 2 is developed to study the thermal behavior of double slab AFSIW cavities and synthesize double slab self-temperature-compensated AFSIW cavities. The transmission line theory is used to determine a characteristic equation between the fundamental TE_{101} mode resonant frequency and the AFSIW cavity dimensions and material electromagnetic properties, all subject to thermal effects.

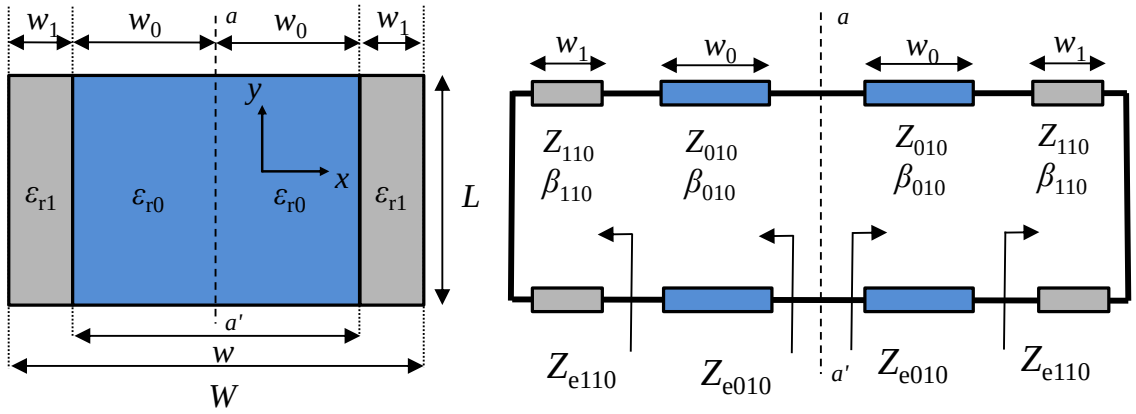

(*a*) (*b*)

Fig. 5.16. Double slab AFSIW cavity (*a*) top view and (*b*) equivalent transmission line model.

Fig. 5.16(*a*) represents a top view of a double slab air-filled cavity of total width W, length L and height h_2. This cavity has a center air-filled region of relative permittivity $\varepsilon_{r0} = 1$ and width w and two sidewalls dielectric slabs of relative permittivity ε_{r1} and width w_1. The equivalent transmission line model is shown in Fig. 5.16(*b*). It is assumed that ε_{r1}, L, W, w_0, and w_1 are dimensions defined at ambient temperature $T_a = 23°C$. The center air-filled region is separated into two Sections of length w_0 with TE_{101} propagating mode guide impedance Z_{010} and propagation constant β_{010}. The two dielectric slabs are represented by transmission lines of length w_1 with TE_{101} propagating mode guide impedance Z_{110} and propagation constant β_{110}. The propagation constant β_{i10} and the guide impedance Z_{i10} of the transmission line model at T_a are the same as the ones (5.1)-(5.2) developed in Section 5. 2.

With a change in temperature of ΔT, the dielectric slab permittivity, and the cavity dimensions, considering essentially linear variations, are given by (5.3), (5.4), and (5.5). Hence, to counterbalance the dimension dilatation with increasing temperature expressed by (5.3) and (5.4), the proposed compensation technique principle is to use wisely the two air-filled cavity sidewall dielectric slabs. Thus, considering a ΔT variation in temperature, (5.6) to (5.11) can be developed. In this particular case, the (*aa*') plane is a plane of symmetry and not a short circuit. Thus, for TE_{101} mode, at the cavity resonance frequency $f = f_{TE101}{}^{T+\Delta T}$, the imaginary part of (5.11) is:

$$\mathrm{Im}\left(Z_{e010}{}^{T+\Delta T}\right)=\infty. \tag{5.17}$$

The same Newton-Raphson method can be used to determine the double slab AFSIW cavity resonance frequency $f_{\mathrm{TE101}}^{T+\Delta T}$.

5. 3. 1. 2 Theoretical Analysis

In the double slab case, RT/Duroid 6010LM substrate material from Rogers is also considered. Using (5.17), the resonance frequency of a double slab AFSIW cavity based on RT/Duroid 6010LM substrate material at T_c = -40°C, T_a and T_h = 80°C (f_{Tc}, f_{Ta} and f_{Th}, respectively), versus the dielectric slabs width w_1, for fixed L = 8.22 mm and W = 13 mm cavity dimensions, are calculated and reported in Fig. 5.17. The frequency shift, defined by (5.13), is also shown in Fig. 5.17.

It can be observed in Fig. 5.17 that for low values of w_1 (<0.87 mm), the cavity resonant frequency decrease with temperature. As w_1 is increased from 0 to 0.87 mm, the frequency shift due to thermal effect is reduced. In this range, a temperature under-compensation is obtained. For w_1 = 0.87 mm, a temperature compensation is obtained; the double slab air-filled cavity is self-temperature-compensated. For large values of w_1 (>0.87 mm), the cavity resonant frequency decrease with temperature; a temperature overcompensation is achieved.

Fig. 5.18 shows the f_{Ta} cavity resonant frequency at T_a, together with the frequency shift obtained in the -40 to 80°C temperature range, versus the cavity length L and slab width w_1, for a fixed W of 13 mm. It can be observed that L and w_1 can be adjusted to simultaneously control the cavity resonant frequency and obtain self-temperature-compensation. It is therefore possible to use this model to determine the geometry of double slab self-temperature-compensated cavities for the design of cavity filters.

For example, the ▼ marker, shown in Fig. 5.17 and Fig. 5.18, corresponds to a double slab self-temperature-compensated AFSIW cavity resonating at 21 GHz, which dimensions, considering continuously metallized sidewalls, are L = 8.22 mm, W = 13 mm and w_1 = 0.87 mm.

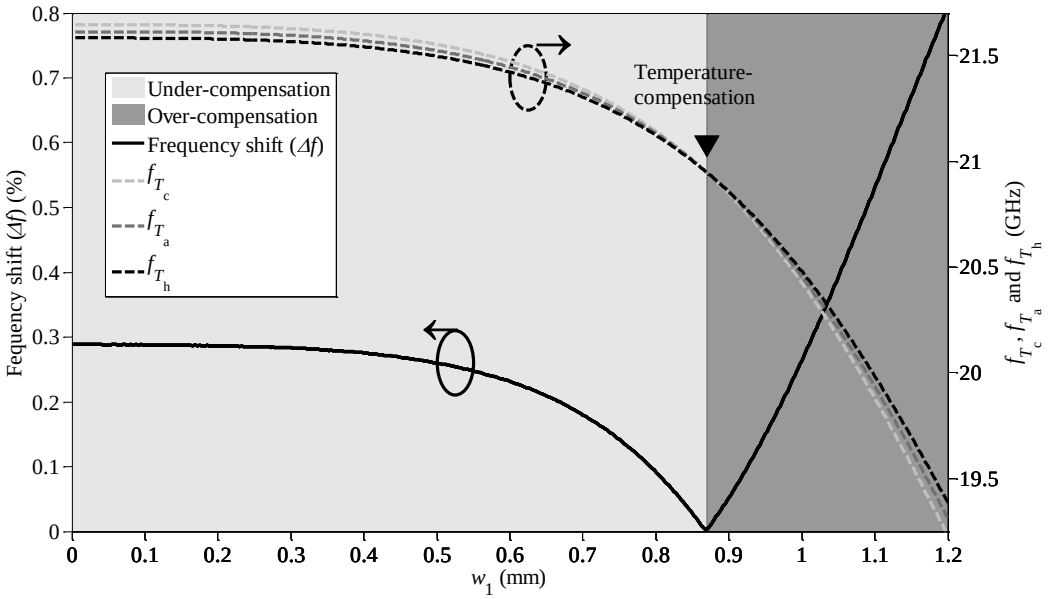

Fig. 5.17. Theoretical frequency shift of the air-filled cavity resonator obtained in the -40 °C to +80 °C temperature range and theoretical air-filled cavity resonance frequency at T_c, T_a and T_h versus the dielectric slab width w_1 (with L = 8.22 mm, W = 13 mm and ε_{r1} = 10.2).

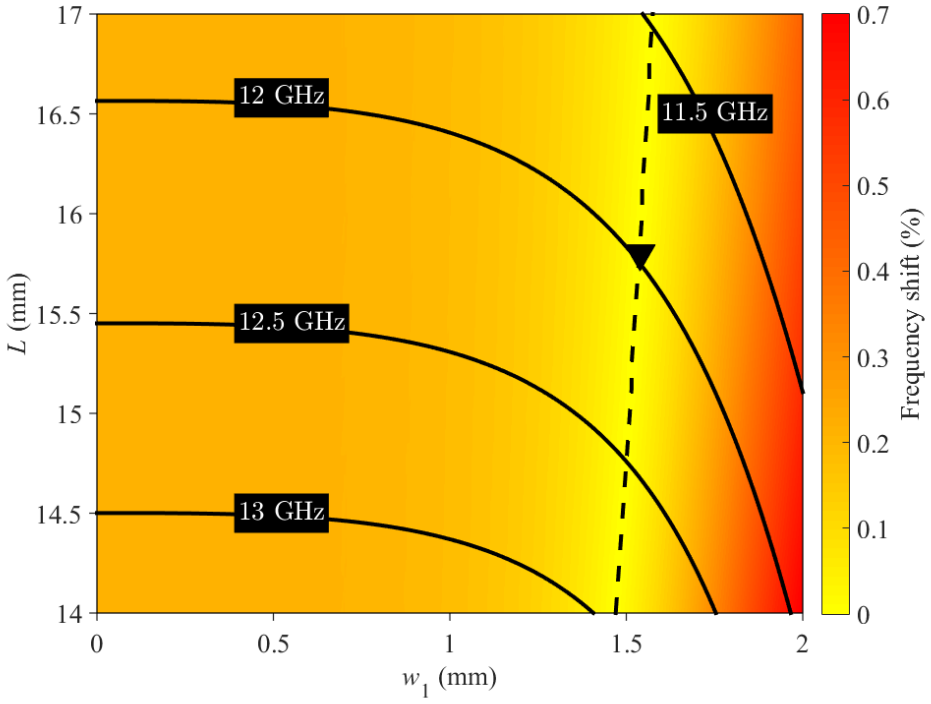

Fig. 5.18. Theoretical frequency shift of the air-filled cavity with isocurves of the resonance frequency at T_a (black straight lines) and optimal temperature-compensation (black dotted lines) versus the cavity length L and dielectric slab width w_1 (with W = 13 mm and ε_{r1} = 10.2) obtained in the -40 °C to +80 °C temperature range.

5. 3. 1. 3 Theoretical and Eigenmode Results Comparison

To validate the proposed multiphysics equivalent model and determine thermal effects, the resonant frequencies of a double slab air cavity and a self-temperature-compensated air-filled cavity, which geometries are illustrated in Fig. 5.19, are studied. Both cavities are designed to resonate at 21 GHz. Their dimensions are reported in Table 5.4.

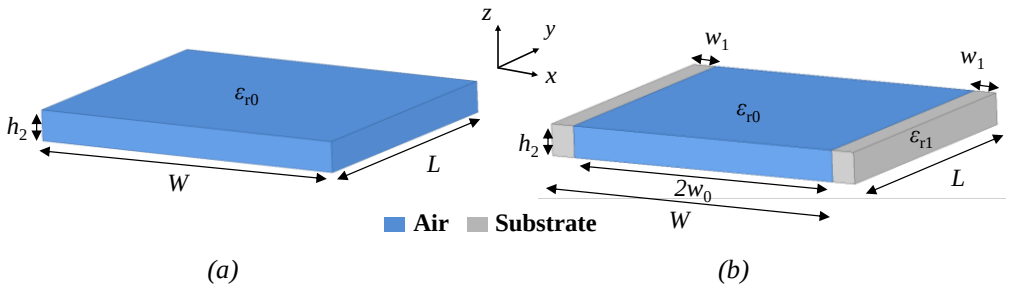

(a) *(b)*

Fig. 5.19. Geometry of the (*a*) air cavity and (*b*) double slab AFSIW cavity.

TABLE 5.4
DIMENSIONS OF THE AIR AND AIR-FILLED CAVITIES

	W (mm)	L (mm)	w_0 (mm)	w_1 (mm)	ε_{r0}	ε_{r1}
Air cavity	13	8.6	/	/	1	/
Air-filled cavity	13	8.22	5.63	0.87	1	10.2

Cavity resonance frequencies versus temperature, obtained in theory solving (5.17) and in simulations using the ANSYS HFSS electromagnetic (EM) software eigenmode solver, are compared in Fig. 5.20. It can be observed that a good agreement between theory and simulation is obtained for both cavities. The air cavity has a theoretical frequency drift (relative to the resonant frequency at T_a) of 29.3 MHz at -40 °C and -28.1 MHz at 80 °C, whereas the self-temperature-compensated AFSIW cavity has a frequency drift of 0.01 MHz at -40 °C and -0.01 MHz at 80 °C. Therefore, the air cavity shows a theoretical frequency resonance stability of 22.15 ppm/°C at -40 °C and 23.46 ppm/°C at 80 °C. While the double slab self-temperature-compensated air-filled cavity shows a theoretical frequency resonance stability of 0.01 ppm/°C at -40 °C and -0.01 ppm/°C at 80 °C.

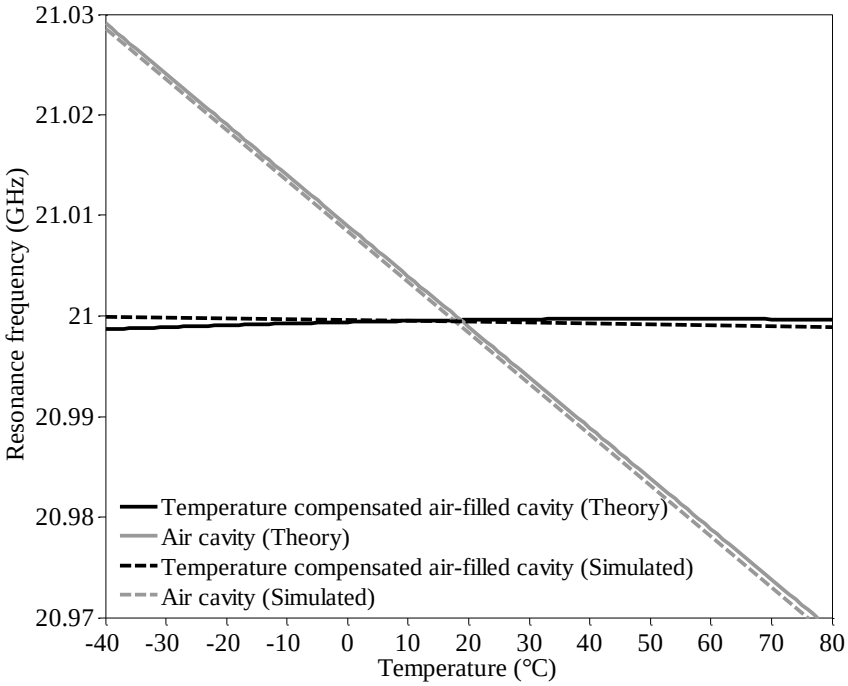

Fig. 5.20. Theoretical and simulated resonance frequencies of the air cavity and the double slab self-temperature-compensated AFSIW cavity versus temperature.

5. 3. 1. 4 Post-Process Temperature Compensation Tuning

As manufacturing errors can happen and that any fabrication process as tolerances, it is of high interest to be able to post-process AFSIW cavities to tune (or fine-tune) temperature compensation. Post-process tuning is common and crucial in the PCB industry, especially for narrowband filters [19]. In the case of an obtained overcompensation, one way to tune temperature compensation is to remove some material from the dielectric slabs. For instance, through-holes can be drilled from the top substrate into the inner substrate. However, removing dielectric material will also decrease the resonance frequency, which can be tuned afterward using a capacitive post as introduced in [20]. A temperature compensation and resonant frequency tuned double slab AFSIW cavity based on those principles is illustrated in Fig. 5.21.

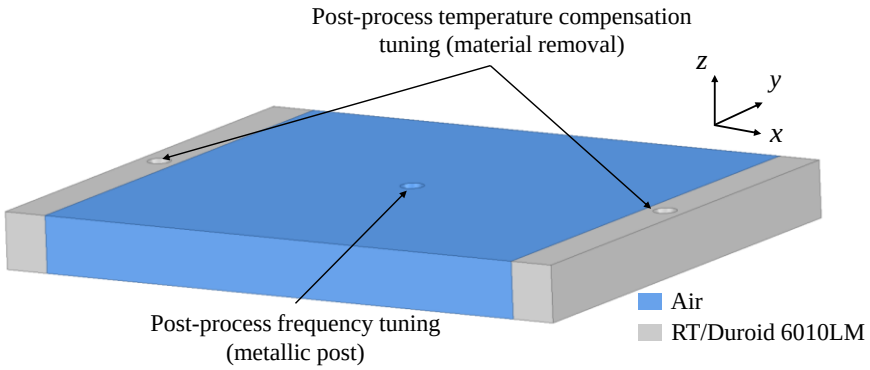

Fig. 5.21. Illustration of a post-process temperature-compensation and resonant frequency tuned air-filled cavity.

Fig. 5.22 shows the simulated results of a double slab temperature overcompensated cavity which has a simulated frequency drift of -10.72 MHz at -40 °C and 9.7 MHz at 80 °C. With a post-process tuning consisting in drilling small holes in the dielectric slabs, as illustrated in Fig. 5.21, the temperature compensation is tuned. To compensate for the induced resonant frequency shift, a capacitive post tuning is used at the cavity center. After post-processing, a simulated frequency drift as low as 0.2 MHz is obtained in the -40 to 80°C temperature range.

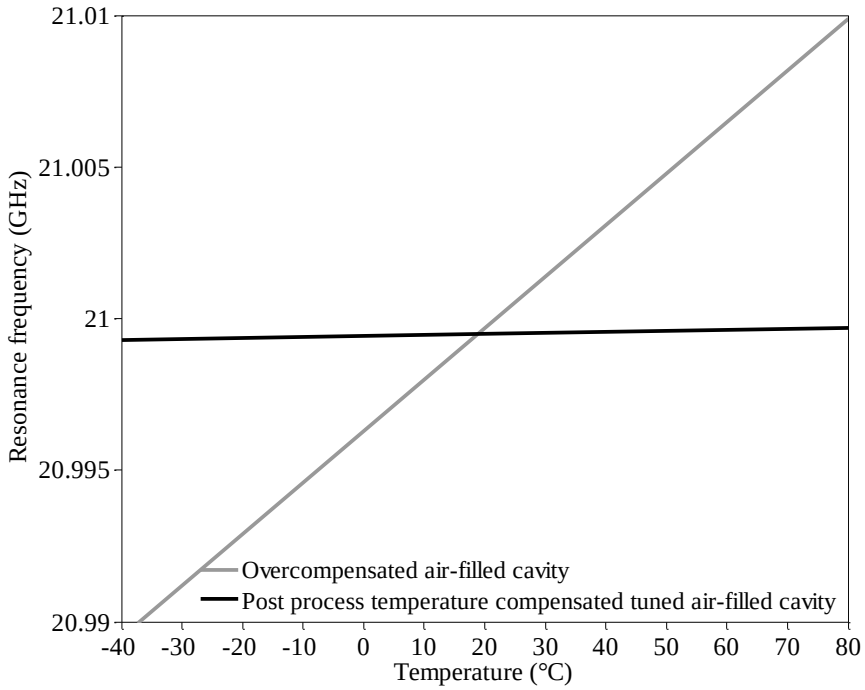

Fig. 5.22. Simulated resonance frequencies of the temperature overcompensated air-filled cavity and the post-process temperature-compensation and resonant frequency tuned air-filled cavity versus temperature.

5. 3. 2 Double Slab Self-Temperature-Compensated AFSIW Cavities

In this Section, the equivalent width of an AFSIW cavity fabricated with rows of metallic via holes is introduced. Then, for demonstration purposes, a double self-temperature-compensated AFSIW cavity is

synthesized, optimized, fabricated, measured, post-process tuned and compared to a temperature-uncompensated dielectric-less cavity.

5. 3. 2. 1 Metallized Via-Hole Double Slab Self-Temperature-Compensated AFSIW Cavity Equivalent Width

The multiphysics model developed in this Section is based on the same principle as the one developed in Section 5. 2. Therefore, a double slab self-temperature-compensated AFSIW cavity can be synthesized using the theoretical model described previously. Then, its via rows center-to-center width W, can be determined using (5.14).

5. 3. 2. 2 Experimental Validation

For demonstration purposes, the proposed temperature compensation technique is applied to a first-order double slab AFSIW cavity filter (consisting of a single cavity). The theoretical model introduced in Section 5. 3, together with the effective width relation (5.14), are used to synthesize a double slab self-temperature-compensated AFSIW cavity. Even though the input and output coupling windows do not have a significant impact on the temperature compensation, a step of optimization using an EM simulator is needed to fine-tune the first-order cavity filter. For comparison purposes and to highlight the high interest of this technique, a dielectric-less first-order filter is also designed and fabricated without temperature compensation. Both filters are designed at the center frequency of 21 GHz.

The manufactured uncompensated and compensated filters are shown in Fig. 5.23 and Fig. 5.24, respectively. Both filters are fabricated with RT/Duroid 6010LM with thicknesses h_2 = 1.27 mm. The metallized via holes have a diameter of d = 0.4 mm and a center-to-center pitch of p = 0.6 mm.

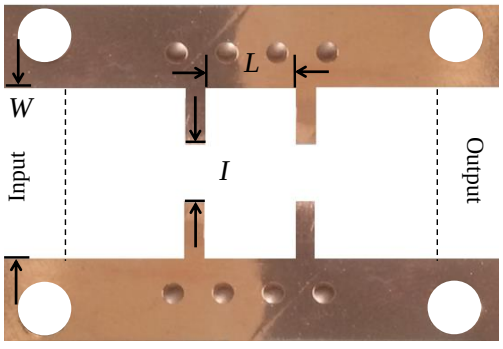

Fig. 5.23. Photographs of the fabricated temperature-uncompensated dielectric-less first-order filter inner substrate (with W = 13 mm, I = 4.54 mm and L = 7.31 mm).

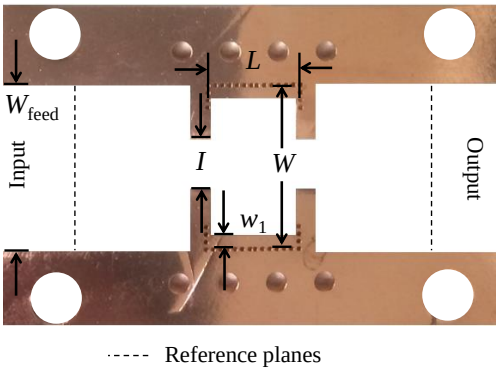

Fig. 5.24. Photographs of the fabricated temperature-compensated first-order AFSIW filter inner substrate (with W_{feed} = 13 mm, I = 4.49 mm, w_1 = 0.82 mm, W = 12.674 mm and L = 6.85 mm).

Both filters are measured using a N5225A PNA microwave network analyzer from Keysight with the WR-51 test fixture introduced in [17]. The measurements are done in the -40 °C to 80 °C temperature range using the same WK3-600 climatic chamber from Weiss Umwelttechnik GmbH introduced in Section 5. 2. WR-51 waveguides are used to keep the WR-51 adapter out of the climatic chamber, as shown in Fig. 5.25. Each filter is measured with the same conditions as described in Section 5. 2. The effects of the cables, WR-51 waveguides and test fixture are de-embedded using a thru-reflect-line (TRL) AFSIW calibration kit. Reference planes are shown in Fig. 5.23 and Fig. 5.24.

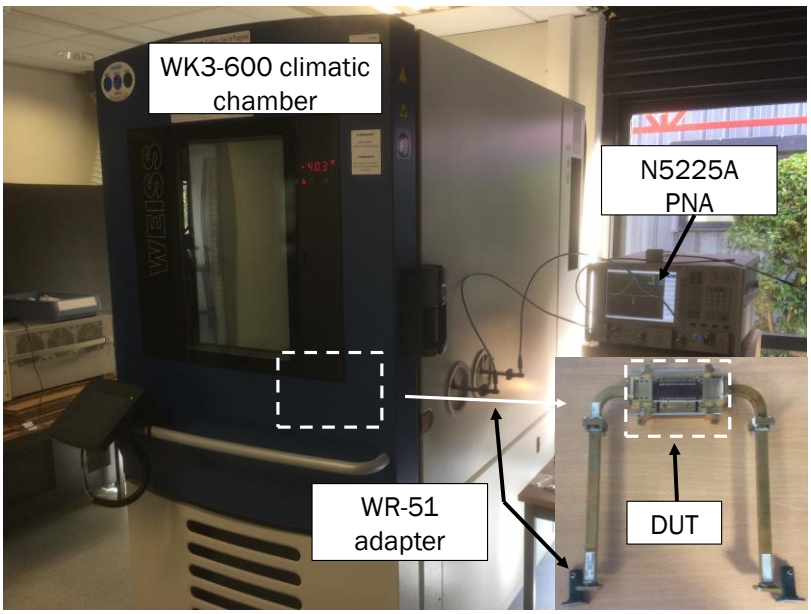

Fig. 5.25. Photographs of the thermal measurement set-up.

The measured S-parameters of the temperature-uncompensated dielectric-less and double slab self-temperature-compensated AFSIW filters are shown in Fig. 5.26 and Fig. 5.27, respectively. It can be observed that the resonance frequency of both filters is centered at 20.8 GHz. This frequency shift is due to a fabrication error from the PCB manufacturer in the filter dimensions that has been identified using an optical profilometer.

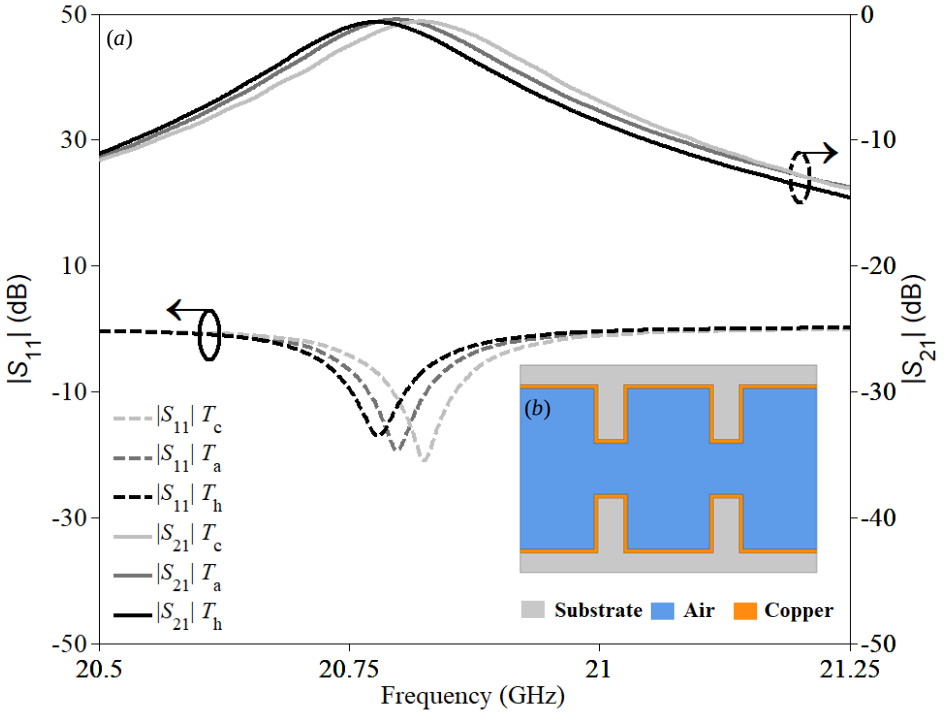

Fig. 5.26. (*a*) Measured S-parameters of the temperature-uncompensated dielectric-less first-order filter and (*b*) its geometry.

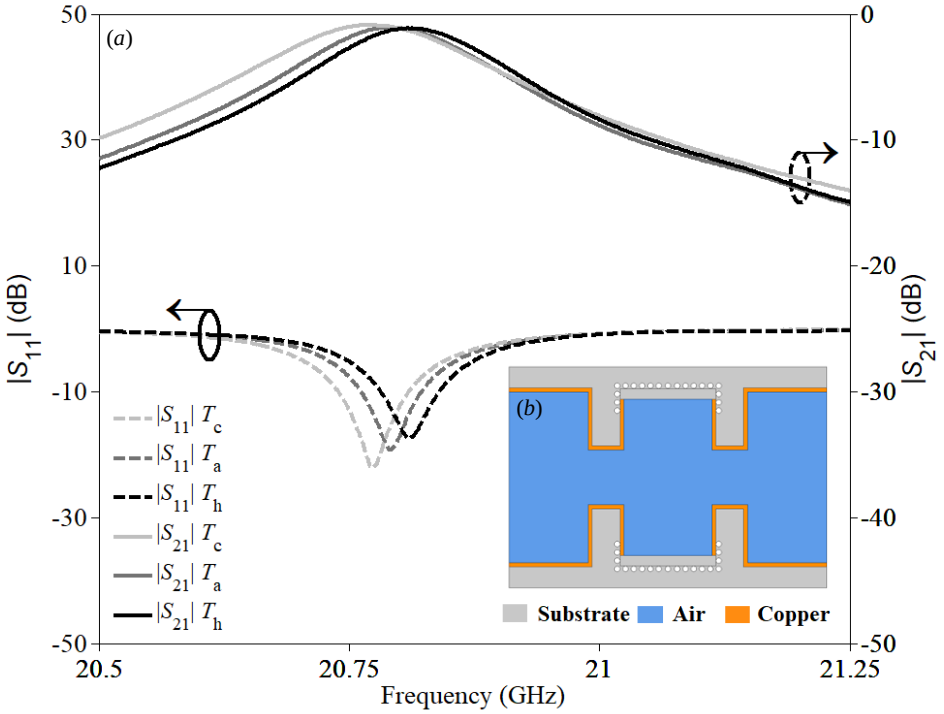

Fig. 5.27. (*a*) Measured S-parameters of the temperature-compensated first-order AFSIW filter and (*b*) its geometry.

The dielectric-less temperature-uncompensated first-order filter shows a 24.9 MHz frequency drift at -40 °C and a -21.1 MHz frequency drift at 80 °C as shown in Fig. 5.26. Those values are very close to values obtained from theory and EM simulations. However, for the double slab self-temperature-compensated first-order filter, the fabrication error not only impacted the resonant frequency, but also the temperature

compensation. As shown in Fig. 5.27, an overcompensation is obtained. The measured results show a -23.8 MHz frequency drift at -40 °C and a 21.2 MHz frequency drift at 80 °C. Still, this first fabrication run allowed to validate the double slab temperature compensation principle.

Both filters can also be compared in terms of achieved quality factor. First, the loaded quality factor (Q_l) is calculated using:

$$Q_l = \frac{f_0}{\Delta f_{3dB}}, \tag{5.18}$$

where f_0 is the resonant frequency and Δf_{3dB} is the -3 dB bandwidth. Then, the unloaded quality factor (Q_u) is calculated to take into account the insertion losses (IL) in dB of the cavities using:

$$Q_u = \frac{Q_l}{10^{\frac{IL(dB)}{20}}}. \tag{5.19}$$

Finally, the external quality factor (Q_e) can be determined from:

$$\frac{1}{Q_e} = \frac{1}{Q_u} - \frac{1}{Q_l}. \tag{5.20}$$

Table 5.5 reports the measured results of both cavities, having similar resonant frequencies, -3 dB bandwidths, and reflection coefficients. The drawback of this temperature-compensation technique is an increase in dielectric loss. It can be observed that with an increase in temperature, both filters have increasing loss, resulting in decreasing *Q*-factors (due to a lower conductivity).

TABLE 5.5
MEASURED PERFORMANCES OF THE PROTOTYPED DOUBLE SLAB FIRST-ORDER FILTERS

Performances	Temperature-uncompensated dielectric-less first-order filter			Temperature-over-compensated first-order filter			Post-process temperature-compensation tuned first-order filter		
Temperature	T_c	T_a	T_h	T_c	T_a	T_h	T_c	T_a	T_h
Centre frequency (GHz)	20.824	20.799	20.778	20.765	20.789	20.810	21.013	21.015	21.016
Centre frequency drift (MHz)	24.9	0	-21.1	-23.8	0	21.2	-2	0	1
Centre frequency shift, Δf(%) between -40 and +80°C	0.221			0.216			0.014		
-3 dB bandwidth (MHz)	195	186	187	192	187	189	218	208	209
Return loss (dB)	> 22	> 20	> 19	> 22	> 20	> 19	> 22	> 22	> 19
Insertion loss (dB)	0.61	0.61	0.64	0.89	1.05	1.12	0.78	0.86	0.92
Q_u	1547	1514	1435	1002	842	806	1050	960	902

5. 3. 2. 3 Experimental Post-Process Temperature Compensation Tuning Validation

The fabrication error that occurred during a first fabrication run was the opportunity to validate the post-process temperature compensation tuning introduced in Section 5. 3. 1. This principle is applied to the fabricated temperature overcompensated first-order filter. Two small holes are drilled from the top substrate to the inner substrate in the dielectric slabs to remove some dielectric loading material. Thus, with less dielectric material, the compensation has a lower impact and the resonance frequency is increased. Measured S-parameters of the double slab self-temperature-compensated AFSIW filter after post-processing are presented in Fig. 5.28.

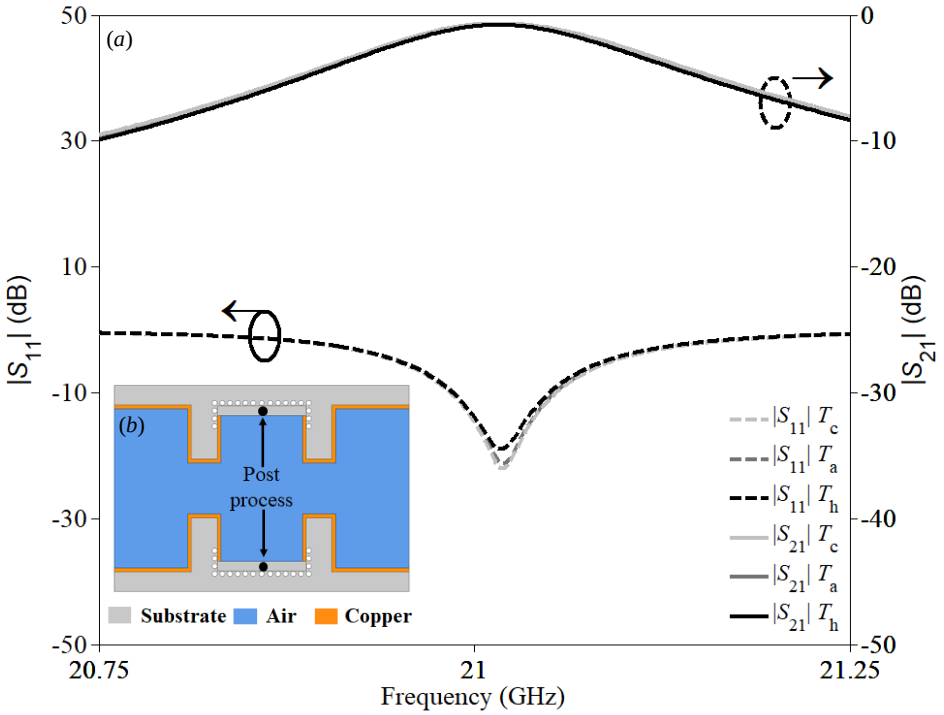

Fig. 5.28. (*a*) Measured S-parameters of the post-process double slab self-temperature-compensation tuned first-order filter and (*b*) its geometry.

A quasi-perfect thermal compensation has been achieved using the post-processing principle. The tuning procedure consisted in drilling increasing through-hole diameters, starting from 0.4 mm, until temperature compensation has been achieved. Finally, in that particular case, 0.8 mm drilled holes resulted in an almost perfect temperature compensation. Also, these holes resulted in a resonant frequency of 21 GHz, therefore no capacitive post was used for resonant frequency tuning.

In Fig. 5.28, it is shown that a frequency drift of -2 MHz at -40 C and 1 MHz at 80 °C are obtained. Furthermore, it can be observed that the -3 dB bandwidth remains almost constant over the temperature range. The post-process tuned double slab AFSIW first-order filter measured results are also reported in Table 5.5. The increase in resonant frequency, and the decrease in insertion loss resulting in increased Q factor due to dielectric material removal can be observed.

5. 3. 3 Double Slab Self-Temperature-Compensated AFSIW Filters

5. 3. 3. 1 Design of a Self-Temperature-Compensated Fourth-Order AFSIW Filter Demonstrator

For comparison purposes, a temperature-uncompensated dielectric-less (without dielectric slabs) filter, is designed and fabricated to evaluate the frequency drift due to dilatation with temperature variation in the Ka-band. Then, a double slab self-temperature-compensated AFSIW filter, which cavities have been synthesized using the introduced design procedure, is also designed and fabricated. Both filters are designed to achieve a center frequency of 21 GHz with a 300 MHz (1.42%) -3 dB bandwidth. For both filters, based on the study of coupling coefficient drifts, it was decided not to compensate the inductive iris.

These fourth-order filters have been fabricated in a second manufacturing run, after solving the fabrication error with the PCB manufacturer for Ka-band applications. Both filters are made of three layers of RT/Duroid 6010LM with thicknesses h_2 = 1.27 mm. The metalized via holes have a diameter of d = 0.4 mm and the via rows have a center-to-center pitch of p = 0.6 mm. A pre-design is made using the theoretical model introduced in Section 5. 3. 1. Then the filter dimensions are optimized taking into consideration the coupling windows using the ANSYS HFSS EM software.

The temperature-uncompensated dielectric-less filter and the double slab self-temperature-compensated AFSIW filter are shown, with their dimensions, in Fig. 5.29 and Fig. 5.30, respectively. The measurement reference planes, obtained using a TRL calibration kit, are illustrated in those figures.

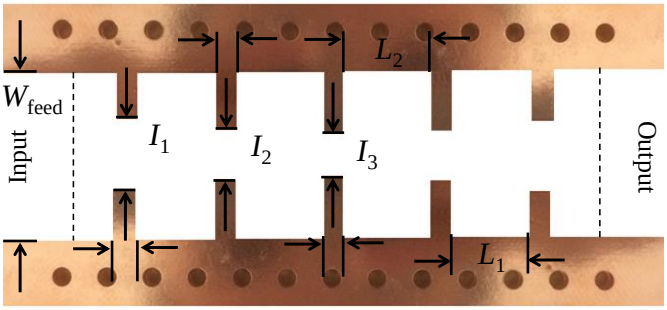

Fig. 5.29. Photographs of the fabricated temperature-uncompensated dielectric-less fourth-order filter (with W_{feed} = 13 mm, I_1 = 5.369 mm, I_2 = 3.309 mm, I_3 = 3.073 mm, L_1 = 7.246 mm and L_2 = 7.978 mm).

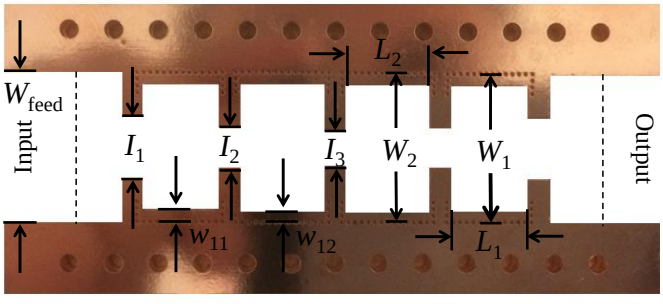

Fig. 5.30. Photographs of the fabricated self-temperature-compensated fourth-order filter (with W_{feed} = 13 mm, I_1 = 5.49 mm, I_2 = 3.389 mm, I_3 = 3.132 mm, w_{11} = 0.76 mm, w_{12} = 0.71 mm, W_1 = 12.674 mm, W_2 = 12.674 mm, L_1 = 6.85 mm and L_2 = 7.56 mm).

5. 3. 3. 2 Experimental Results at Ambient Temperature

The assembled double slab self-temperature-compensated AFSIW filter on the developed WR-51 test fixture is shown in Fig. 5.31.

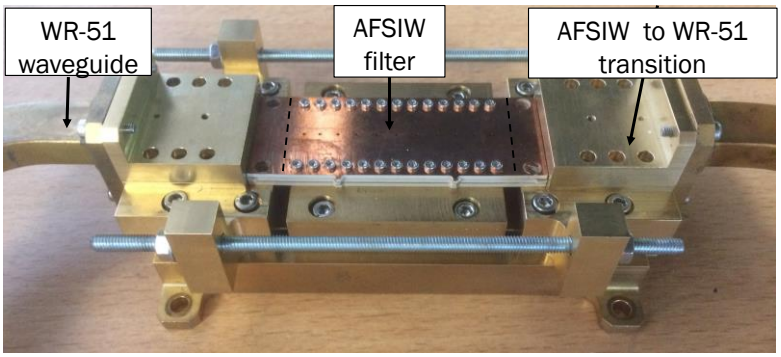

Fig. 5.31. Fabricated double slab self-temperature-compensated fourth-order AFSIW filter mounted on the WR-51 test fixture.

Results obtained in simulation and experiment at T_a for both fabricated fourth-order filters are compared in Fig. 5.32 and Fig. 5.33. Having taken into account the lesson learned from the first fabrication run, it can be observed that a good agreement between simulated and measured results is obtained for both filters. Reflection coefficients in the pass band of better than 20 dB are achieved in the experiment without involving any post-process tuning. Simulated and measured results are compared in Table 5.6. The dielectric-less filter achieves an insertion loss of 0.7 dB, while the double slab self-temperature-compensated AFSIW filter has an insertion loss of 1.08 dB.

It can be observed in Fig. 5.32 and Fig. 5.33, that the measured filter bandwidth is about 10% higher than in the simulation. This is due to the PCB process tolerances. However, simulated and measured insertion losses are in good agreement for both filters.

TABLE 5.6
COMPARISON OF SIMULATED AND MEASURED PERFORMANCES AT AMBIENT TEMPERATURE OF THE PROTOTYPED FOURTH-ORDER FILTERS

Performances ($@T_a$)	Uncompensated filter		Compensated filter	
	Simulated	Measured	Simulated	Measured
Return loss (dB)	> 25	> 20	> 25	> 20
Insertion loss (dB)	0.76	0.70	1.05	1.08
-3 dB bandwidth (MHz)	300	331	300	327

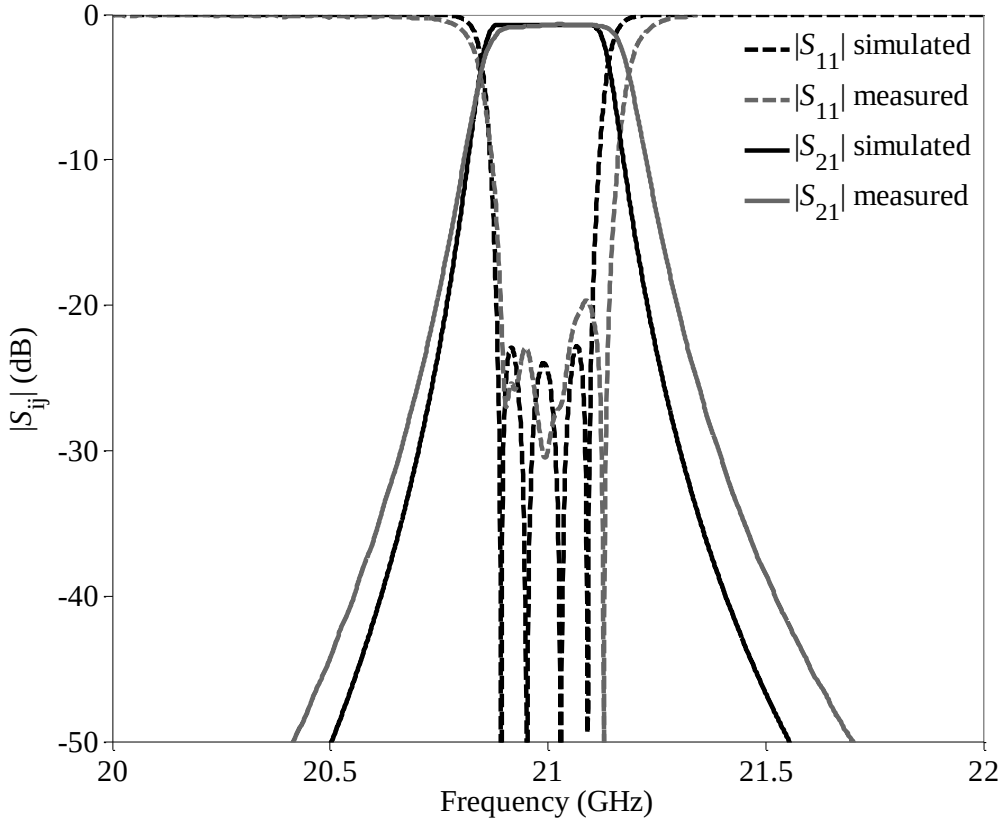

Fig. 5.32. Measured and simulated temperature-uncompensated dielectric-less fourth-order filter S-parameters at T_a.

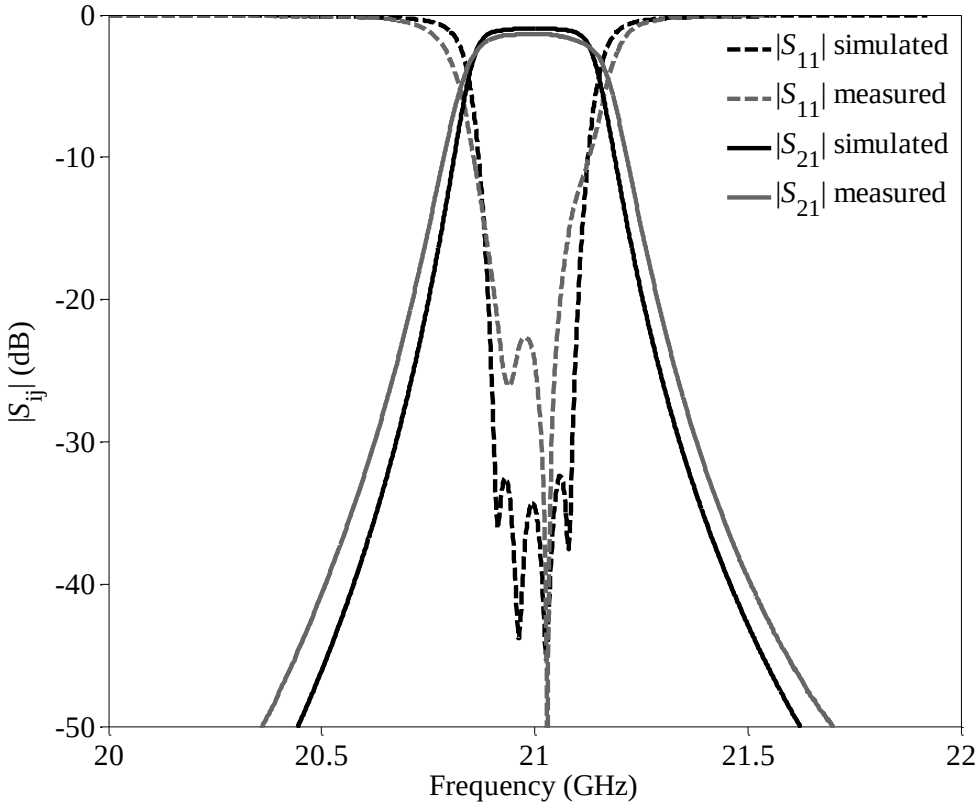

Fig. 5.33. Measured and simulated self-temperature-compensated fourth-order AFSIW filter S-parameters at T_a.

5. 3. 3. 3 Experimental Results Versus Temperature Variation

Measurements of the temperature-uncompensated dielectric-less filter and the double slab self-temperature-compensated AFSIW filter are done in the climatic chamber in the -40 °C to 80 °C temperature range. Measured S-parameters at T_c, T_a and T_h, are shown in Fig. 5.34 and Fig. 5.35, respectively. A net improvement in thermal stability using the proposed technique is obtained. It can be observed that both filters achieve a reflection coefficient in the pass band that is better than 18 dB at all temperatures.

Simulated and measured results are reported in Table 5.7. The self-temperature-compensated filter shows a thermal stability of 2.3 ppm/°C at -40 °C and 1.7 ppm/°C at 80 °C, while the dielectric-less temperature-uncompensated filter has a thermal stability of -17.4 ppm/°C at -40 °C and -18.4 ppm/°C at 80 °C.

Fig. 5.36 shows the comparison in measurement between the two prototypes. It can be observed that temperature compensation is achieved at the cost of about 0.3 dB in insertion loss at 21 GHz using RT/6010LM substrate.

TABLE 5.7
MEASURED PERFORMANCES OF THE PROTOTYPED FOURTH-ORDER FILTERS

Performances	Uncompensated filter			Compensated filter		
Temperature	T_c	T_a	T_h	T_c	T_a	T_h
Centre frequency (GHz)	21.029	21.006	20.984	21	21.003	21.005
Centre frequency drift (MHz)	23	0	-22	-3	0	2
Centre frequency thermal stability, δ_f (ppm/°C)	-17.4	/	-18.4	2.3	/	1.7
Centre frequency shift, Δf (%) between -40 and +80°C	0.214			0.023		
-3 dB bandwidth (MHz)	331	334	333	328	336	338
Return loss (dB)	> 22	> 20	> 19	> 22	> 19	> 18
Insertion loss (dB)	0.61	0.7	0.74	0.83	1.08	1.15
Q_u	1759	1514	1449	1300	975	910

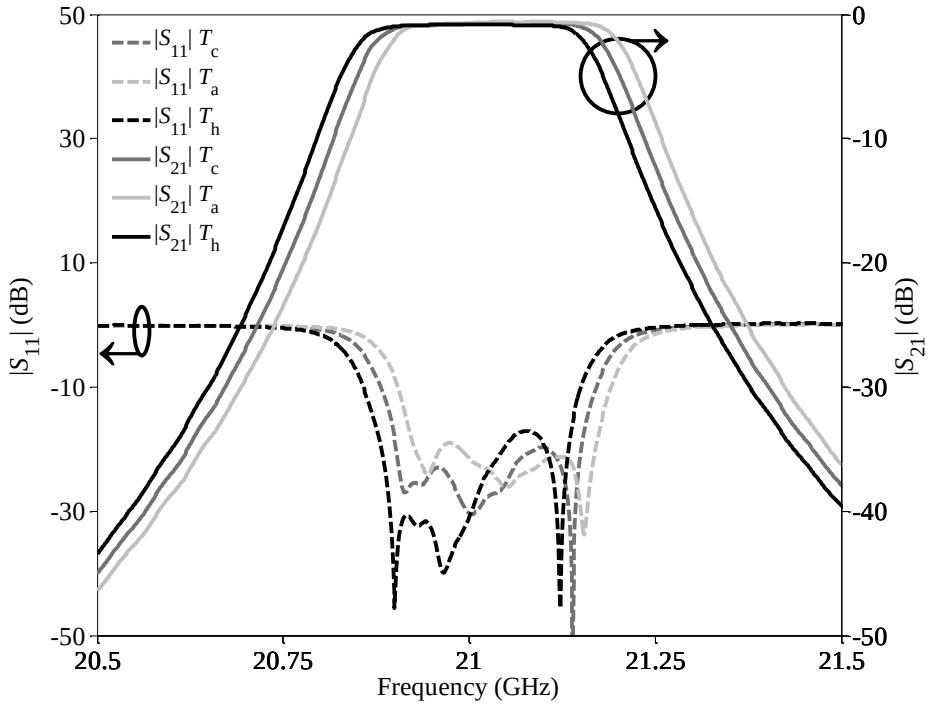

Fig. 5.34. Measured temperature-uncompensated dielectric-less fourth-order filter S-parameters at T_c, T_a and T_h.

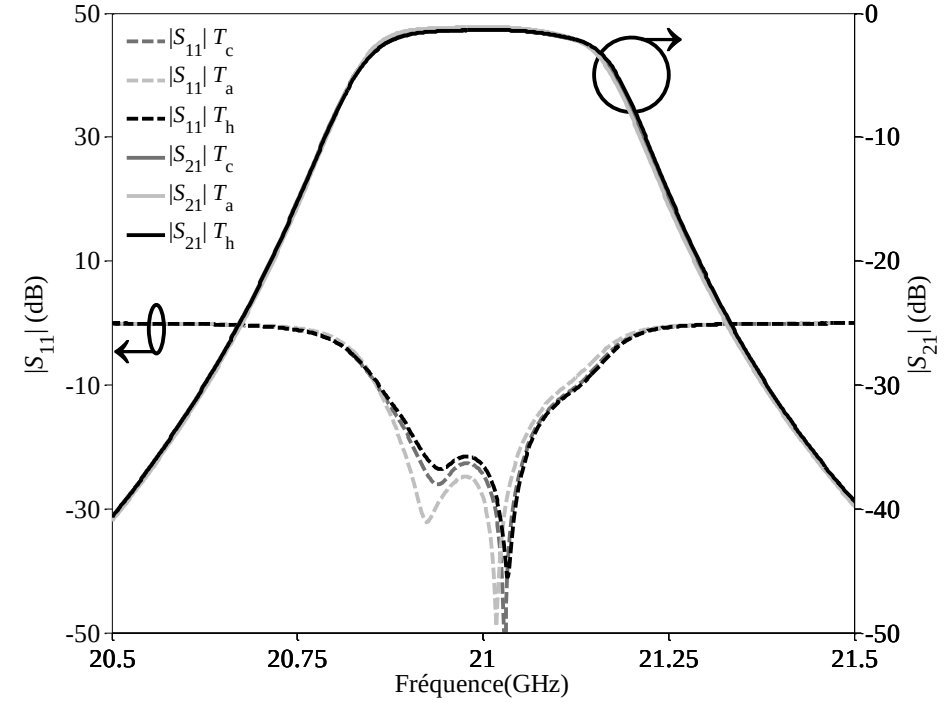

Fig. 5.35. Measured double slab self-temperature-compensated fourth-order AFSIW filter S-parameters at T_c, T_a and T_h.

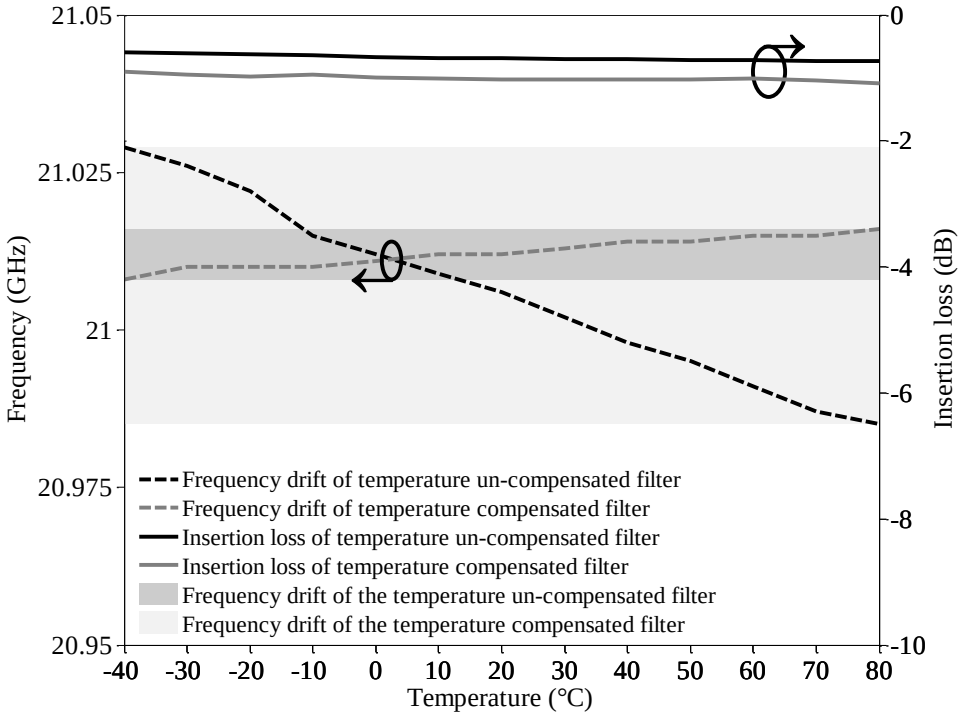

Fig. 5.36. Measured center frequency and insertion loss of the temperature-uncompensated dielectric-less fourth-order filter and double slab self-temperature-compensated fourth-order AFSIW filter versus temperature.

5. 4. Conclusions

In this Chapter, two novel temperature compensation techniques for AFSIW cavities and filters are theoretically studied and validated from simulated and experimental results. The proposed techniques can be implemented in the conventional filter configurations (in-line arrow, in-line folded, folded…). Moreover, the thermal drift of the resonators coupling and transmission zeros created by non-adjacent resonators coupling (cross-coupling) are discussed, and demonstrated to be negligible compared to the thermal drift of uncompensated resonators. Furthermore, a post-process temperature compensation tuning technique is introduced to counterbalance fabrication errors. For demonstration purposes, single and double slab self-temperature-compensated AFSIW filters, operating in the Ku- and Ka-band, have been designed, fabricated, and measured. The two fabricated filters demonstrate a nearly perfect stability over the -20 to 70 °C, and the -40 to 80 °C, respectively. The temperature compensation techniques are implemented on filters but can be implemented in the design of thermally stable IMUX for the emerging low-cost and high-performance satellite communication systems for the new space applications. This principle was patented with the IMS Research Center and Cobham Microwave [21].

References

[1] A. E. Atia, "A 14-GHz high-power filter," *IEEE MTT-S Int. Microw. Symp.*, Orlando, FL, USA, 1979, pp. 261-261.

[2] S. J. Fiedziuszko, "Dual-mode dielectric resonator loaded cavity filters," *IEEE Transactions on Microwave Theory and Techniques*, vol. 30, no. 9, pp. 1311-1316, Sep. 1982.

[3] C. Kudsia, R. Cameron, and W. C. Tang, "Innovations in microwave filters and multiplexing networks for communications satellite systems," *IEEE Transactions on Microwave Theory and Techniques*, vol. 40, no. 6, pp. 1133-1149, Jun. 1992.

[4] Yidong Wang and Qiang Sui, "A new temperature compensation method of rectangular waveguide resonant cavities," *Asia-Pacific Microw. Conf.*, Suzhou, 2005, pp. 4-8.

[5] B. F. Keats, R. R. Mansour, and R. B. Gorbet, "Design and testing of a thermally stable filter using bimetal compensation," *IEEE MTT-S International Microwave Symposium*, Honolulu, HI, 2007, pp. 1293-1296.

[6] S.-W. Chen, K. A. Zaki, and R. F. West, "Tunable, temperature-compensated dielectric resonators and filters," *IEEE Transactions on Microwave Theory and Techniques*, vol. 38, pp. 1046–1052, Aug. 1990.

[7] Jilong Ju, "A novel configuration of temperature compensation in the resonant cavities", *IEEE Transactions on Microwave Theory and Techniques*, vol 52, pp. 139-143, Jan. 2004.

[8] S. Adhikari, A. Ghiotto, and K. Wu, "Simultaneous electric and magnetic two-dimensionally tuned parameter-agile SIW devices," *IEEE Transactions on Microwave Theory and Techniques*, vol. 61, no. 1, pp. 423-435, Jan. 2013.

[9] C. Tomassoni, L. Silvestri, A. Ghiotto, M. Bozzi, and L. Perregrini, "Substrate integrated waveguide filters based on dual-mode air-filled resonant cavities," *IEEE Transactions on Microwave Theory and Techniques*, vol. 66, no. 2, pp. 726-736, Fev. 2018.

[10] L. Silvestri, A. Ghiotto, C. Tomassoni, M. Bozzi, and L. Perregrini, "Partially air-filled substrate integrated waveguide filters with full control of transmission zeros," *IEEE Transactions on Microwave Theory and Techniques*, vol. 67, no. 9, pp. 3673 - 3682, Sep. 2019.

[11] Y. Cassivi, L. Perregrini, P. Arcioni, M. Bressan, K. Wu, and G. Conciauro, "Dispersion characteristics of substrate integrated rectangular waveguide," *IEEE Microw. Wireless Compon. Lett.*, vol. 12, no. 9, pp. 333-335, Sep. 2002.

[12] S. B. Cohn, "Direct-coupled-resonator filters," Proc. IRE, vol. 45, pp. 187–196, Feb. 1957.

[13] P. Couffignal, H. Baudrand and B. Theron, "A new rigorous method for the determination of iris dimensions in dual-mode cavity filters," *IEEE Transactions on Microwave Theory and Techniques*, vol. 42, no. 7, pp. 1314-1320, Jul. 1994.

[14] B. F. Keats, "Bimetal temperature compensation for waveguide microwave filters", Ph.D dissertation, School of Elect. and Comp. Eng., Waterloo Univ., Waterloo, 2007.

[15] R. J. Cameron, C. M. Kudsia, and R. R. Mansour, *Microwave Filters for Communication Systems*, Hoboken, NJ, USA: Wiley, 2007, ch. 14, pp. 501-530.

[16] T. Martin, A. Ghiotto, T.P. Vuong, F. Lotz, and K. Wu "Compact quasi-elliptic and highly selective AFSIW filter with multilayer cross-coupling," *IEEE MTT-S International Microwave Symposium*, Boston, MA, USA, 2019, pp. 718-721.

[17] T. Martin, A. Ghiotto, A. Marque, T.P. Vuong, F. Lotz, P. Monteil, and L. Carpentier "Broadband air-filled SIW to waveguide transition for interconnect, instrumentation and measurement applications," *IEEE MTT-S International Microwave Workshop Series on Advanced Materials and Processes*, Italy, Pavia, Sep. 2017.

[18] V. Turgaliev, D. Kholodnyak, J. Mueller, and M. A. Hein, "Small-size low-loss bandpass filters on substrate-integrated waveguide capacitively loaded cavities embedded in low temperature co-fired ceramics," *J. Ceram. Sci. Technol.*, vol. 6, no. 4, pp. 305–314, 2015.

[19] M. Schallner, "Temperature compensated planar narrowband notch filter with fully automated laser-trimming," *IEEE MTT-S International Microwave Symposium*, Phoenix, AZ, Jun. 2001, pp. 1919-1922.

[20] T. Martin, A. Ghiotto, T.P. Vuong, F. Lotz, and P. Monteil, "High performance air-filled substrate integrated waveguide filter post-process tuning using capacitive post," *IEEE MTT-S International Microwave Symposium*, Hawaii, HI, Jun. 2017, pp. 196-199.

[21] A. Ghiotto, F. Lotz et T. Martin, "Composant micro-ondes et procédé de fabrication associé", dépôt brevet d'invention / patent registration, FR 17 63412, Dec. 2017.

Chapter 6

Very Compact IMUX for Broadband Applications

Previous Chapters have dealt with the demonstration of high-performance filters using the AFSIW technological platform. In this Chapter, the previously demonstrated principles are implemented in a multiport network, also called multiplexer. The proposed input multiplexer consists of 4 channel filters coupled with a manifold. The IMUX is foreseen to be implemented in the future generation of satellite payload, and thus is subjected to space environmental requirements such as operating temperature range, vibration levels, and shock levels. The specifications, the chosen configuration, and the simulated results are presented in this Chapter. Unfortunately, the measured results were not yet completed at the time this Chapter was written. Hopefully, the measurements will be presented during the oral presentation of this Doctoral thesis.

6. 1. Background and Objectives

Different configurations of input multiplexers are employed in multibeam payloads where the received signals pass through different frequency conversions before high-power amplification. In many payload configurations, an input multiplexer is placed after the frequency conversion. This leads to a large number of wideband multiplexers that are required and hence mass and volume are critical design drivers for the multiplexer channel filters.

Additionally, due to the frequency re-use in broadband systems, a high number of identical multiplexers are required. Significant size and mass reduction potential, while keeping the required RF performance (in-band flatness, group delay, rejection, etc.), has been demonstrated thanks to new circuit theories developed in recent years. These enable their implementation with an alternative technology allowing the development of low-cost and compact input multiplexer.

The objective of this Chapter is to develop a compact Ku-band input multiplexer for broadband applications. An engineering model of a four-channel multiplexer shall be manufactured and tested to fully validate the developed novel concepts.

6. 2. Design Specifications

The specification of the IMUX are given in Table 6.1, where the centre frequencies, bandwidth, near rejection, insertion loss variation, group delay variation, out-of-band rejection, and in-band return loss are detailed. The IMUX is composed of four channel filters, the two “outer” channel filters and the two “inner” channel filter have a bandwidth of 500 MHz and 236 MHz, respectively. Moreover, the environmental specifications given in Table 6.2 require the IMUX to be operating in the -20 °C to 70 °C temperature range.

TABLE 6.1
SPECIFICATION OF THE REQUIRED KU-BAND IMUX

Specification	Value		
Frequency plan and channel bandwidths	Channel	Central frequency (GHz)	Bandwidth (MHz)
	Ch01	12.45	500
	Ch02	12.05	236
	Ch03	11.795	236
	Ch04	11.395	500
236 MHz channels			
Maximum centre insertion loss	10 dB		
Insertion loss stability over lifetime and temperature range (at f_c)	1 dBpp		
Near rejection	f_c ± 144 MHz	20 dB	
	f_c ± 380 MHz	40 dB	
	f_c ± 430 MHz	40 dB	
Insertion loss variation	f_c ± 70 MHz	0.25 dBpp	
	f_c ± 100 MHz	0.4 dBpp	
	f_c ± 118 MHz	1.1 dBpp	
Group delay variation	f_c ± 70 MHz	3 nspp	
	f_c ± 100 MHz	6 nspp	
	f_c ± 118 MHz	20 nspp	
500 MHz channels			
Maximum centre insertion loss	10 dB		
Insertion loss stability over lifetime and temperature range (at f_c)	1 dBpp		
Near rejection	f_c ± 300 MHz	20 dB	
	f_c ± 800 MHz	40 dB	
	f_c ± 900 MHz	40 dB	
Insertion loss variation	f_c ± 150 MHz	0.25 dBpp	
	f_c ± 200 MHz	0.4 dBpp	
	f_c ± 250 MHz	1.1 dBpp	
Group delay variation	f_c ± 150 MHz	3 nspp	
	f_c ± 200 MHz	6 nspp	
	f_c ± 250 MHz	20 nspp	
All channels			
Out-of-band rejection	1 – 10.5 GHz	60 dB	
	13.2 – 27 GHz	60 dB	
	27 – 30 GHz	35 dB	
In-band input return loss	> 20 dB		
In-band output return loss	> 20 dB		
Mass	To be minimized		
Volume	To be minimized		

TABLE 6.2
ENVIRONMENTAL REQUIREMENTS

Temperature	Value
Operating temperature range	-20 °C to 70 °C
Non-operating temperature range	-30 °C to 90 °C

6. 3. IMUX Configuration

In a satellite communication, a multiplexer is required for separation or combination of different frequency bands [1]. The different IMUX configurations are detailed in [2], a simple trade-off sum up is given in Table 6.3. The aim of this thesis is not to explain all the possible configurations of an IMUX. The readers are

invited to read the extensive work made in this area [1]-[9]. The chosen configuration is based on a manifold coupled approach. It is composed of bandpass filters, corresponding to channel filters, interconnected with a manifold using a transmission line. In this configuration, channel filters are not isolated from each other, in other words, a signal of a given channel filter will perturb the response of the other channels. Nevertheless, this approach is widely implemented in many space applications as it offers the best trade-off in terms of miniaturization and absolute insertion loss in the channel filters. By saving mass and being compact, it also allows to save money for the launch of the satellite payload. Therefore, the manifold-coupled configuration is identified as the most compact design with optimum performances over other multiplexer configurations for the desired specifications. This configuration has several geometrical structures represented in Fig. 6.1. In the detailed application, as a requirement is to minimize the total volume of the IMUX, the herringbone configuration is chosen.

TABLE 6.3
COMPARISON OF MULTIPLEXER CONFIGURATION

Performances	Hybrid-coupled MUX [1],[2]	Hybrid-branched MUX [1],[2]	Circulator-coupled MUX [1],[2]	Directional filter MUX [1],[2]	Star-junction MUX [2]	Manifold-coupled MUX [1],[2]
Insertion loss (without filters)	Medium	High	Medium	Low	Low	Low
Modular concept	Yes	Yes	Yes	Yes	No	No
Interaction between channels	Low	None	None	Low	High	High
Assembly	Easy	Easy	Easy	Easy	Hard	Medium
Size	Large	Large	Large	Medium	Medium	Medium
Weight	High	Medium	High	Low	Low	Low
Cost	High	High	High	Medium	Low	Low
Design	Easy	Easy	Easy	Easy	Hard	Medium
Versatile	Yes	Yes	Yes	No	No	No
Number of channels	/	/	/	/	< 4	/

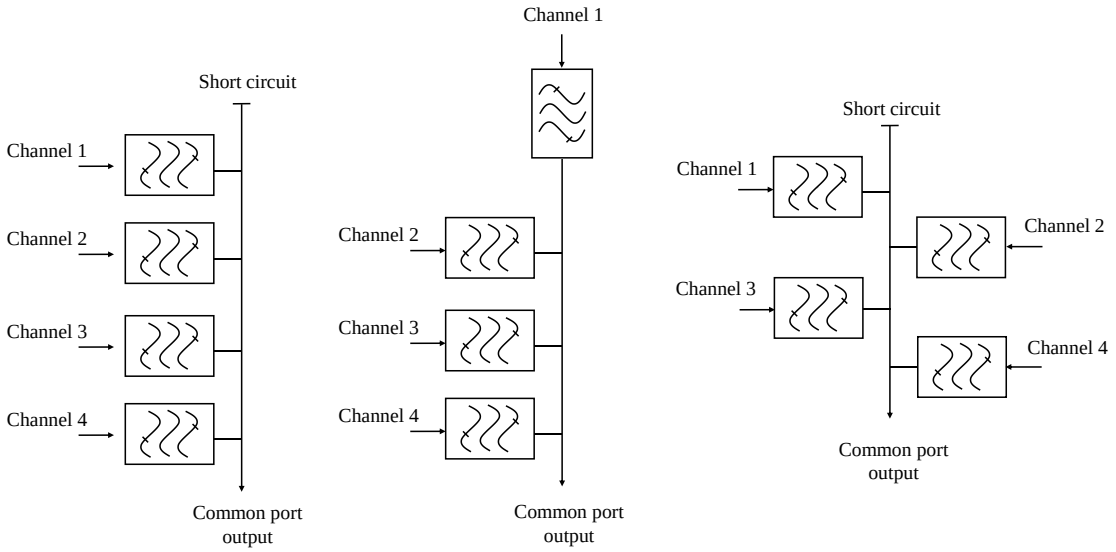

(*a*) (*b*) (*c*)

Fig. 6.1. Common geometrical structure for manifold-coupled multiplexer configurations: (*a*) comb, (*b*) one filter feeding directly into the manifold, and (*c*) herringbone [1].

6. 4. IMUX Design

The design method employed for the IMUX is conventional and consists in designing the different channel filters, then combine them with a manifold, to finally optimize the IMUX with standard procedures explained in [1].

6. 4. 1 Channel Filters

The four individual channel filters are designed to have an ideal response. The design is based on the methodology presented in Chapters 4 [10] and 5 [11]. In order to be compliant with the specifications in terms of near-rejection, the proposed topology for channel filters is a seventh-order filter, introducing a pair of transmission zeros located below and above the passband thank to cross-couplings, and implementing a single slab self-temperature-compensation on each cavity of the filter. The temperature compensation allows reducing the margins on the near-rejection to be compliant with the required specifications, hence minimizing the footprint of the IMUX.

The methodology to design the channel filters is the same presented in Chapter 4 and Chapter 5. All the channel filters are based on a multilayer PCB consisting of a Rogers RT/Duroid 6002 substrate with thickness h_1 = 0.508 mm, a Rogers RT/Duroid 6010 with h_2 = 1.905 mm, and a Hi-*Tg* FR4 substrate with h_3 = 1.524 mm. The geometric configuration of the proposed structure is given in Fig. 6.2. The dimensions of the 4 channel filters are reported in Table 6.4.

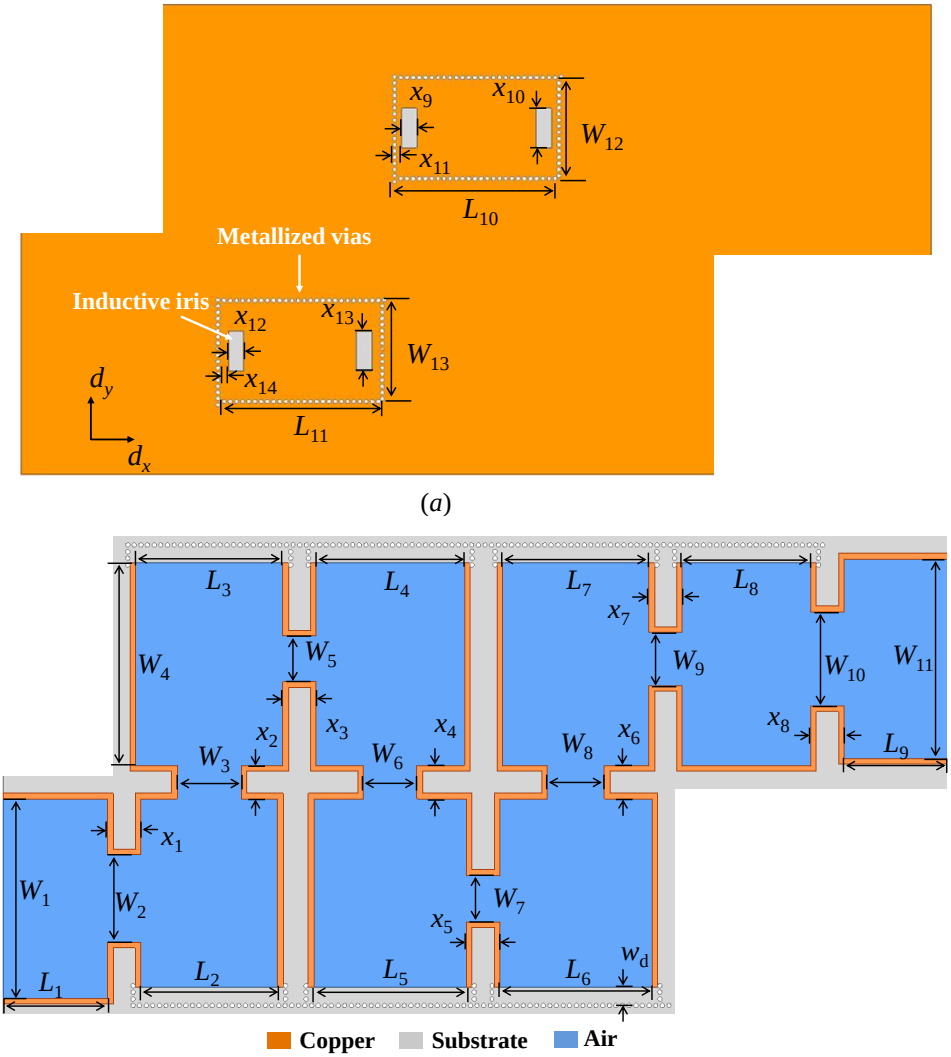

Fig. 6.2. Top views of (*a*) substrate 1, implementing the secondary path with the 1-4 and 3-6 cross-couplings, and (*b*) substrate 2 implementing the primary path of the quasi-elliptic folded filter.

TABLE 6.4
DIMENSIONS OF THE DESIGNED AFSIW CHANNEL FILTERS WITH W_D = 1.5 MM

Dimension	i = 1	i = 2	i = 3	i = 4	i = 5	i = 6	i = 7	i = 8	i = 9	i = 10	i = 11	i = 12	i = 13	i = 14
Channel 1														
L_i (mm)	10	11.94	13.2	13.33	13.62	13.64	13.22	11.71	10	14.23	13.87	/	/	/
x_i (mm)	2	2	2	2	2	2	2	2	1.5	4.11	0.75	1.5	4.11	0.75
W_i (mm)	19.05	9.78	8.8	20.3	6.1	7.33	6.09	7.53	6.45	9.62	19.05	10	10	/
Channel 2														
L_i (mm)	10	13.42	14.38	14.45	14.85	14.83	14.28	12.67	10	15.84	15.41	/	/	/
x_i (mm)	2	2	2	2	2	2	2	2	1.5	3.77	0.75	1.5	3.77	0.75
W_i (mm)	19.05	8.93	6.8	20.3	5.15	5.84	5.21	6.14	5.81	9.52	19.05	10	10	/
Channel 3														
L_i (mm)	10	13.83	14.84	14.94	15.4	15.41	14.86	13.51	10	16.5	15.79	/	/	/
x_i (mm)	2	2	2	2	2	2	2	2	1.5	3.65	0.75	1.5	3.65	0.75
W_i (mm)	19.05	9.25	6.95	20.3	5.29	5.9	5.29	6.03	5.57	9.03	19.05	10	10	/
Channel 4														
L_i (mm)	10	13.68	15.06	15.26	15.76	15.73	15.1	13.3	10	17.75	17.16	/	/	/
x_i (mm)	2	2	2	2	2	2	2	2	1.5	5.36	0.75	1.5	5.36	0.75
W_i (mm)	19.05	10.64	8.85	20.3	6.74	7.46	6.78	7.46	6.78	10.49	19.05	10	10	/

To ensure the respect of the different requirements, the simulated responses are plotted together with the desired specifications. It can be observed in Fig. 6.3 that the near-rejection specifications are respected for the four individual channels. For the insertion loss variations, Fig. 6.4 shows that the responses are compliant with the prescribed requirements. Finally, the group delay variation specifications and the comparison with the simulations are presented in Fig. 6.5. It can be observed that the different channel filters have a good behavior in group delay variation.

The four channel filters are based on single slab self-temperature-compensated cavities. Thus, the different channel filters have a centre frequency thermal stability of less than 1 ppm/°C and a transmission zero position thermal stability of less than 3 ppm/°C, ensuring the good behavior of the filters in the operating temperature range (-20 °C to 70 °C).

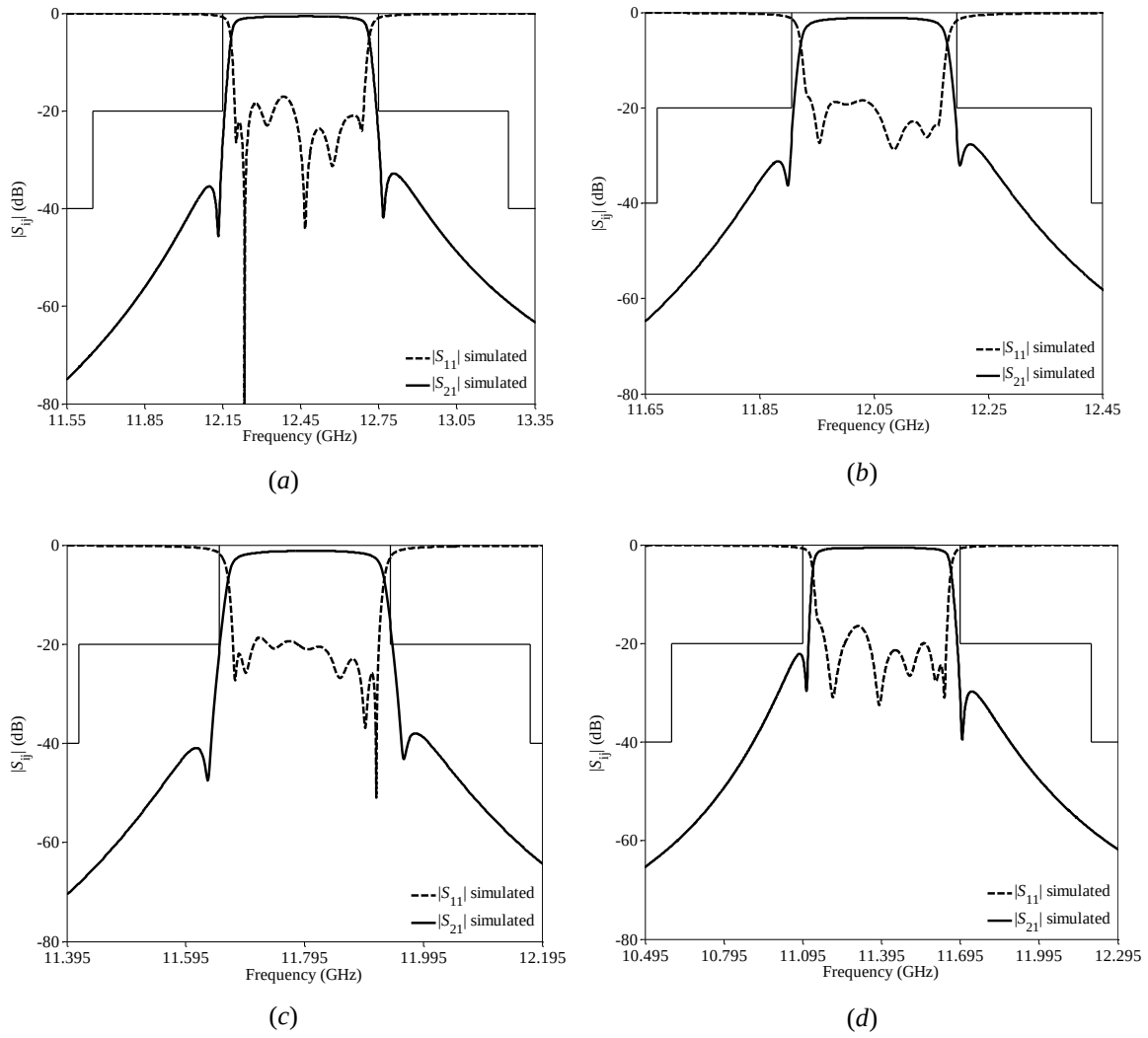

Fig. 6.3. Simulated S-parameters of the (*a*) channel 1, (*b*) channel 2, (*c*) channel 3, and (*d*) channel 4 with the specification masks.

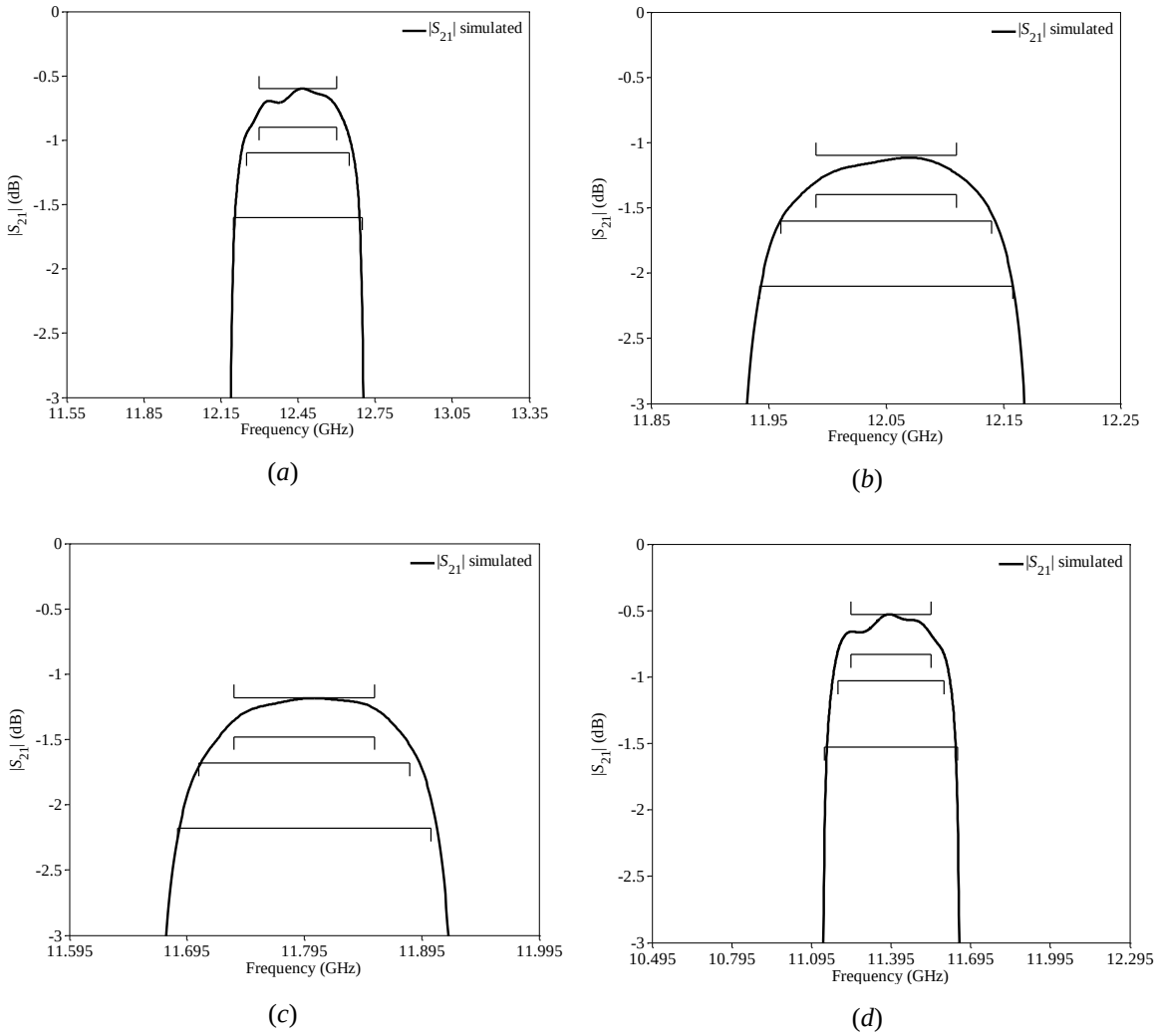

Fig. 6.4. Simulated insertion loss variation of the (*a*) channel 1, (*b*) channel 2, (*c*) channel 3, and (*d*) channel 4 with the specification masks.

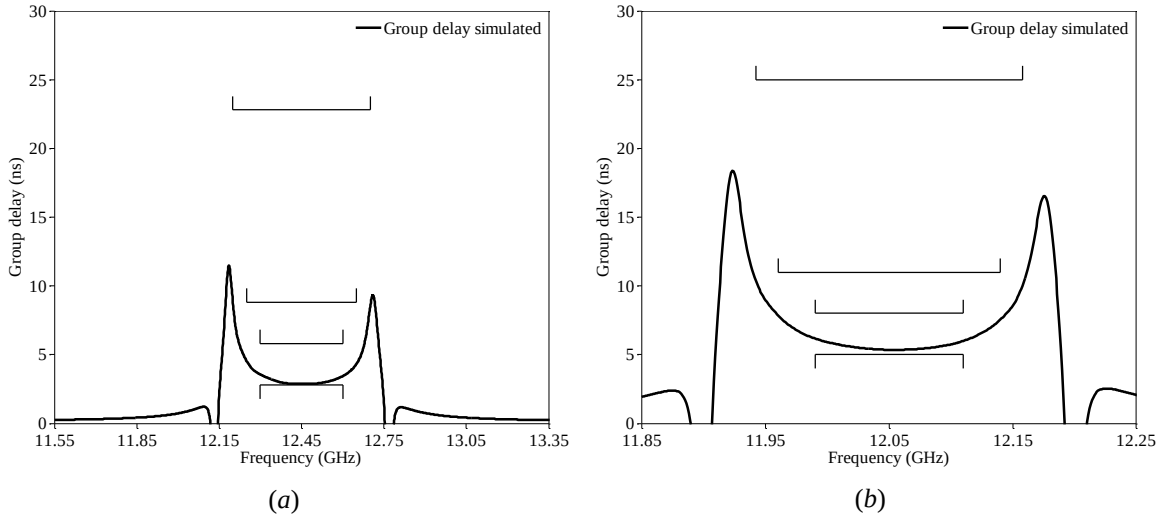

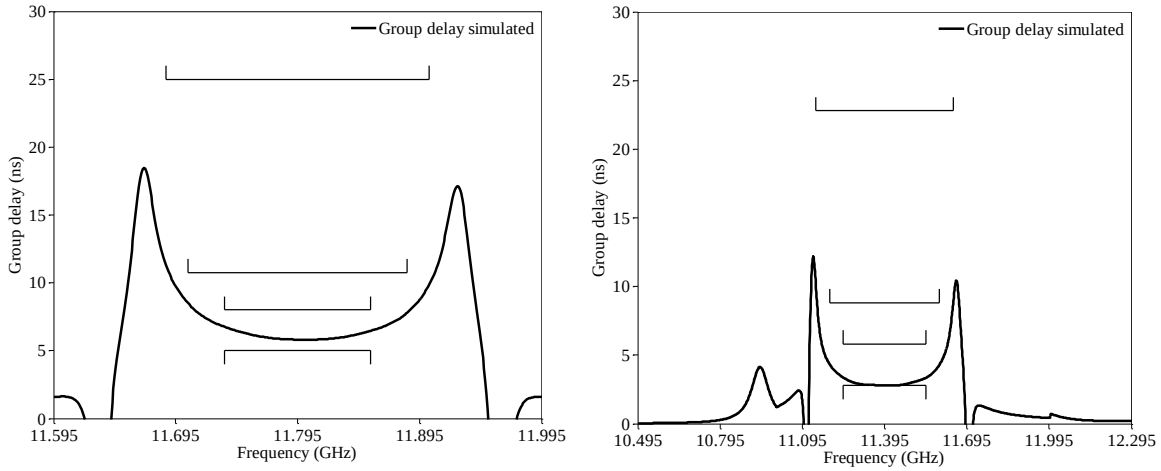

(*c*) (*d*)

Fig. 6.5. Simulated group delay variation of the (*a*) channel 1, (*b*) channel 2, (*c*) channel 3, and (*d*) channel 4 with the specifications mask.

6. 4. 2 Manifold Coupled Channel Filters

Once the different channel filters are designed and fulfill the desired requirements, a manifold is used to couple the filters, thus achieving the function of IMUX. To connect the filters, the herringbone configuration has been chosen. This configuration is of a particular interest as it allows minimizing the total footprint of the IMUX. Moreover, this configuration is well suited for in-line folded configuration as it allows reducing the electric length between two adjacent channels.

A manifold is a low loss propagation medium, in this particular case, AFSIW transmission line sections, acting as AFSIW H-plane T-junctions. As the relative bandwidths of the channel filters are medium (around 2% for channels 2 and 3 and 4% for channels 1 and 4) and as the channel are continuous, it is convenient to have short transmission line sections between the adjacent channels to minimize or suppress the unwanted resonance in the desired frequency range. Usually, the channel filters are organized along the manifold taking into account their centre frequencies. This was applied to this IMUX as the channel with the highest centre frequency is the further away from the common port of the manifold.

Conventionally, an input cavity is implemented between the manifold and the different channel filters. This cavity makes it easier for the designer to have a correct matching for the overall response of the IMUX, without changing too much the dimensions of the filters. In this application, the channel filters were connected directly to the manifold, as shown in Fig. 6.6, in order to minimize the total footprint and the unwanted resonances due to the manifold connections. The procedure explained in [1] is then followed to place the t channel filters. A conventional optimization is then run to achieve the desired response.

The geometric configuration of the proposed IMUX is shown in Fig. 6.6. Due to industrial intellectual property constraints, the dimensions cannot be given. The IMUX, as the channel filters, is based on three stacked PCB layers made of a Rogers RT/Duroid 6002 substrate with thickness $h_1 = 0.508$ mm, a Rogers RT/Duroid 6010 with $h_2 = 1.905$ mm, and a Hi-*Tg* FR4 substrate with $h_3 = 1.524$ mm.

The Engineering Model of the IMUX is being fabricated during the writing of this thesis, therefore, it is not possible yet to present the measured results. However, simulated results are presented hereunder. Fig. 6.7

represents the response of the IMUX in the 10.2 - 13.2 GHz. Taking into consideration the specifications of Table 6.1, the simulated IMUX is compliant with the channel filters specifications such as the maximum centre insertion loss, near-rejection, insertion loss variation, and group delay variation. For the operating temperature range, as the channel filters are self-temperature compensated and as the manifold has a negligible impact on the centre frequency of the channel filters, it is assumed the IMUX has an operating temperature range from -20 °C to 70 °C.

Nevertheless, from simulations, it can be stated that the wideband response of the IMUX is not compliant with the required out-of-band rejections (13.2 – 27 GHz at -60 dB and 27 – 30 GHz at 35 dB). Additional details concerning the implementation of the first AFSIW low-pass filter will be given during the oral presentation as it is a sensitive subject for the industrial partner of this thesis.

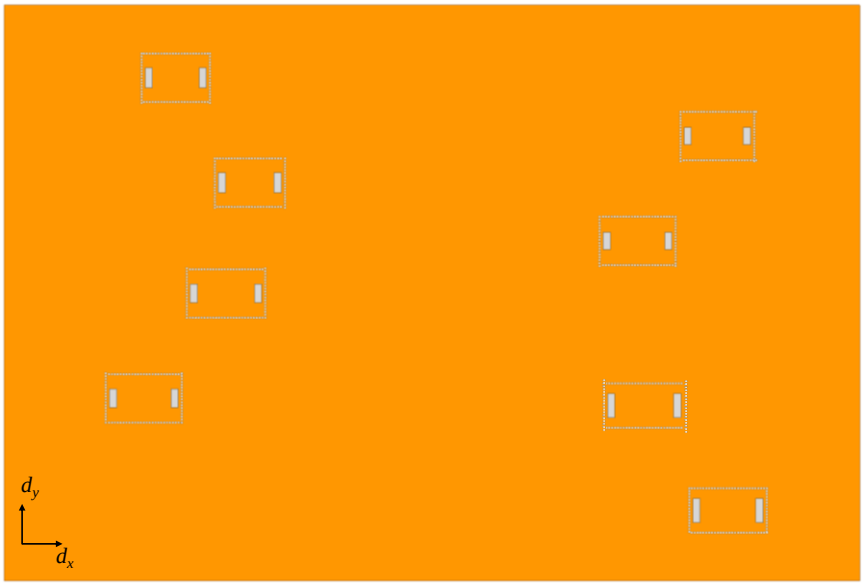

(*a*)

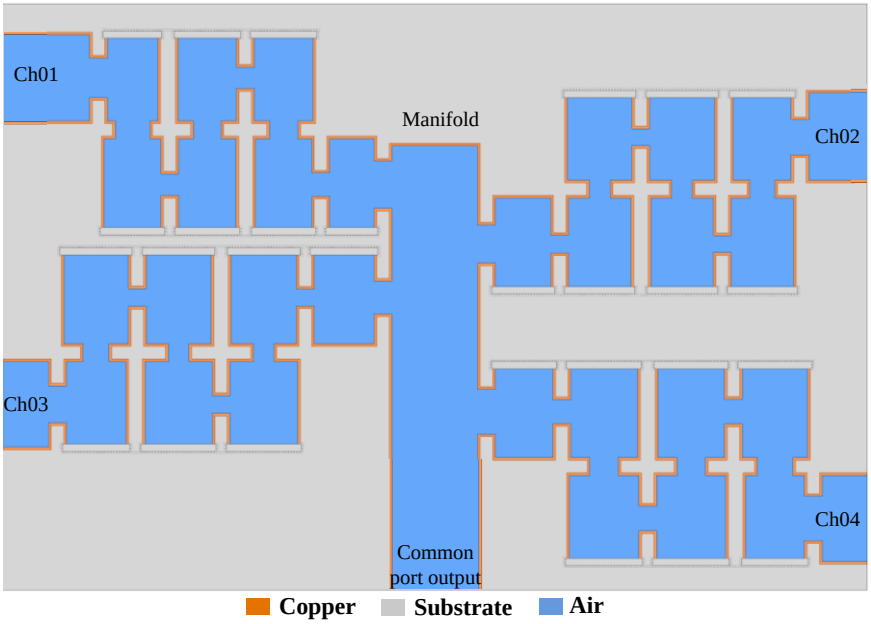

(*b*)

Fig. 6.6. Top views of (*a*) substrate 1, implementing the secondary paths with the cross-couplings, and (*b*) substrate 2 implementing the primary path of the proposed IMUX.

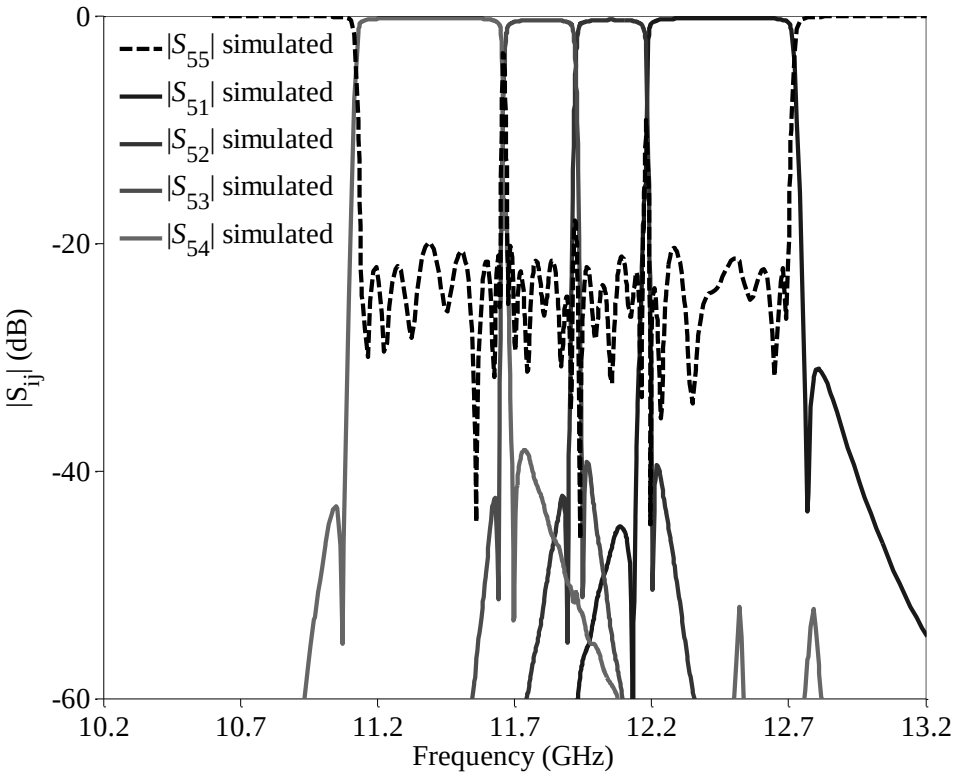

Fig. 6.7. Simulated S-parameters of the proposed AFSIW IMUX.

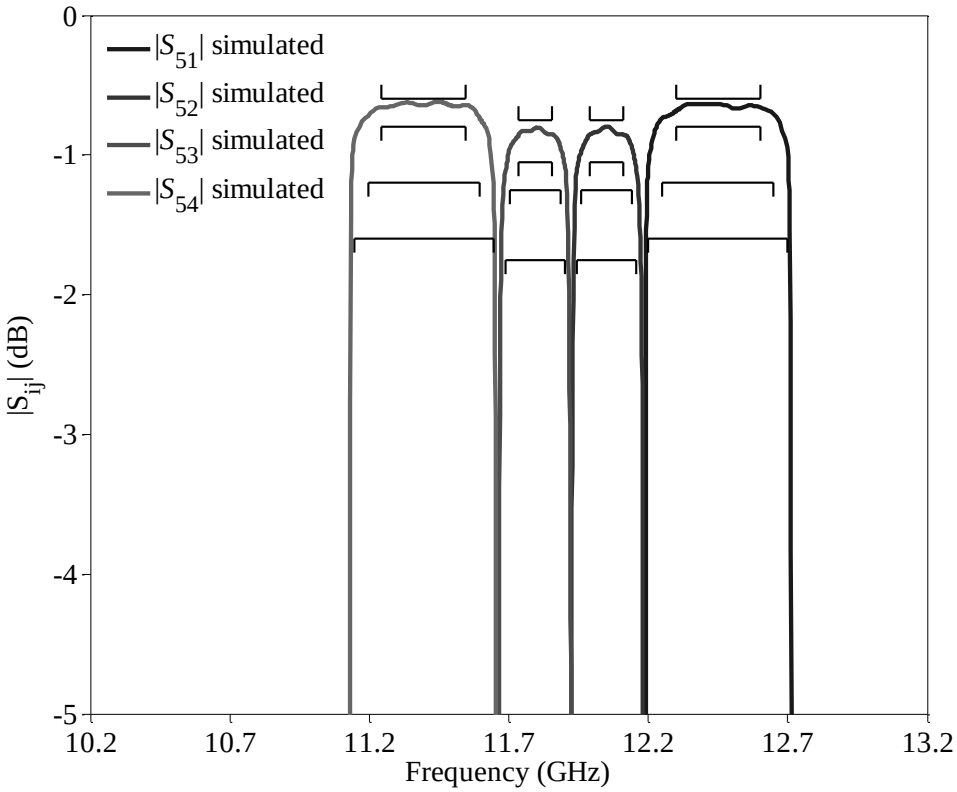

Fig. 6.8. Simulated insertion loss variation of the proposed AFSIW IMUX.

Due to the stringent specifications, the fabrication EM is supposed to implement post-process tuning to be able to tune the channel filters, as described in [12]. It is also possible to implement the frequency tuning explained in [13] to add a degree of freedom for the fine-tuning phase.

6. 5. Conclusions

In this Chapter, the first Input Multiplexer (IMUX) based on the AFSIW technology is presented. The IMUX implements 4 channel filters coupled by a manifold and operates in the Ku-band. The channel filters of the proposed IMUX are designed taking into considerations the principles developed in Chapters 2, 4 and 5. Hence, the channel filters are based on the AFSIW technology, with the introduction of transmission zeros thank to cross-couplings, and with the implementation of a single slab to self-temperature-compensate the filters in the -20 °C to 70 °C temperature range. The channel filters are coupled with a manifold, also based on the AFSIW technology. To maximize the compactness of the structure, the herringbone configuration was chosen to save money for the launch of the payload. The high interest of the technology is highlighted with this type of component as it is possible to fabricate the entire sub-system with single PCB fabrication. With the proposed IMUX, a filtering System-on-Substrate (SoS) is introduced. The concept is foreseen to be extended implementing other passive functions, such as circulators or isolators. In this Chapter, due to fabrication time, only simulated results were presented. Nevertheless, the measured results of the proposed IMUX should be presented during the oral presentation of this Doctoral thesis.

References

[1] J. Uher, J. Bornemann, and U. Rosenberg, *Waveguide Components for Antenna Feed Systems—Theory and CAD*. Norwood, MA: Artech House, 1993.

[2] R. J. Cameron, C. M. Kudsia, and R. R. Mansour, *Microwave Filters for Communication Systems*, Hoboken, NJ, USA: Wiley, 2007, ch. 14, pp. 501-530.

[3] G. Matthaei, L. Young, and M.T. Jones, *Microwave Filters, Impedance Matching Networks and Coupling Structures*. Norwood, MA: Artech House, 1985.

[4] E.G. Cristal and G.L. Matthaei, "A technique for the design of multiplexers having contiguous channels," *IEEE Transactions on Microwave Theory and Techniques*, vol. MTT-10, pp. 88–93, Jan. 1964.

[5] A.E. Atia, "Computer aided design of waveguide multiplexers," *IEEE Transactions on Microwave Theory and Techniques*, vol. MTT-22, pp. 322–336, Mar. 1974.

[6] J.D. Rhodes and R. Levy, "Design of general manifold multiplexers *IEEE Transactions on Microwave Theory and Techniques*, vol. 27, no. 2, pp. 111–123, Feb. 1979.

[7] J.D. Rhodes and R. Levy, "A generalized multiplexer theory," *IEEE Transactions on Microwave Theory and Techniques*, vol. 27, no. 2, pp. 99–111, Feb. 1979.

[8] J. Bandler, S. Daijavad, and Q.-J. Zhang, "Exact simulation and sensitivity analysis of multiplexing networks," *IEEE Transactions on Microwave Theory and Techniques*, vol. MTT-34, pp. 111–102, Jan. 1986.

[9] C. Kudsia, R. Cameron, and W.C. Tang, "Innovation in microwave filters and multiplexing networks for communication satellite systems," *IEEE Transactions on Microwave Theory and Techniques*, vol. MTT-40, pp. 1133–1149, Jun. 1992.

[10] T. Martin, A. Ghiotto, T.P. Vuong, F. Lotz, and K. Wu "Compact quasi-elliptic and highly selective AFSIW filter with multilayer cross-coupling," *IEEE MTT-S International Microwave Symposium*, Boston, MA, USA, 2019, pp. 718-721.

[11] T. Martin, A. Ghiotto, T.P. Vuong, and F. Lotz, "Self-temperature-compensated air-filled substrate integrated waveguide (AFSIW) cavities and filters," *IEEE Transactions on Microwave Theory and Techniques*, vol. 66, no. 8, pp. 3611-3621, Aug. 2018.

[12] T. Martin, A. Ghiotto, T.P. Vuong, F. Lotz, and P. Monteil, "High performance air-filled substrate integrated waveguide filter post-process tuning using capacitive post," *IEEE MTT-S International Microwave Symposium*, Hawaii, HI, Jun. 2017, pp. 196-199.

[13] T. Martin, A. Ghiotto, T.P. Vuong, and F. Lotz, "Configurable perforated air-filled substrate integrated waveguide (AFSIW) for generic high-performance systems on substrate," *IEEE Transactions on Microwave Theory and Techniques*, to be published.

Conclusions and Future Work

This thesis has been focused on the demonstration of the Air-Filled SIW technological platform for space applications. In particular, the implementation of microwave filters and multiplexers has been investigated, up to the design of an Input Multiplexer (IMUX) for the need of ESA (European Space Agency) and CNES (Centre National d'Études Spatiales). The IMUX specifications proposed by these agencies address most of the filter problematic, such as high *Q*-factor, high selectivity, operating temperature range… In the next paragraphs, more details on the main conclusions and the foreseen future research derived from this research work are given.

Conclusions

A general introduction of the context and the microwave milestones applied to space applications are reported in Chapter 1. The context of the new space is given, explaining the need for future generations of satellite payload to benefit from an alternative technology (compared to conventional technology such as air-filled waveguides, dielectric resonator …). Different emerging technologies are also presented in this Chapter. The high interest of the AFSIW technology is also discussed with a comparison of the unloaded *Q*-factor, cost, and size of microwave resonators based on different technologies.

In Chapter 2, the AFSIW technology is introduced. The structure of the technology is presented, as well as a comparison in terms of unloaded *Q*-factor of the different ways to implement electric sidewalls. Theoretical, simulated, and measured transmission line performances allow highlighting the interest of the technology for high-performance applications. To characterize the technology, power-handling tests under vacuum conditions have been carried out at Cobham facilities. It was demonstrated that the fabricated transmission line prototype can handle 190 W in continuous wave input power under vacuum condition (10^{-5} mbar) with a stabilized temperature of 120 °C. Additionally, it was demonstrated in this Chapter that AFSIW technology is a good candidate for the introduction of microwave filter. A classical fourth-order filter operating at 21 GHz with a relative bandwidth of 1.43% was designed, fabricated, and measured. As the AFSIW is subjected to its implementation in future satellite payload, power-handling tests, including multipactor test, and corona test were performed. It was demonstrated in measurement that the filter showed no multipactor effect with a pulsed input power of 190 W. The corona test presented no corona discharge with an applied critical pressure of 26 mbar and input power of 9 W. To further investigate the capability of the technology, the input power was increased up to 10 W where a corona effect occurred.

A novel transmission line structure, named PAFSIW (Perforated Air-Filled SIW) was addressed in Chapter 3. This structure takes advantage of the multilayer aspect of the technology conjugated with conventional PCB process, namely THM (through-hole-mounted). The proposed transmission line is fabrication-tolerant compared to conventional geometry and allows the implementation of configurable PAFSIW components, such as phase shifters, resonators, and filters. The structure opens new possibilities to

configure and post-process components based on PAFSIW cavities. Indeed, a new post-process frequency tuning has been introduced, allowing fine-tuning a resonator frequency. The high density of the drilled via farm also allows discretizing the couplings in a microwave filter and to fine-tune it. The proposed structure also enhanced the thermal dissipation compared to its AFSIW counterpart.

In Chapter 4, the design of AFSIW filters with advanced performances has been investigated. The transmission zeros were introduced using the classical cross-couplings between non-adjacent cavities. It has been proved that the proposed implementation of cross-coupling ensures a high flexibility in filter design, as the transmission zeros positions can be controlled. Moreover, this technique is well suited for AFSIW multilayer aspect, as it maintains a high degree of compactness while being self-packaged. To demonstrate that, a variety of filters have been proposed, designed, and measured. The concept has been extended to higher order filter, faced to real industrial specifications. The prototyped filter showed good agreement between simulation and measurement thus pushing its implementation in a complex filtering system.

Two novel techniques to thermally compensate AFSIW resonators are proposed and demonstrated in Chapter 5. The techniques can be implemented not only on microwave filters but on any component based on AFSIW cavity. It is based on the introduction of a single or double dielectric slab that has an opposite behavior on the resonance frequency compared to dimension dilatations. The techniques are developed theoretically based on transmission line equivalent model and validated with eigenmode simulations. The techniques allow AFSIW filters to have a centre frequency thermal stability equal to less than 1 ppm/°C, which is comparable to high thermal stability and costly filters based on material such as Invar. The temperature compensation of transmission zeros created by cross-couplings is also discussed in this Chapter. It is demonstrated that the transmission zeros positions have a frequency thermal stability of less than 2.5 ppm/°C. This technique is implemented using the standard of PCB manufacturing, allowing the designers to fabricate the thermally-compensated filter in a single PCB fabrication without any additional process to introduce the temperature compensation.

Finally, the last objective of this thesis is the implementation of all the developed principles in a complex filter function, namely an Input Multiplexer (IMUX). The proposed IMUX has a manifold coupled configuration to implement 4 channel filters. The manifold coupled configuration is the best tradeoff in terms of insertion loss, compactness, and low mass. It is operating in the Ku-band and to save even more mass and allow a higher compactness, the herringbone geometric structure is chosen. To be able to minimize the total footprint of the IMUX and respect the near rejection specifications, transmission zeros, developed in Chapter 4 are introduced in each channel filter. Moreover, the temperature compensation, demonstrated in Chapter 5, is implemented in channel filters. It allows reducing the taken margins due to the thermal frequency shift as the filters behaves like Invar-made filters from -20 °C to 70 °C. Additionally, due to the stringent specifications, the post-process tuning techniques introduced in Chapter 3 can be applied on the future Engineering Model.

Future Work

Although many developments using the AFSIW technological platform for space applications have been carried out successfully, there are still some extended work and improvements that can be studied. The writer would like to suggest some interesting work that could be done to enhance the demonstrated results.

As it has been demonstrated in Chapter 2, a formula allowing calculating the cutoff frequency considering the dimension of the dielectric slab in the AFSIW technology was given. It was also concluded in this Chapter that the dielectric slabs have a negligible impact on the performances of the AFSIW transmission if they remain small. It could be of high interest to theoretically study the behavior of a cavity loaded with dielectric slabs in terms of insertion loss, propagation mode behavior, tradeoff between size and unloaded *Q*-factor.

The work introduced in Chapter 3 using a configurable PAFSIW transmission line could be extended to the implementation of complex System-on-Substrates, where basic components, such as phase shifters are essential. A classic example would be the implementation of a feeding network for antenna arrays. In fact, antennas based on AFSIW technology have already been demonstrated in a previous work. Implementing a feeding network based on PAFSIW topology could be of high interest as the different phase shifts between antennas can be controlled thank to the through-hole-mounted (THM) process. Moreover, in this Chapter, a discretized coupling iris has been developed. This abacus given for this coupling iris is correct for a particular frequency. It could be interesting to extend the study to other frequencies. One could also implement a genetic algorithm to reach the optimum design with the discretized coupling coefficients. The thermal behavior of AFSIW filters could be studied to locate the hot points in the filter and find an optimum implementation of the PAFSIW sections to find a better tradeoff between thermal dissipation and insertion loss. It should also be of high interest to characterize the PAFSIW structure in EMC (Electromagnetic compatibility).

Chapter 4 demonstrates the implementation of advanced filter functions introducing transmission zeros. An interesting work to carry out could be to fabricate hundreds of filters in order to have a real yield analysis on such function. This yield analysis could help us characterize the achievable performances of the technology without any post-process. Another relevant study could be the implementation of imaginary transmission zeros instead of real transmission zeros. Even though it has already been studied in the literature, it could help to introduce more advanced filter response, such as self-equalized filters. Moreover, as a part of the signal is propagating through a dielectric, it could be pertinent to study the behavior of the cross-couplings in power-handling and thermal tests. Finally, the introduction of transmission zeros can also be created by means of non-resonating modes or extracted pole techniques. It should be a nice work to focus on. It is probably linked to the study of a dielectric loaded cavity proposed for the future work of Chapter 2.

It has been demonstrated in Chapter 5 that temperature compensation techniques can be implemented in AFSIW technology using a single and double dielectric slab. An obvious extended work could be to study the case of a triple and quadruple dielectric slab. Following this study, it should be of a particular interest to establish a comparison between the different techniques in terms of unloaded *Q*-factor, compactness, ease of integration, versatility to filter topologies and achievable thermal stability. The proposed work in this Chapter used Rogers RT/Duroid 6010. A possible idea is to characterize the best existing material to achieve a

temperature compensation and establish a tradeoff between unloaded *Q*-factor, compactness, ease of integration, versatility to filter topologies and achievable thermal stability.

Chapter 6 presents the implementation of an AFSIW IMUX. One could ask if the AFSIW technology is suitable for Output Multiplexer (OMUX) applications. Thus, an AFSIW OMUX could be designed, fabricated, and measured to know the power-handling and thermal limits of this technology. An interesting idea in the so-called System-on-Substrate could be to integrate more functions into the IMUX. A low-pass filter to eliminate the spurious peaks could be integrated in the IMUX. Based on the same idea, it is also possible to imagine an implementation of an isolator coupled IMUX configuration. This configuration could help the filter designer a lot as it allows the implementation of a modular concept, independent of the operating frequency or bandwidth of the channel filters.

Generally speaking, the AFSIW technology, taking advantage of the PCB process, could be investigated for the development of other low-cost passive components. Speaking of, the work done in this thesis has led to another thesis investigating the use of the AFSIW technology to develop Ka-band circulators and isolators. As it is based on PCB process, the AFSIW technology is also well-suited to implement active functions, such as surface-mounted LNAs or PAs and could lead to the development of low-cost and self-packaged active modules.

List of Publications

The list of publications realized, and awards obtained during my Ph.D., are given below, with a subdivision in: International Journals, International Conferences, International Workshops, National Conferences, Awards, and Patents.

International Journals Publications

- **T. Martin**, A. Ghiotto, T.P. Vuong and F. Lotz, "Self-temperature-compensated air-filled substrate integrated waveguide (AFSIW) cavities and filters," in *IEEE Transactions on Microwave Theory and Techniques*, vol. 66, no. 8, pp. 3611-3621, Aug. 2018.

- **T. Martin**, A. Ghiotto, T.P. Vuong and F. Lotz, "Configurable perforated air-filled substrate integrated waveguide (AFSIW) for generic high-performance systems on substrate," in *IEEE Transactions on Microwave Theory and Techniques*, vol. 67, no. 11, pp. 4308-4321, Nov. 2019.

- **T. Martin**, A. Ghiotto, T.P. Vuong and F. Lotz, "Single slab self-temperature-compensated air-filled substrate integrated waveguide (AFSIW) cavities and quasi-elliptic filters," in *IEEE Transactions on Microwave Theory and Techniques*, (Submitted in August 2019, Revision resubmitted in January 2020).

- **T. Martin**, A. Ghiotto, T.P. Vuong and F. Lotz, "Compact G-CPW fed AFSIW filters for systems on substrate," in *IEEE Microwave and Wireless Components Letters*, (Submitted in October 2019).

- N.H Nguyen, A. Ghiotto, T.P. Vuong, A. Vilcot, **T. Martin**, and K. Wu, "Dielectric slab air-filled substrate integrated waveguide (AFSIW) bandpass filters," in *IEEE Microwave and Wireless Components Letters*, (Submitted in January 2020).

International Conferences Publications (*Speaker)

- **T. Martin**, F. Parment, A. Ghiotto*, T. P. Vuong, and K. Wu, "Air-Filled SIW interconnections for high performance millimeter-wave circuit and system prototyping and assembly," *IEEE MTT-S International Conference on Numerical Electromagnetic and Multiphysics Modeling and Optimization for RF, Microwave, and Terahertz Applications,* Seville, 2017, pp. 302-304.

- **T. Martin***, A. Ghiotto, T.P. Vuong, F. Lotz, and P. Monteil, "High performance air-filled substrate integrated waveguide filter post-process tuning using capacitive post," *IEEE MTT-S International Microwave Symposium*, Honolulu, HI, Jun. 2017, pp. 196-199.
  - 2017 IEEE MTT-French Chapter Honorable Mention Award

- **T. Martin***, A. Ghiotto, A. Marque, T.P. Vuong, F. Lotz, P. Monteil, and L. Carpentier, "Broadband air-filled SIW to waveguide transition for interconnect, instrumentation and measurement applications," *IEEE MTT-S International Microwave Workshop Series on Advanced Materials and Processes,* Italy, Pavia, Sep. 2017.

- A. Ghiotto, F. Parment, **T. Martin***, T. P. Vuong, and K. Wu, "Air-filled substrate integrated waveguide — A flexible and low loss technological platform," *13th International Conference on*

Advanced Technologies, Systems and Services in Telecommunications, Nis, 2017, pp. 147-149. (invited paper)

- **T. Martin***, A. Ghiotto, F. Lotz, and T.P. Vuong, "Fabrication-tolerant reconfigurable AFSIW filters based on through-hole mounted metallic posts for versatile high performance systems," *IEEE MTT-S International Microwave Symposium*, Philadelphia, PA, Jun. 2018.
  - 2018 IEEE MTT-French Chapter Best Student Paper Award

- **T. Martin***, A. Ghiotto, T.P Vuong, and F. Lotz. "Fabrication-tolerant AFSIW filters based on quadruplet through-hole mounted inductive posts," *7th International Workshop on Microwave Filters (IWMF)*, Apr 2018, Noordwijk, Netherlands. 2018.
- **T. Martin***, A. Ghiotto, F. Lotz, and T.P Vuong. "Air-filled SIW filters for K to E-band substrate integrated systems," *IEEE MTT-S International Conference on Numerical Electromagnetic and Multiphysics Modeling and Optimization for RF, Microwave, and Terahertz Applications,* Reykjavik, 2018.

- **T. Martin***, A. Ghiotto, T.P. Vuong, and F. Lotz, "Fabrication-tolerant AFSIW filters based on quadruplet through-hole mounted inductive posts," *2018 48th European Microwave Conference (EuMC)*, Madrid, Spain, 2018, pp. 749-752.

- A. Ghiotto*, N. H. Nguyen, T.P. Vuong, **T. Martin**, K. Wu, "High performance air-filled SIW technology for antenna beam forming networks," *PHAROS Conference*, Bordeaux, France, 5-7 Dec. 2018.

- **T. Martin***, A. Ghiotto, F. Lotz, and T.P Vuong. "Recent advances in filter design using the AFSIW technological platform," *IEEE 23rd Workshop on Signal and Power Integrity (SPI),* 18-21 Jun. 2019, Chambery, France.

- N.H Nguyen*, A. Ghiotto, **T. Martin**, A. Vilcot, K. Wu, and T.P. Vuong "A 90° self-compensating slab Air-Filled Substrate Integrated Waveguide phase shifter," *IEEE MTT-S International Microwave Symposium*, Boston, MA, Jun. 2019.

- **T. Martin***, A. Ghiotto, T.P. Vuong, F. Lotz, and K. Wu "Compact quasi-elliptic and highly selective AFSIW filter with multilayer cross-coupling," *IEEE MTT-S International Microwave Symposium*, Boston, MA, Jun. 2019.
  - Selected as IMS2019 Student Paper Competition Finalist
  - 2019 IEEE MTT-French Chapter Best Student Paper Award

- I. Marah*, A. Ghiotto, J-M. Pham, **T. Martin**, and A. Boisse "AFSIW termination with full and partial-height absorbing material loading," *2019 49th European Microwave Conference (EuMC)*, Paris, France, 2019.

International Conferences Workshops Publications (*Speaker)

- A. Ghiotto* and **T. Martin***. "Air-filled SIW – A disruptive technological platform," 7th International Workshop on Microwave Filters (IWMF), Apr 2018, Noordwijk, Netherlands. 2018. (invited workshop)

- A. Ghiotto*, **T. Martin***, T-P. Vuong, and F. Lotz "AFSIW technology for space application filters," *2019 49th European Microwave Conference (EuMC)*, Paris, France, 2019. (invited workshop)

National Conferences Publications (*Speaker)

- **T. Martin***, A. Ghiotto, T.P. Vuong, F. Lotz, et P. Monteil, "Accord d'un filtre intégré haute performance en SIW-creux après fabrication en utilisant des plongeurs capacitifs," *Journées Nationales Microondes*, France, Saint-Malo, May. 2017.

- **T. Martin**, A. Ghiotto, A. Marque, T.P. Vuong*, F. Lotz, P. Monteil, et L. Carpentier "Transition large bande guide d'onde vers SIW creux pour des applications d'instrumentation et mesures," *Assemblée générale du GDR-Ondes*, France, Sophia Antipolis, Oct. 2017.

- **T. Martin***, A. Ghiotto, F. Lotz, et T.P. Vuong, "Compensation thermique de cavité et filtre AFSIW," Journées Nationales Microondes, France, Caen. May. 2019.

- **T. Martin***, A. Ghiotto, F. Lotz, et T.P. Vuong, "Filtre AFSIW robuste et configurable pour applications agiles," *Journées Nationales Microondes*, France, Caen, May. 2019.

- **T. Martin***, A. Ghiotto, F. Lotz, et T.P. Vuong, "Filtre AFSIW quasi-elliptique avec cross-coupling multicouche," *Journées Nationales Microondes*, France, Caen, May. 2019.

Awards

- 2017: IEEE MTT-S French chapter honorable mention award at the International Microwave Symposium Conference

- 2018: IEEE MTT-S French chapter best student paper award at the International Microwave Symposium Conference

- 2019: IEEE MTT-S French chapter best student paper award at the International Microwave Symposium Conference

- 2019: Selected as International Microwave Symposium (IMS) student paper competition finalist

Patents

- A. Ghiotto, F. Lotz, **T. Martin**, A. Marque, et P. Monteil, "Composant micro-ondes et procédé de réglage associé," dépôt brevet d'invention / patent registration, FR 16 61964, Dec. 2016.

- A. Ghiotto, F. Lotz et **T. Martin**, "Composant micro-ondes et procédé de fabrication associé", dépôt brevet d'invention / patent registration, FR 17 63412, Dec. 2017.

Other

- A. Ghiotto, **T. Martin**, and D. Gaidioz, "MTT-S Bordeaux, France, Student Branch Chapter BEE Week 2017 [MTT Society News]," *IEEE Microwave Magazine*, vol. 19, no. 4, pp. 122-124, Jun. 2018.

Titre : Filtres et multiplexeurs hyperfréquences en technologie Air-Filled Substrate Integrated Waveguide pour applications spatiales

Résumé :

L'émergence de nouvelles applications micro-ondes et millimétriques dans les secteurs de l'automobile et des communications, y compris l'Internet des objets (IoT), la cinquième génération de mobile (5G) et le nouvel espace, nécessite le développement de nouvelles technologies alternatives offrant un compromis approprié en termes de taille, de poids, de puissance et de coût (SWaP-C). Ce changement de paradigme est essentiellement dû à l'augmentation du débit de données, conduisant à la croissance des différentes bandes passantes. Étant donné qu'un nombre de plus en plus important de systèmes sont en concurrences pour l'occupation du spectre fréquentiel, la communauté des hyperfréquences est poussée à développer de nouveaux systèmes innovants à des fréquences plus élevées avec une efficacité accrue et un degré d'intégration élevé.

Ce changement de paradigme a fortement stimulé le développement de systèmes micro-ondes et millimétriques à faible coût, à haute performance, hautement intégrés, compacts et pouvant être produits en masse. Au cœur d'un système, les filtres micro-ondes et millimétriques sont des dispositifs essentiels permettant de sélectionner l'information utile. Les filtres à faibles pertes sont très recherchés dans les circuits d'émission et de réception pour obtenir un rendement élevé et un faible niveau de rapport signal à bruit. La façon conventionnelle d'obtenir de faibles pertes est d'utiliser des résonateurs à haut facteur de qualité. Pour la plupart des applications à haute performance, la technologie des guides d'ondes rectangulaires (RWG) est utilisée pour être conforme aux spécifications sévères requises par l'industrie. Néanmoins, cette technologie devient prohibitive en termes de coût lorsqu'une production de masse est nécessaire. Pour réduire le coût de ces composants, l'utilisation de la technologie émergente des guides d'ondes intégrés au substrat (SIW) a été proposée. Cette technologie bénéficie d'un faible coût de fabrication et est facilement intégrable dans un système basé sur des circuits imprimés. La technologie SIW est une bonne candidate pour les applications qui nécessitant un faible coût avec des performances électriques moyennes, mais pour les applications de hautes performances, comme le nouvel espace, les performances atteintes ne sont pas conformes aux spécifications demandées, ce qui rend l'implémentation de la technologie SIW restrictive pour les applications haute performance.

Récemment, le guide d'ondes intégré au substrat rempli d'air (AFSIW), basé sur les procédés standards de circuit imprimé multicouche (PCB), semblerait répondre aux exigences des applications de constellation de satellites, car il offre un compromis entre les technologies classiques RWG et SIW. Cette structure vise à réduire considérablement les pertes d'insertion du milieu de propagation, tout en maintenant le fort aspect d'intégration à faible coût. C'est donc une bonne candidate pour la future génération de charges utiles de satellites.

Compte tenu du contexte présenté, les travaux menés au cours de cette thèse de doctorat ont été orientés vers la mise en œuvre de la technologie AFSIW pour les nouvelles applications spatiales. Une attention particulière a été accordée à la proposition, à l'analyse, au développement et à la mise en œuvre de concepts novateurs et originaux pour les fonctions de filtrage hyperfréquence. Le travail proposé est basé sur la théorie

classique des guides d'ondes en tirant parti des procédés de fabrication standards des circuits imprimés pour permettre le développement de filtres et de multiplexeurs répondant aux spécifications des applications spatiales.

Cette thèse de doctorat met en lumière les dernières avancées réalisées dans le développement de filtres hyperfréquences et de multiplexeurs utilisant la technologie AFSIW. Elle détaille, en partant des idées de départ, des démonstrations théoriques, des simulations et des validations expérimentales avec les prototypes fabriqués. Les résultats de ces travaux sont prometteurs et démontrent la pertinence de la technologie pour sa mise en œuvre dans les futurs systèmes de charges utiles de satellites. Il est à noter qu'un sous-système de filtrage pour charge utile de satellite a été développé dans cette thèse pour répondre aux besoins de l'Agence Spatiale Européenne (ESA) et du Centre National d'Études Spatiales (CNES). Les concepts démontrés à partir de cette thèse peuvent être considérés comme une bonne base pour le développement et la vulgarisation de la technologie AFSIW, non seulement pour les applications spatiales, mais aussi pour les systèmes terrestres.

Mots clés : Guide d'ondes intégré au substrat rempli d'air (AFSIW), filtres, multiplexeurs, applications spatiales.

Unité de recherche

Laboratoire IMS, CNRS UMR5218, 351 Cours de la Libération, 33400 Talence

Title : Air-Filled Substrate Integrated Waveguide (AFSIW) Filters and Multiplexers for Space Applications

Abstract:

The emergence of novel microwave and millimeter-wave applications in the automotive and communication sectors including the internet of things (IoT), the fifth generation of mobile (5G), and the new space, require the development of new alternative technologies providing a suitable tradeoff in terms of size, weight, power, and cost (SWaP-C). This change of paradigm is essentially due to the increase of data rate, leading to the growth of bandwidth. As a substantially increasing number of systems are competing for frequency spectrum occupancy, the microwave community is pushed to develop new innovative systems at higher frequency with an increased efficiency.

This change of paradigm has highly stimulated the development of low-cost, high-performance, highly integrated, compact, and mass-producible microwave and millimeter-wave systems. At the heart of a system, microwave and millimeter-wave filters are essential devices allowing to select the desired information. Low-loss filters are highly desired in transmitter and receiver circuits to achieve high efficiency and low noise figures. The conventional way to achieve low-loss performance is to use high quality factor resonators. For most high-performance applications, the air-filled rectangular waveguide (RWG) technology is used to comply with the severe specifications requested by the industry. Nevertheless, this technology becomes prohibitive in terms of cost where a mass-production is needed. To reduce the cost of such components, the use of the so-called substrate integrated waveguide (SIW) emerging technology has been proposed. This technology benefits from low-cost and highly integrated properties. The SIW technology is a good candidate for application that needs low-cost with medium insertion loss, but for high performance applications, such as the emerging new space, the achieved performances are not compliant with the severe specifications, making the implementation of the SIW technology for high performance applications restrictive.

Recently, the alternative air-filled substrate integrated waveguide (AFSIW), based on multilayer printed circuit board (PCB) is expected to fulfill satellite constellation application requirements as it offers a compromise between the conventional RWG and SIW technologies. This structure aims to dramatically reduce the insertion loss of the propagation medium, while maintaining the high integration and low-cost aspect. Hence making it a potential good candidate for future generation of satellite payloads.

Taking into consideration the presented context, the work carried out during this Ph.D. thesis has been led towards the implementation of the AFSIW for the new space applications. A particular attention has been given to the proposal, analysis, development, and implementation of innovative and original concepts for microwave filtering functions. The proposed work is based on the classic waveguide theory taking advantage of the standard PCB process to allow the development of improved and novel filters and multiplexer for space applications.

This Ph.D. thesis highlights the last advances made on the development of microwave filters and multiplexer using the AFSIW technology. This includes the starting ideas, theoretical demonstrations, simulations, and experimental validations with fabricated prototypes. The results of this work are promising and demonstrate the relevance of the technology for its implementation in future satellite payload systems. In fact, a sub-system of a satellite payload has been developed in this thesis to answer the need of European Space

Agency (ESA) and Centre National d'Études Spatiales (CNES). The demonstrated concepts developed in this thesis can be considered as a good base to further develop and popularize the AFSIW technology, not only for space applications but also for ground systems.

Keywords: Air-filled substrate integrated waveguides (AFSIW), filters, multiplexers, space applications.

Research Institute

Laboratoire IMS, CNRS UMR5218, 351 Cours de la Libération, 33400 Talence